Investigating the Reactivities and Stabilities of Protic Small Molecule Bioregulators

by

Amanda G. Davis

A dissertation accepted and approved in partial fulfillment of the

requirements for the degree of

Doctor of Philosophy

in Chemistry

Dissertation Committee:

Dr. Amanda K. Cook, Chair

Dr. Michael D. Pluth, Advisor

Dr. Ramesh Jasti, Core Member

Dr. Raghuveer Parthasarathy, Institutional Representative

University of Oregon

Spring 2025

© 2025 Amanda G. Davis

This work is openly licensed via CC BY-NC-ND 4.0.



DISSERTATION ABSTRACT

Amanda G. Davis

Doctor of Philosophy in Chemistry

Title: Investigating the Reactivities and Stabilities of Protic Small Molecule Bioregulators

Protic small molecule bioregulators (PSMBs) are a class of molecules that serve important roles in biology and are essential for maintaining various physiological processes. PSMBs are defined by their physiological relevance and protic nature, as opposed to gasotransmitters, which are narrow in definition, focus on physical state, and exclusively include CO, NO, and H_2S. While gasotransmitters are known for their toxicity at unregulated high concentrations, at low physiological concentrations they are essential bioregulators. PSMBs, however, often are less toxic and also participate in important bioregulatory processes including cellular signaling, cardioprotection, vasodilation, angiogenesis, and inducing anti-/pro-inflammatory responses, among many others. Many PSMBs are the result of intermolecular gasotransmitter crosstalk and/or are regarded as gasotransmitter storage vehicles as they can release gasotransmitters upon their decomposition.

The physiological pathways that PSMBs are involved in are under investigation, however their distinct molecular reactivities and stabilities are still not well understood. Herein, Chapter 1 gives a brief review of select PSMBs and their relevance in biology, endogenous generation, and crosstalk mechanisms. Building off the importance of PSMBs, Chapter II discusses the modes of interconversion between SNO^- and $SSNO^-$, two PSMBs that are regarded as H_2S and NO crosstalk species. Reported are new experimental insights into the fundamental reaction chemistry of pathways to form SNO^- and $SSNO^-$, including mechanisms for proton-mediated interconversion. In addition, new modes of reactivity are demonstrated with other sulfur-containing potential crosstalk species, including carbonyl sulfide (COS). Additionally, Chapters III & IV discuss the stabilities of several PSMBs and other anions using molecular recognition with various rationally designed synthetic C–H hydrogen bonding anion receptors. Using a series of imidazole and imidazolium host molecules, the role of preorganization and charge on anion binding is investigated using both solution-state as well as solid-state characterization methods.

The anions investigated range from PSMBs such as HS^-, NO_2^-, and NO_3^-, to more commonly studied anions within the supramolecular community, Cl^- and Br^-. Finally, Chapter V summarizes the impact of this work in the field as well as current outlooks and future perspectives on the molecular reactivities and stabilities of PSMBs.

Supplemental materials for Chapters II–IV can be found in the appendices.

This dissertation includes previously published and unpublished co-authored materials.

CURRICULUM VITAE

NAME OF AUTHOR: Amanda G. Davis

GRADUATE AND UNDERGRADUATE SCHOOLS ATTENDED:

University of Oregon, Eugene OR
California Polytechnic University, San Luis Obispo CA
Moorpark College, Moorpark CA

DEGREES AWARDED:

Doctor of Philosophy, Chemistry, 2025, University of Oregon
Master of Science, Chemistry, 2023, University of Oregon
Bachelor of Science, Chemistry, 2020, California Polytechnic University
Associate of Science, Chemistry, 2018, Moorpark College

PROFESSIONAL EXPERIENCE:

Graduate Researcher, University of Oregon, 2020–2025
Graduate Employee, University of Oregon, 2020–2024
Undergraduate Researcher, California Polytechnic University, 2019–2020
Learning Assistant, California Polytechnic University, 2019
Biochemistry Stockroom Assistant, California Polytechnic University, 2019

GRANTS, AWARDS, AND HONORS:

F31 NRSA Fellowship, The Development of Novel Anion Receptors for Reactive Sulfur, Oxygen, and Nitrogen Species, National Institute of Health, 2024

Women in Graduate Science Leadership Award, 2024

A Community for Minorities in STEM, Community Engagement Travel Award, 2024

NSF Research Traineeship, Molecular Probes and Sensors for Complex Environments, National Science Foundation, 2021

Promising Scholar Award Fellowship, University of Oregon, 2020

Frost Summer Undergraduate Research Fellowship, California Polytechnic University, 2019

PUBLICATIONS:

Davis, A. G.; Zakharov, L. N.; Pluth M. D. Probing the Reversible Binding of Anionic Reactive Sulfur and Nitrogen Species in Imidazolium Receptors with Directional C-H Hydrogen Bonds. *Inorg. Chem*. **2025**, *64* (15) 7774–7783. https://pubs.acs.org/doi/10.1021/acs.inorgchem.5c00821

Davis, A. G.; Pluth, M. D. Experimental Insights into the Formation, Reactivity, and Crosstalk of Thionitrite (SNO^-) and Perthionitrite ($SSNO^-$). *Angew. Chem., Int. Ed.* **2025**, *64* (1), e202413092. https://doi.org/10.1002/anie.202413092.

Davis, A. G.; Zakharov, L. N.; Pluth, M. D. Reversible Hydrosulfide (HS^-) Binding Using Exclusively C–H Hydrogen-Bonding Interactions in Imidazolium Hosts. *Inorg. Chem.* **2024**, *63* (6), 3057–3062. https://doi.org/10.1021/acs.inorgchem.3c03922

Hurst, M. H., Davis, A. G., Cook, A. K. The Influence of Silane Steric Bulk on the Formation and Dynamic Behavior of Silyl Palladium Hydrides. *Organometallics* **2022** *41* (8), 997-1005. https://doi.org/10.1021/acs.organomet.2c00055

ACKNOWLEDGMENTS

I have to start by thanking my brother Jacob, for always challenging me to become a better student, being my biggest cheerleader, and being my biggest motivator. Sorry for always blaming you whenever science didn't go my way. Thank you to my parents for always encouraging me to pursue my passions and being endlessly supportive throughout my academic career. I am forever grateful for your love. Thank you to the Galan Families and my cousin Ally, every single one of you inspire me and I love you so very much.

To all the friends and family I've made in Oregon, thank you! Willow Davis, thank you for being such an incredible friend, roommate, and birthday buddy. Your silliness always brightens up a room. Haley Smith, thank you for unwillingly assimilating into our friend group and becoming one of my best friends and lab mates. Thank you to the Smith Family, for letting me join in on the family gatherings and to Hayden Cooksy for letting me thirdwheel constantly. Allison LaSalvia, thank you for weaseling your way into the friend group and always being down to kiki. Harrison Reid, thank you for bringing Hannah Beskind into our lives and for living in my backyard. Alex Rosen, the greatest dungeon master, thank you for putting up with our party's shenanigans and for always being down to go to an Em's game and heckle the players. Nick D'Antona, thank you for being such a joy to be around, but I'll never forgive you for abandoning us for Berkeley. Finally, thank you to everyone I've ever had the pleasure of playing volleyball with.

I would also like to thank Prof. Mike Pluth for pushing me to be a better scientist. I am endlessly grateful for you as my advisor and all the endless hours spent mentoring me as a student, writer, communicator, and chemist. I look back at the fledgling student I was during first year and see all the growth I've made and challenges I've overcome over the last five years, thanks to your support as my advisor. You've helped me to learn whether or not it's worth it to chase down that rabbit hole in pursuit of great science. I appreciate you putting up with the Haley-Andy Double Trouble for so many years. I would also like to thank my committee for all their support and feedback throughout the years, Prof. Amanda Cook, Prof. Ramesh Jasti, and Prof. Raghu Parthasarathy.

To the Pluth lab, past and present, thank you for your support, companionship, and advice. Specifically, I would like to thank Keyan Li for putting up with me and all my nonsense.

Thank you for all the helpful lab advice, despite my grumpiness about getting roped into doing additional experiments. Thank you to Dr. Toby Sherbow for always being down to grab a drink at Oakshire. Dr. Shivaaaaaaa Moaven thank you for your endless optimism and positivity! Thank you, Dr. Turner Newton, for being such an incredible mentor and for showing me that grad school isn't all serious, all the time. I would also like to especially thank all my other previous mentors, especially Dr. Kiana Kawamura, Dr. Alison Chang, and Dr. Annie Gilbert, who, whether you knew or not, really helped me get through the trials of first year. Dr. Ismail, Dr. Michael Wade Wolfe, Dr. Arman Garcia, Dr. Kaylin Fosnacht, Jasmine Collins, Juan Hernandez, Mia Ramos, Kaitlyn Klotz, Jonathan Pines, Andrew Sosa, Addison Sattler, Aleanna Lengkong, Christopher Steven, thank you all.

Thank you to the Alliance for Diversity in Science and Engineering for helping me realize the importance of DEI and community outreach. Thank you to all members, past and present, for their companionship and support. Thank you to everyone at Lane Community College who helped me establish my passion project: Science by the Slice – A STEM Seminar Series. Specifically, thank you Dr. Jeneva Anderson, for being incremental to the success of ADSE's LCC outreach throughout the years.

I would be remiss to not shoutout the Los Angeles Dodgers for winning two championships while I was in Oregon, thank you for being the perfect company while writing this dissertation. Looking forward to many more perfect summer days spent in Chavez Ravine.

Lastly, I would like to thank the University of Oregon Chemistry Department, specifically the academic support unit that keeps the department running. I would like the acknowledge my various sources of scholarships and fellowships that enabled my research. I would like to thank the Division of Graduate Studies for the 2020-21 Promising Scholar Award, Women in Graduate Science for the 2024 Leadership Award, and Community for Minorities in STEM for the 2024 Community Engagement Travel Award (that I forgot to use, my bad). I would like to acknowledge the funding sources that supported my research projects including the National Science Foundation (CHE-2107602), the NSF Research Trainee Program (DGE-2022168), and the National Institute of Health (F31GM151758).

DEDICATION

For Jacob M. Davis

FLY EVER HIGHER

TABLE OF CONTENTS

Chapter Page

I. PROTIC SMALL MOLECULE BIOREGULATORS 17

1.1 Introduction 17

1.2 Nitric Oxide and Related Reactive Nitrogen Species (RNS) 20

1.3 Hydrogen Sulfide and Related Reactive Sulfur Species (RSS) 22

1.4 Thionitrite and Perthionitrite: NO/H_2S Crosstalk Species 24

1.5 Dioxygen and Related Reactive Oxygen Species (ROS) 25

1.6 Hydrogen Selenide and Related Reactive Selenium Species (RSeS) 27

1.7 Hydrogen Cyanide and Related Cyano-Species 29

1.8 Conclusions 30

II. EXPERIMENTAL INSIGHTS INTO THE FORMATION, REACTIVITY, AND CROSSTALK OF THIONITRITE (SNO^-) AND PERTHIONITRITE ($SSNO^-$) 32

2.1 Introduction 32

2.2 Results and Discussion 35

2.2.1 Proton-Mediated $SSNO^-$ Formation 35

2.2.2 Identification of Nitrogen-Containing Products 39

2.2.3 Reactions with SNO^-/$SSNO^-$ with COS 41

2.3 Conclusions 43

III. REVERSIBLE HYDROSULFIDE (HS^-) BINDING USING EXCLUSIVELY C–H HYDROGEN-BONDING INTERACTIONS IN IMIDAZOLIUM HOSTS 45

3.1 Introduction 45

3.2 Results and Discussion 47

3.2.1 Determination of Binding Affinities (K_a) 47

Chapter Page

3.2.2 Solid State Binding 51

3.3 Conclusions 53

IV. PROBING THE REVERSIBLE BINDING OF ANIONIC REACTIVE SULFUR AND NITROGEN SPECIES IN IMIDAZOLIUM RECEPTORS WITH DIRECTIONAL C-H HYDROGEN BONDS 54

4.1 Introduction 54

4.2 Results and Discussion 57

4.2.1 Anion and Receptor Scope 57

4.2.2 Solution State Binding 59

4.2.3 Structural Characterization of Host-Guest Interactions 62

4.3 Conclusions 66

V. CONCLUSIONS 68

APPENDICES 70

A. Chapter II Supplementary Information 70

A1. Additional Schemes 70

A2. Experimental Methods 70

A3. UV-Vis/IR Experiments 73

A4. NMR Experiments 88

A5. GC Headspace Analysis 95

B. Chapter III Supplementary Information 96

B1. Experimental Methods 96

B2. ^{1}H NMR Titrations 106

B3. X-Ray Crystallographic Data 121

Chapter Page

B4. CCDC Database Search Parameters..... 123

C. Chapter IV Supplementary Information..... 124

C1. Experimental Methods 124

C2. ^{1}H NMR Titrations 142

C3. X-Ray Crystallography 194

REFERENCES CITED..... 200

LIST OF FIGURES

Figure Page

1. **Figure 1.1**. Different classes of various biologically relevant small molecules. The subclass of protic small molecule bioregulators is highlighted in red..... 19

2. **Figure 1.2**. Comparison of the pK_a values of various physiologically relevant small molecules. Each pK_a value corresponds to reported values for H^+ dissociation of the species listed..... 20

3. **Figure 2.1**. UV-Vis spectrum of [PPN][SNO] (0.50 mM, λ_{max} = 332 nm) in MeCN, treated with glacial AcOH (1 equiv.) results in SSNO formation (λ_{max} = 445 nm) over 100 minutes 37

4. **Figure 2.2.** UV-vis spectra of aliquots taken from a solution of [PPN][SNO] (0.50mM, ★, λ_{max} = 332 nm) in MeCN, treated with HCl (0.5 equiv.) resulting in the instantaneous formation of $SSNO^-$, (•, λ_{max} = 445 nm). Treatment of the resultant $SSNO^-$ with PPh_3 (excess) reforms SNO^- (▪, λ_{max} = 332 nm) over 3 hours. Inset:^{15}N NMR (versus NH_3 (*l*)) spectra of [PPN][$S^{15}NO$] (18 mM, CD_3CN) treated with HCl (0.5 equiv.) followed by PPh_3 (1 equiv.)..... 38

5. **Figure 2.3**. (top) Summary of cascading reactions from NO_2^- treated with COS to generate SNO^-, $SSNO^-$, and S^0. (bottom) UV-Vis spectra of $SSNO^-$ generated by treatment of treating [PPN][SNO] with COS (•, λ_{max} = 445 nm in MeCN) decomposing into S^0 (▲ , $\lambda \sim 300$ nm) over 2 hours. Inset: Stacked ^{15}N NMR spectra of [PPN][$^{15}NO_2$] in CD_3CN treated with COS (excess) to generate $S^{15}NO^-$, which further reacts with excess COS to generate $SS^{15}NO^-$ 42

6. **Figure 3.1**. (a–c) Prior examples of H-bonding host molecules demonstrated to bind HS^- and (d) this work using exclusively C–H H-bond donors for HS^- recognition 47

7. **Figure 3.2**. Imidazole/imidazolium receptors **1**–**4** 48

8. **Figure 3.3**. (a) General guest binding scheme for binding HS^- in $\mathbf{4}^{2+}$. (b) Representative ^{1}H NMR titration of $\mathbf{4}^{2+}$ with [TBA][SH]. General conditions: $[\mathbf{4}^{2+}]_i$ = 0.97 mM, CD_3CN, 25 °C. The yellow highlighted peak at negative ppm in panel (b) corresponds to the HS^- signal..... 49

9. **Figure 3.4**. (a) Side on and (b) top views of the molecular structure of the $[(\mathbf{4}^{2+})_2 \cdot HS^-][PF_6]_3$. Thermal ellipsoids are drawn at a 50% probability level. Noninteracting H atoms, solvent molecules, and PF_6^- counter anions are omitted for clarity..... 52

Figure Page

10. **Figure 4.1**. Selected prior examples of H-bonding receptors demonstrated to bind (a) HS^- or (b) NO_2^- 56

11. **Figure 4.2**. Imidazolium receptors **1–7**$^{3+}$ used to investigate anion binding 58

12. **Figure 4.3**. (a) Example of the general guest binding scheme for binding X^- in **5**$^{2+}$. (b) Representative ^{1}H NMR titration of **5**$^{2+}$ with [TBA][SH]. The yellow highlighted peak at negative ppm corresponds to the HS^- signal. (c) Representative ^{1}H NMR titration of **5**$^{2+}$ with [TBA][NO_2]. General conditions: [**5**$^{2+}$]$_i$ = 1.58 mM, CD_3CN, 25 °C 60

13. **Figure 4.4.** (a) Summary of the 1:1 binding affinities (Log($K_{a,\,1:1}$)) of receptors **2**$^+$–**7**$^{3+}$ with each anion. (b) The 1:1 binding affinity (Log($K_{a,1:1}$)) of receptors **4**$^{2+}$–**7**$^{3+}$ with Cl^-, Br^-, NO_2^-, and NO_3^- (data in ●) as a function of anion volume (Å^3). Measured Log($K_{a,1:1}$) values for HS^- (△) for each receptor do not fit with the general trend. Displayed linear fits and R^2 values exclude HS^- 62

14. **Figure 4.5**. Molecular structure of each macrocyclic host-guest complex with C–H···X^- contacts highlighted. (a) 5^{2+}•NO_2^-, (b) 5^{2+}•NO_3^-, (c) 5^{2+}•Cl^-, (d) 5^{2+}•Br^-, (e) 5^{2+}•PF_6^-, (f) 6^{2+}•HS^-, (g) 6^{2+}•NO_3^-, (h) 6^{2+}•Cl^-, (i) 6^{2+}•Br^-, (j) 6^{2+}•PF_6^-. Thermal ellipsoids are drawn at a 50% probability level. Noninteracting H atoms, solvent molecules, and additional anions outside the binding pocket are omitted for clarity..... 63

15. **Figure 4.6**. (a) Molecular structure of unbound, chair-like **6**$^{2+}$•2PF_6^- and (b) bowl-like **6**$^{2+}$•2NO_3. Thermal ellipsoids are drawn at a 50% probability level. Noninteracting H atoms, solvent molecules, and additional anions are omitted for clarity..... 64

LIST OF TABLES

Table Page

1. **Table 3.1.** Binding Affinities for HS^- and Cl^- in Receptors 1–4 in CD_3CN 50

2. **Table 4.1.** Binding Affinities for anions in receptors $1{-}7^{3+}$ in CD_3CN 61

3. **Table 4.2.** Summary of C–H···X bond distances and angles of receptors 5^{2+} and 6^{2+} host-guest complexes 63

LIST OF SCHEMES

Scheme Page

1. **Scheme 1.1.** Different oxidized and reduced forms of NO-related species 21

2. **Scheme 1.2.** Enzymatic and nonenzymatic pathways of H_2S generation and related RSS..... 23

3. **Scheme 1.3.** A selection of simplified reactions to generate and interconvert between SNO^- and $SSNO^-$..... 25

4. **Scheme 1.4.** Reactive oxygen species and their modes of generation and degradation..... 26

5. **Scheme 1.5.** Summary of relevant selenium species and their biological pathways 28

6. **Scheme 1.6.** Reactive cyano-compounds and their modes of generation 29

7. **Scheme 2.1.** Simplified modes of crosstalk between various reactive species to both generate and consume SNO^- and $SSNO^-$. Protons and atom balancing are omitted for clarity 33

8. **Scheme 2.2.** Selected examples of HSNO/SNO^- and $SSNO^-$ formation reactions from prior literature. Examples of $SSNO^-$ and SNO^- crosstalk reactions investigated in this work. The reactions listed focus on SNO^-/$SSNO^-$ formation rather than other identified or speculated byproducts for simplicity 34

9. **Scheme 2.3**. Proposed mechanism of the protonation of SNO^- to generate observed products $SSNO^-$, $NO^{\bullet}$, H_2S, and N_2O. The speciation of gaseous byproducts is likely dependent proton inventory. Framed species have been confirmed by either UV-Vis, NMR, FTIR, and/or GC analysis..... 40

10. **Scheme 2.4**. Summary of pathways for SNO^- and $SSNO^-$ production/ interconversion, including (a) protonation of SNO^-, (b) reduction of $SSNO^-$ by PPh_3, (c) COS-mediated conversion of NO_2^- to SNO^-, and (d) COS-mediated conversion of SNO^- to $SSNO^-$..... 43

CHAPTER I

PROTIC SMALL MOLECULE BIOREGULATORS

This dissertation includes previously published and unpublished co-authored materials. This dissertation was written by Amanda G. Davis with editorial assistance by Professor Michael D. Pluth. The projects in this dissertation were conceived of by Amanda G. Davis and Professor Michael D. Pluth. The experimental work was performed by Amanda G. Davis. Crystal structure determination was performed by Dr. Lev N. Zakharov. Some experimental support performed by Dr. Michael Wade Wolfe, Haley M. Smith, Keyan Li, and Marissa Burden-Dyke.

1.1 Introduction

The prebiotic geologic landscape was much different to our current terrestrial environment, yet gives hints about the types of molecules that were present throughout evolution. Although contemporary metabolism functions in an oxygen-rich environment, the prebiotic atmosphere was more reducing and likely abundant in volcanic gases, such as CO_2, SO_2, H_2S, and CO. These and other small molecules likely comprised simple small molecule feedstocks that led to the emergence of early prebiotic complex biomolecules. These reducing, atmospheric conditions also impeded accumulation of normally UV-blocking ozone in the atmosphere, resulting in rich photochemical reaction pathways that would otherwise be absent under current conditions. Work aimed at probing available reaction pathways under these and related prebiotic conditions support complex biomolecule synthesis ranging from nucleobases and amino acids from common metal-supporting motifs likely involved in early catalysis. For examples, HCN formed through atmospheric UV-irradiation and high energy electrical storms likely provided a significant feedstock for prebiotic nucleobase synthesis.[1–4] Similarly, classic experiments, such as the Miller-Urey experiment, demonstrated that a primordial soup of reducing atmosphere containing methane (CH_4), ammonia (NH_3), hydrogen sulfide (H_2S), and hydrogen (H_2) can serve as feedstocks for prebiotic amino acid synthesis.[5–8]

Expanding beyond these atmospheric gases, the high-pressure and anoxic conditions found in mineral- and sulfide-rich hydrothermal vents, were thought to have formed the first enzymatic cofactors, iron-sulfur clusters.[9] These iron-sulfur clusters likely comprised early catalytic subunits involved in prebiotic chemistry and opened new opportunities for redox chemistries.[10,11] Over time, these iron-sulfur clusters evolved into ferredoxins found in early

archaea and modern day bacteria, now playing important roles in metabolism, photosynthesis, and N_2/CO_2 fixation and reduction.[12,13]

As archaea evolved under otherwise anoxic conditions, the development of microbial photosynthesis led to the transformation of the weakly reducing atmosphere into a more oxidizing one with abundant free oxygen (O_2).[14,15] This rise of atmospheric, reactive O_2 lead to the devastation of anaerobic microbes allowing early aerobic eukaryotes to rise.[16,17] Despite the drastic change in evolutionary conditions from ancient microbes to modern day organisms, biology relies on small molecule building blocks to facilitate physiological processes.

Small molecule precursors are essential for larger biomolecules/structures, cellular signaling and maintaining cellular homeostasis. For example, ATP synthase enzymatically converts free phosphate (PO_4^{3-}) and ADP into ATP for molecular energy storage. Additionally, phosphate, when trapped in a Ca/OH matrix, is known as hydroxyapatite and is the primary structural component of bones. Expanding on signaling pathways, gasotransmitters are a class of endogenously formed gaseous signaling molecules that historically have included CO, NO, and H_2S. In general these molecules often provide cardioprotective & anti-/pro-inflammatory effects and undergo both independent and codependent roles in biological processes such as vasodilation and angiogenesis.[18,19] While the "Gasotransmitter Club" is rather exclusive, other small molecule bioregulators also play fundamental and crucial roles across different organisms, with additional evidence supporting expansion include methane (CH_4), carbonyl sulfide (COS), hydrogen selenide (H_2Se), and hydrogen cyanide (HCN) for their own important roles in physiology.[20–24]

One challenge in classifying molecules as a gasotransmitter is that it focuses on the physical state and biological activity within the organism of generation. Despite the abundance of small molecule bioregulators, not all will be able to meet the criteria to be considered a gasotransmitter. Instead, many may fit into broader class of compounds that includes some established gasotransmitters, emerging gasotransmitters, and other related small molecules. Focusing on H_2S as an example, the lipophilicity of H_2S in its neutral form likely facilitates membrane permeability, whereas its nucleophilicity and metallophilicity likely correlates to the more common anionic, HS^-, form impacting its participation in redox biology and interaction with metal centers. These properties are distinct from the other canonical gasotransmitters, NO and CO, but are more similar with other small molecule bioregulators in which the protonation

state impacts function and activity. Based on these criteria, we propose the new classification of protic, small molecule bioregulators (PSMBs, Figure 1.1).

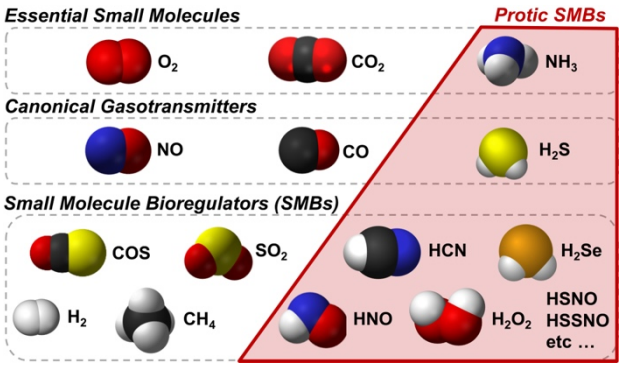

Figure 1.1. Different classes of various biologically relevant small molecules. The subclass of protic small molecule bioregulators is highlighted in red.

Notably, many important small molecule bioregulators (including gasotransmitters) may not gases at all, a common feature of many bioregulators is their protic nature, allowing for ionization upon protonation/deprotonation. While physiological pH is regarded as ~7.4, various cellular compartments expand that range from pH 4.5 in the lysosome to 8 in the mitochondria. Additionally, molecular environments can drastically change the pK_a of a species, for example protein environment can change the pK_a values of cysteine residues depending on the local stability of the deprotonated thiolate.[25] At physiological pH, many PSMBs are preferentially deprotonated, and even outside of that range, the speciation of acid and conjugate base makes the deprotonated forms chemically accessible (Figure 1.2). For example, HCN has a pK_a value of 9.4, and at pH 7, the ratio of CN^-/HCN would be 1:251 but depending on if the molecular environment can stabilize the anion, the speciation of CN^- could be greater. The protic nature of these species is largely what makes them great cellular signaling agents allowing for membrane permeability, post-translational modifications, and intermolecular crosstalk. Herein, we discuss a selection of PSMBs, their defining characteristics, intermolecular crosstalk pathways, and their physiological relevance, with the goal of drawing attention to this important class of molecules.

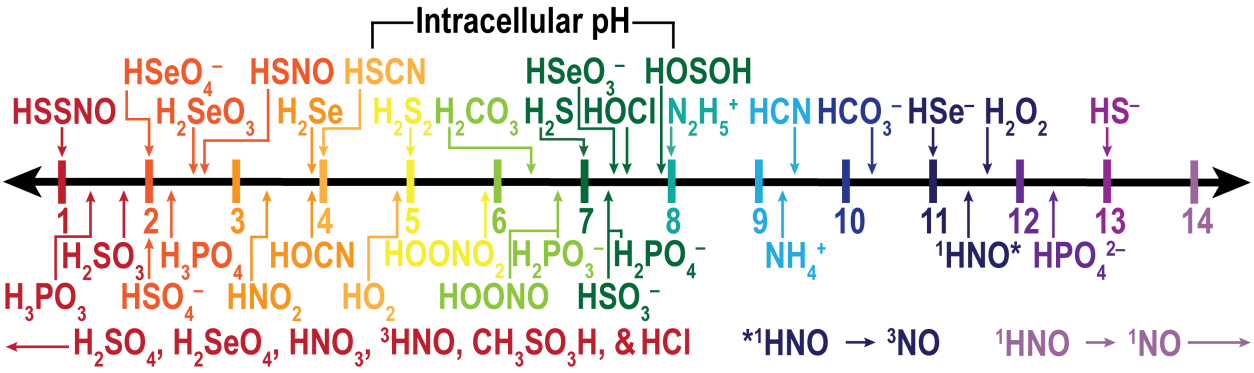

Figure 1.2. Comparison of the pK_a values of various physiologically relevant small molecules.[26] Each pK_a value corresponds to reported values for H^+ dissociation of the species listed.

1.2 Nitric Oxide and Related Reactive Nitrogen Species (RNS)

Since its discovery as the endothelial derived relaxing factor, the roles of nitric oxide (NO) in biology have continued to expand and now include immune system signaling, mitochondrial respiration, cellular adhesion, platelet function, and cardioprotection.[18,19] These and additional wide-ranging biological activities have been reviewed in detail.[27–32] Mammalian NO is generated endogenously from L-arginine by three different isoforms of nitric oxide synthases (NOS). These include neuronal NOS (nNOS) found in the nervous system and responsible for smooth muscle relaxation, blood pressure regulation, and vasodilation; inducible NOS (iNOS) found in the cardiovascular system and is responsible for immune response; and endothelium NOS (eNOS) found in the endothelium and responsible for vasodilation and blood pressure regulation.[33] The combination of enzymatic synthesis and action on molecular targets at physiological concentration made NO the inaugural member of the gasotransmitter family and opened the door to thinking about other reactive small molecules in biology.

Nitric oxide chemistry is also intertwined with other small molecule chemistry. For example, some NO cardioprotective pathways are codependent with H_2S suggestive of the formation of some crosstalk species (*vide infra*).[34] A well-established example of NO/sulfur species crosstalk is in the nitrosylation of biological thiols, generating nitrosothiols (RSNO). Nitrosothiols have significantly longer cellular lifetime than free-NO and provide a source of reductant-labile NO. Perhaps more importantly, S-nitrosylation is an important NO-mediated oxidative post-translational modification involved in various processes ranging from nitrosylation of hemoglobin in hypoxic vasodilation to the activation of inflammatory responses through nitrosylation of nuclear factor-kappa B (NF-κB).

In addition to interactions with adjacent small molecules, the inherent oxygen sensitivity of NO enables a rich redox landscape of small molecule NO_x species, including nitrite (NO_2^-, pK_a 3.3) and nitrate (NO_3^-, pK_a = -1.3). The physiological effects of NO and NO_2^- are deeply entwined, and the ease of interconversion between the two species often makes parsing the specific species responsible for certain physiological functions difficult. Under high oxygen tension and higher pH conditions, NO_2^- is likely to be prominent. Because of this, NO_2^- is regarded as a "hypoxic buffer" for its ability to regulate hypoxic vasodilation, hypoxic mitochondrial respiration, and ischemia-reperfusion tissue injury and infarction.[35] Moreover, NO_2^- has been demonstrated to increase cyclic guanosine monophosphate (cGMP) formation, inhibit cytochrome P450 activity, and affect protein expression.[36] Complicating the differentiation of these two species, common analytical methods for NO detection, such as the Griess Assay, measure NO_2^- rather than NO directly.

Moving to the more oxidized NO_3^-, this anion is readily abundant in the environment, with most of our biological nitrate acquired from dietary sources. While there is some evidence supporting the existence of eukaryotic nitrate reductases,[37] a primary method for reducing NO_3^- to NO_2^- is via nitrate reductases found in symbiotic oral bacteria.[38] This NO_2^- can then be converted to NO through different hypoxic conditions but also by endogenous nitrite reductases as well as by non-enzymatic, acid-dependent mechanisms in the stomach (Scheme 1.1).[39] In addition to acquiring NO_3^- through our diets, excess toxic NO can also oxidated back into NO_3^- by oxygenated hemeproteins in a process called NO-dioxygenation.[40,41]

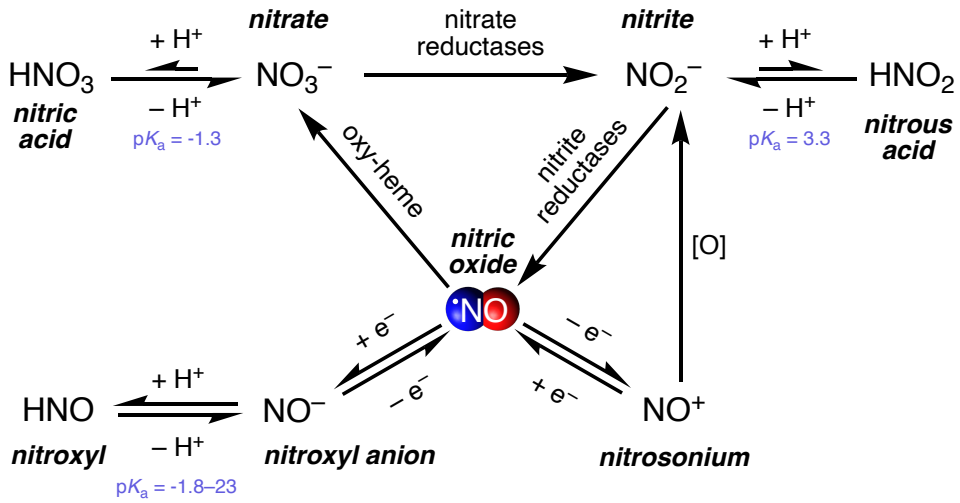

Scheme 1.1. Different oxidized and reduced forms of NO-related species.

One property that sets NO apart from other gasotransmitters is that it is a radical, and is further connected to 1e– reduced and oxidized species, including nitroxyl (HNO), nitroxyl anion (NO^-), and nitrosonium (NO^+), with the latter being unstable under physiological conditions, quickly converting to NO_2^- (Scheme 1.1).[30] The deprotonation of HNO to NO^- is unusual in that the pK_a value is highly dependent on the spin-state of the acid and conjugate base. The spin forbidden ^{1}HNO deprotonation to $^3NO^-$ has a pK_a of 11.3, whereas the deprotonation of ^{1}HNO to $^1NO^-$ (pK_a = 23) and ^{3}HNO to $^3NO^-$ (pK_a = -1.8) are both spin-allowed.[42] More broadly, HNO has been discussed as an alternative signaling agent for NO with analogous cardiovascular effects.[43–45] Endogenous formation of (H)NO could be attributed to the reaction of nitroxylamine (NH_2OH) with NO[46] or conversion of NO via N-hydroxyguanidine,[47] ubiquinol,[48] or even free Fe(II).[49] Under physiological conditions, NO^- can dimerize and undergo a subsequent dehydration to form nitrous oxide (N_2O), better known as laughing gas, which can go on to react with ferrous heme.[50] Additionally, NO^- can react with biological thiols in a sulfhydryl oxidation to form a RSNOH intermediate.[51] Highlighting this diverse reactivity and interaction with adjacent small molecules, NO^- can also react with molecular oxygen (O_2) to generate peroxynitrite ($ONOO^-$), a potent biological oxidant involved in immune response (*vide infra*).[52]

The breadth of biological redox chemistry available from NO provides a rich platform for reactive nitrogen species (RNS). This diversity may help explain why NO was an early addition to the growing list of gaseous small molecule bioregulators. In particular, the ability of RNS to react with other small molecule bioregulators, protein thiols, or reactive oxygen species (ROS) forms a rich array of downstream crosstalk species, each with their own unique chemistries.

1.3 Hydrogen Sulfide and Related Reactive Sulfur Species (RSS)

Sulfur is unique amongst the canonical gasotransmitters in its ability to exist at a wide range of oxidation states from –2 (H_2S) to +6 (SO_4^{2-}), which allows access to diverse chemistry across a large swath of biologically relevant organic and inorganic compounds. As a relic from the ancient anoxic landscape, sulfate-reducing microorganisms (SRM), play an essential role in the sulfur and carbon cycles, by metabolizing a variety of sulfur compounds.[53] SRMs have been demonstrated to convert thiosulfate ($S_2O_3^{2-}$) and sulfite (SO_3^{2-}) into SO_4^{2-} and H_2S, as well as easily reduce free sulfate (SO_4^{2-}) through various processes to produce H_2S.[53,54] Even today,

SO_4^{2-} is one of the most abundant anions in human plasma (300 mM) and plays important roles in detoxification and activation of substrates and in tissue and brain development.[55]

Building from this evolutionary past, it perhaps should come as no surprise that H_2S, classically known for its signature rotten egg smell, is also an established gasotransmitter.[56] Although often written as H_2S, the pK_a (7.0) means that the majority of H_2S exists as HS^- under physiological conditions. In eukaryotes, H_2S is formed endogenously by both enzymatic and nonenzymatic pathways involving cysteine or other oxidized sulfide (Scheme 1.2). H_2S is formed endogenously by three primary enzymes: cystathionine γ-lyase (CSE), cystathionine β-synthase (CBS), and 3-mercaptopyruvate sulfurtransferase (3-MST). CSE is able to produce H_2S through the conversion of L-cysteine, or homocysteine, into thiocysteine, which is then broken down further into H_2S.[57] CBS has been shown to produce H_2S through the condensation of cystathionine with homocysteine by a β-replacement reaction.[58] Alternatively, 3-MST, enabled by cysteine aminotransferase metabolism, produces H_2S via cysteine and α-ketoglutarate.[59] Additionally, recent work has shown that cysteinyl-tRNA synthetases (CARSs) can generate cysteine hydropersulfides which can be subsequently reduced downstream in the electron transport chain to generate H_2S.[60] Nonenzymatic pathways of generating H_2S include the reduction of oxidized sulfide such as persulfides (RSSH), polysulfides (RS_nH), and $S_2O_3^{2-}$ via NADH and glutathione mediated pathways.

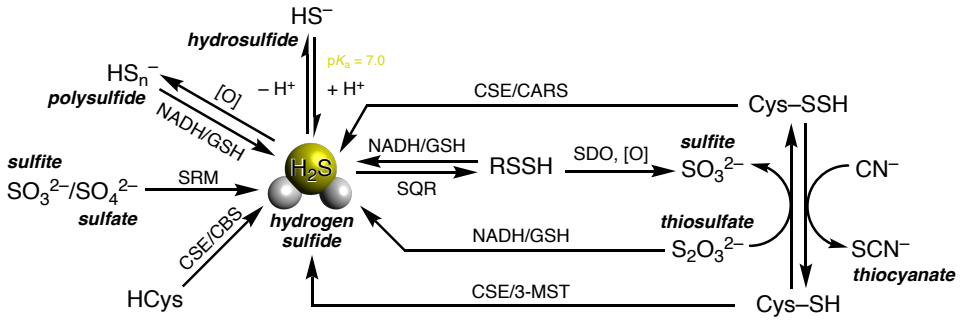

Scheme 1.2. Enzymatic and nonenzymatic pathways of H_2S generation and related RSS.

Although the biological activities continue to expand, H_2S is now well established as an important cardioprotective agent with roles in angiogenesis as well as serving as an anti-oxidant, and as an anti-inflammatory agent.[61] Upregulation of endogenous H_2S and/or exogenous treatment improves cardiac function and reduces complications relating to various pathogenic

cardiovascular conditions.[61] For example, in porcine models with myocardial I/R injury, administration of exogenous H_2S resulted in suppressing cardiomyocyte apoptosis and autophagy.[62] Highlighting the entwined nature of H_2S with O_2 and reactive oxygen species (ROS), H_2S has anti-oxidant properties and may also serve as an O_2-sensor by scavenging mitochondrial ROS. H_2S is also used by sulfur quinone oxidoreductase (SQR) to convert a cysteine disulfide into a persulfide (RSSH). Further reaction with sulfur dioxygenase (SDO) uses O_2 and H_2O to oxidize the persulfide into sulfite (SO_3^{2-}) and eventually thiosulfate ($S_2O_3^{2-}$) through further action by SQR.[63] These oxidized forms of sulfide can then be reduced using endogenous reductants to regenerate H_2S, in an O_2 mediating redox cycle.[64]

Expanding to other ROS-related involvement, H_2S can activate nuclear-factor-E2 related factor-2 (Nrf2) pathways to reduce ROS induced ferroptosis and mitochondrial apoptosis.[65] The role of H_2S functioning as is often regarded as an anti-inflammatory agent and can mediate inflammation by modulating response from inflammatory cytokines.[66] Alternatively, H_2S can regulate inflammation by activating K^+ ion channels or inhibiting Ca^{2+} & Cl^- ion channels, essential for maintaining ionic homoeostasis.[67] Aside from inflammation, modulation of these ion channels can also attenuate heart arrhythmias with increased cell viability[68] and are also involved in H_2S-mediated angiogenesis.[69] An additional mode of angiogenesis involves H_2S upregulating expression of vascular endothelial growth factor (VEGF) and activating protein kinase B and phosphatidylinositol 3-kinase (PI3K).[70]

1.4 Thionitrite and Perthionitrite: NO/H_2S Crosstalk Species

As outlined briefly above, in some cases NO and H_2S can share codependent physiological mechanisms,[34,71–73] implying that potential crosstalk species may be at play. Both thionitrous acid (HSNO) and perthionitrous acid (HSSNO) can been proposed to be components involved in these crosstalk species and can also function as H_2S and NO reservoirs as H_2S and NO are releases upon decomposition.[74–76] Both of these species are anions under physiological conditions, with pK_a values estimated both qualitatively and computationally to be 2.6–7.0 and 1.0–5.0 for HSNO/SNO^- and HSSNO/$SSNO^-$, respectively.[77,78]

One example of this crosstalk can be seen through the reaction of nitrosothiols with H_2S to liberate free thionitrite (SNO^-) and NO.[75,79,80] Moreover, H_2S and NO can react directly under oxidative conditions to form HSNO.[81] Additionally, other nitrosothiols, such as exogenous S-

nitrosopenicillamine (SNAP), have been shown to react with HS^- to produce perthionitrite ($SSNO^-$) via an SNO^- intermediate (Scheme 1.3). Further expanding on this reactivity, $SSNO^-$ and its subsequent decomposition products, NO and polysulfides ($S_n^{\bullet-}$), stimulate sGC and activates the Keap-1/Nrf2 pathway, both of which are traditionally considered NO- or H_2S/NO-mediated pathways.[82–84] Though the actual physiological relevance of $SSNO^-$ has been debated as various groups have demonstrated slow but steady decomposition of $SSNO^-$ (minutes–hours) in semi-aqueous conditions.[85,86]

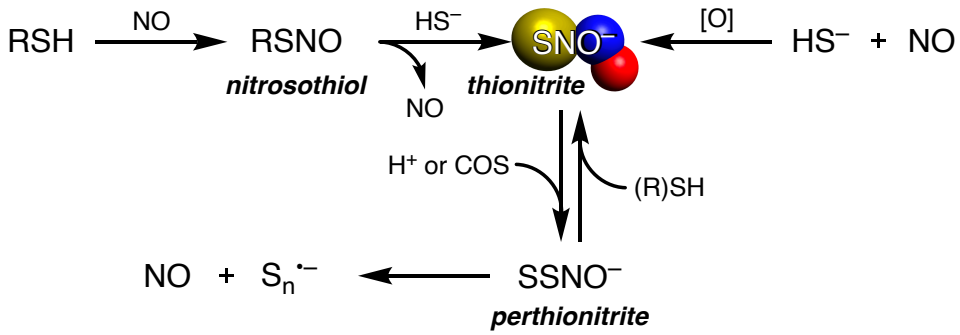

Scheme 1.3. A selection of simplified reactions to generate and interconvert between SNO^- and $SSNO^-$.

The interconversion between SNO^- and $SSNO^-$ has been investigated under various conditions (Scheme 1.3). Prior work from our group has demonstrated that both by protonation of SNO^- or reaction with gaseous carbonyl sulfide (COS) can generate $SSNO^-$ and a host of other signaling molecules including N_2O (via HNO), H_2S, NO, and S^0 (via $S_n^{\bullet-}$).[86] Additionally, it has been demonstrated that SNO^- can be generated from $SSNO^-$ upon reaction with HS^-, cyanide (CN^-), and glutathione (GSH).[87] Clearly, SNO^- and $SSNO^-$ have increasingly rich chemistries and reactivities. With the interconnection with H_2S and NO, there is much more to be explored regarding their biological relevance, abundance, and signaling pathways.

1.5 Dioxygen and Related Reactive Oxygen Species (ROS)

Dioxygen (O_2) is one of the most studied small signaling molecules as it plays many important physiological roles, most widely known for its role in aerobic respiration. Although O_2 is not considered a gasotransmitter, it is clearly an important gaseous transmitter with intwined roles with the signaling pathways of other small molecule bioregulators, including the canonical gasotransmitters. O_2 is also not a PSMB, but associated metabolic or crosstalk byproducts, such

as superoxide ($O_2^{\bullet-}$), peroxynitrite ($ONOO^-$), and peroxide (HOO^-), would all fall into this classification. The acid forms of these species are hydrogen superoxide (HO_2, pK_a = 4.9), peroxynitrous acid (HONOO, pK_a ~ 6.7), and hydrogen peroxide (H_2O_2, pK_a = 11.6) (Scheme 1.4).

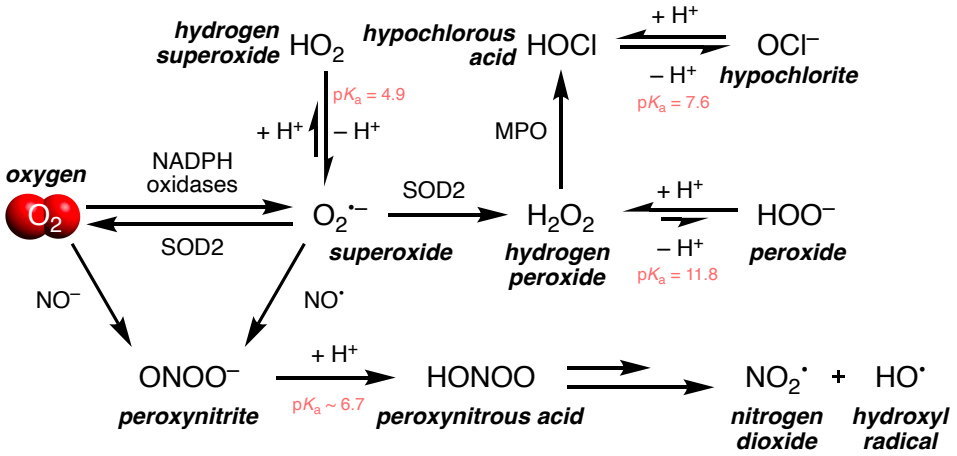

Scheme 1.4. Reactive oxygen species and their modes of generation and degradation.

Superoxide is generated by NADPH oxidases from O_2 and the conversion NADPH into $NADP^+$. Superoxide itself is a toxic, and extremely reactive free radical that plays key roles in phagocyte host defense,[88] but can cause DNA damage and can deactivate iron-sulfur clusters leading to downstream generation of other ROS.[89,90] High levels of $O_2^{\bullet-}$ can lead to oxidative stress and subsequent inflammation, and a number of enzymes, including superoxide dismutase II (SOD2), are responsible for scavenging reactive $O_2^{\bullet-}$ to generate less toxic H_2O_2 or O_2.

NO can also scavenge $O_2^{\bullet-}$, leading to formation of the strong oxidant $ONOO^-$.[47] Alternatively, $ONOO^-$ can be generated through reaction of NO^- and O_2.[52,91] Protonation of $ONOO^-$ generates unstable HONOO, then decomposes into other radical products such as nitrogen dioxide (NO_2) and $HO^{\bullet}$. $ONOO^-$ is a potent oxidant and contributes to the nitration of substrates, such as protein tyrosine residues,[91,92] and the oxidation of biomolecules such as iron-sulfur clusters,[90] zinc fingers,[93] and various enzymes.[94] In fact, protein nitration can be used as a biomarker for certain neurodegenerative disease states such as amyotrophic lateral sclerosis (ALS).[95,96]

Hydrogen peroxide, the $1e^-$ reduced derivative of $O_2^{\bullet-}$, is generated endogenously as a leaky byproduct of the mitochondrial respiratory chain via SOD2 as well as by cell surface

NADPH oxidases.[97,98] H_2O_2 also functions as a biological redox mediator by oxidizing specific protein thiols, and its transport can be mediated by membrane-bound Aquaporin-3 (AQP3), which functions as a water pump.[99] H_2O_2 is responsible for modulating the activity of transcription factors[100] as well as protein tyrosine phosphatases.[101] Peroxiredoxins are scavengers for H_2O_2 and have been demonstrated to propagate downstream oxidative signaling to the redox-regulated transcription factor STAT3.[102]

Downstream, myeloperoxidase (MPO) can convert H_2O_2 into hypochlorous acid (HClO, pK_a = 7.6), a potent oxidant and chlorinating agent that serves a key role in immune response and pathogenic defense. However, misregulation of HOCl is a biomarker for various disease states such as atherosclerosis, chronic inflammation, and some cancers.[103] HOCl can cause tissue injury by chlorinating protein thiols and amino groups or by adversely binding to heme.[104]

Oxidative stress is mediated by redox signaling and plays important fundamental roles in biology with roles regulating various processes such as hypoxia, inflammation, apoptosis, muscle contraction, and wound healing, among many others.[105–107]

1.6 Hydrogen Selenide and Related Reactive Selenium Species (RSeS)

Selenium, sulfur's downstairs neighbor on the periodic table, is an essential dietary micronutrient and is found in trace amounts across biology. Despite the similarities in atomic size and electronegativity, selenium is remarkably more reactive than sulfur,[108,109] likely due to the greater polarizability and the redox properties of selenium.[110,111] Similar to the other gasotransmitters, hydrogen selenide (H_2Se) is an endogenously produced gaseous signaling molecule with important roles in cardiovascular health,[112] bone homeostasis,[113] cancer[114,115], and other disease states.[116–118] Notably, the pK_a value of H_2Se (3.9) is much lower than that of H_2S, meaning that nearly all H_2Se exists as hydroselenide (HSe^-) at physiological pH. A number of recent reviews have highlighted the emerging molecular biology, redox biology and metabolism of selenium and related species (H_2Se, Se-derived amino acids, and selenoproteins),[111,115,119–121] and we will focus here on the more narrow scope of small molecule reactive selenium species (RSeS).

Most selenium is acquired through diet in the form of inorganic selenate (SeO_4^{2-}) and selenite (SeO_3^{2-}), with smaller contributions from selenomethionine (SeMet). SeMet is metabolized in the trans-sulfuration pathway resulting in the intermediate formation of

selenohomocysteine (HSec) and selenocysteine (Sec) prior to the generation of H_2Se and subsequent incorporation into selenoproteins.[122] Fully oxidized SeO_4^{2-} is reduced into the intermediate SeO_3^{2-} prior to the reduction into elemental Se^0 or H_2Se via glutathione-mediated pathways alongside enzymatic and nonenzymatic processes (Scheme 1.5).[123,124]

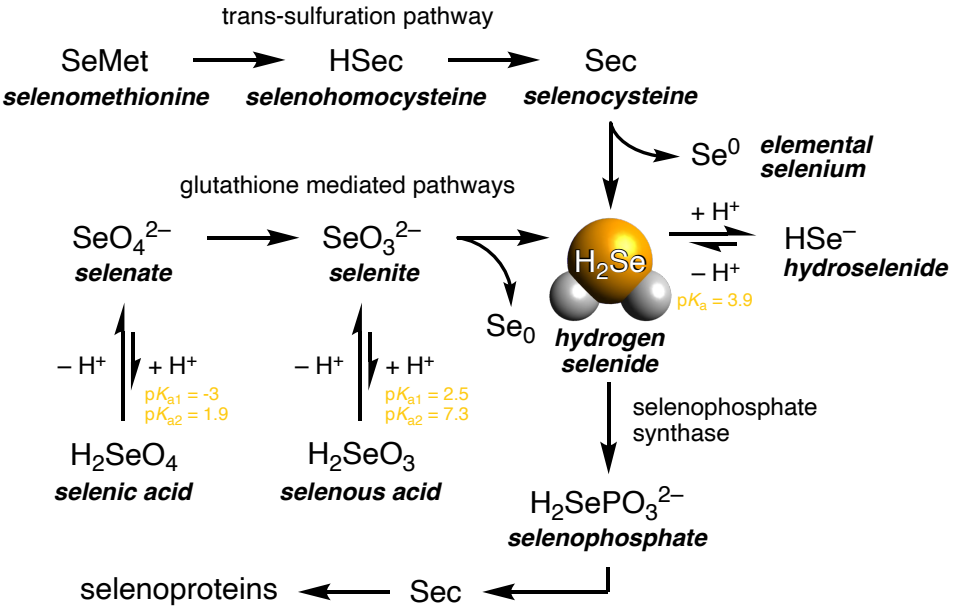

Scheme 1.5. Summary of relevant selenium species and their biological pathways.

Once formed, H_2Se likely functions as an important substrate for selenophosphate ($H_2SePO_3^{2-}$) generation by selenophosphate synthase. This conversion of H_2Se and ATP results in formation of a much more stabilized form of selenium, which likely functions as a reservoir for bioactive selenium, for the generation of other selenium species.[125] Selenophosphate synthase catalyzes the generation of $H_2SePO_3^{2-}$ which is used downstream as a source of selenium for the incorporation of Sec into various selenoproteins with essential physiological implications.[126–128]

The narrow and specific regulation of H_2Se concentrations in biology is important and misregulation of H_2Se corresponds with specific disease states. Based on the known mechanisms of endogenous H_2Se generation, tight regulation, and involvement in specific disease pathways, H_2Se should also be considered to be an emerging gasotransmitter. Much like H_2S, however, the majority of H_2Se under physiological conditions is not a gas, by rather a reactive and diffusible anion. From this perspective, the broader inclusion of H_2Se as a PSMB is likely warranted.

1.7 Hydrogen Cyanide and Related Cyano-Species

Perhaps with the largest reputation of any of the small molecules discussed here, cyanide (CN^-) is well known for its high toxicity. Despite this history, hydrogen cyanide (HCN, pK_a = 9.4) has been recently shown to stimulate certain physiological pathways, including mitochondrial bioenergetics, at low concentrations. HCN is produced endogenously through the HOCl-mediated oxidation of glycine (Scheme 1.6), but can also be acquired through diet with many plants, such as stone fruit, bitter almonds, and apples, containing natural products, cyanogenic glycosides, that are produced as a defense mechanism against herbivores.[129,130]

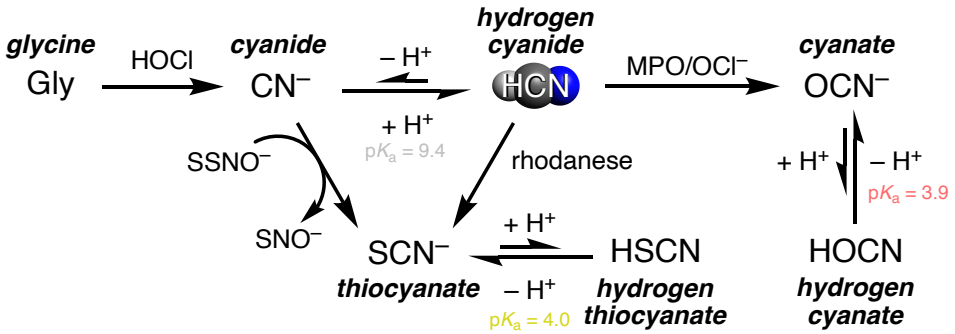

Scheme 1.6. Reactive cyano-compounds and their modes of generation.

Additionally, HCN is produced endogenously through a variety of pathways including as a byproduct of phagocytosis and within neuronal tissues.[131–133] Molecular generation of CN^- in mammals typically results from bacterial synthases but also as a downstream byproduct of MPO activity, which has potential for subsequent formation of cyanate (OCN^-, pK_a = 3.9).[131,134,135] The physiological concentration of CN^- is maintained through a number of degradation pathways, primarily scavenged by rhodanese to generate thiocyanate (SCN^-, pK_a = 4.0) but also through the generation of other small molecule metabolites like formate or CO_2.[136]

At high concentrations, CN^- induces cytotoxic hypoxia by competitively binding to heme and inhibiting Cytochrome C oxidase (CCOx) within Complex IV in the mitochondrial electron transport chain, thus shutting down aerobic production of ATP.[137–139] Additionally, at high concentrations, CN^- can induce nuclear and mitochondrial DNA fragmentation[140,141] as well as cause disruption to microtubules[142] and transcription factors resulting in apoptosis.[143,144] CN^- toxicity is detrimental to the central nervous system as an overabundance of CN^- can cause disruption to the mitochondrial membrane potential,[145] lead to intracellular acidification,[146] and

can induce the release of other neurotransmitters from damaged cells, exacerbating neurotoxic effects.[147,148]

Despite this toxicity, more recent work has also demonstrated that low levels of CN^- are associated with cytoprotective effects supported through calcium mobilization and NMDA receptor activation stimulating neurotransmitter release.[149,150] Additionally, CN^- can act as a mitochondrial activator by stimulating CCOx activity, elevating ATP levels, and increasing cell proliferation as a result.[151] CN^- also has entwined roles with the other gasotransmitters. For example, NO mediates the ability of CN^- to inhibit CCOx activity and inversely, CN^- can also upregulate NOS expression.[149] Additionally, CN^- can also generate SCN^- as a detoxifying crosstalk product from reactions with sulfide as well as $S_2O_3^{2-}$ via 3-MST metabolism.[152] Further, prior reports have demonstrated that $SSNO^-$, upon reaction with CN^-, can also generate SNO^- and SCN^-.[87] Additionally, OCN^- is a spontaneous byproduct of urea, an abundant metabolite, and microbes can use cyanase to detoxify cyanate enzymatically into less toxic metabolites.[153] Finally, oxidized selenium (SeO_4^{2-}/SeO_3^{2-}) has been shown to react with CN^- to form selenocyanate ($SeCN^-$) but the biological relevance remains under investigated.[154]

Much like H_2Se, HCN should be classified as a gasotransmitter, especially now that recent reports support that low concentrations of cyanide induce cytoprotective effects rather than only acting as a cytotoxin. The interconnected roles of HCN with other gasotransmitters, such as H_2S and NO, also support it's physiological relevance and importance. Focusing on known modes of action, most of which rely on the high nucleophilicity and metallophilicity of anionic CN^-, the inclusion of HCN as a PSMB likely more accurately defines the biological chemistry of this reactive signaling molecule.

1.8 Conclusions

The criteria for small molecules to be classified as gasotransmitters is very narrow, and in many cases focuses on a physical property rather than the modes of action. Similarly, the majority of these species (NO, CO, H_2S, H_2Se, HCN) rely on the accessible anion forms/derivatives to exert activity, which highlights the need for a broader class of molecules to encapsule these other important small molecule bioregulators. Focusing on the chemical underpinnings associated with biological activity, the broader class of protic small molecule bioregulators (PSMBs) acknowledges the broad scope of important small molecules, such as

NO_2^-, SO_3^{2-}, $O_2^{\bullet-}$, SNO^-, $HSePO_4^{2-}$, and CN^-, without limiting inclusion based on whether or not such molecules are gases. Importantly, the protic nature of PSMBs is key to their physiology. Molecular environments directly influence the speciation of the protonated/deprotonated forms in turn changing their modes of action. Additionally, many of these species (including the quintessential gasotransmitters) share commonalities including their renowned toxicity, but as discussed here and elsewhere, the dose makes the poison. At physiological concentrations (often mM to high nM) these species act as signaling molecules perpetrating physiological functions, reactive enough to be generated on demand, react quickly where needed, or be efficiently scavenged by other molecules when in excess. Many of these species exert post-translational modifications to proteins that allow for biological redox modulation allowing for the reactivity of certain nucleophilic or electrophilic substrates to be tuned as needed. For example, the conversion of a nucleophilic thiol into an activatable, electrophilic persulfide for H_2S storage and release. The versatility of PSMBs is owed to their protic nature and biology has certainly taken advantage of that to suit its needs. While classification to becoming a gasotransmitter is extremely narrow, classification to be deemed a PSMB is certainly more inclusive without diminishing the importance and relevance of its members. As research progresses and more small molecule bioregulators capture the attention of scientists, this library of PSMBs will continue to expand.

CHAPTER II

EXPERIMENTAL INSIGHTS INTO THE FORMATION, REACTIVITY, AND CROSSTALK OF THIONITRITE (SNO^-) AND PERTHIONITRITE ($SSNO^-$)

This chapter includes previously published and co-authored material from Davis, A.D., Pluth, M.D. Experimental Insights into the Formation, Reactivity, and Crosstalk of Thionitrite (SNO^-) and Perthionitrite ($SSNO^-$). *Angew. Chem. Int. Ed.* **2024**, e202413092. This manuscript was written by Amanda G. Davis with editorial assistance by Professor Michael D. Pluth. The project in this chapter was conceived of by Amanda G. Davis and Professor Michael D. Pluth. The experimental work was performed by Amanda G. Davis. Some experimental support performed by Dr. Michael Wade Wolfe, Haley M. Smith, Keyan Li, and Marissa Burden-Dyke.

2.1 Introduction

Hydrogen sulfide (H_2S) and nitric oxide ($NO^\bullet$) are ubiquitous biological chemical signaling molecules. Often regarded for their toxicity at high or unregulated concentrations, both $NO^\bullet$ and H_2S enable essential biological functions including neurotransmission, angiogenesis, vasodilation, and anti-/pro-inflammatory responses at physiological concentrations.[18,52,56] Despite the different chemical properties of H_2S and $NO^\bullet$, both species also facilitate important post-translational modification of cysteine residues through oxidative S-persulfidation (RSSH) and S-nitrosylation (RSNO) reactions, respectively.[155] In addition to acting independently, certain physiological processes, including angiogenesis, require both H_2S and $NO^\bullet$, suggesting the potential formation of $H_2S/NO^\bullet$ crosstalk species.[34,71,73] Such hybrid species draw parallels to nitrosothiols, which provide a platform for stabilization, translocation, and generation of $NO^\bullet$ equivalents. In addition, nitrosothiols including S-nitroso-N-acetyl-penicillamine (SNAP), nitrosoglutathione (GSNO), and S-nitrosohemoglobin have been shown previously to activate H_2S and $NO^\bullet$ signaling pathways or to provide physiological effects that mimic these pathways.[79,156,157] Taken together, these and other observations have led to thionitrite (SNO^-) and perthionitrite ($SSNO^-$) being identified as likely crosstalk species involved in pathways with H_2S and $NO^\bullet$ codependence.[72,81]

As an example of the intertwined chemistry between reactive sulfur and nitrogen species, H_2S can react with S-nitrosylated proteins to generate the reduced protein thiol and liberate thionitrous acid (HSNO). This HSNO can diffuse away from the site of origin to S-nitrosylate

other protein thiols and release hydrosulfide (HS^-).[75] Similarly, incubation of hemoglobin in S-nitrosylated bovine serum albumin in the presence of H_2S results in formation of S-nitrosylated hemoglobin, further supporting the transnitrosylation ability of free HSNO.[80] Under physiological conditions, HSNO is likely found in the anionic thionitrite (SNO^-) form, although access to both neutral and anionic states may enhance membrane permeability and nucleophilicity, respectively, akin to the impacts of H_2S/HS^- speciation. In addition, $HSNO/SNO^-$ may also serve as a HS^- and $NO^\bullet$ reservoir due to its ability release these gasotransmitters as well as interact with other small reactive molecules (Scheme 2.1).[74,77,80,156,157]

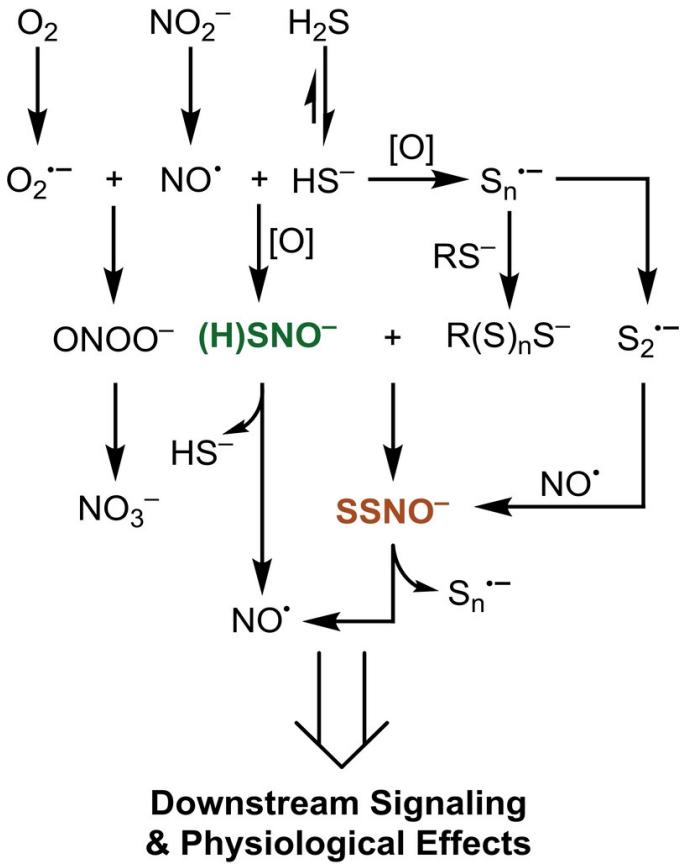

Scheme 2.1. Simplified modes of crosstalk between various reactive species to both generate and consume SNO^- and $SSNO^-$. Protons and atom balancing are omitted for clarity.

Focusing on the chemistry of these hybrid motifs, our understanding of $HSNO/SNO^-$ has been aided by recent progress on generation, isolation, and characterization. Early reports generated HSNO from the reaction of $HS^\bullet$ and $NO^\bullet$ via pulse radiolysis[80] or by isolation and characterization in an argon matrix at 12 K.[158,159] More recent work using biologically relevant

small molecule precursors has provided simpler methods of HSNO/SNO^- formation (Scheme 2.2), such as the liberation of HSNO in water from the aerobic reaction of HS^- with $NO^\bullet$ donors, $NO^\bullet$ gas, or $ONOO^-$;[81] or the reaction between carbon disulfide (CS_2) or thiocarboxylic acids with NO_2^- to generate SNO^- in anhydrous organic solvent.[160] Other reports have suggested potential roles of Cu(II) and related metal complexes or metal surfaces in H_2S and NO_x mediated crosstalk through the generation of RSNO and other related hybrid motifs.[161–163]

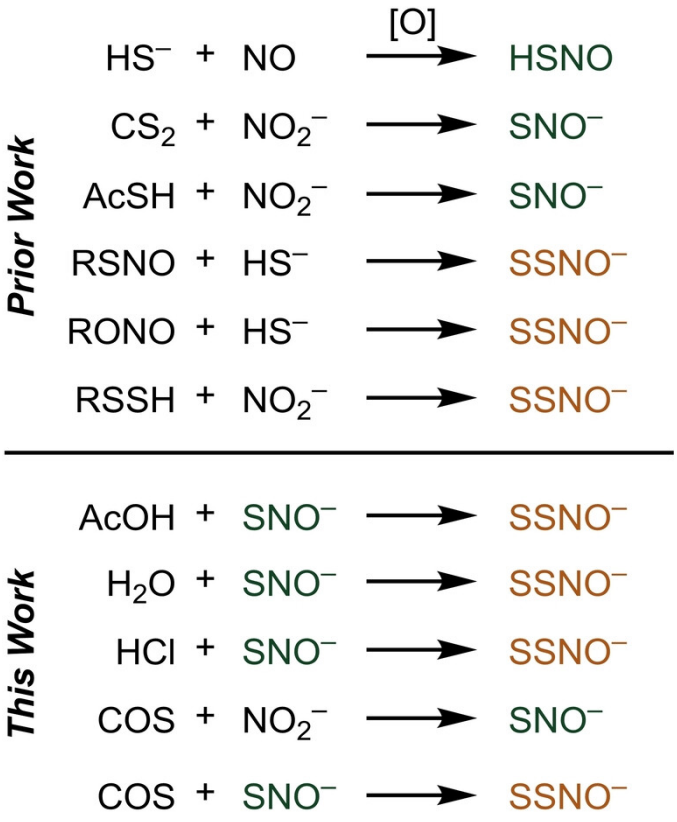

Scheme 2.2. Selected examples of HSNO/SNO^- and $SSNO^-$ formation reactions from prior literature. Examples of $SSNO^-$ and SNO^- crosstalk reactions investigated in this work. The reactions listed focus on SNO^-/$SSNO^-$ formation rather than other identified or speculated byproducts for simplicity.

Much like HSNO, perthionitrous acid (HSSNO) is also proposed in H_2S/NO crosstalk and predominately exists as anionic perthionitrite ($SSNO^-$) at physiological pH. $SSNO^-$ is generated along with polysulfides through the aerobic reaction of sulfide with nitrosothiols, including as SNAP, GSNO, and CysNO in pH 7.4 buffer.[82] Additionally, $SSNO^-$ can be formed through the reaction between isolated persulfides and nitrite in organic solution (Scheme 2.2).[164] Akin to HSNO/SNO^-, HSSNO/$SSNO^-$ is also regarded as a reservoir for other reactive species

through the decomposition into inorganic polysulfides ($S_n^{\bullet-}$) and $NO^{\bullet}$ under physiological conditions, which likely further enables downstream physiological processes (Scheme 2.1).[82,84,85,87]

Further aiding direct investigations into these species, both SNO^- and $SSNO^-$ can be synthesized, isolated, and characterized as bis(triphenylphosphine)iminium (PPN^+) salts by treatment of S_8 with [PPN][NO_2] to form [PPN][SSNO], which is then reduced with PPh_3 to form [PPN][SNO].[165,166] Access to gram-scale quantities of these reactive anions has allowed for direct investigations into the reactivity of $SSNO^-$ and SNO^- with a variety of species ranging from metals to biologically relevant reactive species.[166–169] Computational work has also provided insight into the dynamics of these S/N hybrids.[170] Despite the importance of these species, as well as available access to synthetic precursors, the fundamental experimental chemistry that accounts for SNO^- and/or $SSNO^-$ formation remains limited. Similarly, early controversy on whether SNO^- or $SSNO^-$ was formed under various conditions may suggest yet-uninvestigated pathways of interconversion between these species. Here we report new experimental insights into this reactivity and outline pathways for proton-mediated SNO^- to $SSNO^-$ interconversion. Furthermore, we demonstrate that SNO^- and $SSNO^-$ react with other S-containing small molecules, including carbonyl sulfide (COS), thus establishing additional potential avenues for SNO^-/$SSNO^-$ crosstalk with other species.

2.2 Results and Discussion

2.2.1 Proton Mediated $SSNO^-$ Formation

Physiological pH is typically viewed as ~7.4, but significant variability between organs, tissues, and subcellular organelles broadens the intracellular pH range from 4.5 to 8.0 depending on the molecular environment. Based on this variability in proton availability, we hypothesized that protonation of SNO^- and/or $SSNO^-$ could play an important and yet-uninvestigated role in reactivity. The pK_a values for HSSNO/$SSNO^-$ and HSNO/SNO^- have not been measured experimentally, but computational work and qualitative observations have led to pK_a estimates of 1.0–5.0 and 2.6–7.0 for the two acids, respectively.[77,78] While both of these species are primarily anionic at physiological pH, these pK_a values imply that SNO^- and $SSNO^-$ could both be transiently protonated, thus increasing the electrophilicity of these species significantly and providing potential uninvestigated routes for reactivity to generate additional S/N hybrid species.

To test this hypothesis, we treated PPN^+ salts of SNO^- and $SSNO^-$ with acetic acid (AcOH, pK_a = 4.8) in anhydrous acetonitrile (MeCN) and monitored the reaction by UV/Vis spectroscopy. We chose to investigate these reactions in polar aprotic organic solvents to fully control the proton inventory and to allow for individual reactions to be studied directly. Similarly, we performed all manipulations under an inert N_2 atmosphere to prevent unwanted or adventitious oxidation. Treatment of a solution of [PPN][SNO] with 1 equiv. of AcOH resulted in a color change from light green to dark amber, with an absorbance decrease at 332 nm and respective increase at 445 nm, corresponding to $SSNO^-$ (Figure 2.1), with a well-anchored isosbestic point at 389 nm. Monitoring the change in absorbances over time showed a more complex kinetic profile, (Figure 2.1, inset) suggesting that although the conversion from SNO^- to $SSNO^-$ is clean, the overall reaction pathway involving these species and associate protonation states may be more complex (see below). Treatment of the resultant $SSNO^-$ with PPh_3 resulted in the regeneration of SNO^- as observed by UV/Vis (Figure A1) and also the formation of 1 equiv. of $S{=}PPh_3$ as evidenced by $^{31}P\{^1H\}$ NMR spectroscopy (δ=42 ppm, Figure A27). Treating a solution of [PPN][SNO] with an excess of AcOH accelerated the formation of $SSNO^-$, but also lead led to partial bleaching of the corresponding 445 nm absorbance, which we attribute to protonation or further reactivity of the resultant $SSNO^-$ (Figures A2–A3). These data support that partial protonation of SNO^- by AcOH to form electrophilic HSNO enables subsequent SNO^- attack and $SSNO^-$ formation.

Building from these results, we next investigated the reactivity of SNO^- with H_2O to determine whether the observed $SSNO^-$ formation requires an acidic pK_a or simply a labile proton. Prior literature has reported reactions of $SSNO^-$ with H_2O, but to the best of our knowledge, the direct reaction of isolated SNO^- with H_2O has not been reported.[82,85,87] Treatment of [PPN][SNO] in MeCN with H_2O resulted in the brief formation of a new absorbance at 445 nm in the UV/Vis spectrum corresponding to $SSNO^-$, which subsequently decomposed over the course of about 2 hours (Figure A4). This instability of $SSNO^-$ toward H_2O matches the observed outcome upon treatment of isolated [PPN][SSNO] with H_2O directly over the course of 3 hours (Figure A5). These data suggest that a labile proton is required to facilitate the observed reactivity, although we also acknowledge that H_2O is likely a stronger acid in MeCN than in bulk water. Although the decomposition of both SNO^- and $SSNO^-$ with H_2O is relatively slow, taking 2–3 hours for full decomposition, these results also suggest that these

species may be moderately persistent in dilute aqueous conditions, which further supports the potential generation and translocation under physiological conditions.

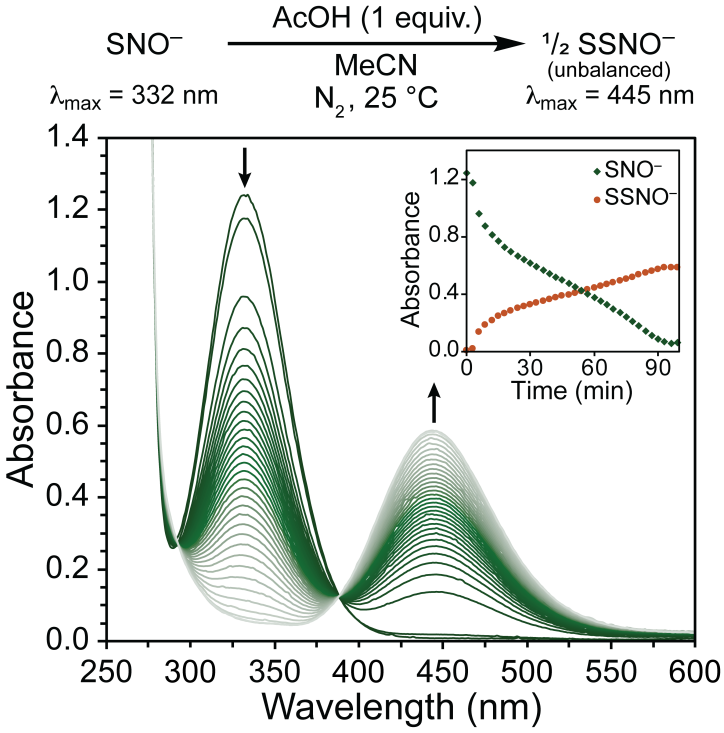

Figure 2.1. UV/Vis spectrum of [PPN][SNO] (0.50 mM, λ_{max}=332 nm) in MeCN, treated with glacial AcOH (1 equiv.) results in $SSNO^-$ formation (λ_{max}=445 nm) over the course of 100 minutes.

Based on the observed reactivity of SNO^- with weak acids, we next investigated the reaction with HCl. Based on our proposed mechanism of $SSNO^-$ formation, we expected that stoichiometric protonation with a strong acid would completely inhibit $SSNO^-$ generation. To test this hypothesis, we treated a solution of [PPN][SNO] with 2 equiv. of anhydrous HCl in Et_2O, which completely bleached the SNO^- absorbance at 332 nm and also failed to generate $SSNO^-$ (Figure A6). Based on prior results, we hypothesize that the electrophilic HSNO intermediate requires free SNO^- to generate $SSNO^-$. To test this hypothesis directly, we first treated a solution of [PPN][SNO] with 1 equiv. of anhydrous HCl to generate the HSNO intermediate, which also quenched the SNO^- absorbance, and then added an additional 1 equiv. of SNO^-, which resulted in $SSNO^-$ generation (Figure A8). When we treated SNO^- with 0.5 equiv. HCl, however, we instead observed immediate $SSNO^-$ formation (Figure A9), which could be converted back to SNO^- by treatment with PPh_3 (Figure 2.2). We also repeated this

sequence with ^{15}N labelled $S^{15}NO^-$ in CD_3CN, and characterized the observed products by ^{15}N, ^{31}P, ^{13}C, and ^{1}H NMR spectroscopy. Treating [PPN][$S^{15}NO$] with HCl results in the disappearance of the characteristic ^{15}N SNO^- peak at 909 ppm and the formation of a new peak at 713 ppm associated with $SSNO^-$. Subsequent treatment with PPh_3 abolished the $SSNO^-$ signal at 713 ppm and regenerated the SNO^- signal at 909 ppm (Figure 2.2, inset). We also observed formation of the expected $S{=}PPh_3$ product in the $^{31}P\{^1H\}$ NMR spectrum (δ=42 ppm, Figure A29). No other byproducts of this reaction were observed in the ^{15}N, ^{13}C, or ^{1}H NMR spectra.

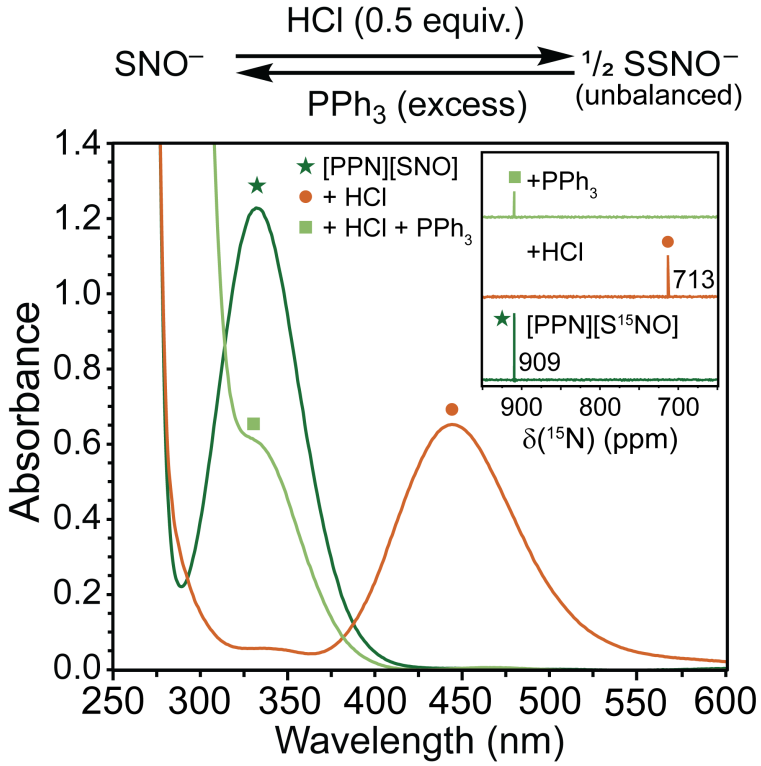

Figure 2.2. UV/Vis spectra of aliquots taken from a solution of [PPN][SNO] (0.50 mM, ★, λ_{max}=332 nm) in MeCN, treated with HCl (0.5 equiv.) resulting in the instantaneous formation of $SSNO^-$, (•, λ_{max}=445 nm). Treatment of the resultant $SSNO^-$ with PPh_3 (excess) reforms SNO^- (▪, λ_{max}=332 nm) over 3 hours. Inset: ^{15}N NMR (versus NH_3 (*l*)) spectra of [PPN][$S^{15}NO$] (18 mM, CD_3CN) treated with HCl (0.5 equiv.) followed by PPh_3 (1 equiv.).

We further confirmed that the observed reactivity is attributed to the labile acidic protons rather than the conjugate bases by titrating [PPN][SNO] and [PPN][SSNO] with [TBA][OAc] and [TBA][Cl]. Treatment of [PPN][SNO] with these anions did not change the characteristic UV/Vis absorbance at 332 nm (Figures A10–A13). We did observe a minor (<15 %) decrease in

the 445 nm absorbance of [PPN][SSNO] with these anions (Figures A14–A17), which we attribute to the weaker S−S bond that may be more susceptible to nucleophilic attack.

2.2.2 Identification of Nitrogen-Containing Products

Using the molar absorptivity of SNO^- (ε=2445±85 M^{-1} cm^{-1} in MeCN) and $SSNO^-$ (ε=2590±320 M^{-1} cm^{-1} in MeCN), we calculated that 0.5 equiv. of $SSNO^-$ are formed from the reaction of SNO^- with 0.5 equiv. of HCl. This observation supports the requirement that two equiv. of SNO^- are needed to form $SSNO^-$. Because full protonation of SNO^- shuts down this reactivity, the reactivity relies on both HSNO and SNO^- present in solution. Charge and atom balancing suggests that HNO may be the additional product of this reaction. HNO is known to be unstable and reactive, meaning that direct observation of free HNO is unlikely, particularly with the other number of reactive species in solution. Analysis of the ^{15}N NMR spectrum at the conclusion of the reaction did not show any additional signals assignable to HNO formation (Figure A30). Furthermore, treatment with PPh_3 failed to generate $HN{=}PPh_3$ and $O{=}PPh_3$ in the $^{31}P\{^1H\}$ NMR spectrum, which would have been expected if HNO were to build up appreciably during the course of the reaction (Figures A27–A29).[171] As an additional trapping method for HNO, we also treated the reaction products of [PPN][SNO] and AcOH with DMPO, which would form a ring-opened nitrosooxime product in the presence of HNO,[172] but again did not directly observe HNO. (Figure A31). We also note that addition of DMPO or cyclohexadiene as radical traps neither stopped the reaction nor generated products derived from radical trapping (Figure A32), which suggests that polysulfide radical pathways are unlikely to be major contributors to the observed reactivity.

To further probe HNO formation indirectly, we also investigated whether N_2O was formed during the course of the reaction due to the established rapid decomposition of HNO to N_2O (and H_2O). Measurement of the FTIR spectrum of the headspace of the reaction mixture revealed new bands at 2235 and 2212 cm^{-1}, which matched those from authentic N_2O (Figures A25–A26) as well as reported values from HNO decomposition to N_2O in related systems.[160]

We also wanted to determine whether $NO^\bullet$ was being formed during the reaction based on the established reactivity of HNO with RSH compounds to generate to generate $NO^\bullet$ and H_2S. To test for $NO^\bullet$ formation, we used Co(II) phthalocyanine (CoPc) as a $NO^\bullet$ trap based on the characteristic change in UV/Vis absorbance for CoPc and CoPc−NO.[164,173] After treating

[PPN][SNO] with HCl (0.5 equiv.) or AcOH (1 equiv.), we sparged the headspace of the reaction through a CoPc solution and observed the expected shift from 656 nm to 662 nm. This change is consistent with conversion of CoPc to CoPc-NO and it also matched a positive control experiment with authentic NO• (Figure A21). In addition, GC analysis of the headspace of the protonation of [PPN][SNO] using a sulfur-selective PFPD system revealed both free H_2S and HSNO (Figure A38), which further support this reaction manifold.

Both the formation of N_2O and NO/H_2S is consistent with intermediate HNO formation. Direct conversion of HNO to N_2O is well established through rapid dimerization and dehydration, with N_2O detection often being used as a proxy for transient HNO formation. In addition, prior work on the reaction of GSNO with HNO was shown to generate NO•, which was thought to proceed through a GS-NONOate type intermediate en route to NO• and GSH formation.[174] Using analogous chemistry, we propose that HNO could react with HSNO to generate an HSN(OH)NO intermediate that should rapidly decompose into H_2S and NO• (Scheme 2.3). These two reaction pathways would account for N_2O, NO•, and H_2S formation, as well as the complex reaction kinetics due to further participation of HNSO in subsequent reactivity, as well as the potential for generated H_2O and H_2S to further participate in the overall reaction (Scheme A1).

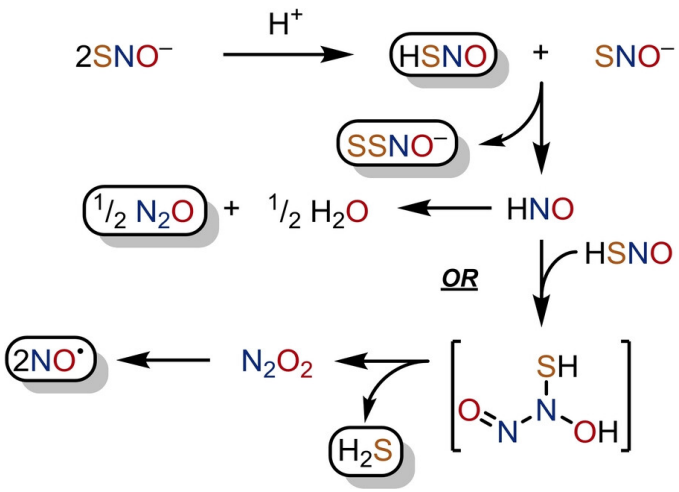

Scheme 2.3. Proposed mechanism of the protonation of SNO^- to generate observed products $SSNO^-$, NO•, H_2S, and N_2O. The speciation of gaseous byproducts is likely dependent proton inventory. Framed species have been confirmed by either UV/Vis, NMR, FTIR, and/or GC analysis.

2.2.3 Reactions with SNO^-/$SSNO^-$ with COS

Complementing the direct connections between hybrid small molecules, we were also curious whether SNO^-/$SSNO^-$ could react with other electrophilic S-containing species, and in particular carbonyl sulfide (COS). COS has been proposed previously to play roles in origin of life chemical ligation, be a potential gasotransmitter, and serve as possible sulfide source after hydrolysis by carbonic anhydrase.[23,175,176] Direct reactions of COS with biologically relevant small molecules are limited due to challenges with working with and measuring COS.[177,178] We reasoned that because COS is an electrophile, it should be poised to react with other small molecules like SNO^-. Aligned with this idea, Kundu and co-workers recently reported SNO^- formation from the reaction between CS_2 and less nucleophilic NO_2^- (Scheme 2.2). In this reaction, the intermediate generation of COS was proposed, which would be scavenged by NO_2^- to generate SNO^- and CO_2.[160] To further advance the potential cross reactivity of COS with other small biomolecules, we directly treated COS gas with both NO_2^- and SNO^- to determine whether additional modes of small molecule crosstalk were observed.

Treating a solution of [PPN][$^{15}NO_2$] in CD_3CN with COS gas resulted in a light green solution characteristic of SNO^- formation, which was confirmed by complete consumption of $^{15}NO_2^-$ to form $S^{15}NO^-$ in the ^{15}N NMR spectrum (Scheme 2.4c). During the time required to acquire the ^{15}N NMR spectrum, we also observed minor formation of $SS^{15}NO^-$ (Figure 2.3 inset) with the $^{13}C\{^1H\}$ NMR spectrum also revealing CO_2 formation (δ=125 ppm, Figure A34). Allowing the reaction to further react overnight resulted in the complete conversion from $S^{15}NO^-$ to $SS^{15}NO^-$ without any additional ^{15}N byproducts. These results demonstrate that NO_2^- does indeed react directly with COS to generate SNO^-, which is consistent with the proposed mechanism by Kundu. The proposal that $SSNO^-$ formation may be due to dissociation of SNO^- into NO• and S_2^{2-}, however, is contrary to our observed stability of SNO^- in solution.

To further investigate this chemistry, we also treated [PPN][$S^{15}NO$] with COS directly to determine whether the products of the NO_2^-/COS reaction could potentially react further to generate $SSNO^-$. Under these conditions we observed both $SS^{15}NO^-$ (Figures A18, A35) and CO_2 (δ=125 ppm, Figure A36) formation as expected (Scheme 2.4d).* The resultant $SSNO^-$

*An analogous experiment with CO_2 was performed in which gaseous CO_2 was sparged through a solution of [PPN][SNO] which resulting in the minor formation of $SSNO^-$. We proposed this reactivity was due to CO_2 acting as a Lewis acid which activated the SNO^- thus being subject to minor nucleophilic attack.

subsequently decomposes into S^0 as observed by UV/Vis (Figure 2.3, A22), with simultaneous liberation of NO•, which was confirmed by CoPc trapping (Figure A21). This COS-mediated conversion of SNO^- to $SSNO^-$ also complements prior work by Hayton and co-workers that demonstrated the NO•-mediated oxidation of SNO^- to $SSNO^-$, although the reaction byproducts in these studies were not identified.[179] Our results demonstrating that SNO^- can react directly with COS is also contrary to the hypothesis that $SSNO^-$ formation stems directly from SNO^- dissociation.

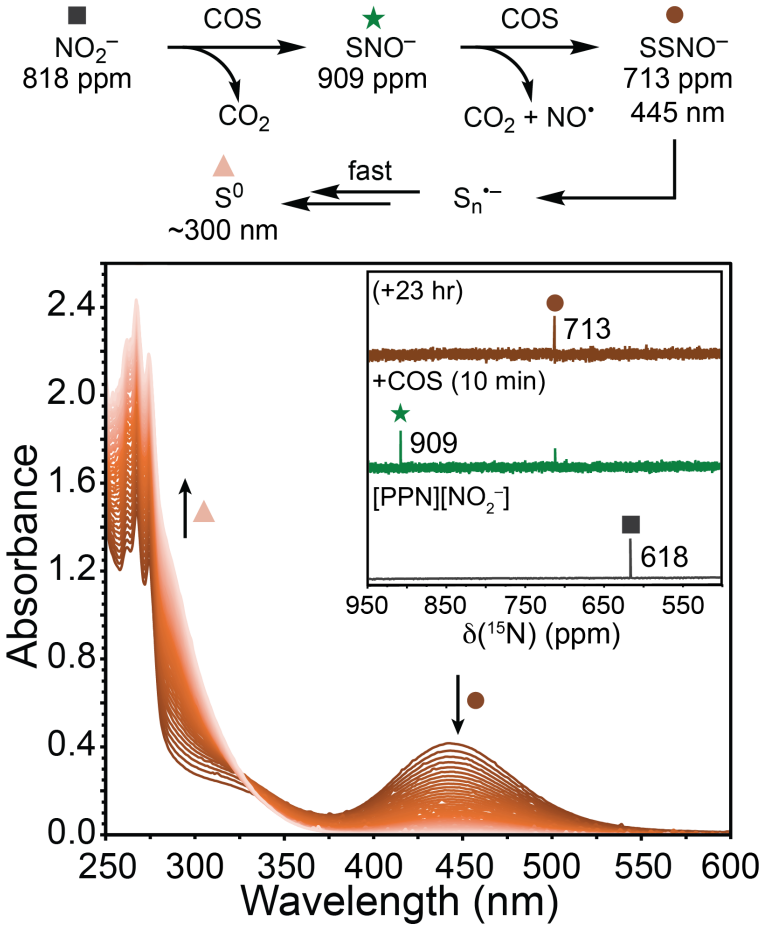

Figure 2.3. (top) Summary of cascading reactions from NO_2^- treated with COS to generate SNO^-, $SSNO^-$, and S^0. (bottom) UV/Vis spectra of $SSNO^-$ generated by treatment of [PPN][SNO] with COS (•, λ_{max}=445 nm in MeCN) decomposing into S^0 (▲, λ ~300 nm) over 2 hours. Inset: Stacked ^{15}N NMR spectra of [PPN][$^{15}NO_2$] (▪) in CD_3CN treated with COS (excess) to generate $S^{15}NO^-$ (★), which further reacts with excess COS to generate $SS^{15}NO^-$ (•).

More broadly, these data suggest that SNO^- and $SSNO^-$ are likely to play important roles as mediators and intermediates in the interconversion between small molecule reactive species

and may help initiate reaction cascades that generate biologically-relevant crosstalk species (Scheme 2.4). In acidic environments, such as the lysosome or certain ischemic and hypoxic tissues, it is possible that SNO^- could undergo proton-mediated chemistry to generate $NO^\bullet$, H_2S, and/or N_2O, although HNO dimerization to generate N_2O at physiological concentrations may be less likely. Similarly, in environments where COS may be present, such as those with bacterial colonization, reaction with NO_2^- or SNO^- may provide additional pathways for NO_x reduction and subsequent $NO^\bullet$ release while bypassing sulfide oxidation machinery. The addition of SNO^- to activated electrophiles may also open new pathways for reactive sulfur or nitrogen species activation through metal coordination, which would broaden the types of motifs compatible with this chemistry.

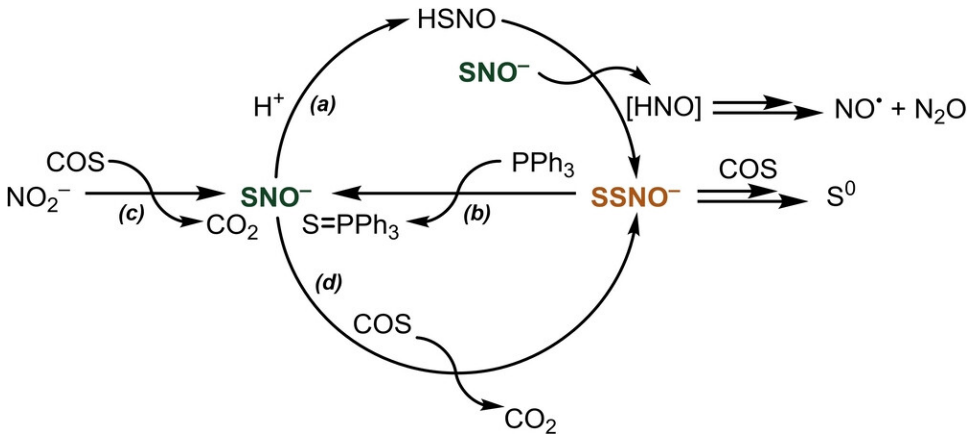

Scheme 2.4. Summary of pathways for SNO^- and $SSNO^-$ production/interconversion, including (a) protonation of SNO^-, (b) reduction of $SSNO^-$ by PPh_3, (c) COS-mediated conversion of NO_2^- to SNO^-, and (d) COS-mediated conversion of SNO^- to $SSNO^-$.

2.3 Conclusions

Both SNO^- and $SSNO^-$ are postulated to be important small S/N hybrid molecules involved in $NO^\bullet$ and H_2S crosstalk and understanding how these reactive anions interact with other small molecule bioregulators is an important challenge. By using different spectroscopic and trapping techniques, we have clearly demonstrated new fundamental pathways for SNO^- and $SSNO^-$ interconversion as well as reactivity with other small biomolecules of interest, including COS. These pathways can then result in the cascading release of various small molecules, including $NO^\bullet$, H_2S, N_2O, CO_2, and S_8. More broadly, these results provide new insights into the fundamental reactivities and potential signaling pathways of SNO^- and $SSNO^-$. These results

also highlight additional opportunities for investigating the reactivity of these S/N hybrids with other biologically important small molecules.

Having demonstrated that Lewis acidic protons could facilitate reactivity of SNO^- and $SSNO^-$, we wanted to employ anion receptors for the molecular recognition of other PSMBs to inform on how molecular environment can impact the stabilization of other reactive species.

CHAPTER III

REVERSIBLE HYDROSULFIDE (HS^-) BINDING USING EXCLUSIVELY C–H HYDROGEN-BONDING INTERACTIONS IN IMIDAZOLIUM HOSTS

This chapter includes previously published and co-authored material from Davis, A.D., Zakharov, L. N., Pluth, M.D. Reversible Hydrosulfide (HS^-) Binding Using Exclusively C–H Hydrogen-Bonding Interactions in Imidazolium Hosts. *Inorg. Chem.* **2024**, 63, 6, 3057–3062. This manuscript was written by Amanda G. Davis with editorial assistance by Professor Michael D. Pluth. The project in this chapter was conceived of by Amanda G. Davis and Professor Michael D. Pluth. The experimental work was performed by Amanda G. Davis. Crystal structure determination was performed by Dr. Lev N. Zakharov.

3.1 Introduction

Small reactive molecules play key roles in diverse areas of science ranging from environmental chemistry to chemical biology, and understanding both the fundamental chemistry and the molecular recognition of such species poses a significant challenge. In many cases, synthetic host molecules have been used to further understand how these reactive analytes can be stabilized, recognized, and/or measured. In particular, the molecular recognition of anionic guests has made significant contributions to the stabilization and detection of environmental analytes, but the application to physiologically relevant anions remains underdeveloped. Prior work toward the recognition of biologically abundant anions has generally focused on Cl^-, Br^-, HPO_4^{2-}, SO_4^{2-}, and other relatively stable species.[180–186] These investigations have laid the foundation for further rational design of supramolecular receptors that can bind more reactive species and inter-mediates.[187–191]

In parallel with advancements in the molecular recognition of small anionic guests has been the expansion and recognition of small molecule signaling molecules in the adjacent fields of chemical biology and pharmacology. Many of these species stem from endogenously produced signaling molecules like H_2S and related species, which have garnered significant attention over the last two decades due to their complex and entwined roles in ubiquitous biological processes.[18,56] H_2S is established to reduce oxidative stress, promote vasodilation, and exert cardioprotection, in addition to other biologicalfunctions.[61,192] What makes small molecules good cellular signaling agents also makes them difficult to study, specifically their propensity to

react rapidly with other biomolecules or through different redox pathways.[19,79,155,164,193] Moreover, this high reactivity also suggests that specific molecular environments may stabilize or recognize these highly reactive species through specific types of interactions or recognition environments. Although generally written as its diprotic neutral form, H_2S exists primarily as hydrosulfide (HS^-) at physiological pH. Despite the prevalence of HS^- anion in biology, little is known about what fundamental motifs contribute to its molecular recognition, although such interactions undoubtedly play key roles in fundamental stabilization, reactivity, and crosstalk.

In designing molecular recognition approaches for anionic guests, supramolecular chemists often draw inspiration from the way nature stabilizes reactive species. For example, electronegative hydrogen-bond (H-bond) donors, such as O or N, with short and linear H-bonding interactions contribute to the defined tertiary structure of proteins and duplex structure in DNA. Analogously, supramolecular chemists incorporate the versatility of H-bonding interactions, often using abiotic H-bond donor motifs, to design different anion receptors, such as Bowman−James's polyamide cryptands,[194,195] Flood's cyanostar,[196,197] and Sindelar's bambusiril.[198,199] In addition to more classical O−H and N−H H-bond donors, recent work establishes that C−H H-bond donors can contribute to strong anion binding, particularly for anions like Cl^-. Expanding to the use of C−H H-bond donors, we have worked with the Johnson and Haley groups to demonstrate that the arylethynyl receptors containing a mixture of urea and C−H motifs can bind HS^- and HSe^-,and also that HS^- appears to have a particular preference for C−H H-bond donors (Figure 3.1a).[200–202] To the best of our knowledge, this arylethynyl receptor provides the sole example of a crystallographically characterized host−guest complex with HS^-. Additional examples of HS^- binding in anion receptors characterized in solution have primarily used C−H H-bond donors although halogen bond donors have also recently been employed.[198,203–205] Further advancing the underappreciated role of C−H···S interactions, we recently analyzed C−H···S close contacts from the Cambridge Structural Database (CSD),which revealed that these interactions are a common yet widely overlooked interaction in organic, inorganic, materials, and biological chemistry.[206]

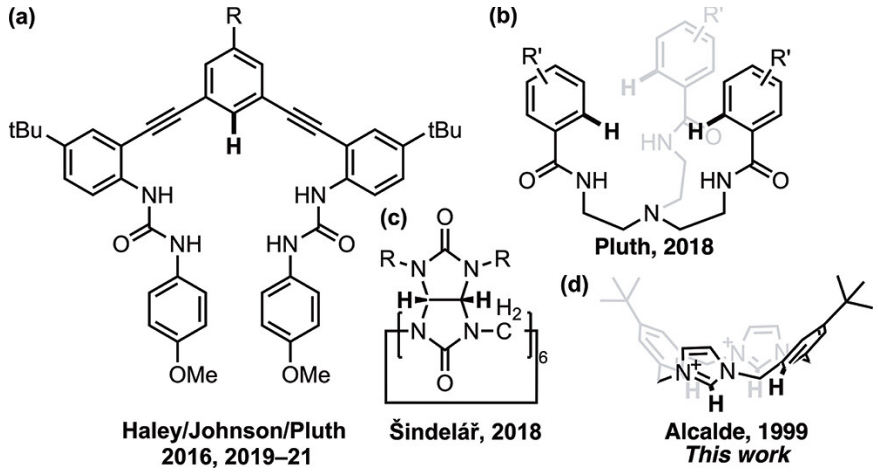

Figure 3.1 (a–c) Prior examples of H-bonding host molecules demonstrated to bind HS^- and (d) this work using exclusively C–H H-bond donors for HS^- recognition.

On the basis of prior work showing that anion receptors containing both N−H and C−H donors can bind HS^-,[199,200,203] as well as prior crystallographic evidence suggesting the importance of C−H···S interactions,[206] we aimed to incorporate modular C−H H-bond donors into highly modifiable receptors. Building upon prior work on HS^- in the receptors described above, here we directly test the hypothesis that using strong C−H H-bond donor motifs in combination with electrostatic interactions can significantly enhance HS^- binding. By using a series of modifiable imidazolium host molecules, including a previously reported bis-imidazolium macrocycle,[207] we demonstrate efficacious HS^- binding both in solution and in the solid state. To the best of our knowledge, this work provides the first example of differential HS^- and Cl^- binding stoichiometry and also provides the first examples of 2:1 host−guest binding for HS^- recognition.

3.2 Results and Discussion

3.2.1 Determination of Binding Affinities

To further advance our understanding of the molecular recognition of HS^- using H-bonding interactions, we chose to investigate HS^- using a modular class of receptors featuring solely C–H H-bond donors. In choosing a donor motif, we focused on imidazole and imidazolium C–H H-bond donors due to the high directionality, prior incorporation into various anion receptors, and earlier work establishing binding polyatomic and halide anions in polar organic solvents.[207–210] In addition, imidazole- and imidazolium-based receptors contain a highly

directional, polarized, and easily trackable C–H bond that can be used to investigate C–H···X^- interactions. Additionally, multiple imidazole motifs can be incorporated into a single receptor to allow for direct investigations into how C–H···X^- interaction multiplicity impacts guest binding. Alkylation of the imidazole nitrogen can further acidify and polarize the C–H H-bond donor, and the resulting positive charge can also favor anion binding due to the Coulombic attraction. Utilizing these design principles, we prepared a small, modular series of imidazole/imidazolium receptors with different charge states, directionality, and preorganization (Figure 3.2) and characterized each receptor by ^{1}H, ^{13}C, ^{19}F, and ^{31}P NMR spectroscopy.

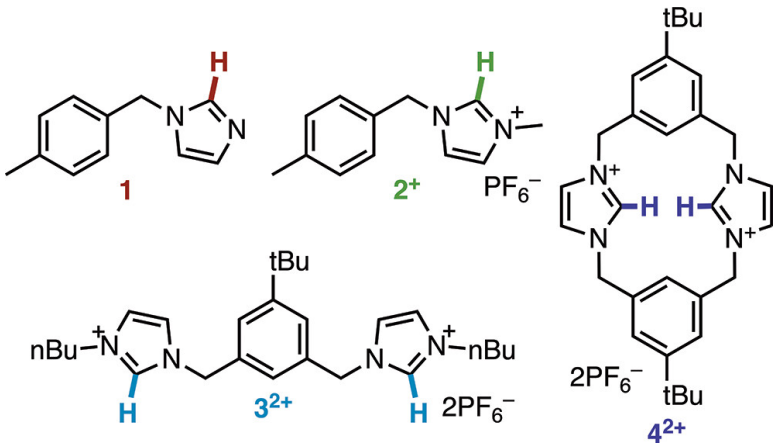

Figure 3.2. Imidazole/imidazolium receptors **1**–**4**.

We used neutral imidazole **1** as a control compound to better understand the impacts of C–H-bond polarization on guest binding. The monoimidazolium $\mathbf{2}^+$ and bis-imidazolium $\mathbf{3}^{2+}$ receptors allow for investigations into how the number of cationic binding motifs influences guest binding. Additionally, both the macrocycle $\mathbf{4}^{2+}$ and its nonmacrocyclic analogue $\mathbf{3}^{2+}$ contain two imidazolium groups, but $\mathbf{4}^{2+}$ further restricts host rotation and provides a highly defined guest binding environment. For cationic receptors **2**–**4**, we prepared the noncoordinating PF_6^- salts to reduce potential counterion binding and to eliminate competing proton signals that could interfere with NMR resonances of interest in the host. Hosts **1** and $\mathbf{2}^+$ are known compounds but have not been used previously for anion binding; receptor $\mathbf{3}^{2+}$ is a new host, and $\mathbf{4}^{2+}$ has been reported previously as an anion-binding host.[207]

After preparing each receptor, we measured the binding affinity (K_a) of receptors **1**–**4** with HS^- using ^{1}H NMR spectroscopy (Figure 3.3). We chose to use HS^- as a guest based on its biological relevance and also the surprising lack of receptors for this anion. Hydrogen sulfide

and hydrosulfide are highly toxic and should be handled with caution to minimize exposure. We also chose to examine the binding affinity of Cl^- as a comparison of receptor binding affinity and selectivity. We used the tetrabutylammonium (TBA^+) salts to ensure anion solubility and performed each titration in anhydrous CD_3CN at 25 °C under N_2 to avoid potential unwanted HS^- oxidation.[211] For each titration, we observed a downfield shift of the imidazolium C–H and phenyl C–H protons upon guest addition and subsequent binding. As expected, the more polarized imidazolium C–H resonances shift farther downfield upon guest addition than the less polarized aryl C–H resonances, which is consistent with a stronger interaction between the guest anion and the imidazolium motif. In addition, the hydrosulfide ^1H NMR signal can also be observed and shifts upfield during the course of the titration, which again is consistent with reversible binding to the host receptors. The chemical shifts of the interacting C–H resonances were measured after each addition of guest, plotted against guest concentration, and fit using the Nelder–Mead method in Bindfit to measure the K_a values.[212–214]

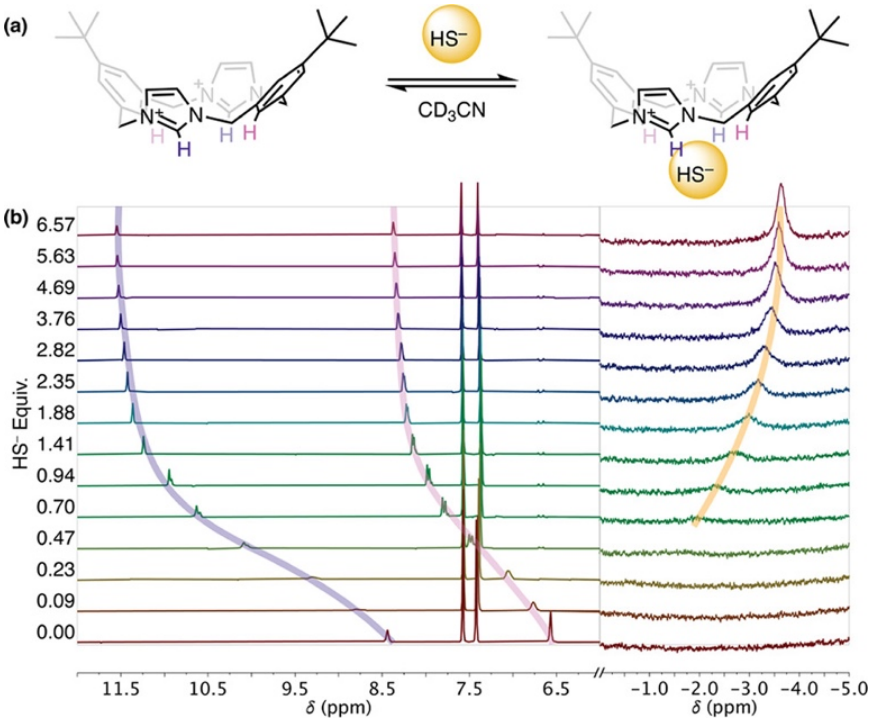

Figure 3.3. (a) General guest binding scheme for binding HS^- in $\mathbf{4}^{2+}$. (b) Representative ^1H NMR titration of $\mathbf{4}^{2+}$ with [TBA][SH]. General conditions: $[4^{2+}]_i$ = 0.97 mM, CD_3CN, 25 °C. The yellow highlighted peak at negative ppm in panel (b) corresponds to the HS^- signal.

The binding affinities for receptors **1**–**4** with HS^- are summarized in Table 3.1. Clear trends for HS^- guest binding were observed when the K_a values were compared for each receptor. First, no binding was observed for neutral imidazole **1**, but the binding affinity increased to 60 M^{-1} upon alkylation of **1** to form cationic imidazolium receptor $\mathbf{2}^+$. This trend was maintained when an additional imidazolium motif was incorporated in receptor $\mathbf{3}^{2+}$, which resulted in an approximately 2 orders of magnitude increase in K_a up to 1000 M^{-1}. This increase in binding is likely due to a combination of both the increased number of C–H interactions and also the increase in the Coulombic attraction from the dicationic receptor to monoanionic HS^-. We next investigated how further preorganization of the imidazolium C–H donors would impact HS^- binding by investigating macrocycle $\mathbf{4}^{2+}$ and found significantly stronger anion binding with the sequential binding constants of 40000 and 5000 M^{-1}, respectively. Interestingly, the binding isotherm for $\mathbf{4}^{2+}$ with HS^- failed to fit cleanly to a 1:1 binding event (Figure B28) but rather fit a 2:1 host−guest binding model (Figure B27). Further supporting this 2:1 binding mode, the Job plot of $\mathbf{4}^{2+}$ binding HS^- shows a maximum at the mole fraction of 0.67, which is consistent with 2:1 host−guest binding (Figure B29). Notably, this apparent binding mode is different from what was observed from the binding isotherms from receptors $\mathbf{2}^+$ and $\mathbf{3}^{2+}$ that were fit to 1:1 models (Figures B15 and B21).

Table 3.1. Binding Affinities for HS^- and Cl^- in Receptors 1−4 in CD_3CN

receptor	anion	K_a (M^{-1})[a]	ΔG (kcal/mol)
1	HS^-	NBO[b]	
	Cl^-	NBO[b]	
2^+	HS^-	60 ± 4	–2.4 ± 0.1
	Cl^-	63 ± 3	–2.5 ± 0.1
3^{2+}	HS^-	1000 ± 90	–4.1 ± 0.1
	Cl^-	1350 ± 75	–4.3 ± 0.1
4^{2+}	HS^-	40000 ± 8000[c]	–6.3 ± 0.1
		5000 ± 1000[c]	–5.0 ± 0.2
	Cl^-	6600 ± 800	–5.2 ± 0.1

[a]From fitting ^{1}H NMR titration data to 1:1 binding unless otherwise noted. The reported error is the standard deviation of triplicate titrations or 5% of the K_a, whichever was greater. [b]NBO, no measurable binding observed. [c]Fit to 2:1 binding; the first value is 1:1 binding followed by the 2:1 binding event.

In an effort to further contextualize the selectivity and binding affinities of the receptors, we also measured the binding affinity of Cl^-. Both HS^- and Cl^- are similar in size, with van der Waals radii of 2.05 and 2.06 Å for Cl and S, respectively.[215] The noted trends and K_a values that were observed for HS^- were also observed for Cl^- with the exception of receptor $\mathbf{4}^{2+}$, which exhibited an unexpected binding stoichiometry with HS^- compared to that of Cl^-. We found that Cl^- binding to $\mathbf{4}^{2+}$ fit to a 1:1 binding isotherm with a K_a value of 6600 M^{-1} in CD_3CN. Moreover, this binding stoichiometry is further supported by the Job plot, which showed a maximum at a mole fraction of ~0.5 (Figure B32). To the best of our knowledge, this is the first observed difference in the binding stoichiometry between HS^- and Cl^- in a host–guest system. In addition, the measured K_a value for Cl^- binding is significantly lower than the measured K_a for $\mathbf{4}^{2+}$ with HS^-, which further supports the potential importance of C–H···S interactions in HS^- recognition.

3.2.2 Solid State Binding

To further investigate the binding stoichiometry and strong affinity of $\mathbf{4}^{2+}$ for HS^-, we also investigated the solid-state binding of HS^- in $\mathbf{4}^{2+}$. Crystals suitable for X-ray diffraction were grown by combining $\mathbf{4}^{2+}$ and 2 equiv. of [TBA][SH] in MeCN under N_2. After mixing, the solvent was then removed under a vacuum, and the resulting solid was washed with CH_2Cl_2 to remove [TBA][PF_6]. This remaining residue was redissolved in minimal MeCN, and Et_2O was diffused into the solution at room temperature in a N_2-filled drybox to yield crystals suitable for X-ray diffraction. The resulting molecular structure confirmed the 2:1 host−guest complex, with one HS^- bound through exclusively C–H···S interactions and three PF_6^- counteranions (Figure 3.4; CCDC# 2270610). The structure crystallized in *P2/c*, with one PF_6^- on a special position. The hydrogen atom on HS^- was not located directly from the residual electron density, but the presence of 3 PF_6^- counterions is consistent with a monoanionic HS^- guest. These data are also supported by the presence of an observable HS^- signal in the ^1H NMR spectrum during the titrations used to measure the K_a values. To the best of our knowledge, this complex is one of the two crystal structures of HS^- bound in a host molecule. Consistent with our hypothesis that C–H···S interactions should drive strong host–guest binding, the C–H···S interactions in the structure are all significantly shorter than the sum of the van der Waals radii (3.00 Å) for H and S. The two imidazolium H···S distances are 2.53 and 2.54 Å with corresponding angles of 159.5

and 157.7°, respectively. The two phenyl H···S distances are 2.76 and 2.79 Å, with corresponding and nearly linear C–H···S angles of 171.6 and 174.8°, respectively. The imidazolium hydrogen atoms were refined using a riding model, but a separate positional refinement of the H atoms did not significantly impact the measured distances. These short distances and near-linear angles are suggestive of strong H-bonds, which support a strong enthalpic interaction leading to the observed large K_a and ΔG measured from the solution binding experiments. Considering that the majority of reported C–H···S contacts in the CSD are longer than the sum of the van der Waals radii and that very few contacts are found with a distance below 2.75 Å, the imidazolium C–H···S contacts observed in $(\mathbf{4}^{2+})_2 \cdot HS^-$ are unusually short.[206] Further analyzing the shortest intermolecular C–H···S contacts reported in the CSD, 2.53 and 2.54 Å distances are among the shortest 0.34% of C–H···S distances.

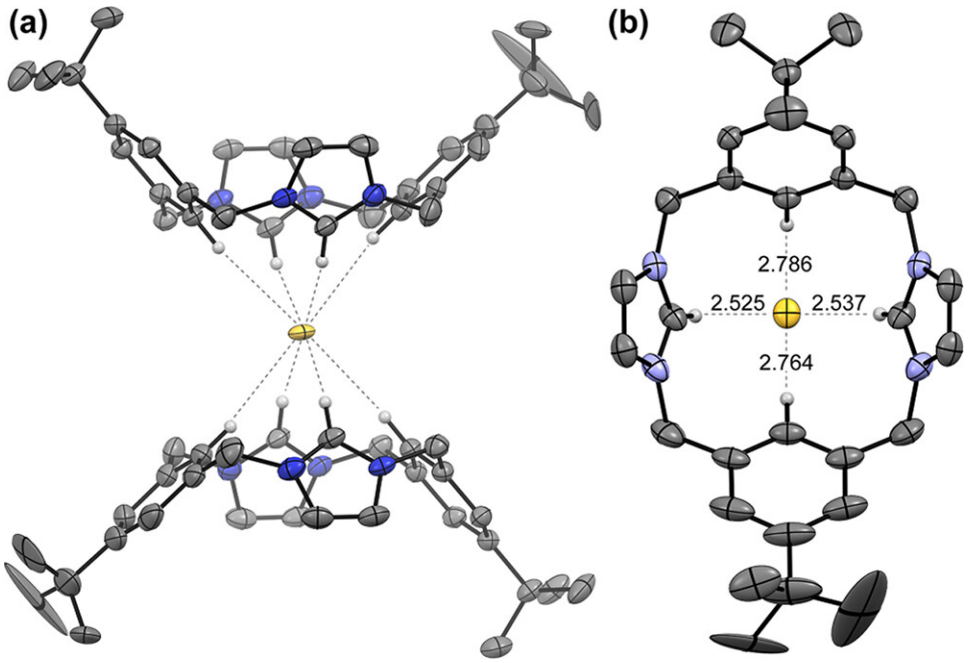

Figure 3.4. (a) Side on and (b) top views of the molecular structure of the $[(\mathbf{4}^{2+})_2 \cdot HS^-][PF_6]_3$. Thermal ellipsoids are drawn at a 50% probability level. Noninteracting H atoms, solvent molecules, and PF_6^- counteranions are omitted for clarity.

Furthering the comparison with Cl^-, the molecular structure of $\mathbf{4}^{2+} \cdot Cl^-$ was previously reported by Alcalde and shows solely 1:1 host−guest binding.[207] This stoichiometry from the $\mathbf{4}^{2+} \cdot Cl^-$ structure also matches our solution binding stoichiometry measured for Cl^- binding in $\mathbf{4}^{2+}$. Moreover, the imidazolium H···Cl distances (2.61 and 2.65) and phenyl H···Cl distances

(2.77 and 3.02) are mostly below the sum of the van der Waals radii for H and Cl (2.95) but are significantly longer than the H···S observed in the HS^- structure. This difference suggests that electrostatic attraction and the strong C–H···S interactions may be sufficient to not only increase the binding affinity for HS^- over Cl^- but also overcome both the increased entropic penalty for forming a 2:1 host−guest complex and also the Coulombic repulsion of assembling two dicationic receptors in solution.

3.3 Conclusions

We demonstrated that simple imidazolium receptors can be used to directly investigate the roles of C–H H-bond donor multiplicity, cationic charge, and preorganization in binding HS^-. Surprisingly, we observed an unprecedented 2:1 binding complex with $(\mathbf{4}^{2+})_2 \cdot HS^-$, in which two dicationic hosts come together to strongly bind HS^-. This stoichiometry was supported by both solution and solid-state investigations. The molecular structure of this host–guest complex is one of only two known structures of host binding HS^- and revealed short C–H···S H-bond interactions that drive HS^- binding. More broadly, these results contribute to the rational design of anion receptors for the stabilization of reactive sulfur species. Building from these design principles, we anticipate that the rational design of anion receptors for related and more reactive anionic small molecule bioregulators is now within reach and can further inform on the fundamental stability, reactivity, and crosstalk of these species in both supramolecular chemistry and biology.

CHAPTER IV

PROBING THE REVERSIBLE BINDING OF ANIONIC REACTIVE SULFUR AND NITROGEN SPECIES IN IMIDAZOLIUM RECEPTORS WITH DIRECTIONAL C-H HYDROGEN BONDS

This chapter includes previously published and co-authored material from Davis, A. G.; Zakharov, L. N.; Pluth, M. D. Probing the Reversible Binding of Anionic Reactive Sulfur and Nitrogen Species in Imidazolium Receptors with Directional C–H Hydrogen Bonds. *Inorg. Chem.* **2025**, Early View. This manuscript was written by Amanda G. Davis with editorial assistance by Professor Michael D. Pluth. The project in this chapter was conceived of by Amanda G. Davis and Professor Michael D. Pluth. The experimental work was performed by Amanda G. Davis. Crystal structure determination was performed by Dr. Lev N. Zakharov.

4.1 Introduction

Nature uses molecular recognition to facilitate specific interactions between molecules, often using noncovalent interactions to bind, activate, or stabilize different molecular fragments. While there is significant diversity in the types and strengths of these interactions, one simple yet powerful molecular recognition motif is the use of electron-deficient hydrogen bond donors, such as O–H, N–H, and more recently accepted C–H motifs, which can form strong and directional hydrogen bonds.[206] Building on these interactions, supramolecular chemists have drawn inspiration from nature to use similar directional H-bonding interactions to develop host–guest systems. For example, directional hydrogen bond donors are commonly incorporated in the development of anion receptors that bind a wide palette of environmentally abundant anions including halides (F^-, Cl^-, and Br^-),[180,184,195,216–220] sulfites and sulfates (SO_3^{2-} and SO_4^{2-}),[196,221–223] nitrate (NO_3^-),[224–227] phosphates ($H_2PO_4^-$ and HPO_4^{2-}),[228–230] and other guests. Using this approach, different research groups have designed receptors with specifically oriented motifs to bind and stabilize reactive anions,[188] engineered high anion specificity,[231] or formed complex structures such as mechanically interlocked molecules.[197,232] Specific examples include Sessler's calix[4]pyrrole receptors modified for selective ion-pair binding and extraction,[233] Beer's redox-modulated fluorescent receptors,[234] and Anslyn's cage exhibiting selective citrate binding and chemosensing.[235,236]

As the scope of molecular recognition has increased, the types of guests investigated have also expanded, with a particular focus on those with biological relevance. As a simple example, chloride (Cl^-) is both environmentally abundant and important for maintaining cellular ionic homeostasis. In biology, chloride is often found ionically paired with K^+ or Na^+, and the coupled movement of these ions across cellular plasma membranes via potassium-chloride cotransporters generates electrochemical gradients that are essential for salt reabsorption/secretion for various organs, auditory system function, cell volume maintenance, and neurotransmission.[237] The heavier congener, bromide (Br^-), does not have the same physiological importance as chloride but has been postulated to play important roles as a cofactor in essential tissue development and architecture.[238]

Expanding to more reactive biologically relevant anions, many small-molecule bioregulators are either anionic at physiological pH or have common oxidation products that are anionic. For example, hydrogen sulfide (H_2S) and nitric oxide (NO) are involved in biological functions ranging from vasodilation to reducing oxidative stress to exerting cardioprotective effects. Although commonly referred to as neutral species, H2S exists primarily as HS^- at physiological pH.[18,19,56] Similarly, although NO is neutral, it has a short cellular lifetime (~milliseconds to seconds)[239] and is rapidly oxidized under physiological conditions to form nitrite (NO_2^-),[39] which is a common analytical target for indirect NO detection and measurements (e.g., Griess Assay). In addition, NO_2^- constitutes the largest intravascular and tissue storage of reactive nitrogen species.[240] Expanding to further oxidized nitrogen species, nitrate (NO_3^-) is also an abundant circulating species, with common dietary sources including leafy greens. More broadly, NO_3^- has been a common target for anion recognition due to its role as an agricultural nutrient.[241–244] Furthering its connection with other reactive nitrogen species, NO_3^- can also be reduced through $NO_3^-/NO_2^-/NO$ pathways, with one example being oral bacteria reduction of NO_3^- to NO_2^-, followed by further reduction to NO via low pH-mediated pathways in the stomach or through the action of nitrite reductases and/or hemoglobin.[38]

Despite the importance of reactive sulfur and nitrogen species in biology, relatively few investigations have focused on the molecular recognition of the more reduced versions of these species. Only a handful of reports have investigated reversible HS^- binding, even though understanding such interactions may help inform on biological activity. Examples of such receptors for binding HS^- include Sindelar's bambusiril,[198] Beer's halogen-bonding receptors,[204]

Haley and Johnson's aryl ethynyl receptors,[200,202] and simple tripodal receptors employed in our recent work (Figure 4.1a).[203] A common theme in many of these receptors is the importance of C–H···S interactions in HS^- binding, with some reports showing highly directional, polarized C–H···S interactions in the solid state[200] or even showing preferential binding HS^- over Cl^- in solution.[245] Similarly, although many studies have focused on NO_3^- binding, fewer examples have focused on the more reduced and biologically relevant NO_2^-. Selected examples include Bowman-James's polyamide pincer macrocycle (no K_a reported),[246] Flood's triazole-based foldamer (K_a = 4000 M^{-1} in MeCN),[247] and Kang's perimidine-based nitrite-selective receptor (K_a = 3500 M^{-1} in DMSO)[248] (Figure 4.1b). Each of these receptors is likewise characterized by numerous directional, polarized N–H and C–H H-bonding interactions. In particular, Bowman–James's pincer macrocycle exhibits extremely short N–H···O H-bonds (1.801 Å) that are significantly below the sum of the van der Waals radii (2.72 Å). In addition, the receptor also seems to employ anion-π interactions, with nitrite sandwiched between two closely stacked pyridine units (N_{py}–N_{py} = 6.634 Å).

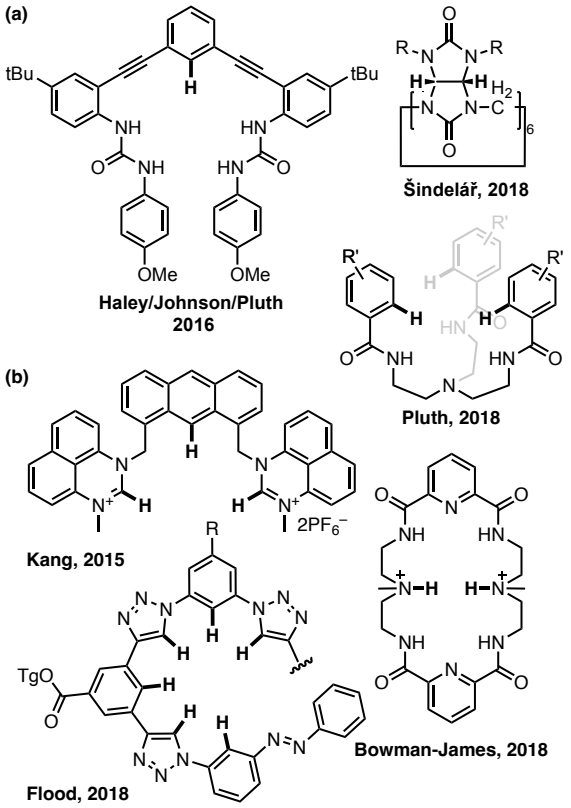

Figure 4.1. Selected prior examples of H-bonding receptors demonstrated to bind (a) HS^- or (b) NO_2^-.

Building from the above examples and prior crystallographic work demonstrating the importance of C–H H-bonding interactions in binding these types of anions,[206] our goal was to further investigate how factors including charge, multiplicity, and preorganization impact the binding, recognition, and selectivity of HS^- and NO_2^-. With these goals in mind, we report here the solution binding and structural characterization of a series of imidazolium-based receptors that use C–H H-bond donors for anion binding of HS^- and NO_2^- and compare the binding profiles with those of NO_3^-, Cl^-, and Br^- to better understand the individual components that impact guest binding.

4.2 Results and Discussion

4.2.1 Anion and Receptor Scope

To further advance our understanding of C–H H-bonding interactions in the context of anion binding, we chose to broaden the scope of anions to include biologically relevant HS^- and NO_2^- as well as the more commonly investigated anions NO_3^-, Cl^-, and Br^-. Complementing the anions of interest, we also wanted to build a larger library of imidazolium receptors to systematically investigate how charge, directionality, and preorganization impact anion binding. In general, imidazolium-based motifs are ideal for investigating C–H···X interactions based on the highly directional, polarizable, and easily modifiable C–H bonds that can be easily tracked by ^{1}H NMR spectroscopy. These imidazole motifs can be easily incorporated into a wide variety of receptors, ranging from simple macrocycles to more complex cages, which have been used to bind other anions such as $H_2PO_4^-$, HSO_4^-, $CH_3CO_2^-$, and Br^-.[208,209,249] With these design aspects in mind, we chose to systematically investigate a library of receptors in which we modify receptor charge, directionality, and preorganization (Figure 4.2). Each of the receptors was characterized by ^{1}H, ^{13}C, ^{19}F, and ^{31}P NMR spectroscopy, with additional solid-state characterization from X-ray structural data for a selection of host–guest complexes.

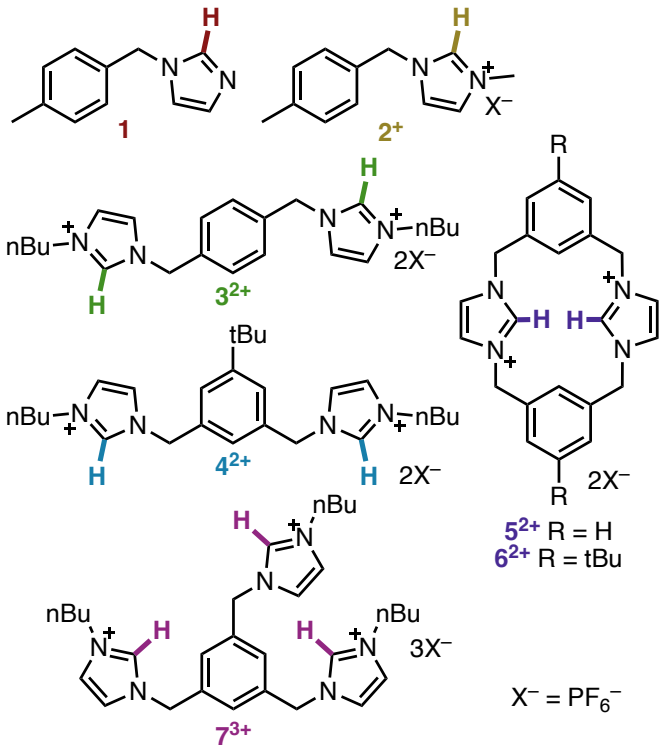

Figure 4.2. Imidazolium receptors **1**–**7**$^{3+}$ used to investigate anion binding.

To deconstruct the multiplicity, directionality, and charge of different imidazolium configurations, we started with simple C–H donors like neutral **1**. To incorporate a positive charge, we prepared **2**$^{+}$, which is the methylated version imidazolium analogue of **1**. Receptor **3**$^{2+}$ includes an additional imidazolium binding site in the *para*-position, thus increasing both multiplicity and charge. Receptor **4**$^{2+}$ maintains the same charge and multiplicity but moves the imidazolium binding site to the *meta*-position, which should provide better preorganization and decrease the entropy for guest binding due to a more favorable binding angle. In addition, receptor **4**$^{2+}$ is a nonmacrocyclic analogue of receptor **6**$^{2+}$, which provides an additional level of comparison for the impacts of preorganization. Receptors **5**$^{2+}$ and **6**$^{2+}$ incorporate the imidazolium motifs into a macrocycle with the addition of phenyl C–H binding motifs, which both increases preorganization and further reduces the entropic penalty for guest binding. Receptor **6**$^{2+}$ differs from receptor **5**$^{2+}$ by the inclusion of a *tert*-butyl group, which could further impact macrocycle orientation for anion binding and reduce motif flipping in solution. As a final nonmacrocyclic receptor, we also chose to include **7**$^{3+}$ to provide an additional imidazolium binding site and further increase the receptor charge. Although receptor **7**$^{3+}$ provides added Coulombic attraction, it may also have a greater preorganization penalty, with all three arms

needing to rotate to face the same direction for optimal C–H orientation for guest binding. For each of the cationic receptors, **2–7**, we used PF_6^- as a counteranion for the parent hosts to reduce competitive binding when investigating guest binding. Although receptors **1**, $\mathbf{2}^+$, $\mathbf{4}^{2+}$, and $\mathbf{6}^{2+}$ were discussed in our prior work focusing on HS^- binding, the expanded series of hosts and guests provides greater coverage to investigate what factors of host design impact binding of the anions investigated.

4.2.2 Solution State Binding

After preparing each receptor, we next performed binding studies using ^{1}H NMR spectroscopy to determine the binding affinities (K_a) of receptors $\mathbf{1–7}^{3+}$ toward HS^-, NO_2^-, NO_3^-, Cl^-, and Br^- (Figure 4.3). We also investigated whether HSe^-, which is an intermediate involved in the incorporation of Se into biomolecules, could be bound in these receptors since only one prior report of HSe^- binding has been demonstrated by Johnson, Haley, and Pluth in an aryl ethynyl receptor,[201] which also showed strong HS^- binding.[202,203] Treatment of the imidazolium receptors with HSe^-, however, resulted in significant host and/or guest decomposition, suggesting that this guest is incompatible with the imidazolium minding motifs. Similarly, treatment with SNO^- and $SSNO^-$, which are anions likely involved in NO/H_2S biological crosstalk,[75,250] also led to decomposition, suggesting that these anions may be too reactive for binding by imidazolium motifs.[86]

To measure binding affinities for each anion investigated, we performed host–guest titrations using the tetrabutylammonium (TBA) salt of each anion in deoxygenated and anhydrous CD_3CN at 25 °C under N_2 to avoid unwanted oxidation from the more reactive guests. Upon guest addition and subsequent binding, we observed downfield shifts of the imidazolium and phenyl C–H signals, which is consistent with C–H interactions facilitating anion binding. In general, the titrations that exhibited a larger change in signal shifts were associated with stronger binding affinities. For titrations involving HS^-, we also observed an upfield shift of the sulfhydryl hydrogen upon guest addition, which is consistent with the reversible formation of a host–guest complex undergoing fast exchange on the NMR time scale. Binding affinities for each host–guest pair were measured by fitting the changes in chemical shifts of interacting C–H protons as a function of host and guest concentrations and fit using the Nelder–Mead method in Bindfit.[212–214]

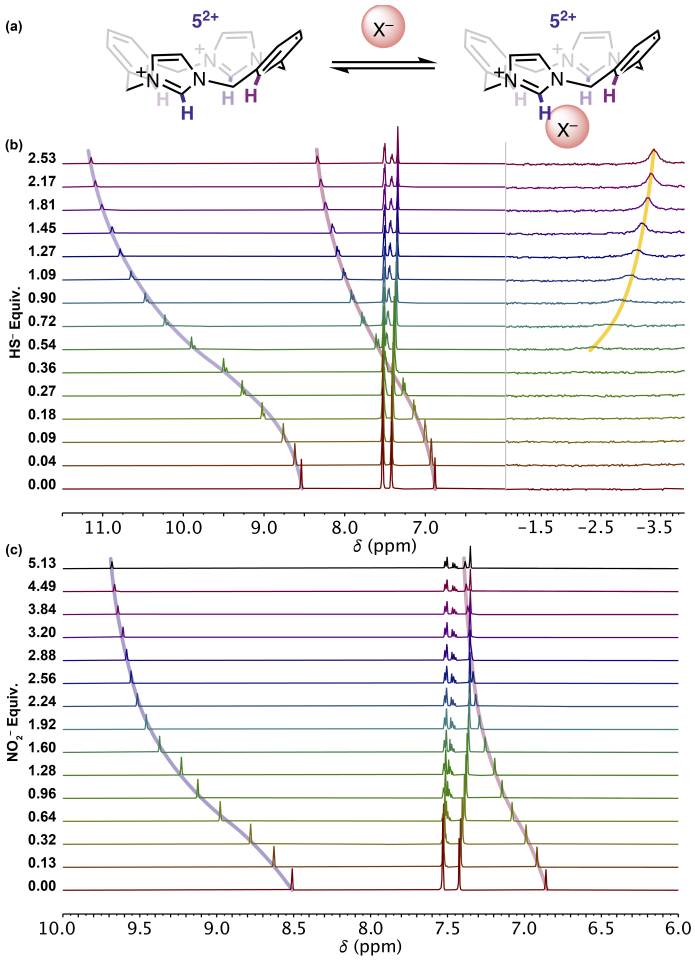

Figure 4.3. (a) Example of the general guest binding scheme for binding X^- in $\mathbf{5}^{2+}$. (b) Representative ^{1}H NMR titration of $\mathbf{5}^{2+}$ with [TBA][SH]. The yellow highlighted peak at negative ppm corresponds to the HS^- signal. (c) Representative ^{1}H NMR titration of $\mathbf{5}^{2+}$ with [TBA][NO_2]. General conditions: $[\mathbf{5}^{2+}]_i$ = 1.58 mM, CD_3CN, 25 °C.

The measured binding affinities are summarized in Table 4.1. None of the investigated anions exhibited observable binding to imidazole **1**, which is consistent with the relatively nonpolarized C–H H-bond donor. All the anions investigated bind to receptor $\mathbf{2}^+$, which has a more polarized imidazolium C–H H-bond donor, with HS^- and Cl^- having similar binding affinities that were ~2–3 fold higher than Br^-, NO_2^-, and NO_3^-. Inclusion of an additional imidazolium motif in $\mathbf{3}^{2+}$ increased anion binding affinity, which was further enhanced by changing the imidazolium connectivity from *para*- to *meta*- in $\mathbf{4}^{2+}$. This enhanced preorganization of the host–guest complex increased the binding affinity by 2–3 fold for NO_2^-, NO_3^-, and Br^- and more significantly by 4–5 fold for HS^- and Cl^-. The macrocyclic receptors $\mathbf{5}^{2+}$ and $\mathbf{6}^{2+}$ generally exhibited similar K_a values (aside from HS^-, vide infra) and significantly

higher binding than receptor $\mathbf{4}^{2+}$, which is likely due to increased preorganization and additional phenyl binding motifs. The addition of a third imidazolium motif in $\mathbf{7}^{3+}$ resulted in the greatest Coulombic attraction but did not result in significantly greater binding when compared to the macrocyclic hosts, highlighting the impact of macrocyclic preorganization for anion binding.

Table 4.1. Binding Affinities for anions in receptors $\mathbf{1}$–$\mathbf{7}^{3+}$ in CD_3CN.

	HS^-		NO_2^-		NO_3^-		Cl^-		Br^-	
	K_a (M^{-1})	ΔG (kcal/mol)	K_a (M^{-1})	ΔG (kcal/mol)	K_a (M^{-1})	ΔG (kcal/mol)	K_a (M^{-1})	ΔG (kcal/mol)	K_a (M^{-1})	ΔG (kcal/mol)
1	NBO[b,c]	-	NBO[b]	-	NBO[b]	-	NBO[b]	-	NBO[b]	-
2	60 ± 4 [c]	-2.4 ± 0.1	27 ± 1	-2.0 ± 0.1	27 ± 1	-2.0 ± 0.1	63 ± 3 [c]	-2.5 ± 0.1	22 ± 1	-1.9 ± 0.1
3	210 ± 25	-3.2 ± 0.1	120 ± 10	-2.8 ± 0.1	170 ± 9	-3.1 ± 0.1	335 ± 15	-3.4 ± 0.1	300 ± 25	-3.4 ± 0.1
4	1000 ± 85 [c]	-4.1 ± 0.1	470 ± 20	-3.7 ± 0.1	400 ± 70	-3.5 ± 0.1	1350 ± 75 [c]	-4.3 ± 0.1	520 ± 25	-3.7 ± 0.1
5	6600 ± 300	-5.2 ± 0.1	1300 ± 100	-4.3 ± 0.1	730 ± 40	-3.90 ± 0.1	5200 ± 300	-5.1 ± 0.1	1200 ± 60	-4.2 ± 0.1
6	40000 ± 8000[c, d]	-6.3 ± 0.1	1500 ± 150	-4.3 ± 0.1	900 ± 300	-4.0 ± 0.2	6600 ± 800 [c]	-5.2 ± 0.1	1540 ± 90	-4.4 ± 0.1
	5000 ± 1000 [c, d]	-5.0 ± 0.1								
7	6900 ± 350[d]	-5.6 ± 0.1	1600 ± 300[d]	-4.3 ± 0.1	1200 ± 70	-4.2 ± 0.1	16500 ± 1400	-5.8 ± 0.1	6400 ± 300[d]	-5.2 ± 0.1
	650 ± 100[d]	-4.4 ± 0.3	500 ± 200[d]	-3.7 ± 0.2					390 + 30[d]	-3.5 ± 0.1

[a]From fitting ^{1}H NMR titration data to 1:1 binding unless otherwise noted. The reported error is the standard deviation of triplicate titrations or 5% of the K_a, whichever was greater. [b]NBO, no measurable binding observed. [c]Values previously reported. [d]Fit to 2:1 binding; the first value is 1:1 binding followed by the 2:1 binding event.

In general, increasing both cationic charge and preorganization positively impacts binding affinity. This can be seen from the trend of increased K_a values through the series of receptors investigated (Figure 4.4a). In searching for parameters that could help further explain these binding preferences, we focused on the most strongly binding receptors, $\mathbf{4}^{2+}$–$\mathbf{7}^{3+}$, and anion volume, which were estimated from either available thermochemical radii or previously published computations for each anion (Figure 4.4b).[247,251] We found a negative correlation between the Log(K_a,1:1) values and anion volumes for Cl^-, Br^-, NO_2^-, and NO_3^-, but found that HS^- did not fit this trend. In each case, the measured K_a values for HS^- were higher than would have been expected solely from the anion volume, suggesting that other components significantly impact HS^- when compared to other anions. We attribute this difference to the significance of C–H···S stabilizing interactions, which may include other factors such as better hard/soft acid-base pairing between HS^- and polarized C–H motifs, changes in polarizability, and the angle dependence of hydrogen bonding preferences for sulfur over other anions.[206]

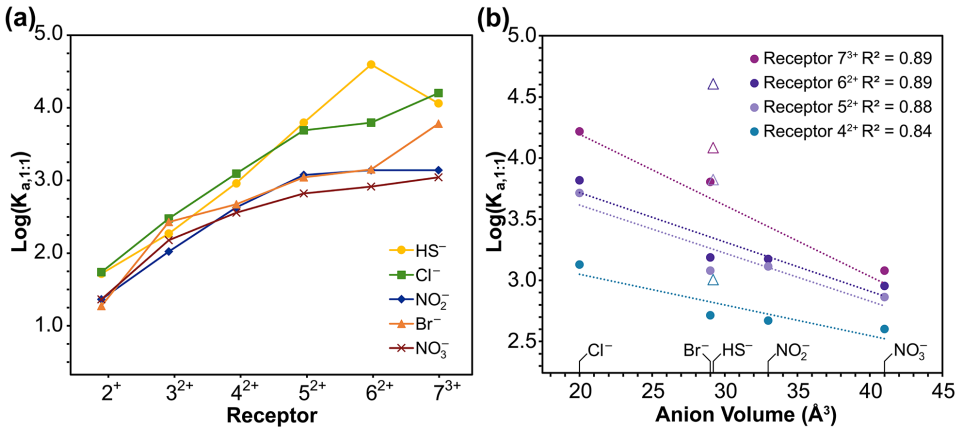

Figure 4.4. (a) Summary of the 1:1 binding affinities (Log($K_{a,\ 1:1}$)) of receptors $\mathbf{2}^{+}$–$\mathbf{7}^{3+}$ with each anion. (b) The 1:1 binding affinity (Log($K_{a,1:1}$)) of receptors $\mathbf{4}^{2+}$–$\mathbf{7}^{3+}$ with Cl^{-}, Br^{-}, NO_2^{-}, and NO_3^{-} (data in ●) as a function of anion volume (Å^3). Measured Log($K_{a,1:1}$) values for HS^{-} (△) for each receptor do not fit with the general trend. Displayed linear fits and R^2 values exclude HS^{-}.

4.2.3 Structural Characterization of Host-Guest Interactions

In our prior work with $\mathbf{6}^{2+}\cdot HS^{-}$, we were able to characterize the host–guest complex using X-ray crystallography to confirm both the 2:1 binding stoichiometry and the extremely short C–H···S H-bonds (2.525 Å, corresponding to the shortest 0.34% of C–H···S contacts in the CCDC). Building from these structural insights, we wanted to further expand our analysis by examining the solid-state molecular structures of $\mathbf{5}^{2+}$ and $\mathbf{6}^{2+}$ with each anion investigated, including PF_6^{-} from the parent host structure. Crystals suitable for X-ray diffraction were grown by combining the PF_6^{-} salts of receptor $\mathbf{5}^{2+}$ or $\mathbf{6}^{2+}$ with the [TBA][X] salt in MeCN and using either vapor or layer diffusion of Et_2O at room temperature. Crystallizations of more sensitive salts (HS^{-} or NO_2^{-}) were carried out in a N_2-filled drybox, whereas others were either started in a drybox and were removed or grown on the benchtop.

Using this approach, we were able to grow X-ray quality crystals for all host–guest complexes, except for $\mathbf{5}^{2+}\cdot HS^{-}$ and $\mathbf{6}^{2+}\cdot NO_2^{-}$ (Figure 4.5). We observed complete anion exchange for each host–guest complex and did not observe any residual PF_6^{-} counteranions in the molecular structures. We note that crystallization conditions, required charge balance, and crystal packing forces may contribute to the 1:2 solid-state stoichiometry despite the 1:1 solution-state guest binding. As expected, each of the host–guest structures shows C–H···X^{-} H-bonding as the primary interaction between host and guest. A summary of the C–H···X^{-} bond distances and angles is included in Table 4.2. Additionally, structural and packing information is included in

the Supporting Information. Table 4.2 also summarizes the sum of the van der Waals radii (Σ_{VDWR})[215] for each H···X interaction, along with the shortest C–H···X contacts and the associated contact angle from each crystal structure. In each case, the shortest C–H···X contacts for the host–guest complexes were associated with the anion binding to the imidazolium C–H bonds, which is consistent with the solution-state titration data in which the imidazolium C–H chemical shifts show the largest change in chemical shift. Only the $\mathbf{6}^{2+}\cdot PF_6^-$ structure was an outlier to this trend, with the PF_6^- being offset from the ideal binding pocket with the shortest contact to a benzyl CH_2 group ($\mathbf{6}^{2+}\cdot PF_6^-$, Figure 4.5j). These data further support the choice of PF_6^- as a nonbinding or noncoordinating anion for the parent host species.

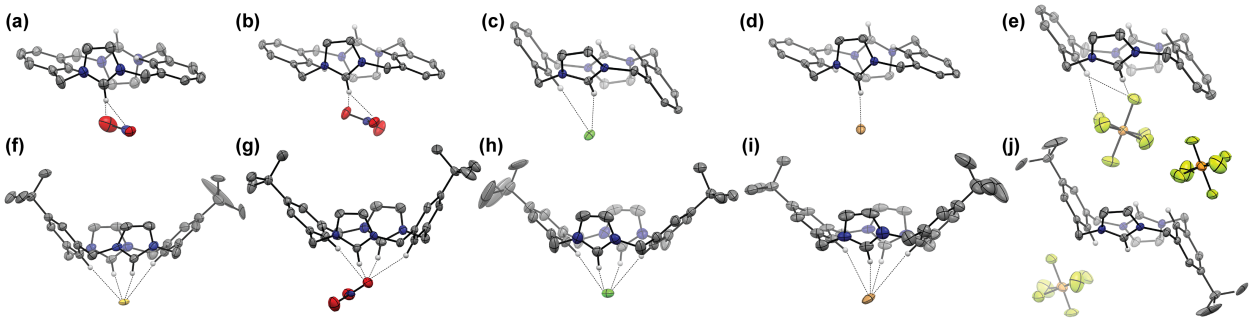

Figure 4.5. Molecular structure of each macrocyclic host-guest complex with C–H···X^- contacts highlighted. (a) $5^{2+}\bullet NO_2^-$, (b) $5^{2+}\bullet NO_3^-$, (c) $5^{2+}\bullet Cl^-$, (d) $5^{2+}\bullet Br^-$, (e) $5^{2+}\bullet PF_6^-$, (f) $6^{2+}\bullet HS^-$, (g) $6^{2+}\bullet NO_3^-$, (h) $6^{2+}\bullet Cl^-$, (i) $6^{2+}\bullet Br^-$, (j) $6^{2+}\bullet PF_6^-$. Thermal ellipsoids are drawn at a 50% probability level. Noninteracting H atoms, solvent molecules, and additional anions outside the binding pocket are omitted for clarity.

Table 4.2. Summary of C–H···X bond distances and angles of receptors 5^{2+} and 6^{2+} host-guest complexes.

		HS^-	NO_2^-	NO_3^-	Cl^-	Br^-	PF_6^-
	H···X Σ_{VDWR} (Å)	3.0	2.72	2.72	2.95	3.05	2.67
$\mathbf{5}^{2+}$	C–H···X Distance (Å)		2.238	2.277	2.587	2.609	2.548
	$\Delta\Sigma_{VDWR}$ (Å)	–	0.48	0.44	0.36	0.44	0.12
	Contact Angle (°)		150.21	152.84	156.25	155.17	147.11
$\mathbf{6}^{2+}$	C–H···X Distance (Å)	2.525		2.269	2.632	2.647	2.370
	$\Delta\Sigma_{VDWR}$ (Å)	0.48	–	0.45	0.32	0.40	0.30
	Contact Angle (°)	159.53		144.70	144.74	162.72	146.51

One notable difference between the solid-state structures pertains to the different binding conformations between receptors $\mathbf{5}^{2+}$ and $\mathbf{6}^{2+}$. If we consider the PF_6^- complexes as "unbound", and the other anionic complexes as "bound", we note that receptor $\mathbf{6}^{2+}$ flips into a "bowl"-like conformation in which the C–H binding motifs all point in the same direction when binding a guest (Figure 4.6). This bowl-like conformation is unique to receptor $\mathbf{6}^{2+}$, since receptor $\mathbf{5}^{2+}$ remains in a chair-like conformation in which pairs of phenyl and imidazole moieties point in opposite directions, regardless of the anion. Interestingly, the conformational flipping into a bowl conformation does not necessarily correlate with shorter host–guest bond distances or strong binding affinities.

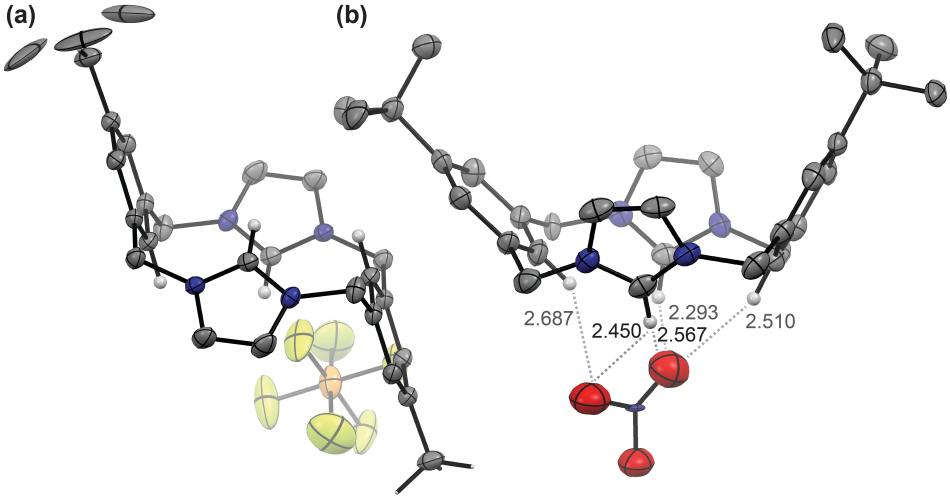

Figure 4.6. (a) Molecular structure of unbound, chair-like $\mathbf{6}^{2+}\bullet 2PF_6^-$ and (b) bowl-like $\mathbf{6}^{2+}\bullet 2NO_3^-$. Thermal ellipsoids are drawn at a 50% probability level. Noninteracting H atoms, solvent molecules, and additional anions are omitted for clarity.

Focusing on key structural aspects of each host–guest complex, a number of observations and differences between the macrocyclic hosts are notable. While we were unable to obtain X-ray quality crystals of complex $\mathbf{5}^{2+}\cdot HS^-$, we have previously reported the structure of the $\mathbf{6}^{2+}\cdot HS^-$ complex that crystallized in *P2/c* as a 2:1 host:guest complex (Figure 4.5f).[245] Unlike the other complexes reported herein, the formation of a 2:1 host:guest complex with extremely short imidazolium C–H···S contacts (2.53 and 2.54 Å) suggests that the electrostatic attraction and strong C–H···S contacts may be sufficient for both the selective binding affinity of HS^- over other anions and also for overcoming the increased entropic penalty for forming a 2:1 host:guest

complex and the Coulombic repulsion associated with assembling two dicationic receptors around one anion.

Complex $\mathbf{5}^{2+}\cdot 2NO_2^-$ crystallized in $P2_1/c$ with each dicationic receptor interacting with two NO_2^- anions exclusively through C–H H-bonding interactions (Figures 4.5a and C96). The NO_2^- is disordered over two positions with 75:25 occupancy. Focusing on the major contributors, there are two unique C–H···O contacts from the imidazolium C–H donors that are below the Σ_{VDWR} (2.72 Å), with associated distances and contact angles of 2.238 and 2.491 Å, and 150.21° and 137.39°, respectively.

Moving to the more oxidized NO_3^- guests, complex $\mathbf{5}^{2+}\cdot 2NO_3^-$ crystallized in $P2_1/c$ with each NO_3^- bound exclusively through C–H interactions (Figures 4.5b and C97). Two unique C–H···O contacts are below the Σ_{VDWR} (2.72 Å). Both contacts are associated with imidazolium C–H donors and have associated distances and contact angles of 2.277 and 2.349 Å, and 152.84° and 140.39°, respectively. The $\mathbf{6}^{2+}\cdot 2NO_3^-$ complex crystallized in $Pca2_1$ with one NO_3^- anion primarily interacting with the imidazolium through C–H H-bonding interactions (Figures 4.5g and C98). This structure contains more groups interacting with H-bond donors than $\mathbf{5}^{2+}\cdot 2NO_3^-$, showing 10 unique C–H···O contacts that are below the Σ_{VDWR} (2.72 Å), with six interactions associated with imidazolium C–H donors and four interactions associated with phenyl C–H donors.

Complex $\mathbf{5}^{2+}\cdot 2Cl^-$ crystallized in $P2_1/c$ with two Cl^- anions bound exclusively through C–H H-bonding interactions, with one water molecule per Cl^- present in the lattice (Figures 4.5c and C99). This water molecule does not engage in any interactions with the host but does provide one H-bond to Cl^-, which could impact the solid-state structure. Five unique C–H···Cl contacts are below the Σ_{VDWR} (2.95 Å). Two of these are associated with imidazolium C–H donors or phenyl C–H donors, with distances and contact angles of 2.587 and 2.787 Å, and 156.25° and 161.15°, respectively. The other three C–H···Cl contacts are associated with either benzyl CH_2 or imidazolium backbone C–H motifs. Complex $\mathbf{6}^{2+}\cdot 2Cl^-$ crystallized in *Pmna* with one Cl^- anion bound exclusively through the imidazolium C–H H-bonding interactions (Figures 4.5h and C100). There are three unique C–H···Cl contacts that are below the Σ_{VDWR} (2.95 Å). One of these is associated with an imidazolium C–H donor, and two are associated with phenyl C–H donor, with distances and contact angles of 2.632, 2.722, and 2.803 Å, and 144.74°, 172.06°, and 175.09°, respectively.

Complex $\mathbf{5}^{2+}\cdot 2Br^-$ crystallized in $P2_1/n$ with two Br^- anions bound exclusively through C–H H-bonding interactions (Figures 4.5d and C101). Three unique C–H···Br contacts are below the Σ_{VDWR} (3.05 Å). One of these is associated with an imidazolium C–H donor, and the others are from imidazolium backbone C–H and benzyl CH_2 contacts of adjacent molecules. The distances and contact angles are 2.609, 3.001, and 3.002 Å, and 155.17°, 128.85°, and 141.90°, respectively. Complex $\mathbf{6}^{2+}\cdot 2Br^-$ crystallized in *P*-1 with one Br^- anion bound exclusively through imidazolium C–H H-bonding interactions with the host (Figures 4.5i and C102). One water molecule per Br^- is present in the lattice, which provides one H-bond to the bromide, which could impact the potential solid-state structure. This structure contains more interactions than $\mathbf{5}^{2+}\cdot 2Br^-$ with eight unique C–H···Br contacts that are below the Σ_{VDWR} (3.05 Å), five of which are associated with imidazolium C–H donors and three associated with phenyl C–H donors.

The parent $\mathbf{5}^{2+}\cdot 2PF_6^-$ complex crystallized in *P*-1 with two PF_6^- counteranions loosely coordinated through C–H H-bonding interactions (Figures 4.5e and C103). Three unique C–H···F contacts are below the Σ_{VDWR} (2.67 Å). Two of these correspond to phenyl C–H donors, one of which corresponding to an imidazolium C–H donor. The contact distances and angles are 2.548, 2.569, and 2.581 Å, and 147.11°, 152.40°, and 156.37°, respectively. The parent $\mathbf{6}^{2+}\cdot 2PF_6^-$ complex crystallized in $P2_1/n$ with two PF_6^- counteranions loosely coordinated through C–H H-bonding interactions (Figures 4.5j and C104). There are five unique C–H···F contacts that are below the Σ_{VDWR} (2.67 Å), associated with benzyl CH_2 and imidazolium backbone C–H contacts.

4.3 Conclusions

Using solution-state binding investigations with a library of imidazolium receptors, we have demonstrated how Coulombic attraction, directionality, and preorganization impact anion binding across a series of guests, including the biologically relevant and under investigated anions, HS^- and NO_2^-. Based on the observed binding affinity trends, increasing Coulombic attraction through increased cationic charge appears to be a primary contributor to binding strength, followed closely by the lowering of enthalpic barriers via preorganization of the host–guest complex. We also observed that the $\text{Log}(K_{a,1:1})$ values for the stronger binding receptors correlated inversely with anion volume, although HS^- was a clear outlier to this trend. Further complementing the solution-state binding affinities of the macrocyclic receptors, we used X-ray crystallography to demonstrate the importance of short C–H···X contacts, many of which are

below the sum of the van der Waals radii of the interacting atoms. This structural analysis also revealed conformational flipping between “chair” to “bowl” upon anion binding that is only exhibited by substituted macrocycle, $\mathbf{6}^{2+}$. More broadly, these results demonstrate how the rational design of anion receptors can impact binding and the stabilization of reactive anionic species. By incorporating these design principles, novel anion receptors can be designed with the goal of binding and stabilizing more reactive small-molecule bioregulators.

CHAPTER V

CONCLUSIONS

The field of gasotransmitters has been long established with huge efforts dedicated to understanding the endogenous production, physiological/toxic concentrations and localizations, detailed molecular signaling pathways, and identification of secondary messengers and molecular targets. Not until more recently has more attention has shifted to gasotransmitter - crosstalk/-related species that have direct ties to molecular gasotransmitter generation. For example, recent research has supplied evidence suggestive of mammalian endogenous conversion of NO_3^- to NO_2^- by some prospective mammalian nitrate reductases. Additionally, considering the post-translational modification of thiols by S-nitrosylation via NO to generate protein RSNO, free HSNO/SNO^- has garnered significant attention as a storage vehicle for H_2S & NO and potentially serving as a distinct cellular signaling species. More research has focused on the generation of bioinorganic (S)SNO^- mimics as well as (S)SNO^- activatable physiological pathways, however, the fundamental chemistries and reactivities involving these species have been largely under investigated.

We were the first to report the fundamental reactivities and mechanisms associated with the proton- and COS-mediated interconversion from SNO^- to $SSNO^-$. The interconversion of these species generates a cascading release of other small molecule bioregulators such as H_2S, NO, N_2O, CO_2, and S^0. This fundamental reactivity is essential for understanding more complicated reaction pathways, understanding how molecular crosstalk can be influenced by proton inventory, and gives insight into the potential lifetime of these species in biological milieu. There is still much that could be built off these fundamental studies, including investigating the specific lifetimes of SNO^- and $SSNO^-$ in buffered aqueous systems, investigating potential interconversion in basic conditions, as well as determining the experimental pK_a values of HSNO and HSSNO in water.

As discussed previously, molecular environment can influence the protonation state, pK_a, reactivity, and stability of a species. Molecular recognition is what enables the active site of receptors to be activatable by only specific substrates, typically requiring complementary non-covalent interactions to enable this specificity. Deriving inspiration from biology, supramolecular chemists can develop anion receptors that employ non-covalent interactions to

reversibly bind and stabilize reactive species. It wasn't until more recently that the anions of choice shifted from environmentally abundant, relatively stable anions such as halides, phosphates, and sulfates, to more elusive physiologically relevant, reactive species such as $O_2^{\bullet-}$, HS^-, or even HSe^-. Previously the Pluth lab, in collaboration with the Johnson and Haley labs, were able to demonstrate the very first examples of reversible binding of both HS^- and HSe^- in modified arylethynyl bis-urea anion receptors, where it was revealed that HS^- demonstrated preference for C–H over N–H hydrogen bonding interactions.

These preference for forming C–H···S interactions spurred further investigations into the development of C–H H-bonding based anion receptors, in the form of imidazolium-based host molecules. Our lab demonstrated that these receptors again showed preferential formation of strong C–H···S interactions with solution state K_a values for HS^- consistently exceeding the values for other anions of comparable volumes, and that across receptors the primary influence on binding strength was coulombic attraction followed by host-guest complex preorganization. Additionally, solid-state characterization of the host-guest complexes revealed extremely short and linear C–H···S hydrogen bonding interactions that were amongst the shortest interactions reported in the CCDC. We were also able to demonstrate moderate K_a values with other under investigated PSMBs, such as NO_2^- and NO_3^-. While we were unsuccessful in using these receptors for reversible binding of other PSMBs, such as HSe^-, SNO^-, and $SSNO^-$, these studies supported the underlying importance of C–H···S interactions and provides insight into future developments of rationally designed anion receptors specifically for binding reactive S/N hybrid species. We have demonstrated that Coulombic attraction is a primary driving force, but have seen in throughout this dissertation that Lewis acidic protons lead to undesirable non-reversible reactivity of SNO^- and $SSNO^-$. Future anion receptors must keep these characteristics in mind as to balance reversible binding with irreversible protonation and decomposition. Overall, this work has demonstrated modes of reactivity and provided mechanistic insight pertaining to reactive S/N hybrid species, SNO^- and $SSNO^-$, and has also provided essential insights into using anion binding to understand the stabilities of various PSMBs. The class of PSMBs is characterized by rich physiology and complex intermolecular crosstalk. Hopefully, the work described herein provides the fundamental insights for future efforts focused on deepening our understanding of distinct crosstalk mechanisms as well as the molecular recognition of other reactive PSMBs, not limited to SNO^- and $SSNO^-$.

APPENDIX A

CHAPTER II SUPPLEMENTARY INFORMATION

A1: ADDITIONAL SCHEMES

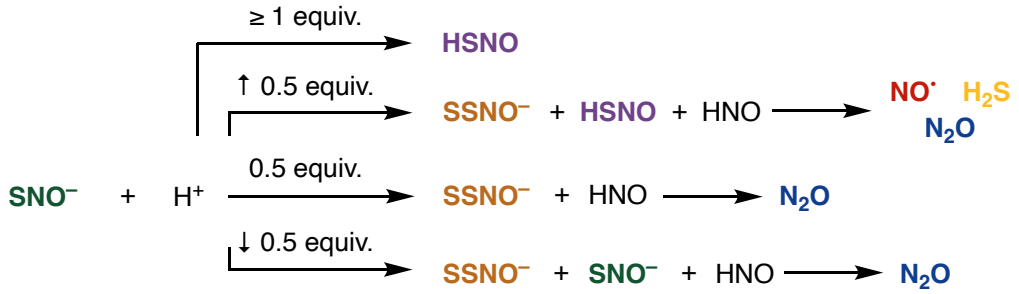

Scheme A1. Reaction pathways highlighting how the difference in acid stoichiometry can influence byproduct speciation.

A2. EXPERIMENTAL METHODS

General methods: All syntheses and experimental manipulations were performed in an Innovative Atmospheres N_2-filled glovebox. All UV-Vis spectra were obtained at room temperature or 25 °C on an Agilent Cary 60 Spectrophotometer. All NMR spectra were obtained on a Bruker Avance III-HD 500 MHz or 600 MHz NMR spectrometer equipped with a multinuclear Prodigy™ CryoProbe. IR spectroscopy was performed on an HP 8453 Nicolet Magna 550. Gas chromatography was performed on an Agilent 8890 Gas Chromatograph with an OI Analytical PFPD sulfur specific detector. All solvents used were anhydrous and air-free unless otherwise noted. Anhydrous and nonoxygenated acetone and CD_3CN were obtained by sparging with N_2, distilling over K_2CO_3, and storing over 3 or 4Å molecular sieves in an inert atmosphere glovebox. Labeled/unlabeled PPN salts, COS, and NO were synthesized according to prior literature. Glacial AcOH was deoxygenated via freeze-pump-thaw method prior to use. All other reagents were purchased from commercial suppliers and stored in the glovebox prior to use. *Note: COS and NO must be handled with caution. COS is a colorless and odorless gas and, upon contact with moisture, readily hydrolyzes to form toxic H_2S gas.*

Synthesis of PPN Salts

Synthesis of [PPN][NO_2]: All PPN salts were synthesized according to prior literature.[166] Outside of a glovebox, both $NaNO_2$ (50.11 g, 725 mmol) and [PPN][Cl] (10.0319 g, 17.4763 mmol) were dissolved separately in warm DI water (625 mL total). The $NaNO_2$ solution was transferred into a separatory funnel and added dropwise to the warmed, stirring [PPN][Cl] solution over the course of 1 hour. The resulting white suspension was cooled to room temperature before cooling in an icebath for at least 1 hour. The suspension was filtered to isolate a white solid which was then dissolved in acetone, dried over $MgSO_4$, filtered, and concentrated under reduced pressure to a pure, white solid. The white powder was subjected to layer diffusion crystallization in acetone/Et_2O and chilled in the freezer overnight. The resultant white [PPN][NO_2] crystals were isolated via filtration, 7.5773 g, 74% yield.

Synthesis of [PPN][SSNO]: All PPN salts were synthesized according to prior literature.[1] In a glovebox, to a solution of [PPN][NO_2] (4.6082 g, 7.8827 mmol) in acetone, S_8 (0.5032 g, 1.9613 mmol) was added and stirred at room temperature overnight. The reaction was filtered through celite before layering Et_2O over top. This first crystallization crystalizes out a significant amount of $S_6O_6^{2-}$ byproduct (red crystals). The remaining solution and any resultant black crystals were subjected to large scale acetone/Et_2O diffusion crystallization. After significant time has allowed crystals to form, the [PPN][SSNO] black crystals were manually separated from the batch. Remaining solution and red crystals can be recrystallized further to obtain additional [PPN][SSNO] crystals.

Synthesis of [PPN][SNO]: All PPN salts were synthesized according to prior literature.[166] In a glovebox, a solution of (crudely crushed) [PPN][SSNO] (551.1 mg, 0.8710 mmol) and PPh_3 (458.0 mg, 1.7462 mmol) in acetone (11 mL) was stirred at room temperature, covered from light, overnight. The solution was partially concentrated down before filtering, layering Et_2O over top, and storing in the freezer overnight. The resultant green crystals were isolated from solution and washed with Et_2O to yield pure [PPN][SNO], 232.2 mg, 44% yield.

Synthesis of ^{15}N Labeled PPN Salts

Synthesis of [PPN][$^{15}NO_2$]: The [PPN][$^{15}NO_2$] was synthesized using a modified version of above procedure in which 1.05:1 equivalent of $Na^{15}NO_2$ (0.2452 g, 3.684 mmol) and [PPN][Cl] (1.996 g, 3.477 mmol) are used; 0.9517 g, 47% yield.

Synthesis of [PPN][SS^{15}NO]: The procedure for [PPN][SS^{15}NO] was performed as described above for [PPN][SSNO] except using previously prepared [PPN][$^{15}NO_2$] rather than [PPN][NO_2].

Synthesis of [PPN][S^{15}NO]: The procedure for [PPN][S^{15}NO] was performed as described above for [PPN][SNO] except using previously prepared [PPN][SS^{15}NO] rather than [PPN][SSNO].

Synthesis of Authentic Gases

Synthesis of COS gas: COS gas was synthesized according to prior literature.[178]

Synthesis of NO gas: NO gas was synthesized according to prior literature.[252]

A3. UV-VIS/IR EXPERIMENTS

Treating [PPN][SNO]/[SSNO] with AcOH

[PPN][SNO] + AcOH (1 equiv.)

(Figure 2.1 in main text)

A stock solution of [PPN][SNO] was prepared in MeCN and stored in the glovebox freezer. From the stock solution, [PPN][SNO] was diluted in MeCN (0.5 mM) into a UV-Vis cuvette. Outside of the box, fresh glacial AcOH was serial diluted in anhydrous MeCN to a working concentration (20 mM). A background UV-Vis spectrum was collected with MeCN, then a scan was taken of [PPN][SNO] solution before injecting 1 equivalent of AcOH and scanning over 3 hours.

[PPN][SNO] + AcOH + PPh_3

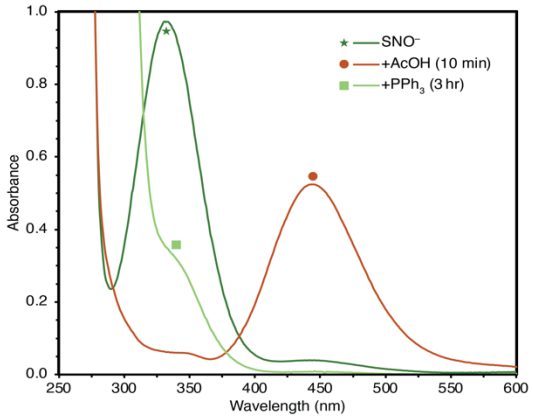

Figure A1. UV-Vis spectra of aliquots taken from a solution of [PPN][SNO] (0.40 mM, ★, λ_{max} = 332 nm) in MeCN, treated with AcOH (1 equiv.) resulting in the formation of $SSNO^-$ (•, λ_{max} = 445 nm). Treatment of the resultant $SSNO^-$ with PPh_3 (excess) reforms SNO^- (▪, λ_{max} = 332 nm).

In the glovebox, a solution of [PPN][SNO] (6.5 mg) was prepared in anhydrous MeCN (1 mL, 10.8 mM) and an aliquot was diluted (0.40 mM) into a UV-Vis cuvette. A stock solution of AcOH in MeCN (0.83 M) was prepared and an aliquot (1 equiv.) injected into the [PPN][SNO]

solution. An aliquot of the reaction was diluted into another UV-Vis cuvette. After about 15 minutes, PPh_3 (excess) was dissolved in anhydrous MeCN (1 mL) and added to the reaction. After 3 hours, an aliquot of the reaction solution was diluted into a UV-Vis cuvette.

[PPN][SNO] + AcOH (excess)

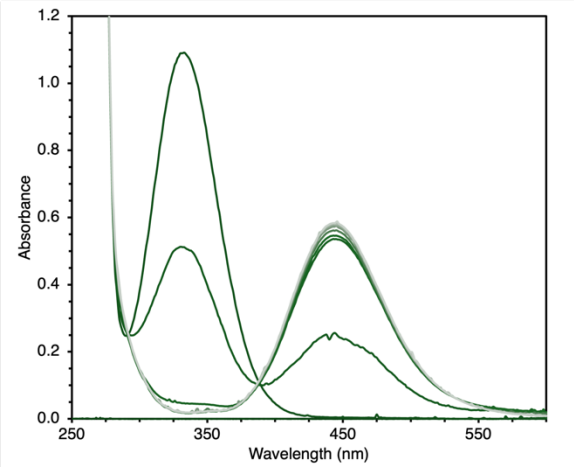

Figure A2. Treatment of [PPN][SNO] (0.46 mM) in MeCN treated with excess AcOH.

In the glovebox, from the previously prepared stock solution, [PPN][SNO] was diluted into a UV-Vis cuvette (0.46 mM). A GC vial was filled with 1 mL of anhydrous MeCN from the glovebox and both cuvettes and vial removed. A small amount of glacial AcOH (25 µL) was diluted into the 1 mL vial to form a stock solution (0.43 M). Initial scans of SNO were taken before injecting AcOH (22 µL, 10 equiv.) into the cuvette and taking scans.

[PPN][SSNO] + AcOH (1 equiv.)

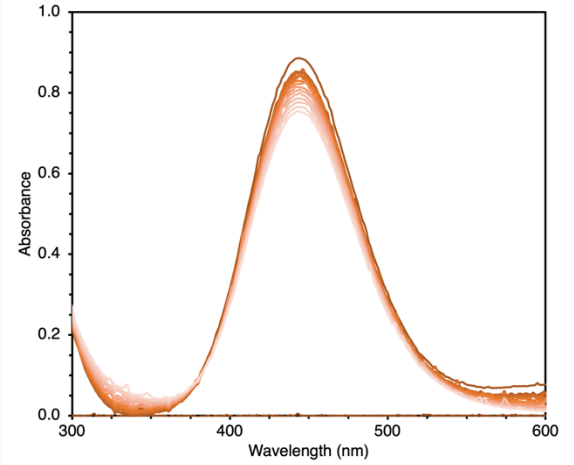

Figure A3. Treatment of [PPN][SSNO] (0.32 mM) in MeCN treated with AcOH (1 equiv.).

In the glovebox, a stock solution of [PPN][SSNO] was prepared in MeCN (6.8 mM, 1 mL) which was further diluted into a working solution in MeCN (0.32 mM, 2.1 mL) in a cuvette with stirbar. Two GC vials and a cuvette were filled with MeCN (1 mL, 2 mL, respectively) and removed from the glovebox. Into one of the GC vial MeCN solutions, glacial AcOH was diluted (172 mM) before being further diluted to a working stock solution in another vial (10.1 mM). A background UV-Vis spectrum was collected with MeCN, before taking a base scan of SSNO and then injecting with 1 equivalent of AcOH (67 μL).

Treating [PPN][SNO]/[SSNO] with H_2O

[PPN][SNO] + H_2O (excess)

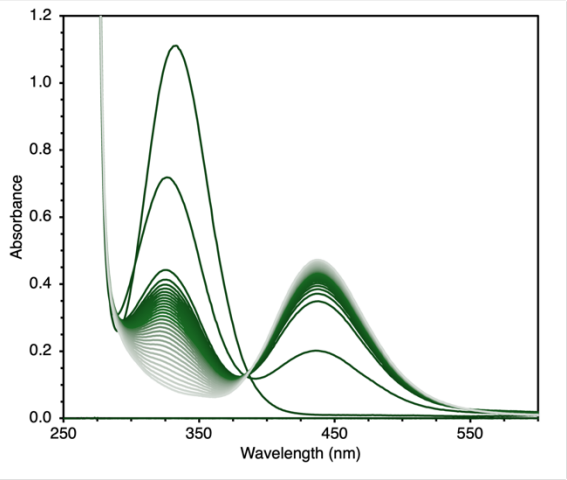

Figure A4. Treatment of [PPN][SNO] (0.46 mM) in MeCN with an excess of N_2-sparged H_2O.

In the glovebox, [PPN][SNO] was added to a GC vial and dissolved in MeCN (2.9 mg, 0.5 mL, 9.7 mM) to make a fresh stock solution. An aliquot of SNO^- solution was then diluted into a UV-Vis cuvette (0.46 mM) and stock solution was afterwards stored in the freezer for future use. The blank and sample cuvettes were removed from the glovebox. A GC vial was filled with MilliQ water and sparged with N_2 for 5 minutes. After taking an initial scan of SNO^- a sample of water (excess, 100 mL) was injected into the cuvette and scans cycled after.

[PPN][SSNO] + H_2O (excess)

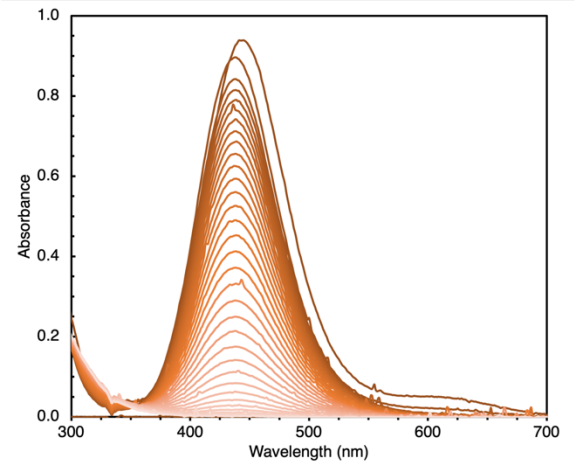

Figure A5. Treatment of [PPN][SSNO] (0.46 mM) in MeCN with an excess of N_2-sparged H_2O.

In the glovebox, [PPN][SSNO] (4.5 mg) was dissolved in MeCN (1 mL, 7.1 mM) to form a stock solution. Cuvettes were filled with MeCN and an aliquot of stock solution was diluted to a final concentration of 0.30 mM [PPN][SSNO]. Outside of the glovebox, a small amount of MilliQ water was sparged with N_2. Scans of [PPN][SSNO] were taken before injecting excess H_2O (100 mL, 800 equiv.) into the cuvette and taking scans every 5 mins for 2.75 hrs.

Treating [PPN][SNO][/[SSNO] with HCl

[PPN][SNO] + HCl (2 equiv.)

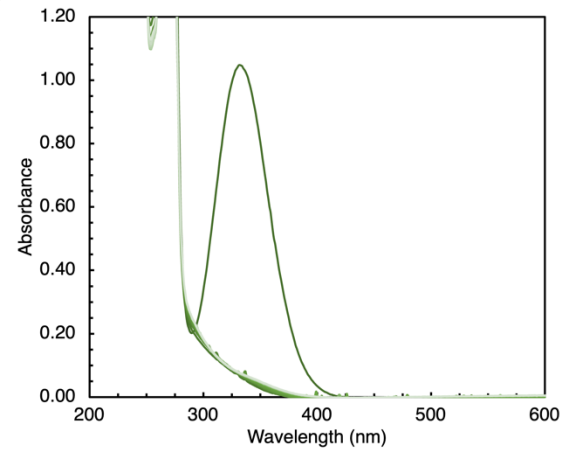

Figure A6. Treatment of [PPN][SNO] (0.44 mM) in MeCN with HCl (2 equiv.).

In the glovebox, [PPN][SNO] (5.6 mg) was dissolved in MeCN (1 mL). The [PPN][SNO] was then diluted (0.44 mM, 2.1 mL) in a UV-Vis cuvette capped and set aside. HCl in Et_2O (1 M) was diluted with MeCN (48 mM) in a GC vial and removed from the glovebox. A background UV-Vis spectrum was collected with MeCN before taking a scan of the [PPN][SNO] and injecting an aliquot of HCl (2 equiv.) into the cuvette and scans were taken promptly after.

[PPN][SSNO] + HCl (1 equiv.)

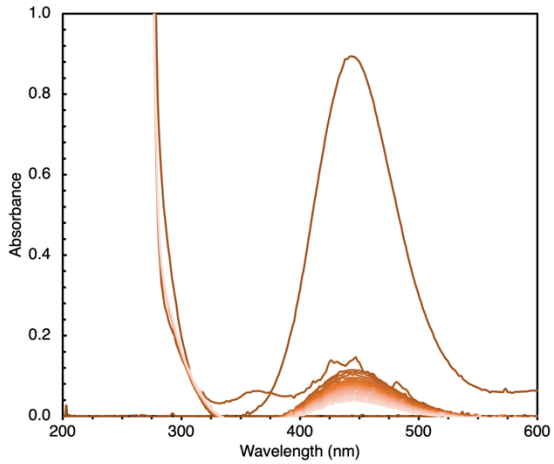

Figure A7. Treatment of [PPN][SSNO] (0.30 mM) in MeCN with HCl (1 equiv.).

In the glovebox, [PPN][SSNO] (4.5 mg) was dissolved in MeCN (1 mL, 7.1 mM) to form a stock solution. The [PPN][SSNO] was then diluted (0.30 mM) in a UV-Vis cuvette capped and set aside. In a separate vial, HCl in Et_2O (1 M) was diluted in MeCN (27 mM) and removed from the glovebox. UV-Vis scans were taken of [PPN][SSNO] before an aliquot of HCl solution (1 equiv.) was injected into solution and scans taken every 3 mins for 1 hr.

[PPN][SNO] + HCl + [PPN][SNO]

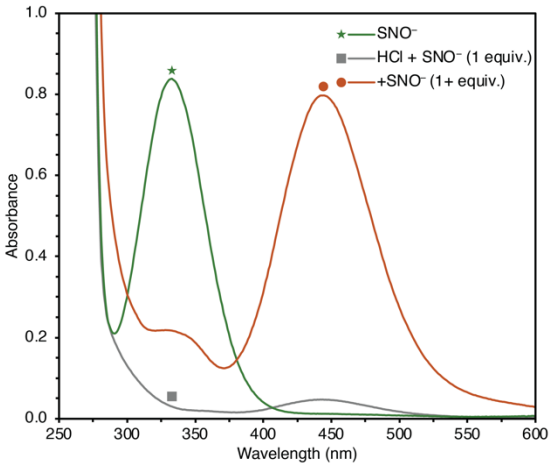

Figure A8. UV-Vis spectra of a solution [PPN][SNO] (0.4 mM, ★, λ_{max}= 332 nm) in MeCN. A solution of HCl treated with [PPN][SNO] (1 equiv.) resulting in the formation of the proposed HSNO intermediate (■, minor absorbance at 445 nm due to the formation of $SSNO^-$ from inadequate mixing). The resultant intermediate then treated with additional [PPN][SNO] (1+ equiv.) to generate $SSNO^-$ (●, λ_{max}= 445 nm).

In the glovebox, a stock solution of [PPN][SNO] (6.1 mg) was prepared in anhydrous MeCN (1 mL, 10.2 mM). In one cuvette, [PPN][SNO] (0.40 mM) was diluted in MeCN. Into another cuvette, HCl was diluted (0.50 mM). The cuvettes and stock solution were removed from the glovebox. A UV-Vis spectrum was taken of the [PPN][SNO] and HCl cuvettes, before [PPN][SNO] (1 equiv.) stock solution was injected into the HCl cuvette and scanned. After, an additional aliquot of [PPN][SNO] (1 equiv.) stock solution was injected into the cuvette and scanned.

[PPN][SNO] + HCl (0.5 equiv.)

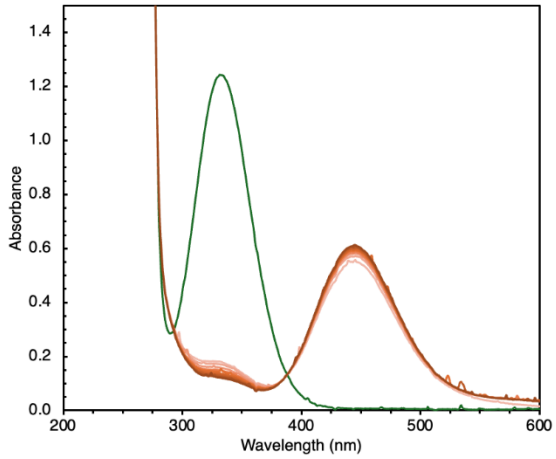

Figure A9. Treatment of [PPN][SNO] (0.50 mM) in MeCN with HCl (0.5 equiv.).

In the glovebox, a stock solution of [PPN][SNO] was prepared in MeCN (11 mM) and then diluted into a UV-Vis cuvette (0.50 mM). An aliquot of HCl in Et_2O was diluted in MeCN (25 mM). Items were removed from the glovebox. A background UV-Vis spectrum was collected with MeCN before taking a scan of the [PPN][SNO], and then injecting an aliquot of HCl (0.5 equiv.). Scans were taken every minute for 10 minutes.

Figure 2.2 in text.

[PPN][SNO] + HCl (0.5 equiv.) + PPh_3

In the glovebox, [PPN][SNO] (9.1 mg) was dissolved in anhydrous MeCN (15 mM). In a separate vial, a stock solution of HCl was made by dilution in anhydrous MeCN (91 mM). In a third vial, PPh_3 (17.8 mg) was dissolved in anhydrous MeCN (226 mM). Five UV-Vis cuvettes were each filled with MeCN. An aliquot of [PPN][SNO] solution was diluted into a UV-Vis cuvette (**1**, 0.5 mM). From the HCl stock solution, 0.5 equivalents of HCl were added to the [PPN][SNO] vial (reaction vial) and an aliquot of this was diluted into a separate cuvette (**2**). The PPh_3 solution was added to the reaction vial, and another aliquot was diluted into a third cuvette (**3**). The reaction vial was left inside the glovebox to let stir. Four cuvettes (Blank, SNO, SNO + HCl, SNO + HCl + PPh_3 (T5)) were removed from the box and UV-Vis scans taken. Additional timed aliquots were taken in individual cuvettes at T = 37, 75, 120, 180 minutes.

Treating [PPN][SNO] with [TBA][OAc]/[Cl]

[PPN][SNO] + [TBA][OAc] Titration

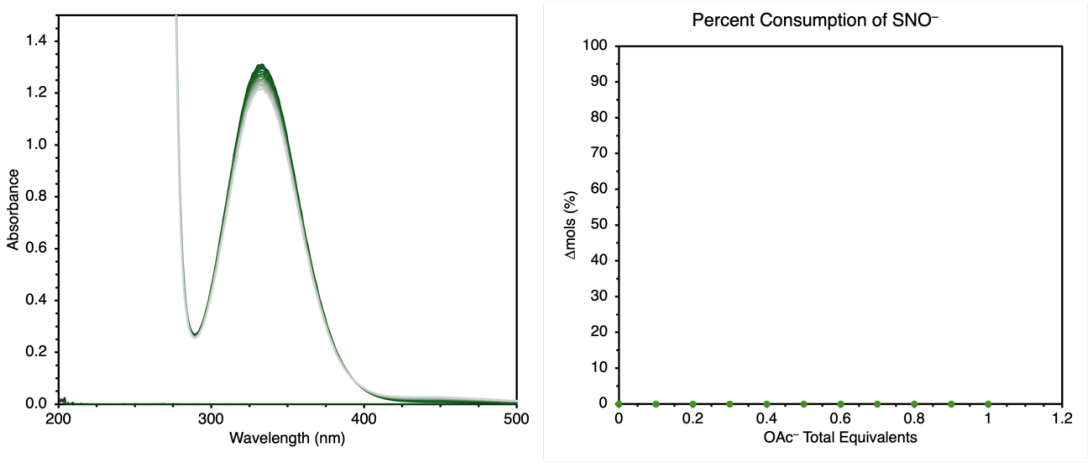

Figures A10-A11. (Left) Treatment of [PPN][SNO] (0.50 mM) in MeCN titrated with aliquots of [TBA][OAc] (up to 1 equiv., 3 min incubations). (Right) The change in moles of SNO^- over the course of the titration as calculated from the molar absorptivity and known volume, accounting for dilution.

In the glovebox, [PPN][SNO] (4.2 mg, 0.0070 mmol) was dissolved in MeCN (0.5 mL, 14 mM) as a stock solution. [PPN][SNO] was then diluted into a UV-Vis cuvette (0.50 mM). [TBA][OAc] (5.6 mg) was dissolved in MeCN (1.8 mL, 10.3 mM). Materials were removed from the glovebox and instrument. An initial scan of [PPN][SNO] was taken before adding aliquots of [TBA][OAc] into solution (3 min incubation, up to 1 equiv.).

[PPN][SNO] + [TBA][Cl] Titration

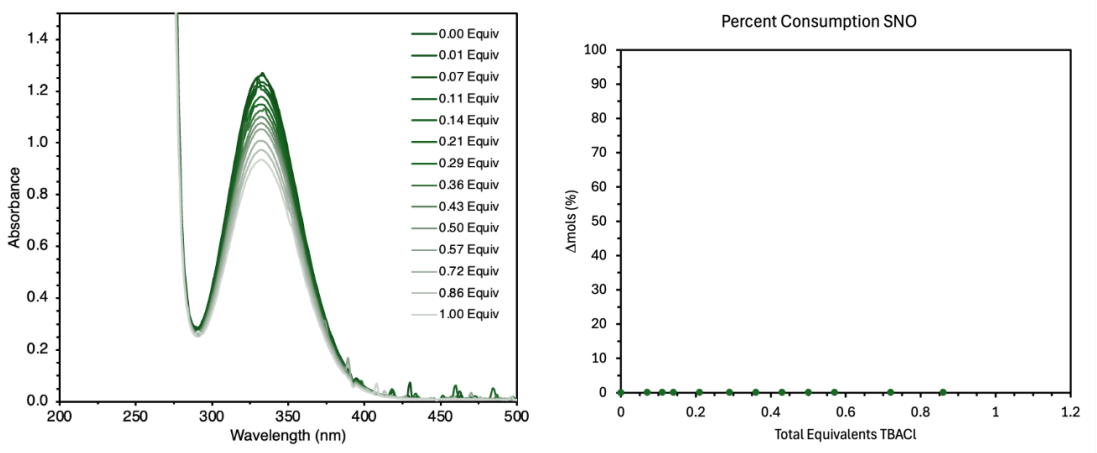

Figures A12-A13. (Left) Treatment of [PPN][SNO] (0.50 mM) in MeCN titrated with aliquots of [TBA][Cl] (up to 1 equiv., 3 min incubations). (Right) The change in moles of SNO^- over the

course of the titration as calculated from the molar absorptivity and known volume, accounting for dilution.

In the glovebox, from the previously prepared stock solution, [PPN][SNO] was diluted with MeCN (0.50 mM) in a UV-Vis cuvette. Separately, a stock solution of [TBA][Cl] was prepared in MeCN (8.8 mM) and then diluted to a working concentration (1.5 mM). An initial scan of [PPN][SNO] was taken before adding aliquots of [TBA][Cl] into solution (3 min incubation, up to 1 equiv.).

Treating [PPN][SSNO] with [TBA][OAc]/[Cl]

[PPN][SSNO] + [TBA][OAc] Titration

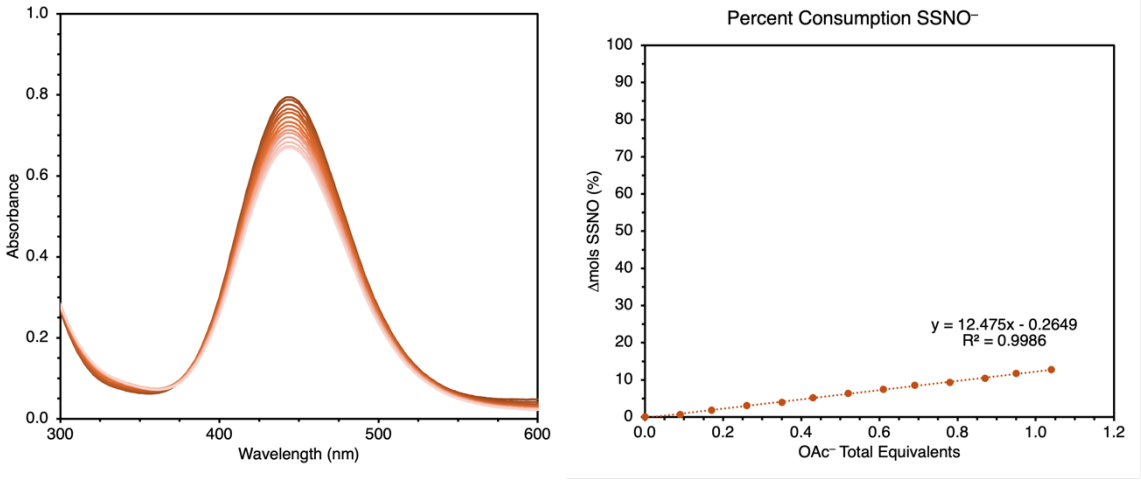

Figures A14-A15. (Left) Treatment of [PPN][SSNO] (0.50 mM) in MeCN titrated with aliquots of [TBA][OAc] (up to 1 equivalent, 3 min incubations). (Right) The change in moles of $SSNO^-$ over the course of the titration as calculated from the molar absorptivity and known volume, accounting for dilution.

In the glovebox, from the previously prepared stock solution, [PPN][SSNO] was diluted with MeCN (0.32 mM) in a UV-Vis cuvette. A background UV-Vis spectrum was taken in MeCN before taking a scan of [PPN][SSNO] and then titrating in aliquots of [TBA][OAc] (previously prepared stock solution, see above; 3 min incubation, up to 1 equiv.).

[PPN][SSNO] + [TBA][Cl] Titration

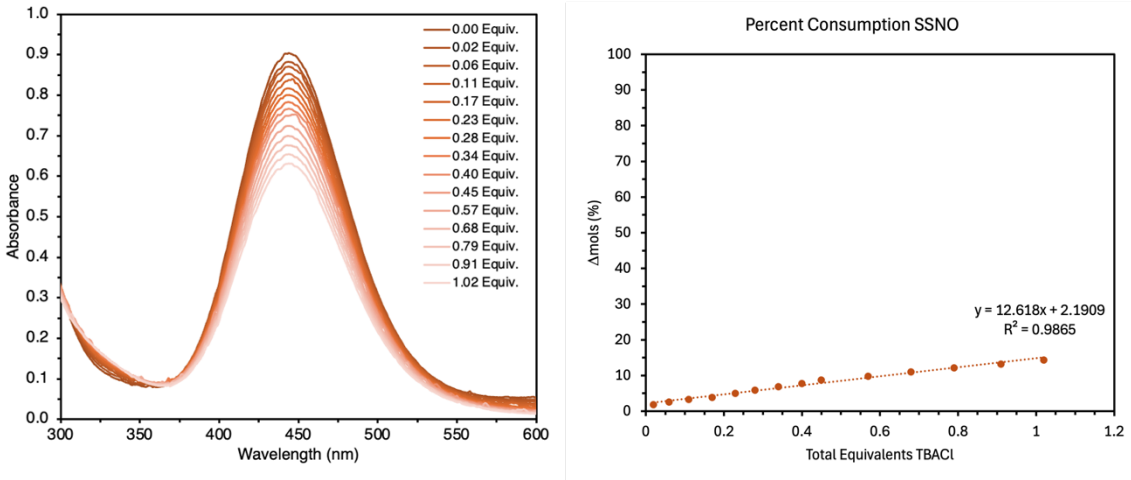

Figures A16-A17. (Left) Treatment of [PPN][SSNO] (0.50 mM) in MeCN titrated with aliquots of [TBA][Cl] (up to 1 equivalent, 3 min incubations). (Right) The change in moles of $SSNO^-$ over the course of the titration as calculated from the molar absorptivity and known volume, accounting for dilution.

In the glovebox, from the previously prepared stock solution, [PPN][SSNO] was diluted with MeCN (0.32 mM) in a UV-Vis cuvette. A background UV-Vis spectrum was taken in MeCN before taking a scan of [PPN][SSNO] and then titrating in aliquots of [TBA][Cl] (previously prepared stock solution, see above; 3 min incubation, up to 1 equiv.).

Treating [PPN][SNO] with COS

[PPN][SNO] + COS

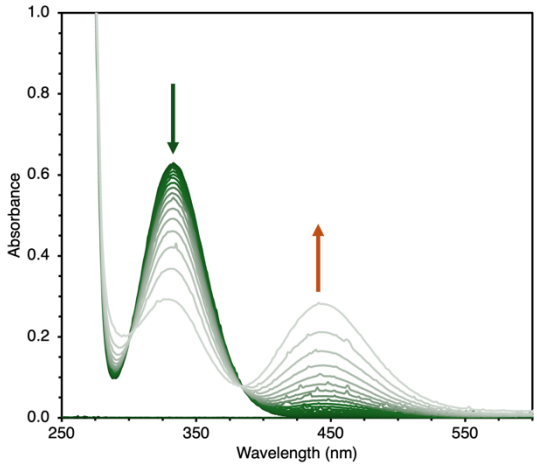

Figure A18. Treatment of [PPN][$S^{15}NO$] (0.3 mM) in MeCN upon treatment with COS gas up to 1 hour.

From a previously prepared stock solution, [PPN][S^{15}NO] was diluted in MeCN (0.3 mM) within a UV-Vis cuvette. A background UV-Vis spectrum was taken in MeCN before taking a scan of SNO^-. Synthesized COS gas was then bubbled briefly into the cuvette before returning to the instrument and taking scans every 3 minutes for 3 hours. Figure 2.3 in text for reaction with resultant $SSNO^-$ (reaction time 1+ hrs after COS addition).

Exposing [PPN][SNO]/[SSNO] to air

SNO^- and $SSNO^-$ are generally regarded as unstable to ambient air and water. Here, we examine how sensitive these species are to ambient air and what happens if these species are oxidized. To investigate this, we took a cuvette of [PPN][SNO] in MeCN and opened the solution to ambient air and observed the slow conversion to $SSNO^-$ as an intermediate before quickly decomposing. When subjecting an authentic solution of [PPN][SSNO] to the same procedure, the direct decomposition was much faster and was complete within 20 minutes. As is, these results suggest that SNO^- may be more resistant to oxidation from air than $SSNO^-$ but ultimately does not survive ambient conditions for prolonged periods of time.

[PPN][SNO] + air

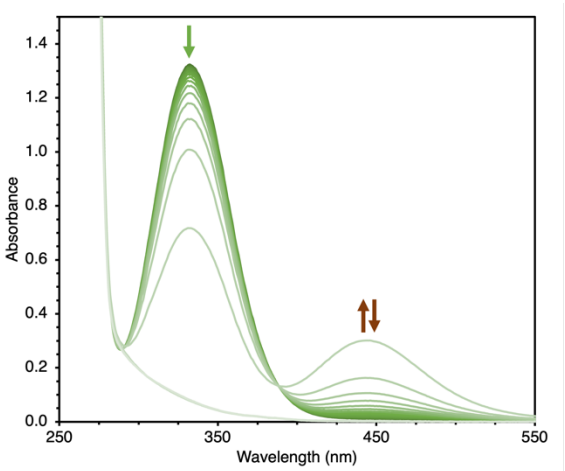

Figure A19. Change in absorbance of [PPN][SNO] (0.5 mM) in MeCN upon exposure to air.

An aliquot of [PPN][SNO] stock solution was diluted into a UV-Vis cuvette (0.50 mM). An initial scan of [PPN][SNO] was taken before opening the cuvette to air and scanned every 3 minutes for just over 1 hour.

[PPN][SSNO] + air

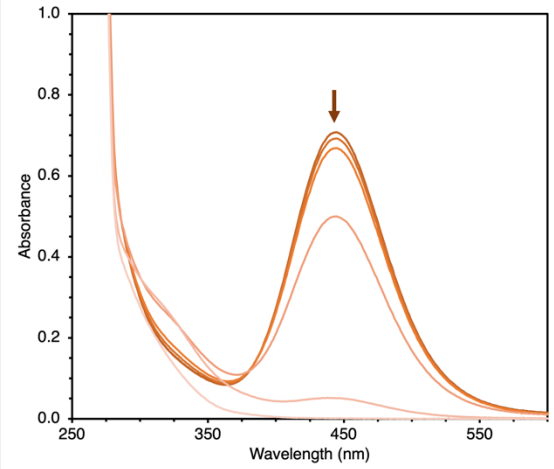

Figure A20. Change in absorbance of [PPN][SSNO] (0.29 mM) in MeCN upon exposure to air.

An aliquot of [PPN][SSNO] stock solution was diluted into a UV-Vis cuvette (0.29 mM). An initial scan of [PPN][SSNO] was taken before opening the cuvette to air and scanning every 3 minutes for 18 minutes.

CoPc NO Trapping Experiments

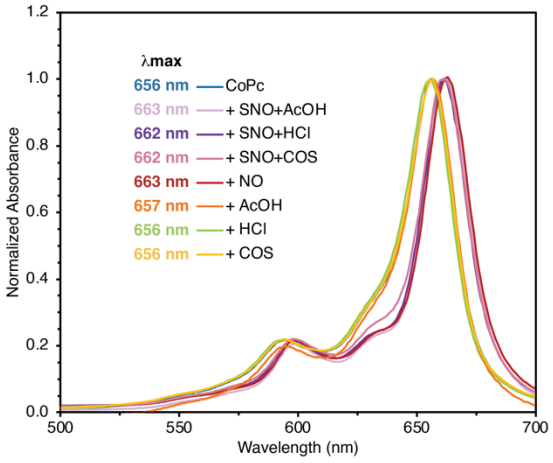

Figure A21. Change in absorbance of CoPc (0.01 mM) in THF (blue) upon addition of SNO^- + AcOH headspace (lavender), SNO^- + HCl headspace (purple), SNO^- + COS headspace (pink), authentic NO gas (red), AcOH headspace (orange), HCl headspace (green), or authentic COS gas (yellow).

In a 4 mL dram vial, CoPc (4.6 mg) was dissolved in THF (4 mL) and an aliquot (10 µL) was diluted into cuvettes (~0.01 mM).

1) In a GC vial, [PPN][SNO] (6.4 mg) was dissolved in MeCN (1 mL) before adding an aliquot of AcOH (1 equiv., 15 μL) via pierced septum cap. To one cuvette the headspace from the [PPN][SNO] + AcOH reaction vial was bubbled through the CoPc solution.
2) In a GC vial, [PPN][SNO] (4.8 mg) was dissolved in MeCN (1 mL) before adding an aliquot of HCl (0.5 equiv., 4 μL) via pierced septum cap. To one cuvette the headspace from the [PPN][SNO] + HCl reaction vial was bubbled through the CoPc solution.
3) To another CoPc cuvette, the headspace from the reaction between [PPN][$S^{15}NO$] + COS (see A18) was bubbled into solution.
4) To another CoPc cuvette, authentic in-house synthesized NO gas was bubbled into solution.
5) To another CoPc cuvette, the headspace from the AcOH stock solution (0.83 M) was bubbled into solution.
6) In a separate vial of MeCN, HCl (4 μL) was added. To another CoPc cuvette, the headspace from the HCl vial was bubbled into solution.
7) To another CoPc cuvette, authentic in-house synthesized COS gas was bubbled into solution.

Reference Spectra

Elemental Sulfur (S_8) in MeCN

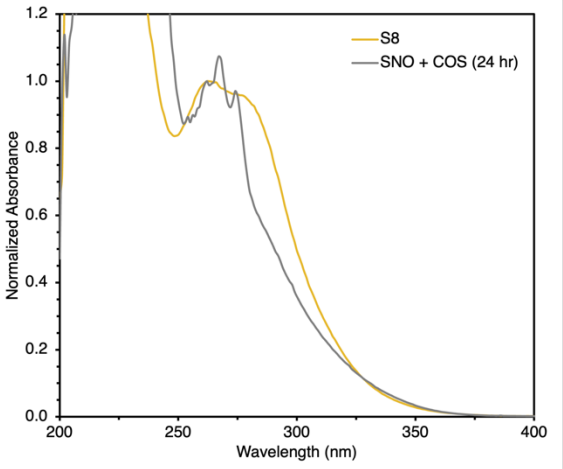

Figure A22. UV-Vis spectrum of a solution of [PPN][SNO] in MeCN 24 hours after being sparged with authentic COS gas overlayed with a spectrum of authentic S_8 in MeCN.

Hydrosulfide/inorganic polysulfides in MeCN

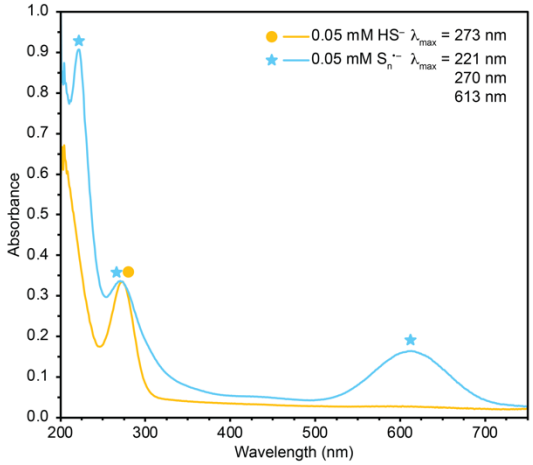

Figure A23. UV-Vis spectrum of a solution of hydrosulfide (NBu_4SH, 0.05 mM, λ_{max} = 273 nm) in MeCN and the resulting inorganic polysulfides ($S_n^{\bullet-}$, 0.05 mM, λ_{max} = 221 nm, 270 nm, 613 nm) after 1:1 reaction with S_8.

Bis(triphenylphosphineiminium) (PPN) Salt Comparison

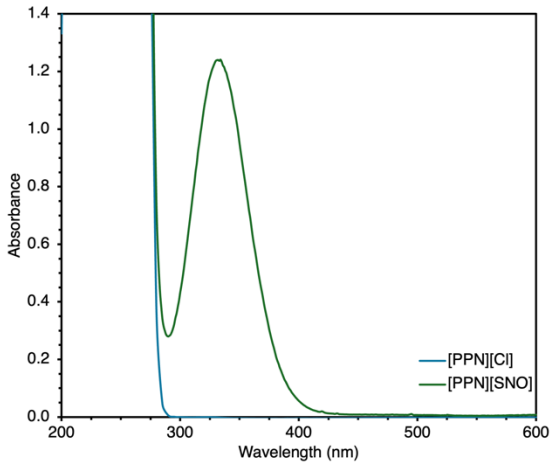

Figure A24: UV-Vis spectrum of [PPN][Cl] (0.48 mM) in MeCN overlayed with [PPN][SNO] (0.50 mM) to show the absorbance in the far-UV region associated with the PPN^+, counter cation.

N_2O IR Spectra

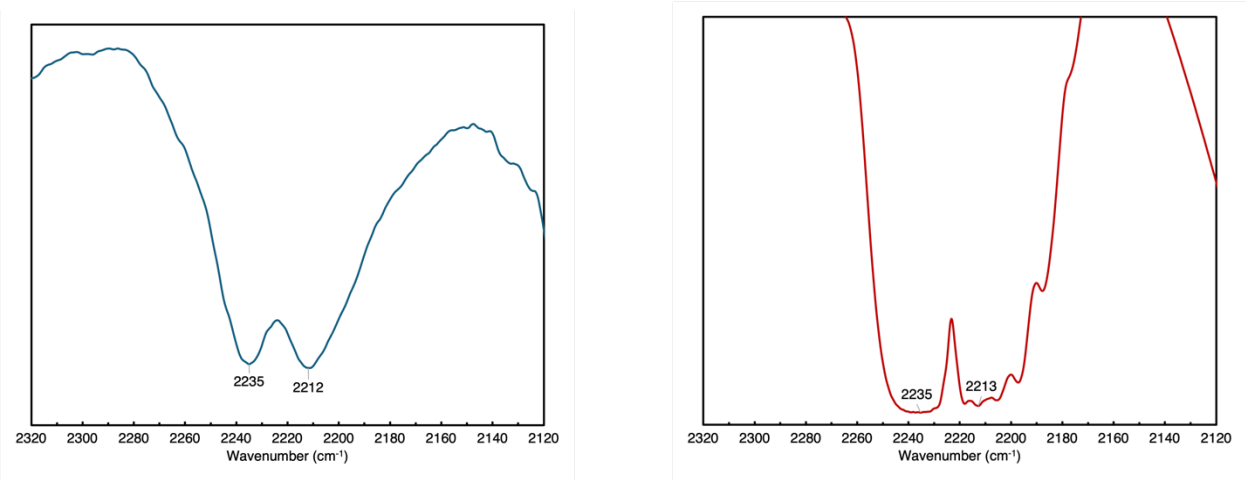

Figure A25-A26: Left: FTIR spectrum of the headspace from the reaction of [PPN][SNO] (8.2 mM) + AcOH (1 equiv.) confirming the presence of gaseous N_2O. Right: FTIR spectrum of authentic N_2O.

A4. NMR EXPERIMENTS

PPh_3 Oxidation Experiments

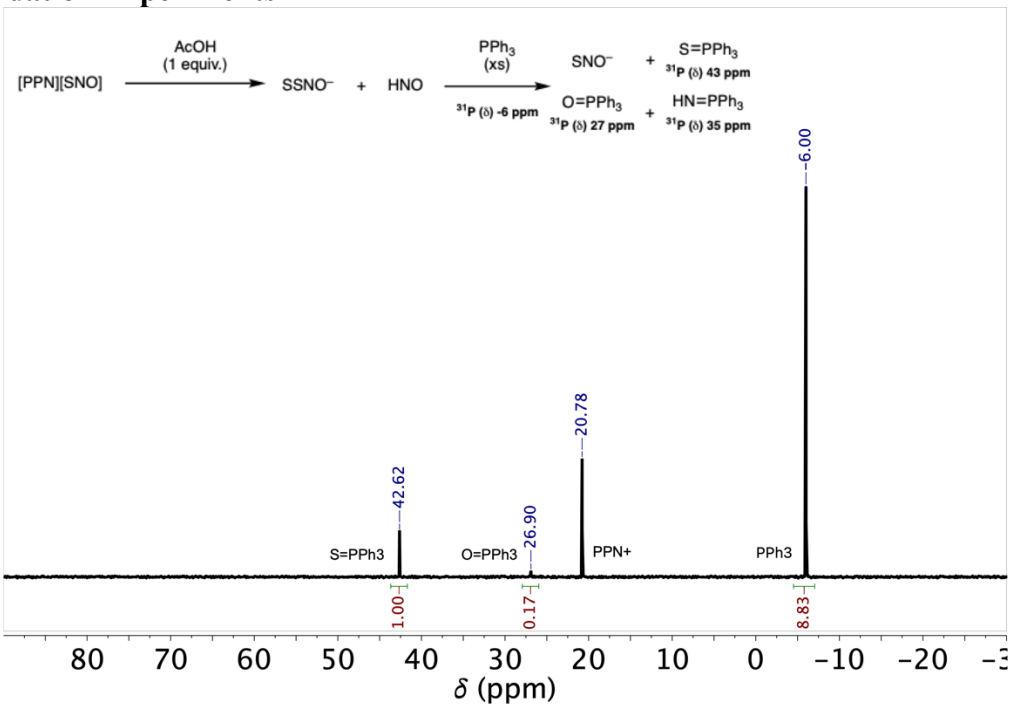

Figure A27. (top) Reaction scheme of expected reactivity with PPh_3 if HNO is generated from the reaction of [PPN][SNO] and AcOH. (bottom) $^{31}P\{^1H\}$ NMR spectrum after treating the resultant $SSNO^-$ with PPh_3 (10 equiv.) to regenerate SNO^-. We did not observe $HN{=}PPh_3$ nor $O{=}PPh_3$ generation, suggesting that HNO is not formed during the initial reaction.

In the glovebox, from the prepared stock solution, [PPN][SNO] was added to an NMR tube and then diluted with additional CD_3CN (3 mM). Separately, PPh_3 (8.6 mg, 33 mM) was dissolved in CD_3CN in a GC vial and set aside. NMR tube and PPh_3 were removed from the glovebox and glacial AcOH (1 equiv.) stock solution was injected. The reaction was left to equilibrate for 1 hour before injecting PPh_3 (10 equiv.) and monitoring by ^{31}P NMR after reaching equilibrium.

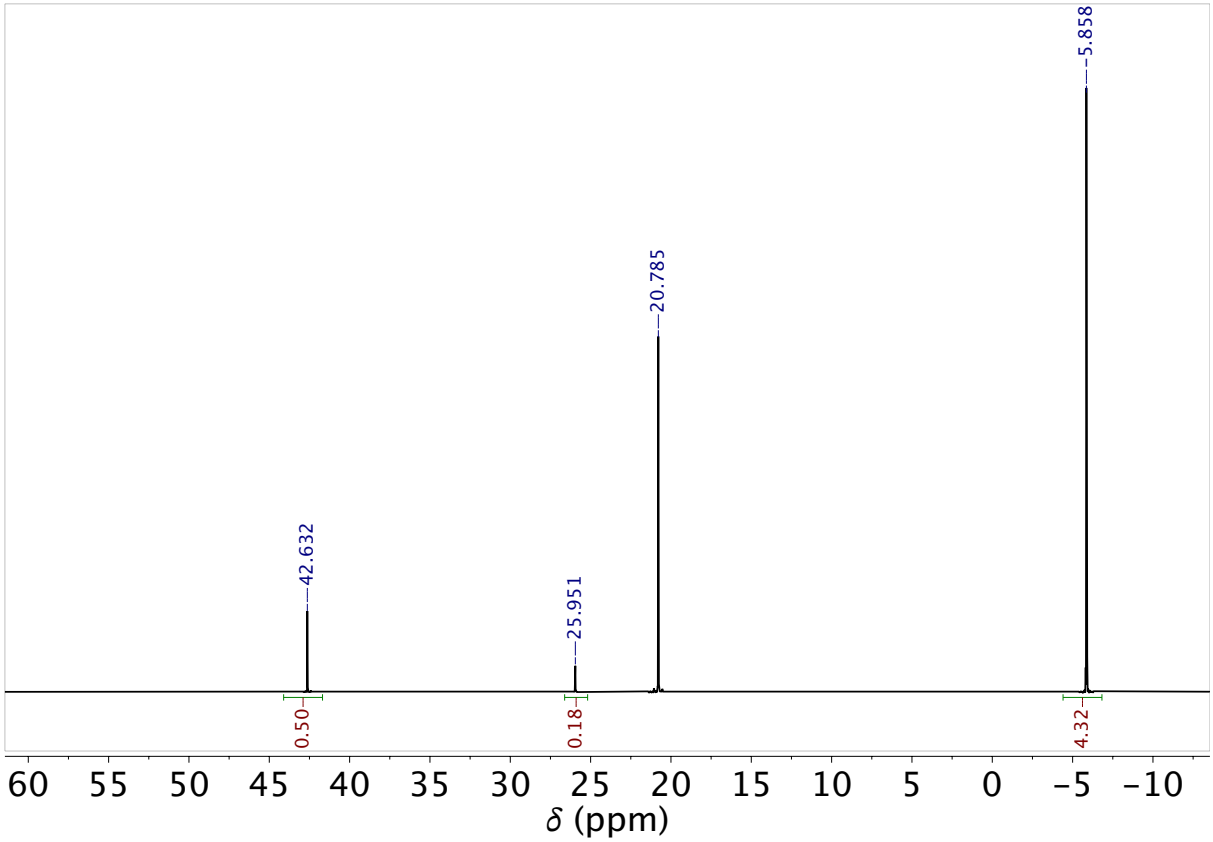

Figure A28: $^{31}P\{^{1}H\}$ NMR spectrum after treating a solution of [PPN][SNO] (19 mM) and PPh_3 (5 equiv.) with AcOH (1 equiv.). No $HN{=}PPh_3$ was observed suggestive that HNO is either not formed as a product of the reaction or that HNO decomposes or reacts to form other byproducts too rapidly to be trapped by PPh_3.

In the glovebox, PPNSNO and PPh_3 were massed out into separate vials before dissolving in CD_3CN (600 μL). A ^{31}P NMR spectrum was acquired to ensure no reactivity prior to injecting an aliquot of AcOH (13.4 μL, 1 equiv.) stock solution into the NMR tube and shaking to mix. After ~30 minutes, another ^{31}P NMR spectrum was acquired.

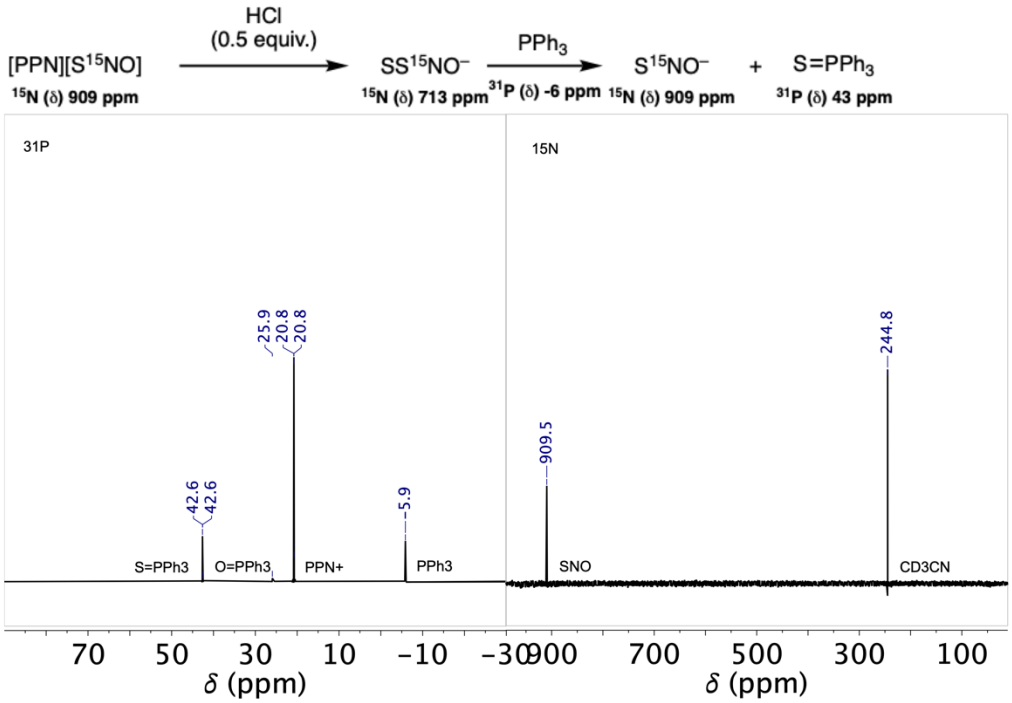

Figure A29-A30. (top) Reaction scheme of the reaction between [PPN][S^{15}NO] and HCl to result in SS^{15}NO^{-}, then treated with PPh_3 to regenerate S^{15}NO^{-} and generate S=PPh_3. (Bottom) The $^{31}P\{^{1}H\}$ NMR spectrum (left) of the regeneration of S^{15}NO^{-} after treatment with PPh_3 and the respective ^{15}N spectrum (right) of the resultant S^{15}NO^{-}.

PPNS^{15}NO (5.3 mg, 18 mM) was dissolved in CD_3CN and transferred to a J-Young tube. An NMR of the solution was taken before bringing back into the glovebox and injecting HCl (4.4 μL, 0.5 equiv.) along the sides of the J-Young tube. The tube was resealed and shaken to combine, immediate solution color change from slightly green to amber. The tube was removed from the glovebox and ^{15}N and ^{13}C NMRs were taken. Formation of SS^{15}NO observed but no other byproducts were observed. A solution of PPh_3 (2.5 mg, 1 equiv.) in CD_3CN was prepared separately and added into the J-Young tube and let react overnight. NMRs were taken of the slightly green solution.

DMPO Radical/HNO Trapping

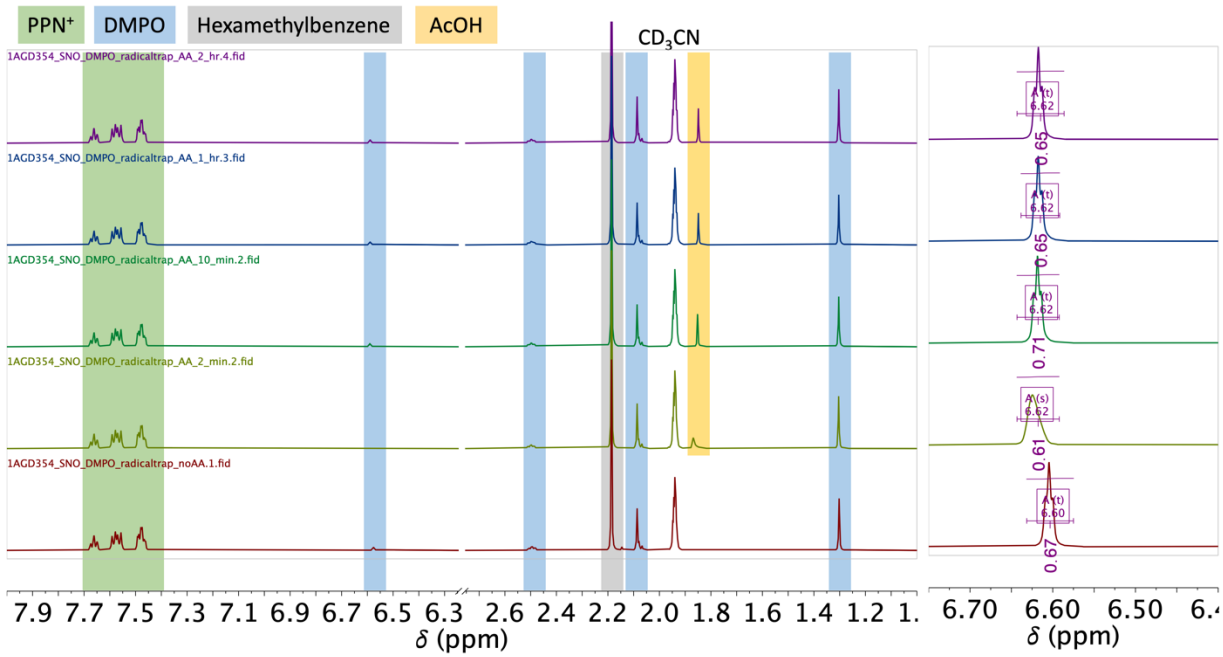

Figure A31. Stacked ^{1}H NMR spectra of a solution of [PPN][SNO] (10 mM), hexamethylbenzene (1 equiv.), and DMPO (1 equiv.), -/+ AcOH (1 equiv.) over 2 hours.

In the glovebox, [PPN][SNO] was dissolved in CD_3CN (6.2 mg, 10 mM) from that solution an aliquot (485 µL) was added to an NMR tube. Hexamethylbenzene was subsequently dissolved in CD_3CN (3.8 mg, 23 mM), from that solution an aliquot (215 µL, 1 equiv.) was added to the same NMR tube and sealed with a septum. Two GC vials were filled with 1 mL of CD_3CN each and removed from the box. Outside of the glovebox, DMPO was dissolved in CD_3CN (2.2 mg, 39 mM) from the box, from that solution an aliquot (130 µL, 1 equiv.) was added to the NMR tube. Glacial AcOH was diluted into one of the vials of CD_3CN. An NMR was taken of the [PPN][SNO]/DMPO/HMB solution before adding an aliquot of the AcOH stock solution (12 µL, 1 equiv.). An NMR was immediately taken after addition. NMRs were subsequently taken after 10 minutes, 1 hr, 2 hr.

1,4-Cyclohexadiene H-atom Abstraction/Radical Trap

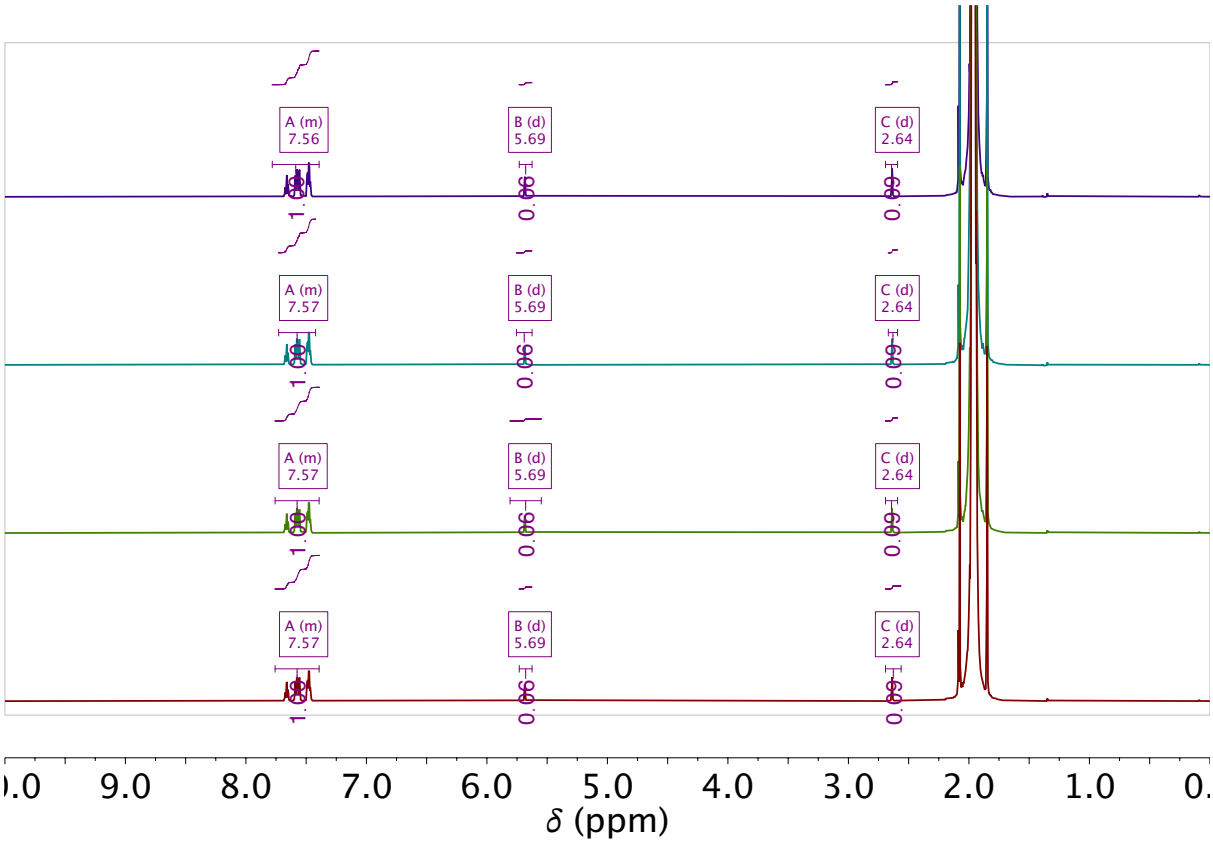

Figure A32. Stacked ^{1}H NMR spectra of a solution of [PPN][SNO] (3 mM), cyclohexadiene (CHD, 1 equiv.), treated with AcOH (1 equiv.) over 3 hours. $[PPN]^{+}$ shifts (A) were used as a reference to measure changes in CHD concentration (B, C). No changes in the concentration of CHD were observed suggestive of no 1-electron processes occurring.

In the glovebox, [PPN][SNO] (6.1 mg) was massed out and dissolved in anhydrous CD_3CN (500 mL, 20 mM) to form a stock solution. Separately, an aliquot of 1,4 cyclohexadiene (CHD, 10 µL) was diluted to form a stock solution (207 mM). To an NMR tube, [PPN][SNO] (89 µL, 3 mM) and CHD (8.75 µL, 3 mM) stock solutions were added, then diluted to volume (600 µL), and removed from the glovebox. An NMR was taken of the solution before an aliquot of glacial AcOH (1 equiv.) stock solution was injected and additional NMR spectra acquired over time.

Treating [PPN][$^{15}NO_2$] with COS gas

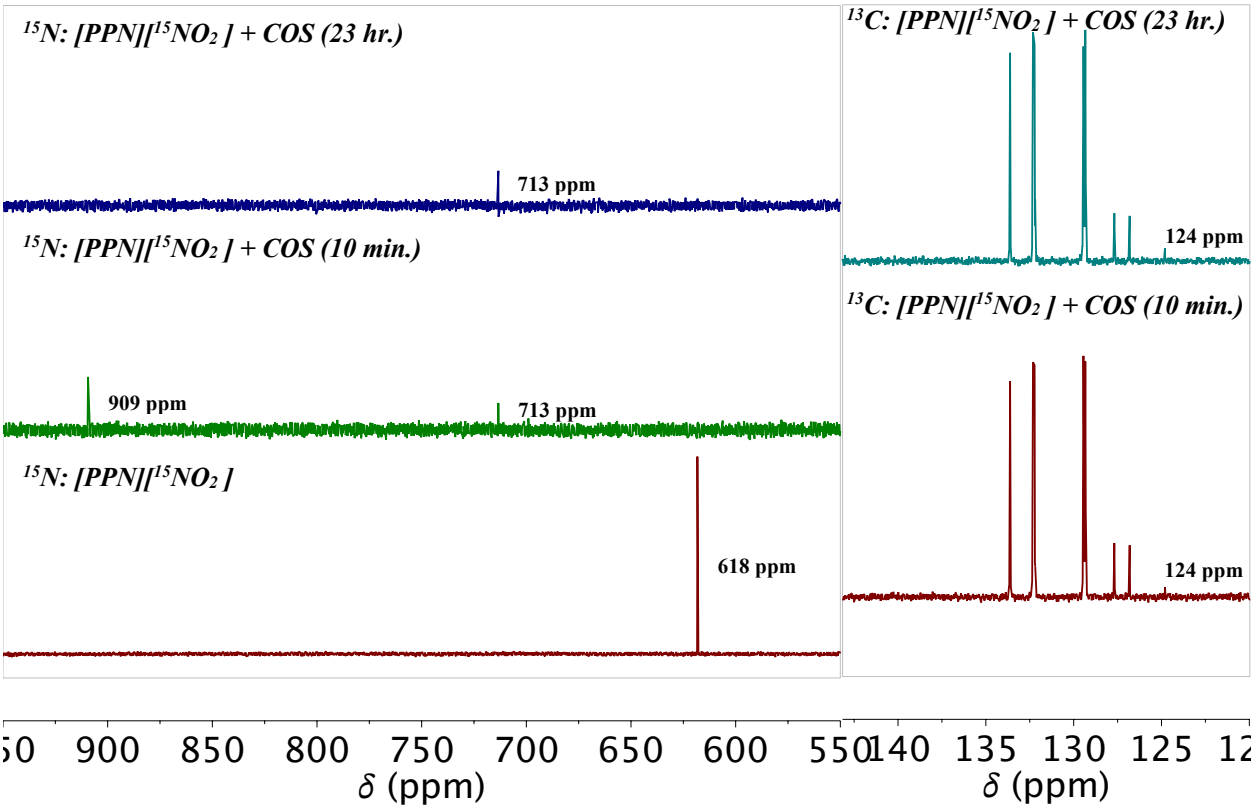

Figures A33-A34. (Left) Stacked ^{15}N NMR spectra of treatment of [PPN][$^{15}NO_2$] (13 mM) with COS. (Right) Stacked $^{13}C\{^1H\}$ NMR spectra of treatment of [PPN][$^{15}NO_2$] with COS.

In the glovebox, [PPN][$^{15}NO_2$] (3.9 mg) was dissolved in CD_3CN (13 mM, 500 μL) and transferred into an NMR tube sealed with a septum cap. The tube was removed from the glovebox and COS gas (3 mL) was slowly sparged through the solution. The clear solution immediately turned to a light green before acquiring ^{15}N and ^{13}C NMR spectra, after 23 hours NMR spectra were acquired of the now amber solution.

Treating [PPN][S^{15}NO] with COS gas

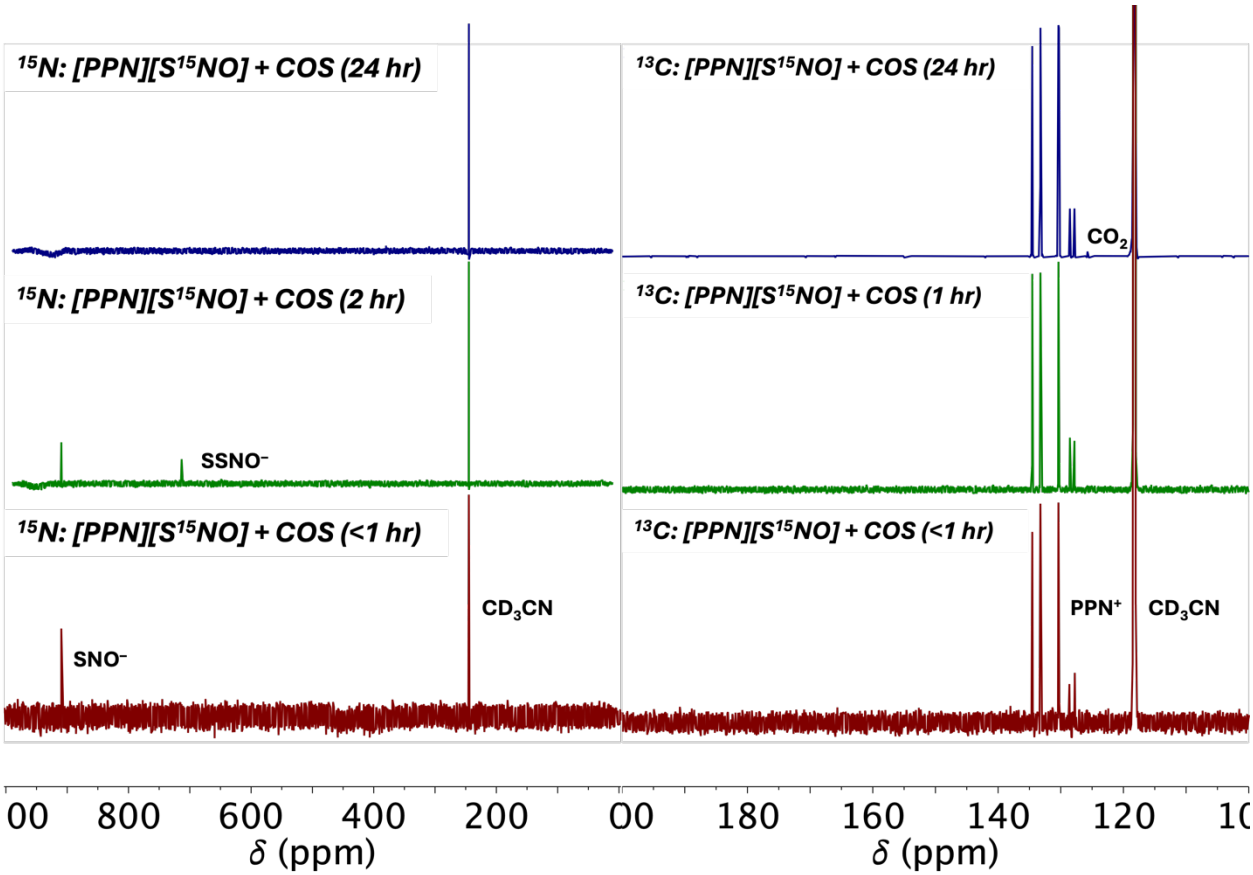

Figures A35-A36. Stacked ^{15}N (left) ^{13}C{^{1}H} (right) NMR spectra of [PPN][S^{15}NO] in CD$_3$CN after injecting COS gas over time.

In the glovebox, [PPN][S^{15}NO] (2.4 mg) was dissolved in CD$_3$CN (0.6 mL). Most of that solution (0.5 mL) was transferred into an NMR tube and capped with a septum. Then, authentic COS (~1 mL, 12 equiv.) was bubbled through the solution. The solution was left to react while acquiring ^{13}C{^{1}H} and ^{15}N NMR spectra over time.

A5. GC HEADSPACE ANALYSIS

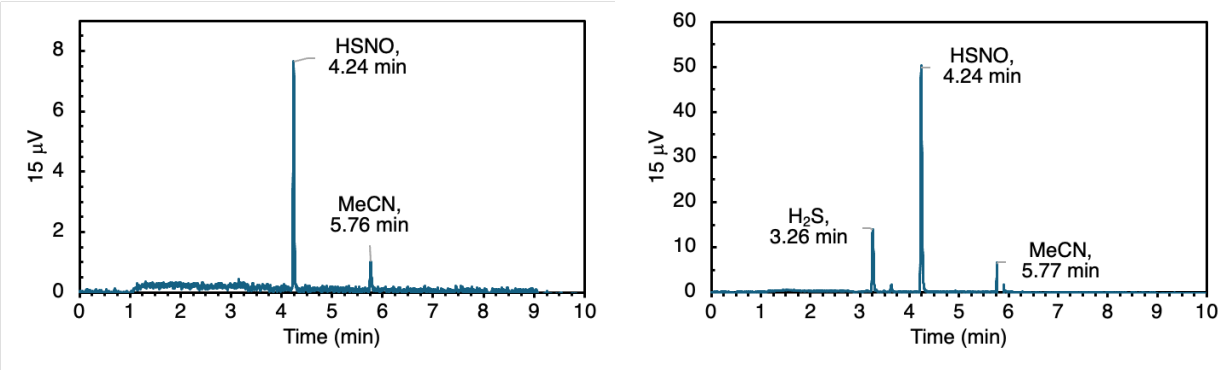

Figures A37–A38: Gas chromatograph traces of the headspace injection from (left) [PPN][SNO] (3.5 mM) + HCl (2 equiv.) in MeCN to generate HSNO and (right) [PPN][SNO] (3.5 mM) + HCl (0.57 equiv.) in MeCN to generate $SSNO^-$ and other byproducts.

In the glovebox, [PPN][SNO] (2.1 mg) was dissolved in MeCN (3.5 mM, 1 mL). Into separate vials, HCl was added (either ~2 equiv. or ~0.5 equiv.). The [PPN][SNO] solution was split between the two HCl vials to either generate HSNO or the $SSNO^-$ reaction pathway. Headspace was manually injected onto the GC for analysis.

APPENDIX B

CHAPTER III SUPPLEMENTARY INFORMATION

B1. EXPERIMENTAL METHODS

General Methods: All drybox manipulations were performed in an Innovative Atmospheres N_2-filled glove box. All NMR spectra for compound characterization were acquired at room temperature unless otherwise noted on a Bruker Avance III-HD 500 NMR spectrometer equipped with a multinuclear Prodigy™ CryoProbe (^{1}H: 500 MHz, ^{13}C: 126 MHz, ^{19}F: 471 MHz, ^{31}P: 202 MHz). All NMR titration spectra were acquired at room temperature on a Bruker Avance III-HD 600 NMR Spectrometer equipped with a multinuclear Prodigy CryoProbe (^{1}H: 600 MHz) or on a Varian INOVA-500 NMR Spectrometer (^{1}H: 500 MHz). ^{1}H and ^{13}C chemical shifts (δ) are reported in ppm relative to residual CD_3CN (^{1}H: 1.94 ppm, ^{13}C: 118.26 ppm). Anhydrous and nonoxygenated CD_3CN was obtained by sparging with N_2, distilling over K_2CO_3, and storing over 4 Å molecular sieves in an inert atmosphere glovebox. Tetrabutylammonium hydrosulfide (TBASH), intermediate 1 (**I1**), and receptor $\mathbf{4}^{2+}$ were all synthesized according to previous reports.[210,211,253] All other reagents were used as received from commercial suppliers.

RECEPTOR SYNTHESES:

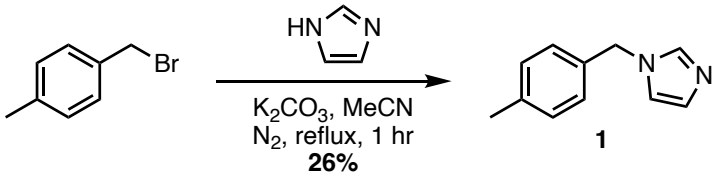

Scheme B1. Synthetic scheme for receptor **1**.

Synthesis of **1**: 4-Methylbenzyl bromide (244.8 mg, 1.323 mmol), imidazole (110.4 mg, 1.622 mmol), and K_2CO_3 (281.4 mg, 2.036 mmol) were dissolved in anhydrous MeCN (25 mL) in a round bottom flask. The solution was brought to reflux and stirred for 1 hour under N_2. The solution was concentrated under vacuum before extracting the crude material into CH_2Cl_2 (20 mL) and washing with a saturated $NaHCO_3$ solution (3 x 20 mL). The organic layer was dried over Na_2SO_4, filtered, and concentrated under vacuum. The crude material was suspended in a 20% EtOAc/hexanes solution and passed through a silicia plug to remove impurities. The pure product was isolated by flushing the plug with EtOAc, 60.9 mg, 26% yield. ^{1}H NMR (500 MHz,

Acetonitrile-d_3) δ: 7.55 (s, 1H), 7.22 – 7.08 (m, 4H), 7.00 (d, J = 1.4 Hz, 1H), 6.92 (s, 1H), 5.09 (s, 2H), 2.31 (s, 3H). $^{13}C\{^1H\}$ NMR (126 MHz, Acetonitrile-d_3) δ: 138.8, 138.3, 135.6, 130.3, 129.9, 128.5, 120.2, 50.8, 21.1. The NMR data matches previously reported data.[254]

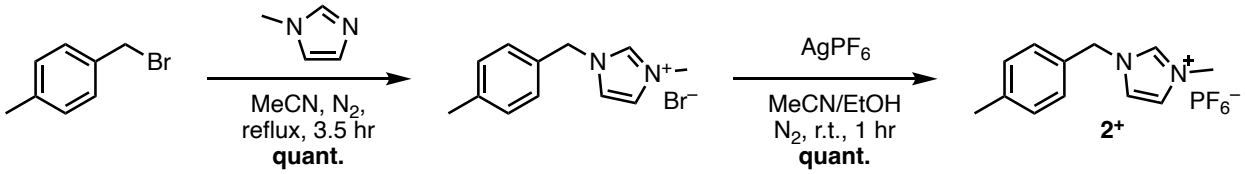

Scheme B2. Synthetic scheme for receptor $\mathbf{2}^+$.

Synthesis of $\mathbf{2}^+$: 4-Methylbenzyl bromide (0.224 g, 1.21 mmol) was dissolved in anhydrous MeCN (7 mL) in a round bottom flask after which 1-Methylimidazole (0.105 mL, 1.33 mmol) was added dropwise. The solution was blanketed with Ar and heated to 40 °C for 3.5 hrs. The solution was concentrated under vacuum to yield the bromide precursor in quantitative yield, 0.315 g. ^1H NMR (500 MHz, DMSO-d_6) δ: 9.23 (t, J = 1.7 Hz, 1H), 7.78 (t, J = 1.8 Hz, 1H), 7.71 (t, J = 1.8 Hz, 1H), 7.33 (d, 8.8 Hz, 2H), 7.23 (d, 7.94 Hz, 2H), 5.37 (s, 2H), 3.85 (s, 3H), 2.30 (s, 3H). The NMR data matches previously reported data.[255]

The bromide precursor (106.9 mg, 0.4001 mmol) was dissolved in a 1:1 MeCN/EtOH mixture (20 mL) in a scintillation vial in a glovebox. $AgPF_6$ (121.3 mg, 0.4801 mmol) was dissolved in minimal MeCN and then added to a stirred solution of the bromide precursor. The reaction mixture was stirred for 1 hour before being filtered through celite and concentrated under vacuum. The resulting solid was triturated with Et_2O to yield receptor $\mathbf{[2]}^+$ in quantitative yield, 0.133 g. ^1H NMR (500 MHz, Acetonitrile-d_3) δ: 8.41 (t, J = 1.8 Hz, 1H), 7.33 (dt, J = 9.1, 1.9 Hz, 2H), 7.26 (m, 4H), 5.25 (s, 2H), 2.35 (s, 3H). $^{13}C\{^1H\}$ NMR (126 MHz, Acetonitrile-d_3) δ 140.4, 136.9, 131.7, 130.8, 129.6, 125.0, 123.2, 53.6, 36.9, 21.1.^{19}F NMR (471 MHz, Acetonitrile-d_3) δ: -73.0 (d, J = 706.6 Hz).$^{31}P\{^1H\}$ NMR (202 MHz, Acetonitrile-d_3) δ: -144.6 (hept, J = 706.3 Hz).

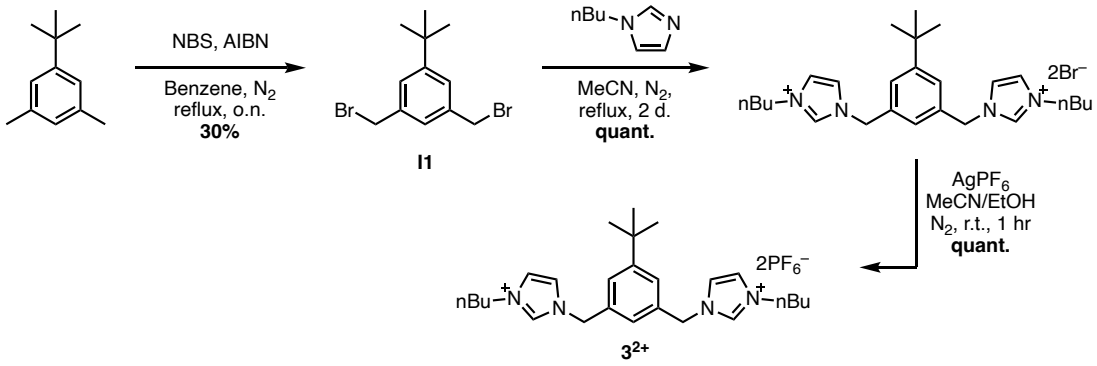

Scheme B3. Synthetic scheme for receptor $\mathbf{3}^{2+}$.

Synthesis of **I1**: Intermediate 1 (**I1**) was synthesized according to published procedure.[253] A 250 mL 3-neck round bottom flask was evacuated and refilled with N_2 3x. Under a positive flow of N_2, N-bromosuccinimide (5.864 g, 32.17 mmol) and 5-tert-butyl-m-xylene (3.0 mL, 16.08 mmol) was added to the 3-neck flask. Sparged benzene was cannula transferred to the 3-neck flask and the reaction mixture was brought to reflux. Azobisisobutyronitrile (AIBN, 0.0263 g, 0.1608 mmol) was added to a separate 25 mL round bottom flask and dissolved in additional sparged benzene. AIBN solution was cannula transferred into the hot, stirring 3-neck round bottom flask before letting stir at reflux overnight under low flow of N_2. The reaction mixture was concentrated under vacuum and the resulting solid was purified by column chromatography. Product was isolated via 0-5% EtOAc/hexanes column as a white solid, 1.5952 g, 30% yield. ^{1}H NMR (500 MHz, DMSO-d_6) δ: 7.42 (d, J = 1.6 Hz, 2H), 7.34 (t, J = 1.8 Hz, 1H), 4.69 (s, 4H), 1.28 (s, 9H). The NMR data matches previously reported data.[253]

Synthesis of receptor $\mathbf{3}^{2+}$: Under a positive flow of N_2, **I1** (0.2508 g, 0.7811 mmol) was dissolved in anhydrous MeCN (50 mL) in a round bottom flask and 1-Butylimidazole (225 µL, 1.72 mmol) was added to stirring solution via an N_2 purged syringe. The reaction mixture was then refluxed for 2 days under N_2. The reaction mixture was concentrated under vacuum and the resulting solid was washed with Et_2O (3 x 20 mL) to yield pure bromide precursor in quantitative yield, 0.444 g. ^{1}H NMR (500 MHz, DMSO-d_6) δ: 9.40 (t, J = 1.6 Hz, 2H), 7.83 (d, J = 1.7 Hz, 4H), 7.45 (d, J = 1.6 Hz, 2H), 7.31 (t, J = 1.6 Hz, 1H), 5.42 (s, 4H), 4.20 (t, J = 7.1 Hz, 4H), 1.78 (p, J = 7.5 Hz, 4H), 1.26 (s, 9H), 1.24 (sxt, J = 7.6 Hz, 4H), 0.89 (t, J = 7.4 Hz, 6H).

In a drybox, the bromide precursor (104.1 mg, 0.1831 mmol) was dissolved in a 1:1 MeCN/EtOH mixture (20 mL) in a scintillation vial. $AgPF_6$ (97.9 mg, 0.387 mmol) was dissolved in minimal MeCN and then added to the stirring bromide precursor solution. The

reaction mixture was stirred for 1 hour before being filtered through celite and concentrated under vacuum. The resulting solid was triturated with Et_2O to yield receptor $\mathbf{3}^{2+}$ in quantitative yield, 123 mg. ^{1}H NMR (500 MHz, Acetonitrile-d_3) δ: 8.48 (t, J = 1.4 Hz, 2H), 7.46 (d, J = 1.7 Hz, 2H), 7.40 (t, J = 1.9 Hz, 2H), 7.34 (t, J = 1.9 Hz, 2H), 7.16 (t, J = 1.9 Hz, 1H), 5.28 (s, 4H), 4.13 (t, J = 7.3 Hz, 4H), 1.81 (p, J = 7.4 Hz, 4H), 1.31 (h, J = 7.5 Hz, 4H), 1.30 (s, 9H), 0.94 (t, J = 7.4 Hz, 6H). ^{13}C{^{1}H} NMR (126 MHz, Acetonitrile-d_3) δ: 154.7, 136.4, 135.5, 127.6, 127.0, 123.8, 123.4, 53.6, 50.5, 35.6, 32.4, 31.3, 20.0, 13.6. ^{19}F NMR (471 MHz, Acetonitrile-d_3) δ: -72.9 (d, J = 706.6 Hz). ^{31}P{^{1}H} NMR (202 MHz, Acetonitrile-d_3) δ: -144.6 (hept, J = 706.4 Hz). TOF MS (ES$^+$, *m/z*): exact mass calc. for $[\mathbf{4}\cdot PF_6]^+$, $C_{26}H_{40}N_4PF_6$, 553.2889; found, 553.2889

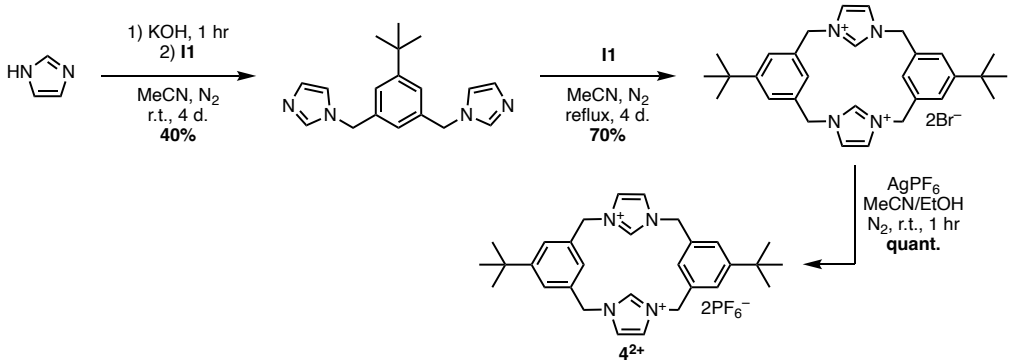

Scheme B4. Synthetic scheme for receptor $\mathbf{4}^{2+}$.

Synthesis of tBu-protophane: The protophane was synthesized according to published procedure.[210] Imidazole (0.3826 g, 5.720 mmol) was dissolved in anhydrous MeCN (80 mL) in a round bottom flask. KOH pellets (0.44 g, 7.4 mmol) were ground in a mortar and pestle and added to the flask. The reaction mixture was stirred for 1 hour under an Ar balloon. **I1** (0.9152 g, 2.859 mmol) was dissolved in anhydrous MeCN (20 mL) and then slowly added to the reaction mixture via N_2 purged syringe. The reaction mixture was stirred at room temperature for 4 days under an Ar balloon. The solution was then filtered and concentrated under vacuum. The resulting oil was diluted with CH_2Cl_2 (20 mL) and then washed with DI H_2O (3 x 20 mL). The organic layer was dried with Na_2SO_4, filtered, and concentrated under vacuum. The oil was then purified via column chromatography (0–10% MeOH/EtOAc) to yield the product as a viscous yellow oil, 0.5459 g, 65% yield. ^{1}H NMR (500 MHz, DMSO-d_6) δ: 7.71 (t, J = 1.5, 2H), 7.22 (d, J = 1.5 Hz, 2H), 7.15 (t, J = 1.7 Hz, 2H), 6.95 (t, J = 1.7 Hz, 1H), 6.89 (d, J = 1.5 Hz, 2H), 5.14 (s, 4H), 1.22 (s, 9H). The NMR data matches previously reported data.[210]

Synthesis of receptor $\mathbf{4}^{2+}$: The macrocycle was synthesized according to published procedure.[210] tBu-protophane (545.9 mg, 1.854 mmol) was dissolved in anhydrous MeCN (400 mL) in a round bottom flask. **I1** (645.4 mg, 2.016 mmol) was dissolved in anhydrous MeCN (100 mL) and then added dropwise to the protophane solution via N_2 purged syringe. The reaction mixture was refluxed for 4 days under an Ar balloon. The solution was then concentrated under vacuum and the resulting solid was triturated with acetone (3 x 10 mL) to yield an off-white solid, 988.2 mg, 87% yield. ^{1}H NMR (500 MHz, DMSO-d_6) δ: 9.34 (t, J = 1.6 Hz, 2H), 7.82 (d, J = 1.6 Hz, 4H), 7.61 (d, J = 1.6 Hz, 4H), 6.68 (t, J = 1.6 Hz, 2H), 5.44 (s, 8H), 1.33 (s, 18H). NMR data matches previously reported. The NMR data matches previously reported data.[210]

In a drybox, the bromide precursor (499.8 mg, 0.8134 mmol) was dissolved in a 1:1 MeCN/EtOH mixture (50 mL) in a round bottom flask. $AgPF_6$ (457.6 mg, 1.810 mmol) was dissolved in minimal MeCN and then added to bromide precursor solution. The reaction mixture was stirred for 1 hour before being filtered through celite and concentrated under vacuum. The resulting solid was triturated with acetone to yield receptor $\mathbf{4}^{2+}$, 550.7 mg, 91% yield. ^{1}H NMR (500 MHz, Acetonitrile-d_3) δ: 8.32 (t, J = 1.7 Hz, 2H), 7.58 (d, J = 1.6 Hz, 4H), 7.43 (d, J = 1.7 Hz, 4H), 6.49 (s, 2H), 5.30 (s, 8H), 1.36 (s, 18H). ^{13}C{^{1}H} NMR (126 MHz, Acetonitrile-d_3) δ: 154.4, 136.3, 136.3, 127.5, 124.4, 123.4, 53.8, 35.7, 31.3. ^{19}F NMR (471 MHz, Acetonitrile-d_3) δ: -72.9 (d, J = 706.5 Hz).^{31}P{^{1}H} NMR (202 MHz, Acetonitrile-d_3) δ: -144.6, (hept, J = 706.6 Hz). The NMR data matches previously reported data.[210]

RECEPTOR CHARACTERIZATION:

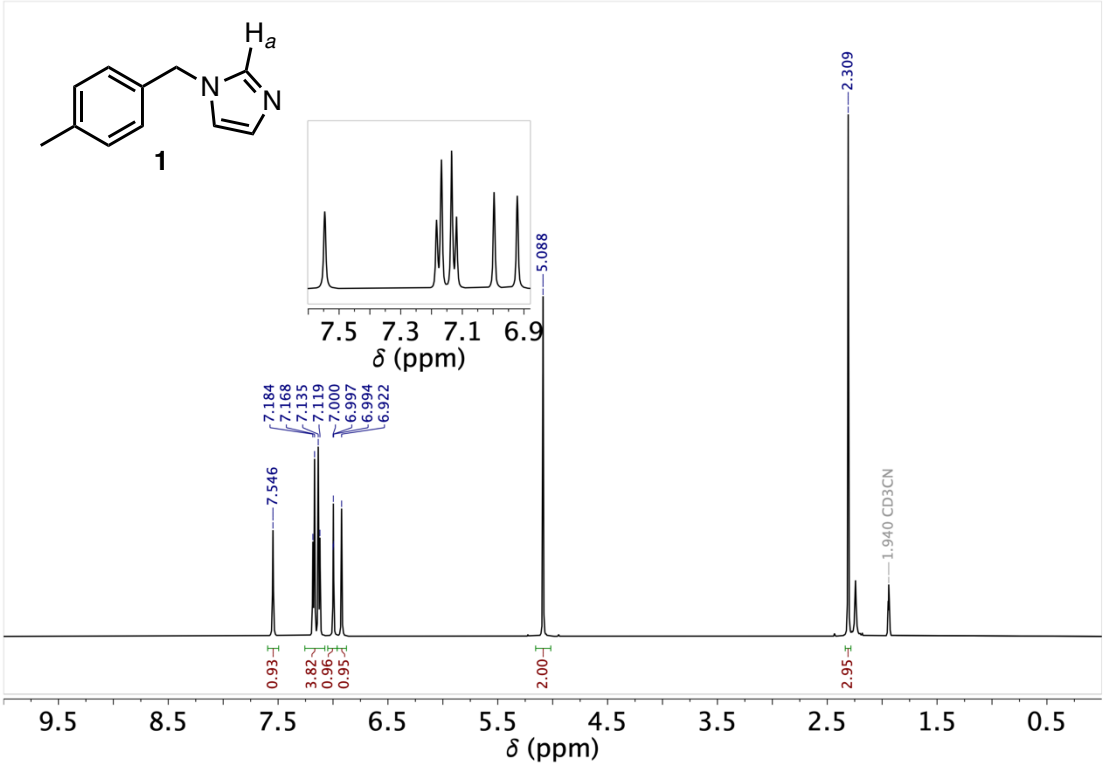

Figure B1. ^{1}H NMR spectrum (500 MHz, CD_3CN) of receptor **1**.

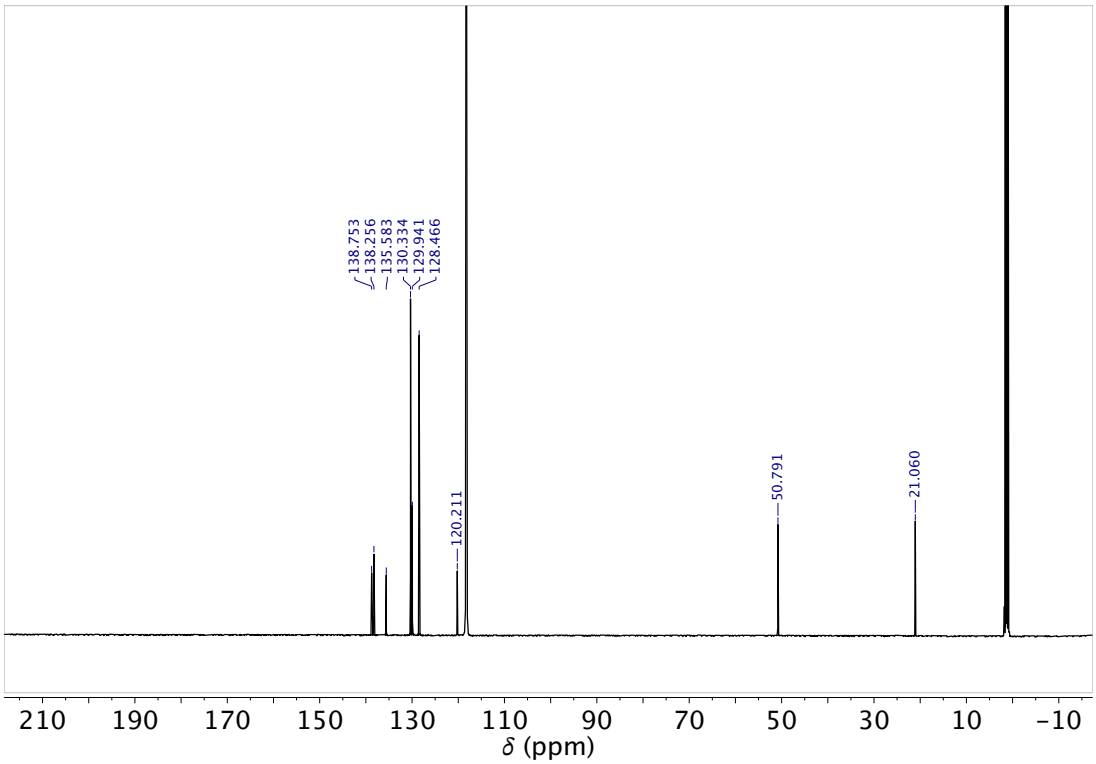

Figure B2. $^{13}C\{^{1}H\}$ NMR spectrum (126 MHz, CD_3CN) of receptor **1**.

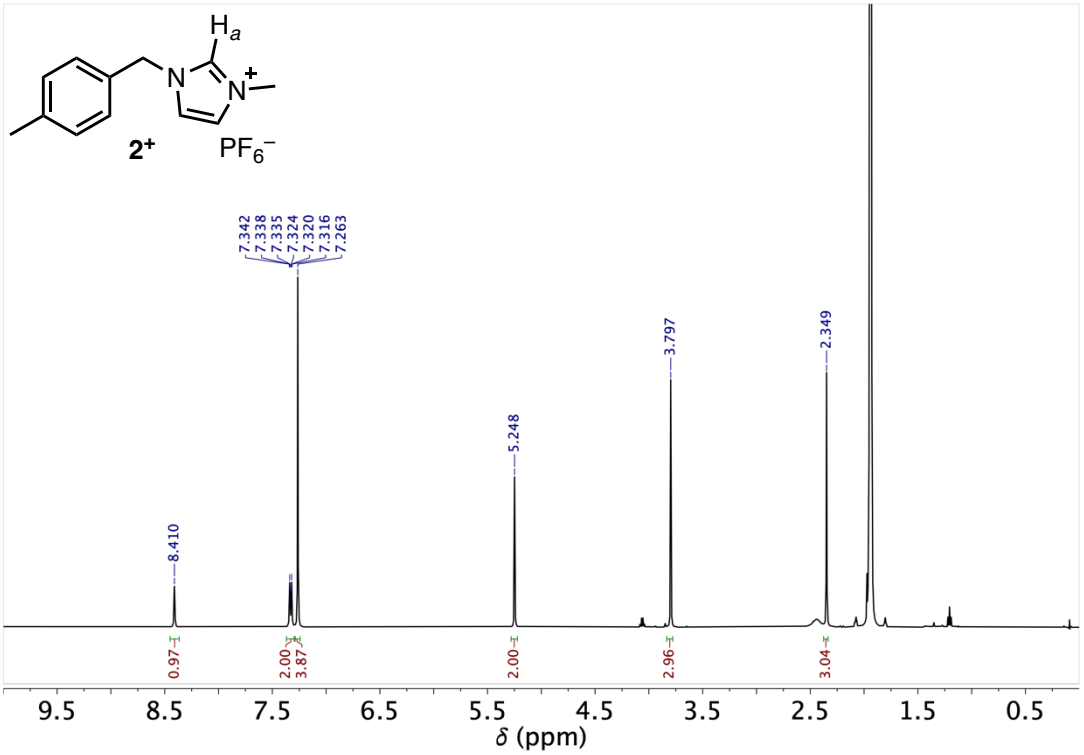

Figure B3. ^{1}H NMR spectrum (500 MHz, CD_3CN) of receptor $\mathbf{2}^{+}$.

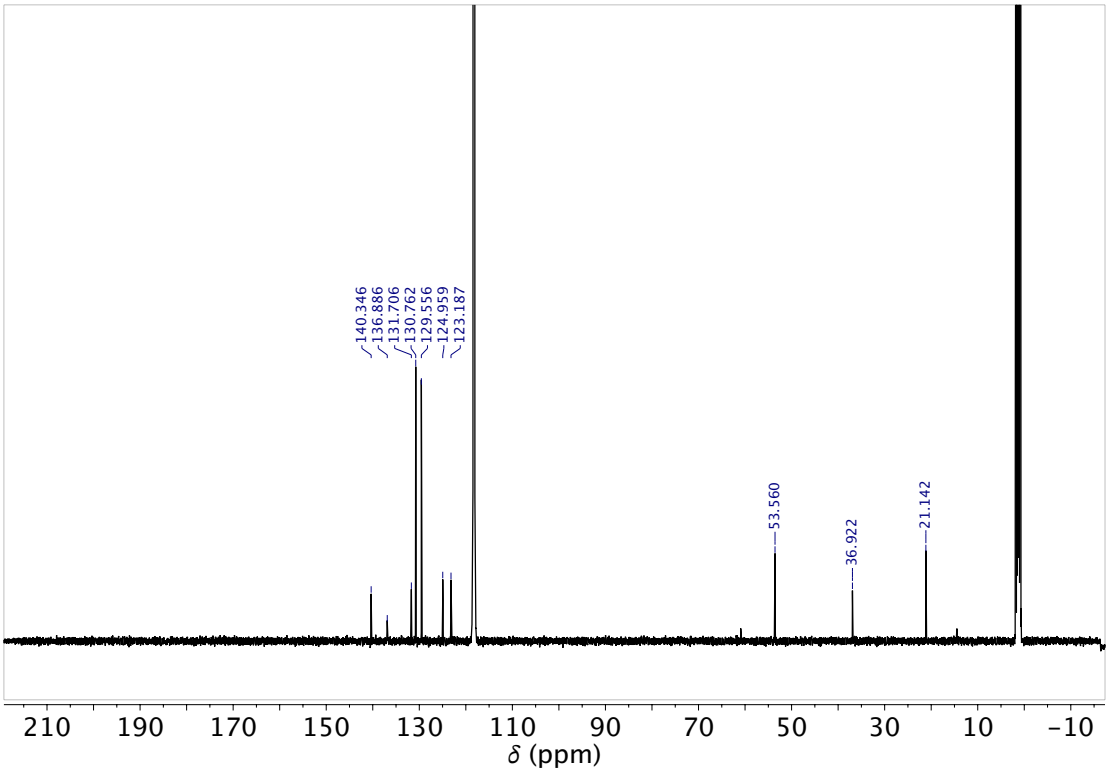

Figure B4: $^{13}C\{^{1}H\}$ NMR spectrum (126 MHz, CD_3CN) of receptor $\mathbf{2}^{+}$.

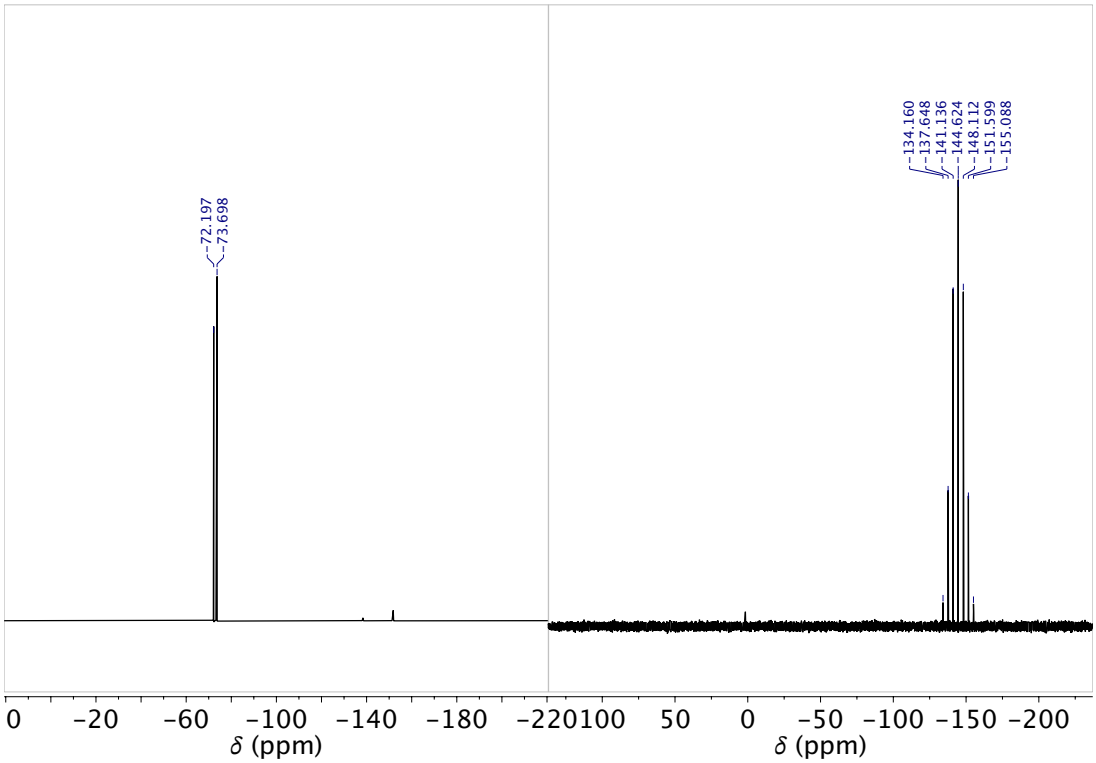

Figure B5. ^{19}F NMR spectrum (471 MHz, CD_3CN) and $^{31}P\{^1H\}$ NMR spectrum (202 MHz, CD_3CN) of receptor $\mathbf{2}^+$.

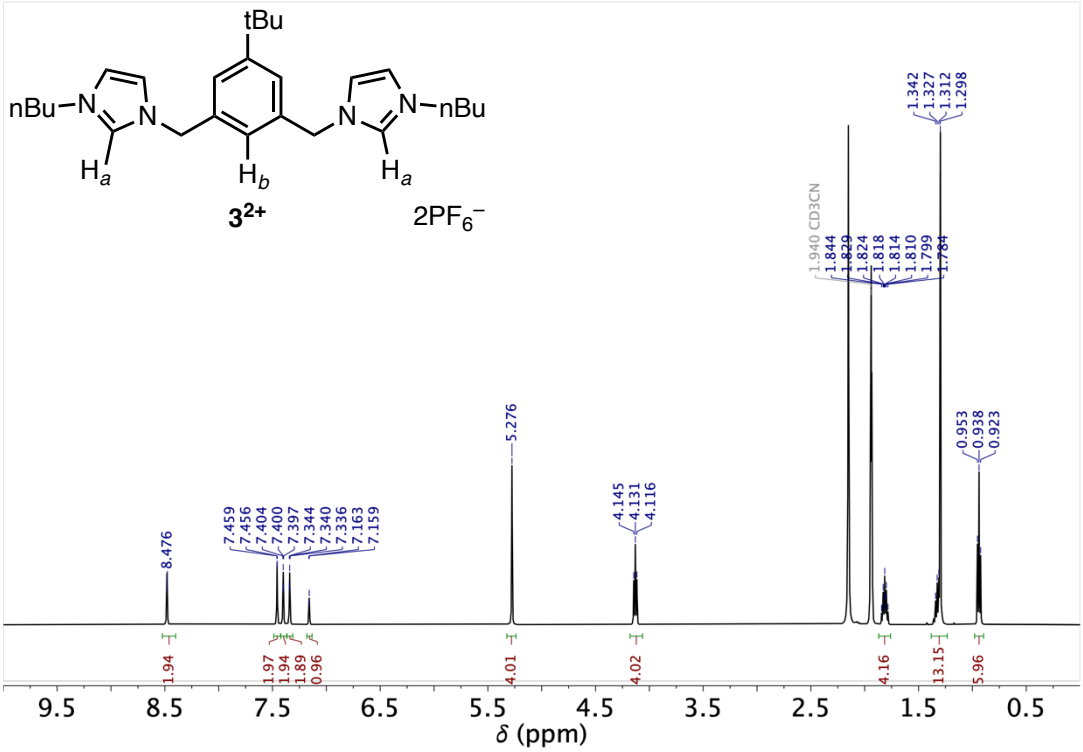

Figure B6. ^1H NMR spectrum (500 MHz, CD_3CN) of receptor $\mathbf{3}^{2+}$.

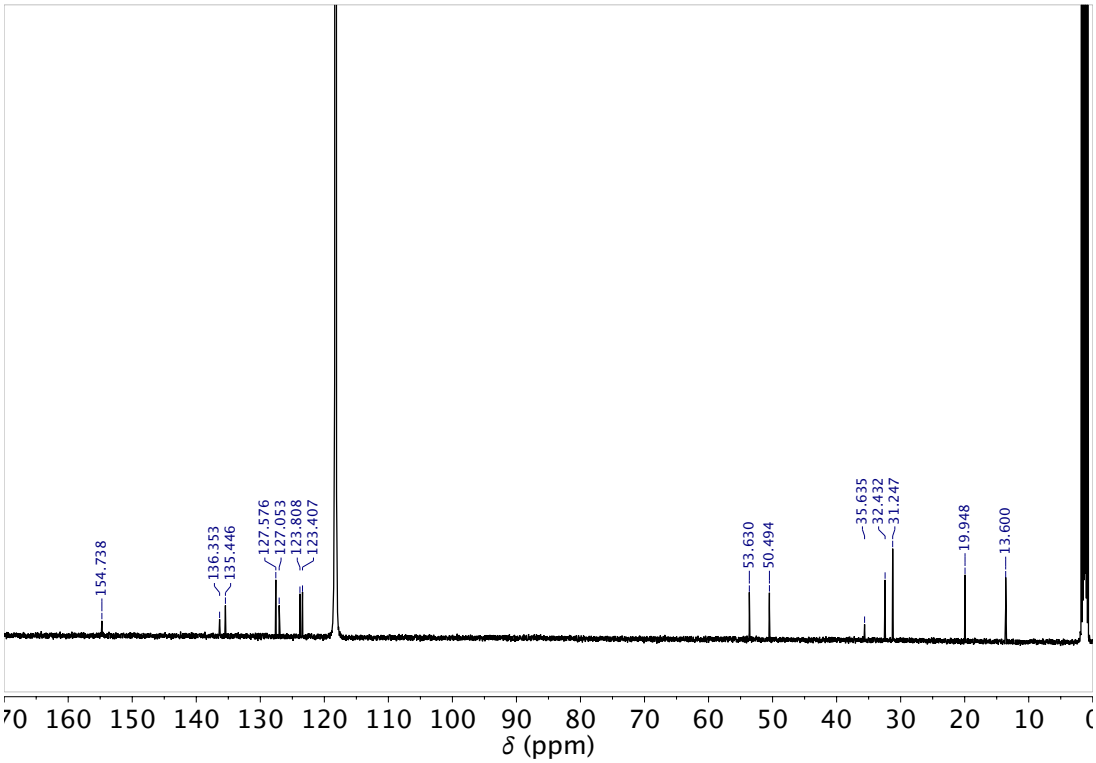

Figure B7. $^{13}C\{^{1}H\}$ NMR spectrum (126 MHz, CD_3CN) of receptor $\mathbf{3}^{2+}$.

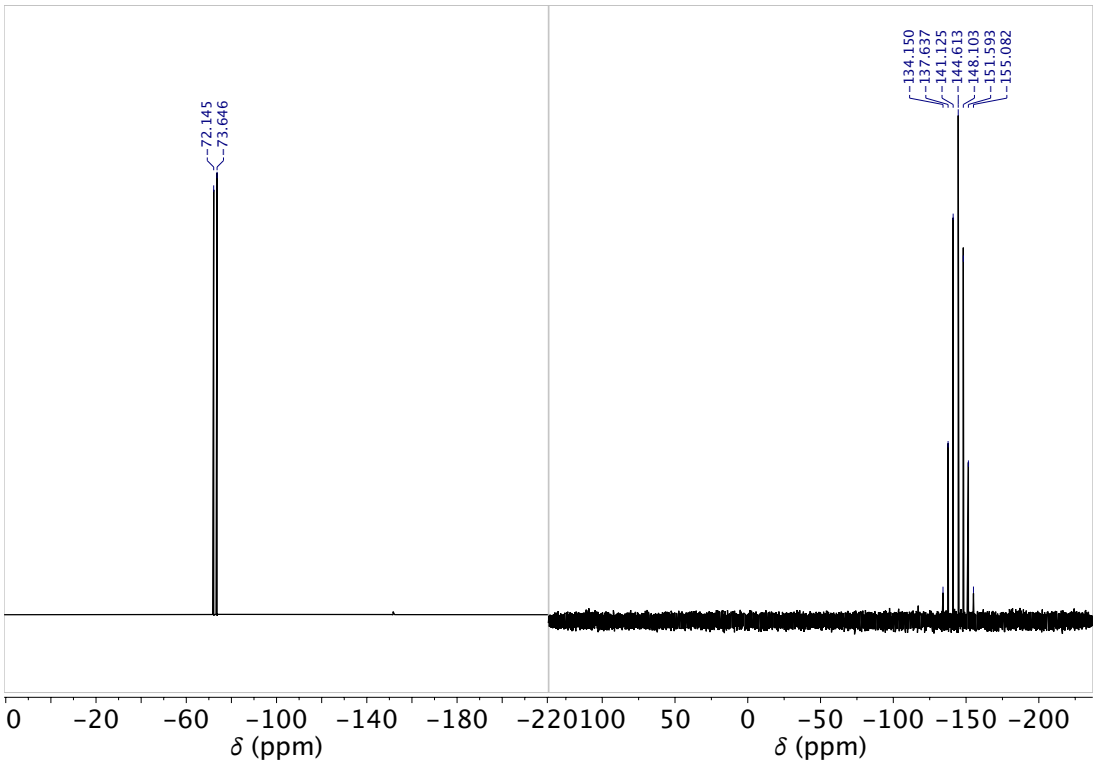

Figure B8. ^{19}F NMR spectrum (471 MHz, CD_3CN) and $^{31}P\{^{1}H\}$ NMR spectrum (202 MHz, CD_3CN) of receptor $\mathbf{3}^{2+}$.

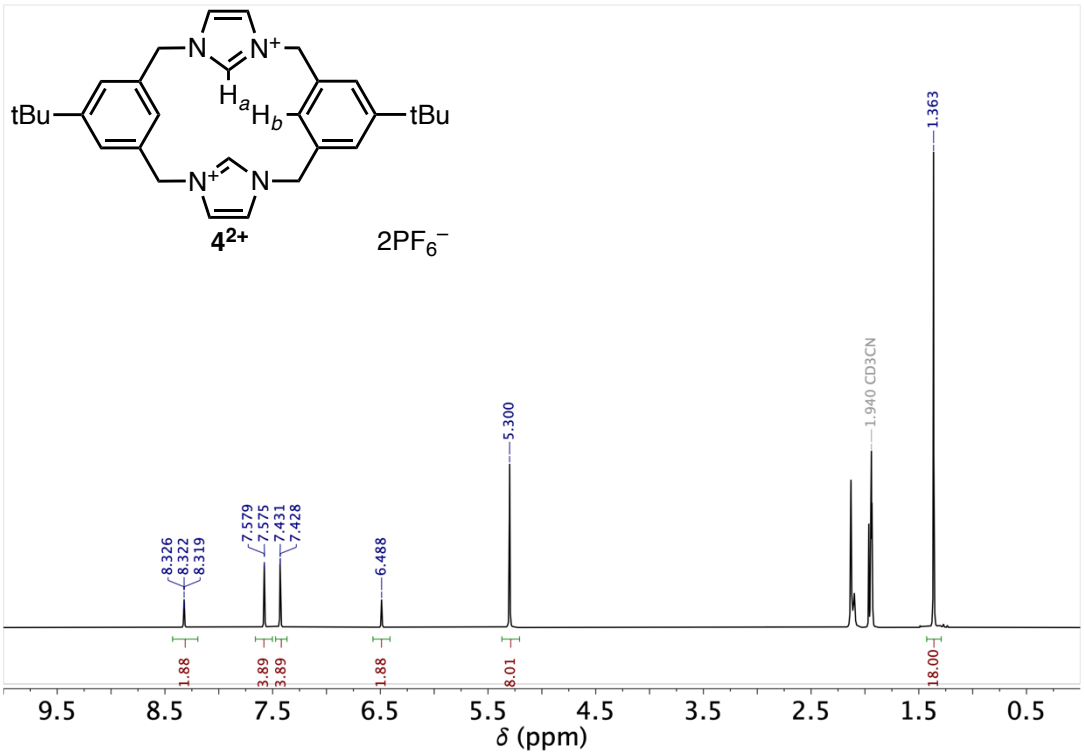

Figure B9. ^{1}H NMR spectrum (500 MHz, CD_3CN) of receptor $\mathbf{4^{2+}}$.

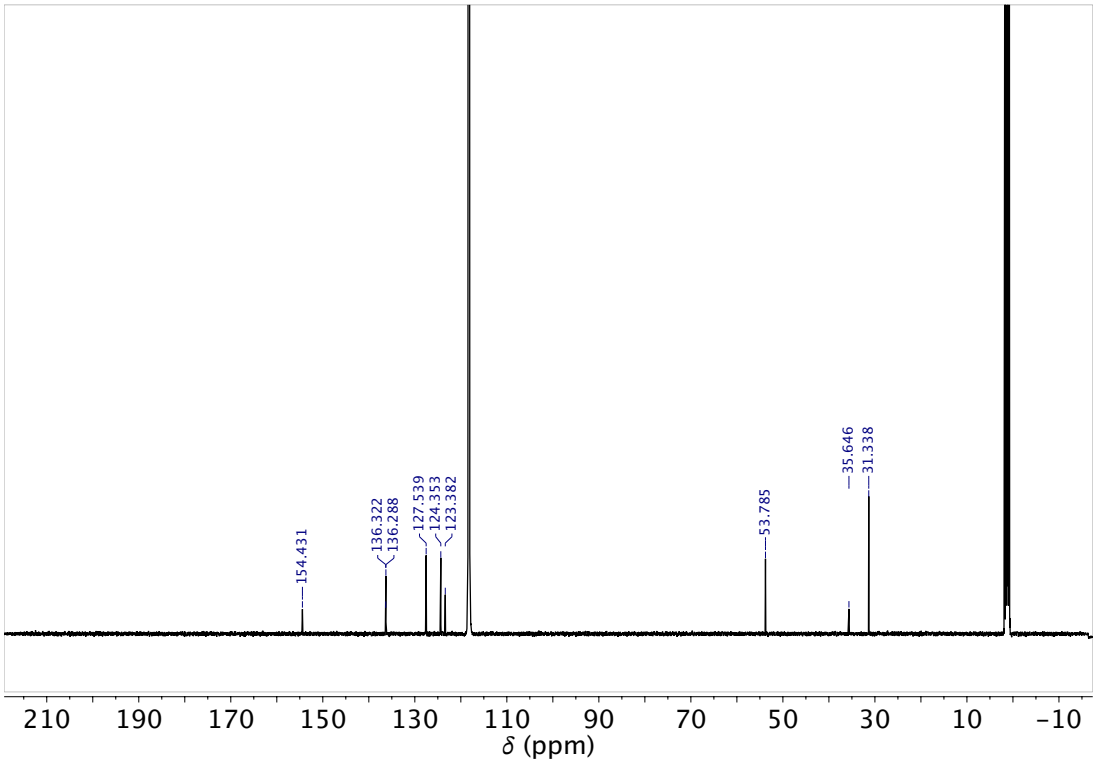

Figure B10. $^{13}C\{^{1}H\}$ NMR spectrum (126 MHz, CD_3CN) of receptor $\mathbf{4^{2+}}$.

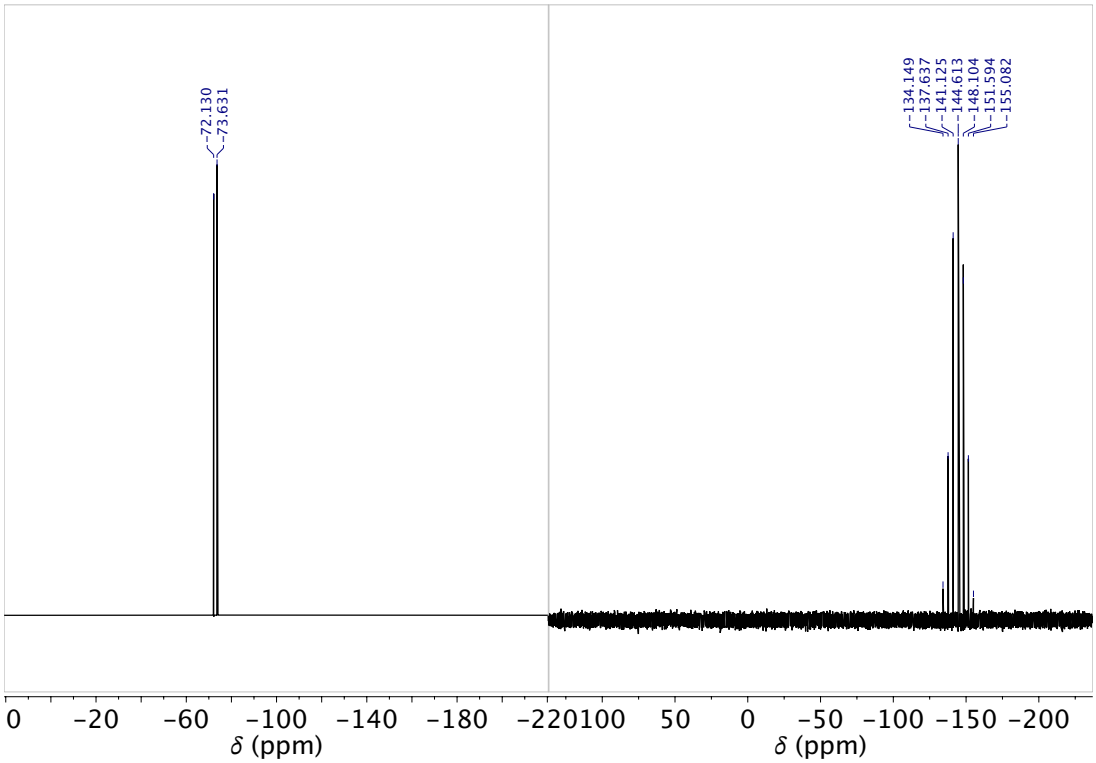

Figure B11. ^{19}F NMR spectrum (471 MHz, CD_3CN) and $^{31}P\{^1H\}$ NMR spectrum (202 MHz, CD_3CN) of receptor $\mathbf{4}^{2+}$.

B2. ^1H NMR TITRATIONS

General Methods: All NMR titration spectra were acquired at room temperature on a Bruker Avance III-HD 600 NMR Spectrometer equipped with a multinuclear Prodigy CryoProbe (^1H: 600 MHz) or on a Varian INOVA-500 NMR Spectrometer (^1H: 500 MHz). All chemical shifts (δ) are reported in ppm relative to residue CD_3CN (^1H: 1.940 ppm).

General Procedure: In a drybox, the desired receptor was dissolved in 1.7–1.8 mL of anhydrous CD_3CN (0.87 mM – 5.8 mM), divided between three NMR tubes (500 μL in each), and sealed with a rubber septum and parafilm. The guest compound (TBASH or TBACl) was dissolved in 2.4–2.6 mL of anhydrous CD_3CN (3.7 mM – 47.7 mM) and divided between three individual vials (~800 μL each). Aliquots of guest stock solution were added to the host solution via gas tight Hamilton syringes. ^1H NMR spectra were recorded at room temperature after each addition of the guest. The change in chemical shift (Δδ) of the C–H imidazolium proton and various C–H aromatic protons were used to follow the progress of the titration. The association constants were determined using the Nedler-Mead method in Bindfit.

Representative ^{1}H NMR Titration Data

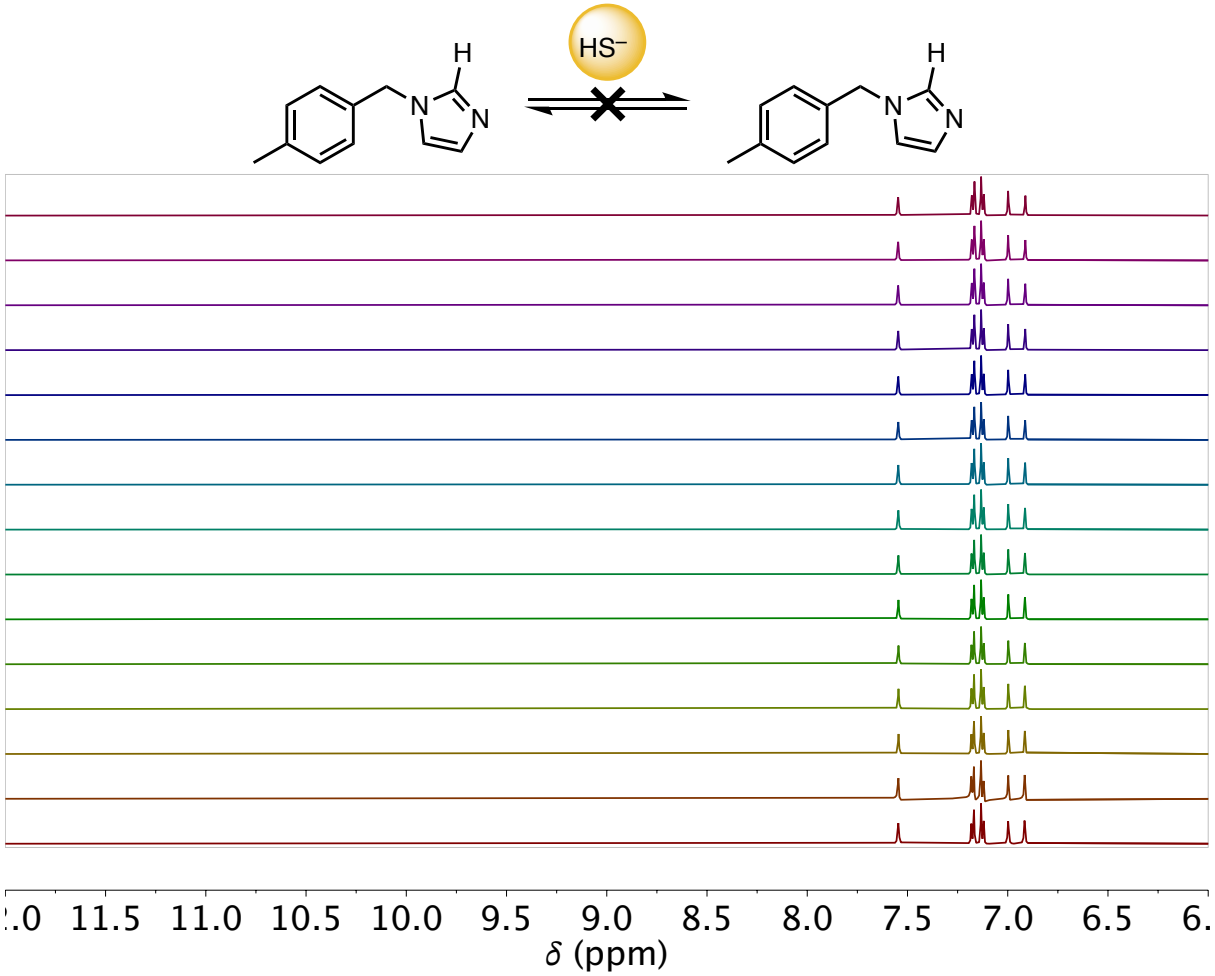

Figure B12. Titration scheme of receptor **1** with HS^- and representative ^{1}H NMR spectra.

Table B1. Representative titration of receptor **1** with HS^- in CD_3CN at room temperature.

Entry	V_{guest} (μL)	[Receptor] (M)	[Guest] (M)	Anion Equiv.	CH_a (ppm)
1	0	5.81E-03	0.00E+00	0.00	7.546
2	10	5.69E-03	9.46E-04	0.17	7.545
3	15	5.53E-03	2.30E-03	0.42	7.545
4	25	5.28E-03	4.39E-03	0.83	7.545
5	25	5.05E-03	6.30E-03	1.25	7.545
6	25	4.84E-03	8.04E-03	1.66	7.545
7	50	4.47E-03	1.11E-02	2.49	7.545
8	50	4.15E-03	1.38E-02	3.33	7.546
9	50	3.87E-03	1.61E-02	4.16	7.546
10	50	3.63E-03	1.81E-02	4.99	7.546
11	50	3.42E-03	1.99E-02	5.82	7.546
12	50	3.23E-03	2.15E-02	6.65	7.546
13	100	2.90E-03	2.41E-02	8.31	7.546
14	100	2.64E-03	2.63E-02	9.98	7.546
15	100	2.42E-03	2.82E-02	11.64	7.546

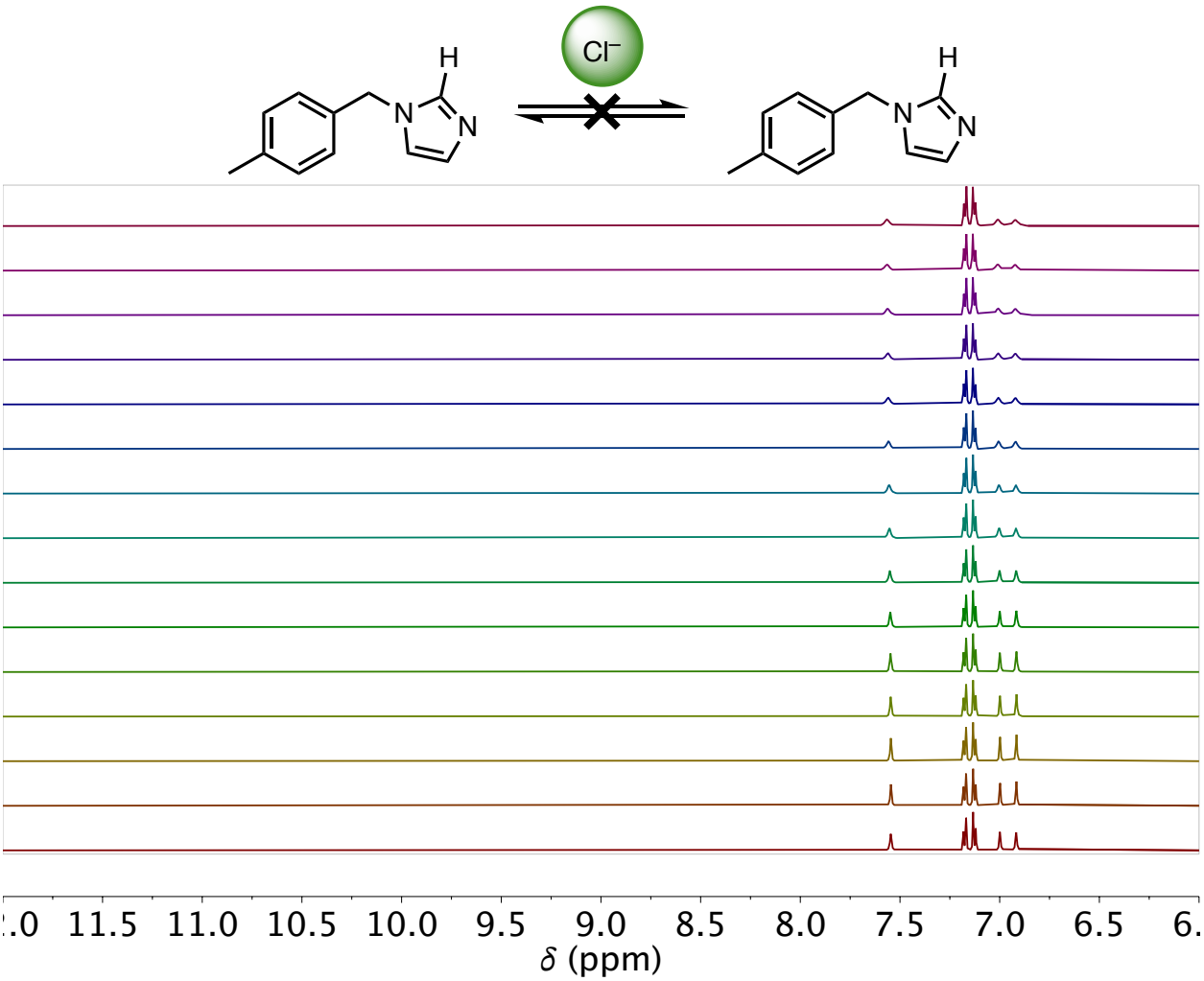

Figure B13. Titration scheme of receptor **1** with Cl^- and representative ^1H NMR spectra.

Table B2. Representative titration of receptor **1** with Cl^- in CD_3CN at room temperature.

Entry	V_{guest} (μL)	[Receptor] (M)	[Guest] (M)	Anion Equiv.	CH_a (ppm)
1	0	5.81E-03	0.00E+00	0.00	7.547
2	10	5.69E-03	9.35E-04	0.16	7.546
3	15	5.53E-03	2.27E-03	0.41	7.546
4	25	5.28E-03	4.33E-03	0.82	7.547
5	25	5.05E-03	6.22E-03	1.23	7.548
6	25	4.84E-03	7.95E-03	1.64	7.549
7	50	4.47E-03	1.10E-02	2.46	7.551
8	50	4.15E-03	1.36E-02	3.28	7.553
9	50	3.87E-03	1.59E-02	4.11	7.555
10	50	3.63E-03	1.79E-02	4.93	7.557
11	50	3.42E-03	1.96E-02	5.75	7.559
12	50	3.23E-03	2.12E-02	6.57	7.560
13	100	2.90E-03	2.38E-02	8.21	7.562
14	100	2.64E-03	2.60E-02	9.85	7.565
15	100	2.42E-03	2.78E-02	11.50	7.566

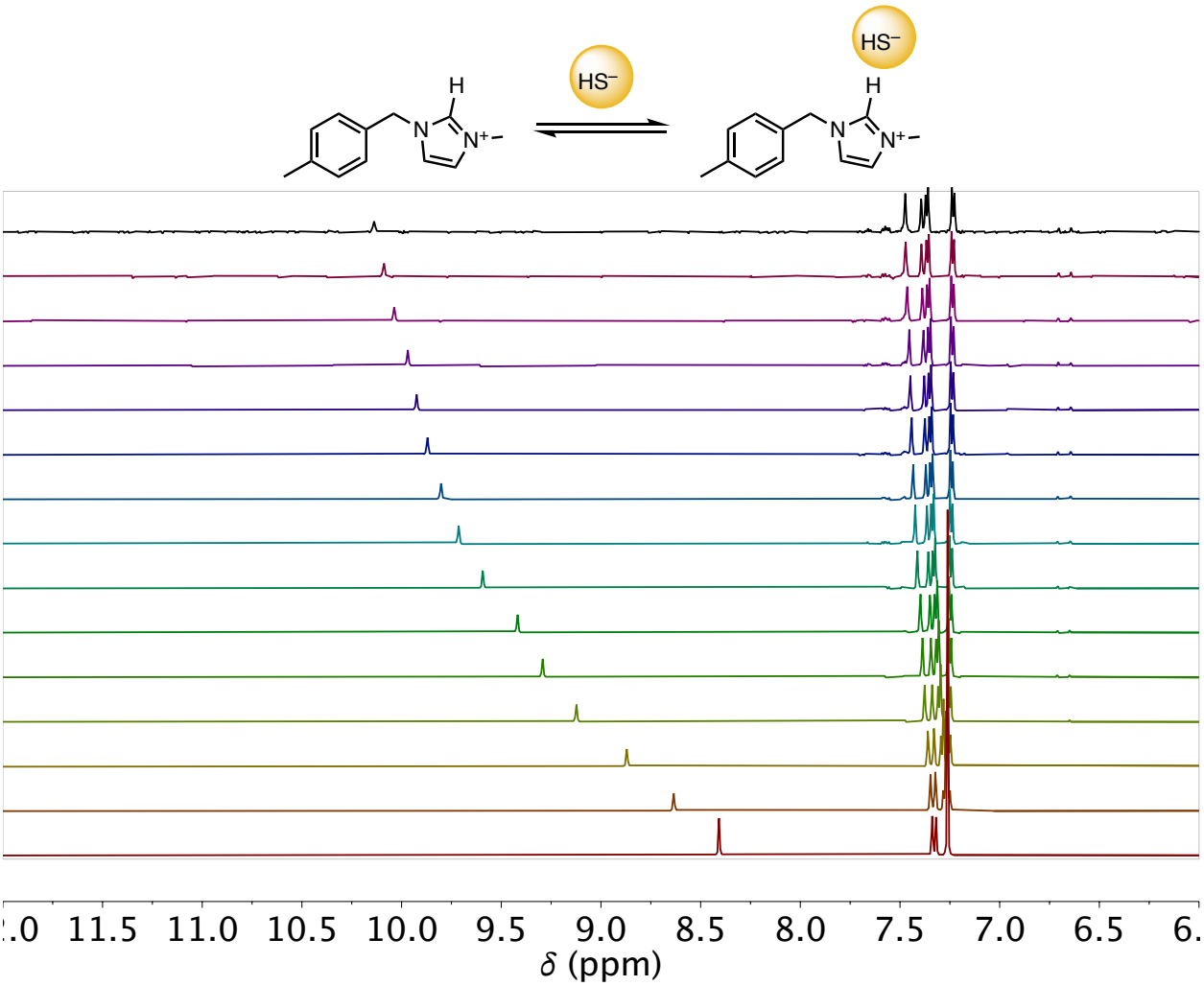

Figure B14. Titration scheme of receptor $\mathbf{2}^+$ with HS^- and representative ^1H NMR spectra.

Table B3. Representative titration of receptor $\mathbf{2}^+$ with HS^- in CD_3CN at room temperature.

Entry	V_{guest} (μL)	[Receptor] (M)	[Guest] (M)	Anion Equiv.	CH_a (ppm)
1	0	2.30E-03	0.00E+00	0.00	8.408
2	10	2.26E-03	1.83E-03	0.81	8.635
3	15	2.19E-03	4.45E-03	2.03	8.871
4	25	2.09E-03	8.50E-03	4.06	9.123
5	25	2.00E-03	1.22E-02	6.09	9.293
6	25	1.92E-03	1.56E-02	8.12	9.418
7	50	1.77E-03	2.16E-02	12.18	9.593
8	50	1.64E-03	2.67E-02	16.24	9.714
9	50	1.53E-03	3.11E-02	20.30	9.802
10	50	1.44E-03	3.50E-02	24.36	9.870
11	50	1.35E-03	3.85E-02	28.42	9.924
12	50	1.28E-03	4.15E-02	32.48	9.969
13	100	1.15E-03	4.67E-02	40.60	10.037
14	100	1.05E-03	5.10E-02	48.72	10.089
15	100	9.59E-04	5.45E-02	56.84	10.138

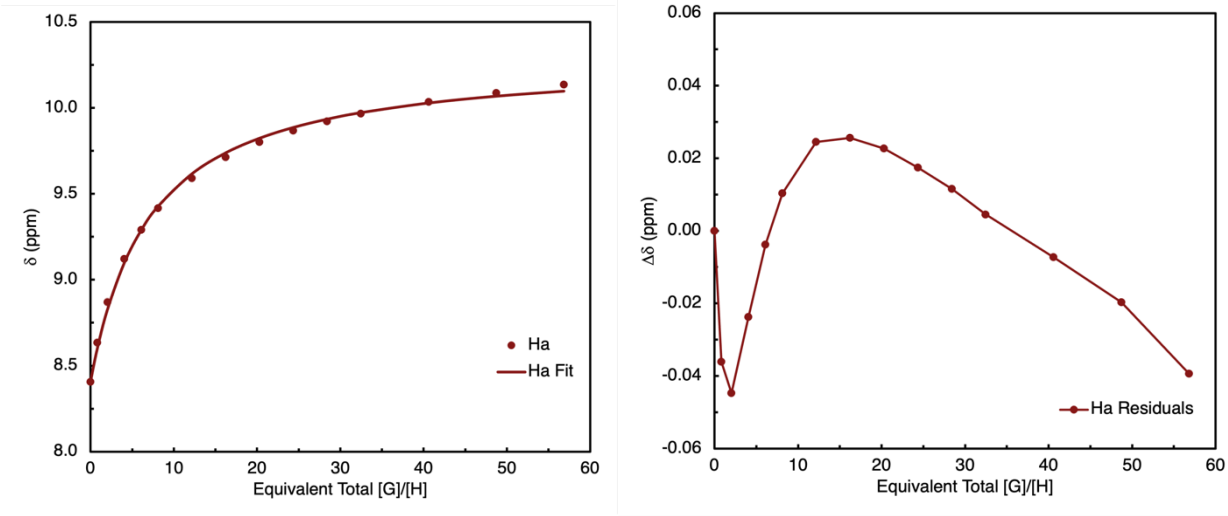

Figure B15. Representative 1:1 binding isotherm and residuals of HS^- titration of $\mathbf{2}^+$ in CD_3CN at room temperature determined via ^1H NMR spectroscopy.

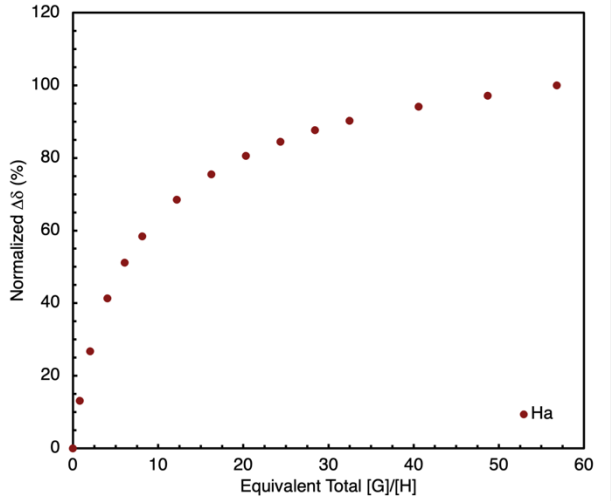

Figure B16. Normalized change in chemical shift of bound protons for HS^- titration of $\mathbf{2}^+$.

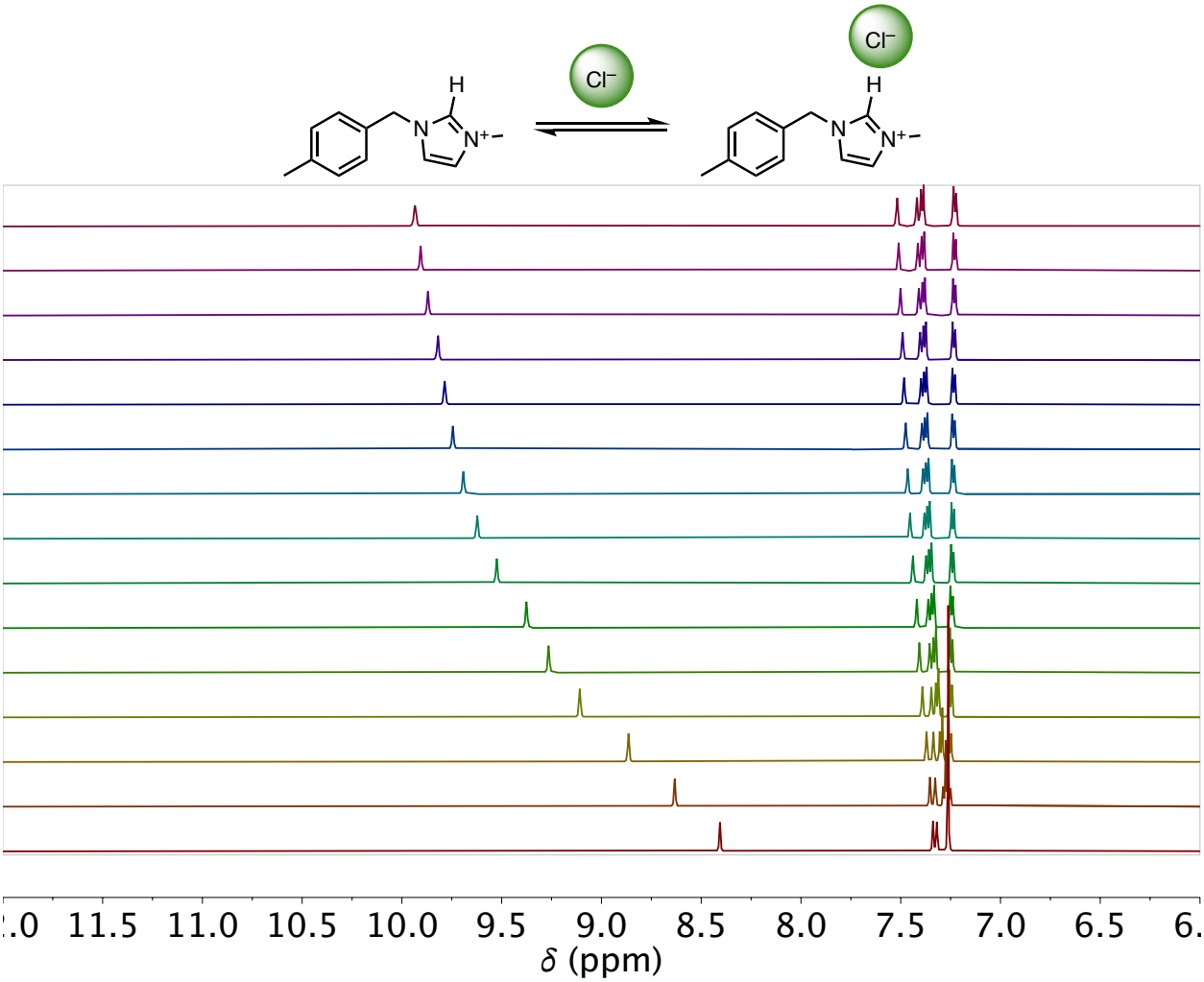

Figure B17. Titration scheme of receptor $\mathbf{2}^{+}$ with Cl^{-} and representative ^{1}H NMR spectra.

Table B4. Representative titration of receptor $\mathbf{2}^{+}$ with Cl^{-} in CD_3CN at room temperature.

Entry	V_{guest} (μL)	[Receptor] (M)	[Guest] (M)	Anion Equiv.	CH_a (ppm)
1	0	2.66E-03	0.00E+00	0.00	8.406
2	10	2.60E-03	2.18E-03	0.84	8.632
3	15	2.53E-03	5.30E-03	2.09	8.864
4	25	2.41E-03	1.01E-02	4.19	9.109
5	25	2.31E-03	1.45E-02	6.28	9.265
6	25	2.21E-03	1.85E-02	8.38	9.376
7	50	2.04E-03	2.57E-02	12.57	9.525
8	50	1.90E-03	3.18E-02	16.76	9.622
9	50	1.77E-03	3.71E-02	20.95	9.692
10	50	1.66E-03	4.17E-02	25.13	9.745
11	50	1.56E-03	4.58E-02	29.32	9.786
12	50	1.48E-03	4.94E-02	33.51	9.819
13	100	1.33E-03	5.56E-02	41.89	9.869
14	100	1.21E-03	6.07E-02	50.27	9.906
15	100	1.11E-03	6.49E-02	58.65	9.934

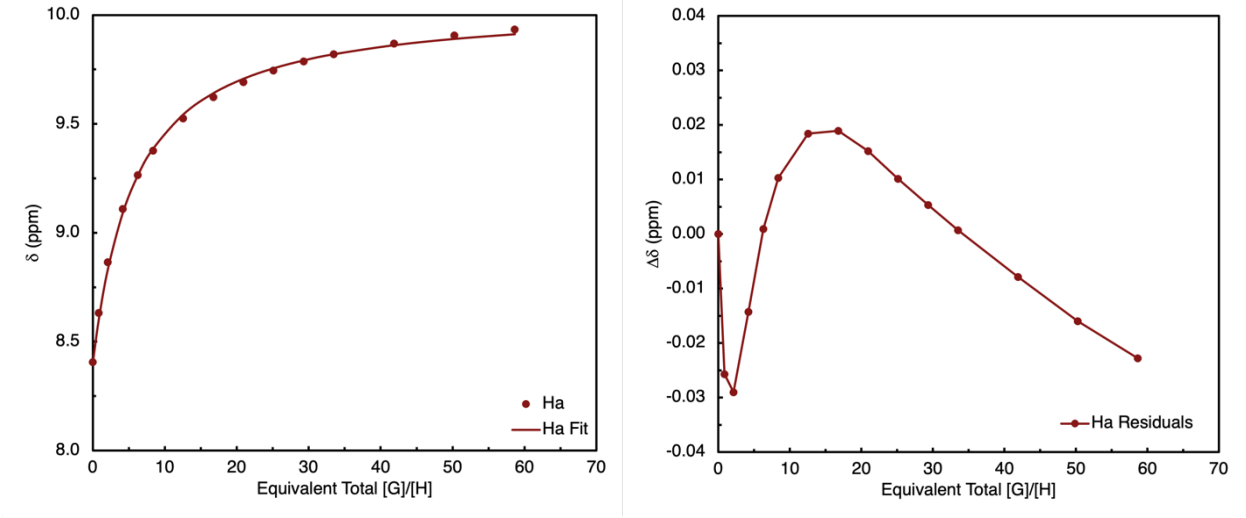

Figure B18. Representative 1:1 binding isotherm and residuals of Cl^- titration of $\mathbf{2}^+$ in CD_3CN at room temperature determined via ^1H NMR spectroscopy.

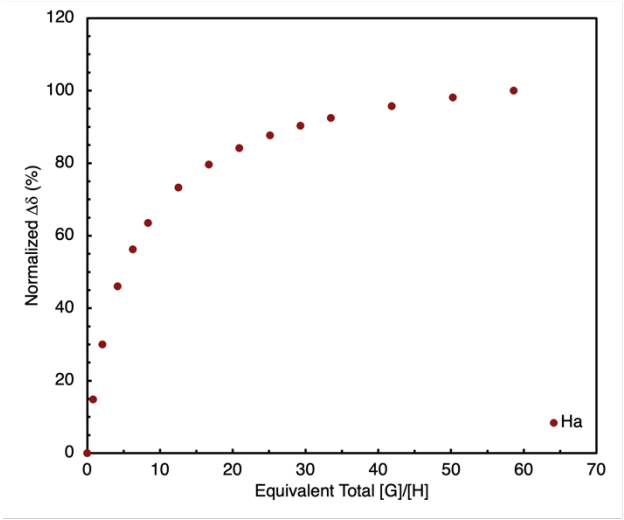

Figure B19. Normalized change in chemical shift of bound protons for Cl^- titration of $\mathbf{2}^+$.

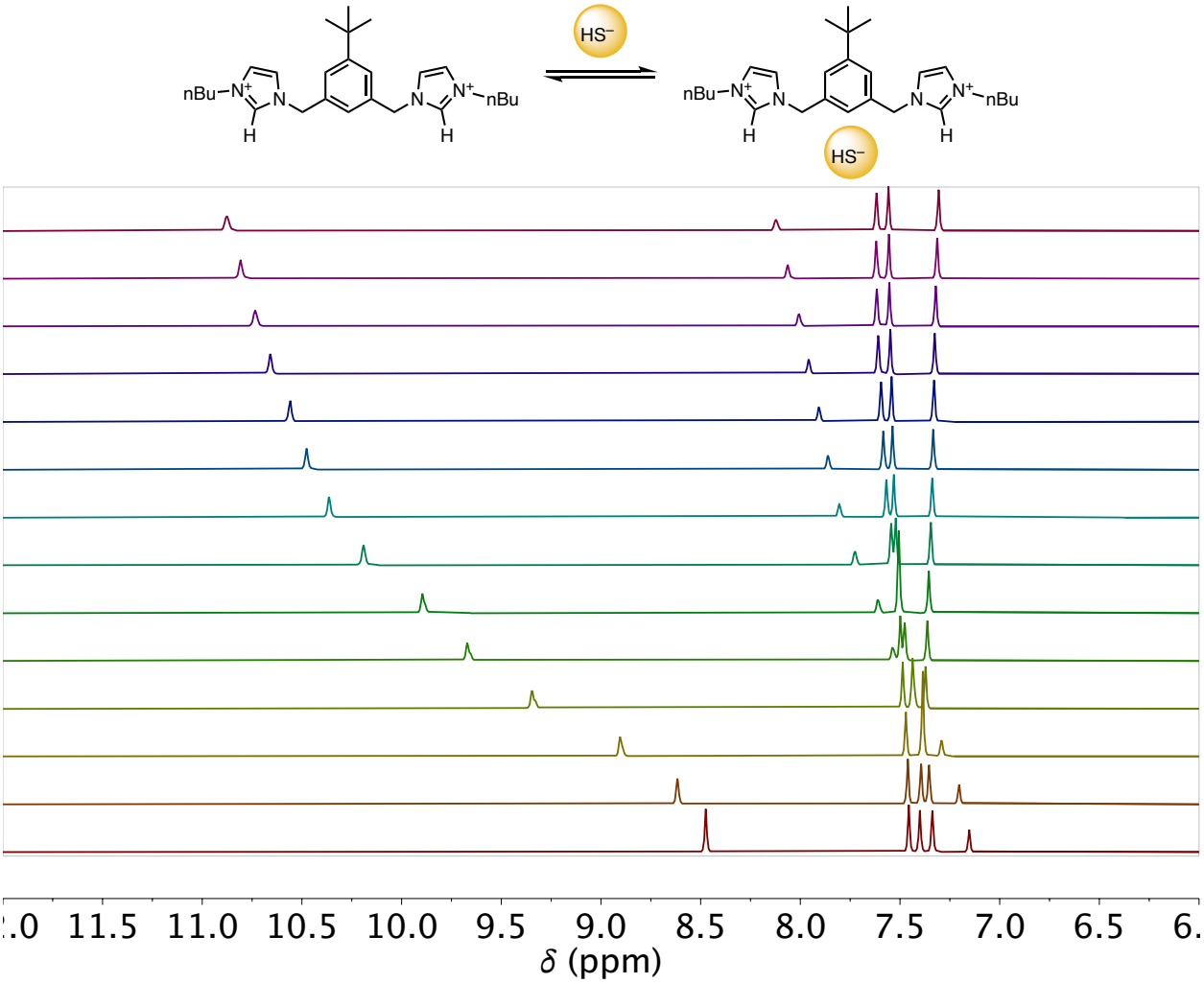

Figure B20. Titration scheme of receptor $\mathbf{3}^{2+}$ with HS^- and representative ^1H NMR spectra.

Table B5. Representative titration of receptor $\mathbf{3}^{2+}$ with HS^- in CD_3CN at room temperature.

Entry	V_{guest} (μL)	[Receptor] (M)	[Guest] (M)	Anion Equiv.	CH_a (ppm)	CH_b (ppm)
1	0	1.60E-03	0.00E+00	0.00	8.474	7.153
2	10	1.57E-03	1.92E-04	0.12	8.617	7.204
3	15	1.52E-03	4.67E-04	0.31	8.901	7.292
4	25	1.46E-03	8.92E-04	0.61	9.341	7.435
5	25	1.39E-03	1.28E-03	0.92	9.666	7.536
6	25	1.33E-03	1.63E-03	1.23	9.896	7.611
7	50	1.23E-03	2.26E-03	1.84	10.191	7.726
8	50	1.14E-03	2.80E-03	2.45	10.364	7.804
9	50	1.07E-03	3.27E-03	3.06	10.477	7.861
10	50	1.00E-03	3.68E-03	3.68	10.559	7.906
11	100	8.89E-04	4.36E-03	4.90	10.658	7.958
12	100	8.00E-04	4.90E-03	6.13	10.734	8.007
13	100	7.28E-04	5.35E-03	7.35	10.808	8.063
14	100	6.67E-04	5.72E-03	8.58	10.877	8.123

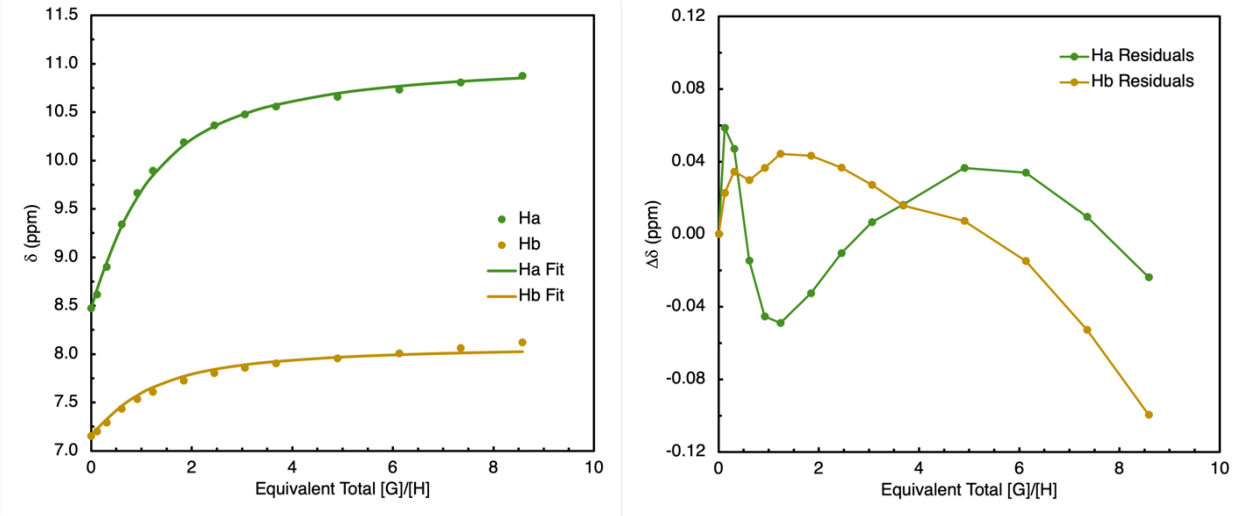

Figure B21. Representative 1:1 binding isotherm and residuals of HS^- titration of $\mathbf{3}^{2+}$ in CD_3CN at room temperature determined via ^1H NMR spectroscopy.

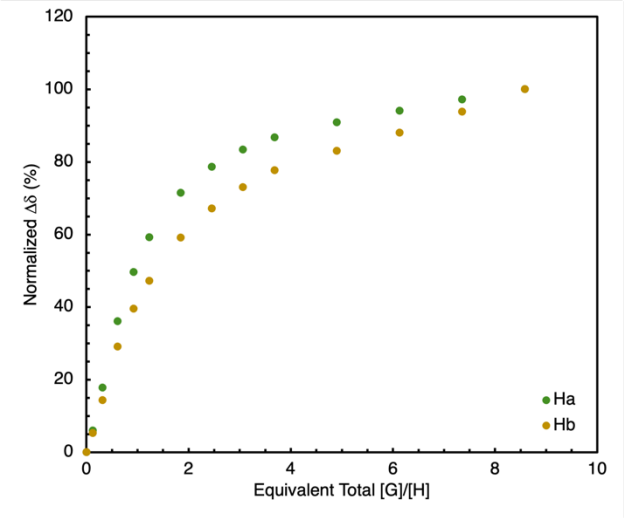

Figure B22. Normalized change in chemical shift of bound protons for HS^- titration of $\mathbf{3}^{2+}$.

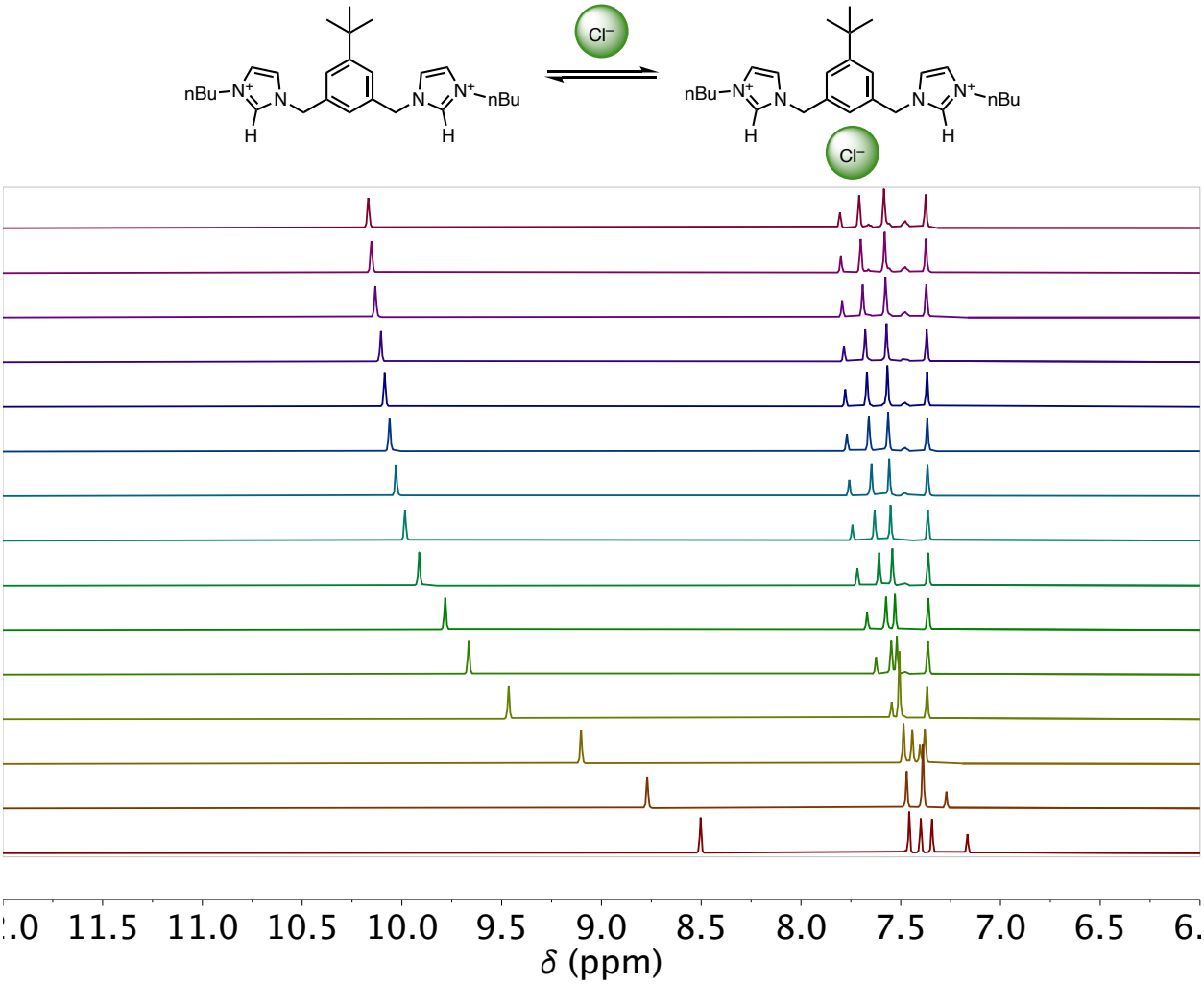

Figure B23. Titration scheme of receptor $\mathbf{3}^{2+}$ with Cl^- and representative ^1H NMR spectra.

Table B6. Representative titration of receptor $\mathbf{3}^{2+}$ with Cl^- in CD_3CN at room temperature.

Entry	V_{guest} (μL)	[Receptor] (M)	[Guest] (M)	Anion Equiv.	CH_a (ppm)	CH_b (ppm)
1	0	1.94E-03	0.00E+00	0	8.503	7.116
2	10	1.90E-03	4.13E-04	0.22	8.770	7.272
3	15	1.84E-03	1.00E-03	0.54	9.102	7.403
4	25	1.76E-03	1.92E-03	1.09	9.465	7.546
5	25	1.68E-03	2.75E-03	1.63	9.665	7.623
6	25	1.61E-03	3.51E-03	2.18	9.783	7.668
7	50	1.49E-03	4.86E-03	3.26	9.913	7.717
8	50	1.38E-03	6.02E-03	4.35	9.984	7.742
9	50	1.29E-03	7.02E-03	5.44	10.030	7.758
10	50	1.21E-03	7.90E-03	6.53	10.062	7.769
11	50	1.14E-03	8.68E-03	7.62	10.086	7.778
12	50	1.08E-03	9.37E-03	8.71	10.105	7.784
13	100	9.68E-04	1.05E-02	10.88	10.113	7.793
14	100	8.80E-04	1.15E-02	13.06	10.153	7.800
15	100	8.07E-04	1.23E-02	15.23	10.168	7.805

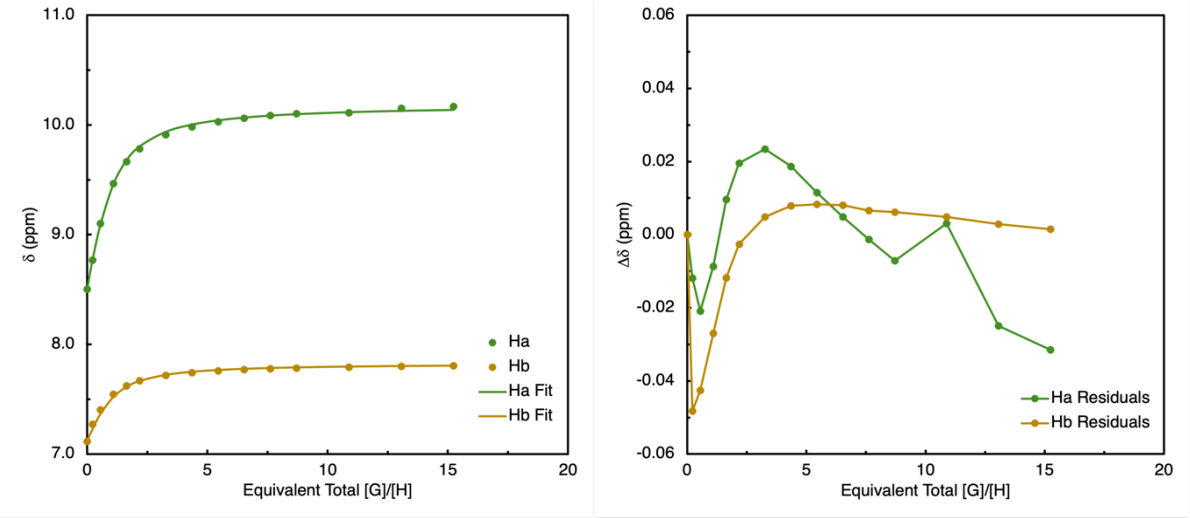

Figure B24. Representative 1:1 binding isotherm and residuals of Cl^- titration of $\mathbf{3}^{2+}$ in CD_3CN at room temperature determined via ^1H NMR spectroscopy.

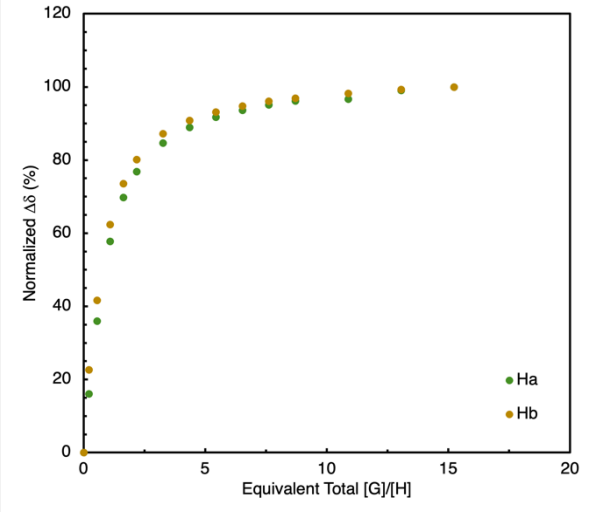

Figure B25. Normalized change in chemical shift of bound protons for Cl^- titration of $\mathbf{3}^{2+}$.

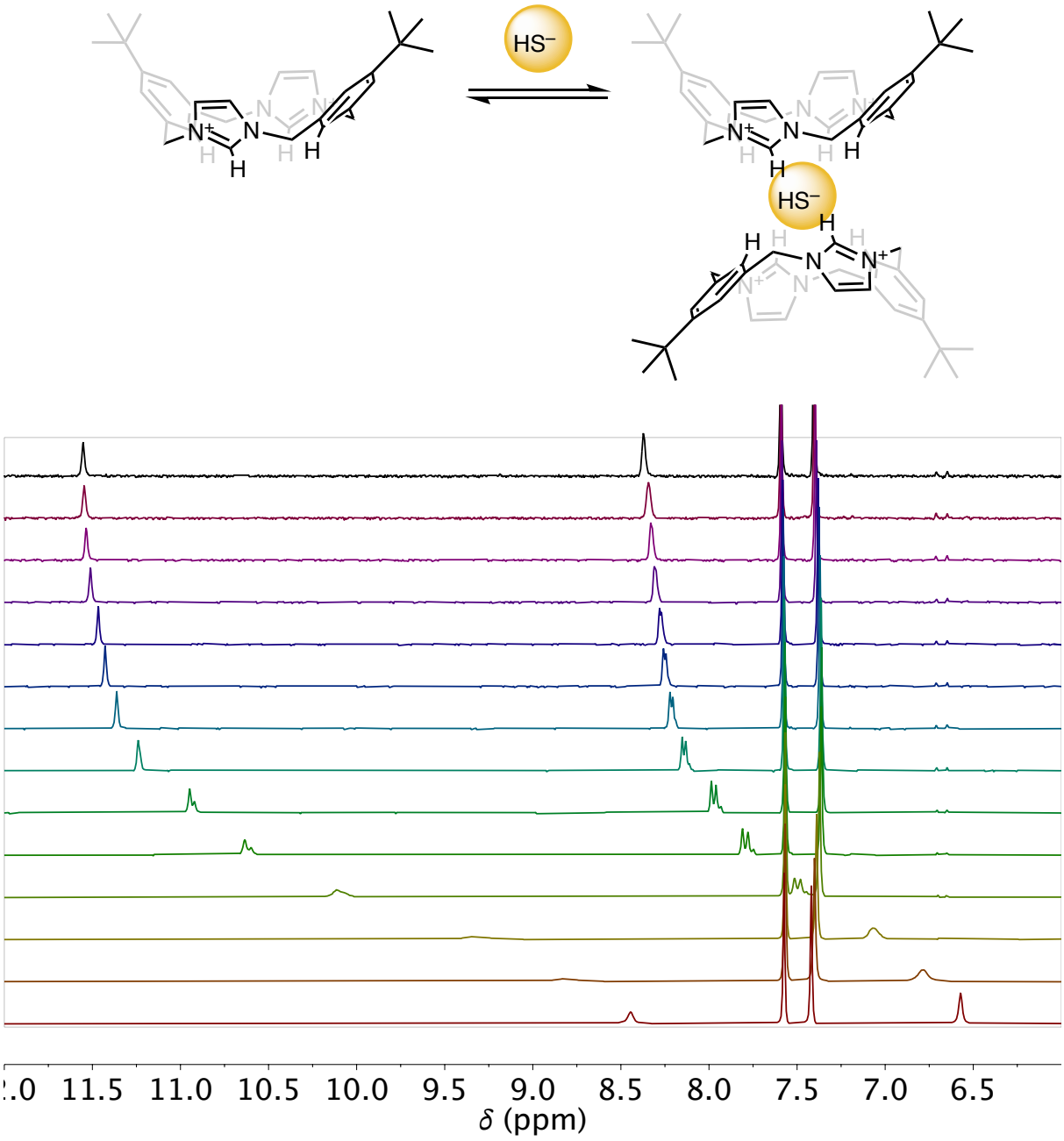

Figure B26. Titration scheme of receptor $\mathbf{4}^{2+}$ with HS^- and representative ^1H NMR spectra.

Table B7. Representative titration of receptor $\mathbf{4}^{2+}$ with HS^- in CD_3CN at room temperature.

Entry	V_{guest} (μL)	[Receptor] (M)	[Guest] (M)	Anion Equiv.	CH_a (ppm)	CH_b (ppm)
1	0	9.70E-04	0.00E+00	0.00	8.447	6.575
2	10	9.51E-04	8.93E-05	0.09	8.819	6.786
3	15	9.24E-04	2.17E-04	0.23	9.326	7.071
4	25	8.82E-04	4.14E-04	0.47	10.098	7.497
5	25	8.43E-04	5.94E-04	0.70	10.619	7.795
6	25	8.08E-04	7.59E-04	0.94	10.938	7.974
7	50	7.46E-04	1.05E-03	1.41	11.237	8.143
8	50	6.93E-04	1.30E-03	1.88	11.362	8.212
9	50	6.47E-04	1.52E-03	2.35	11.428	8.251
10	50	6.06E-04	1.71E-03	2.82	11.467	8.274
11	100	5.39E-04	2.02E-03	3.76	11.511	8.304
12	100	4.85E-04	2.28E-03	4.69	11.536	8.326
13	100	4.41E-04	2.48E-03	5.63	11.546	8.342
14	100	4.04E-04	2.66E-03	6.57	11.552	8.371

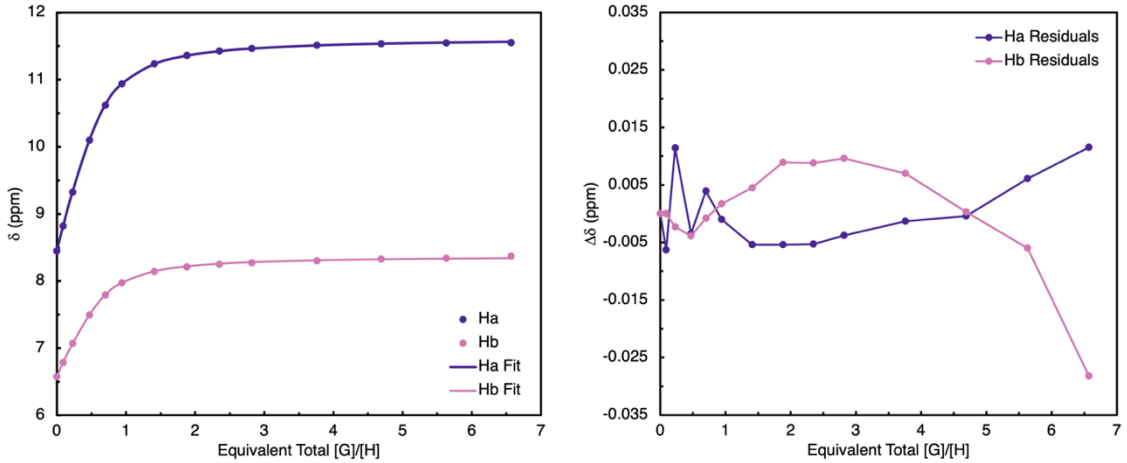

Figure B27. Representative 2:1 binding isotherm and residuals of HS^- titration of $\mathbf{4}^{2+}$ in CD_3CN at room temperature determined via ^1H NMR spectroscopy.

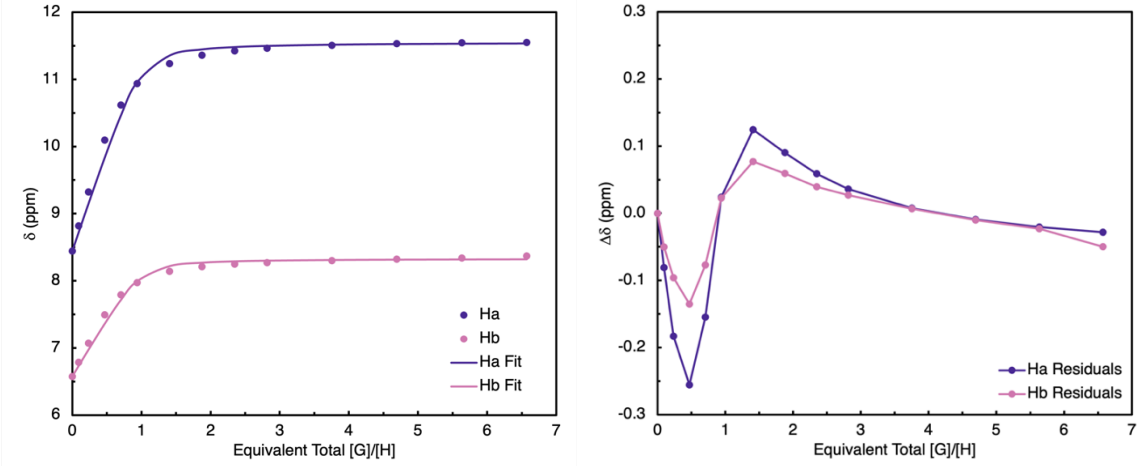

Figure B28. Representative 1:1 binding isotherm and residuals of HS^- titration of $\mathbf{4}^{2+}$ in CD_3CN at room temperature determined via ^1H NMR spectroscopy.

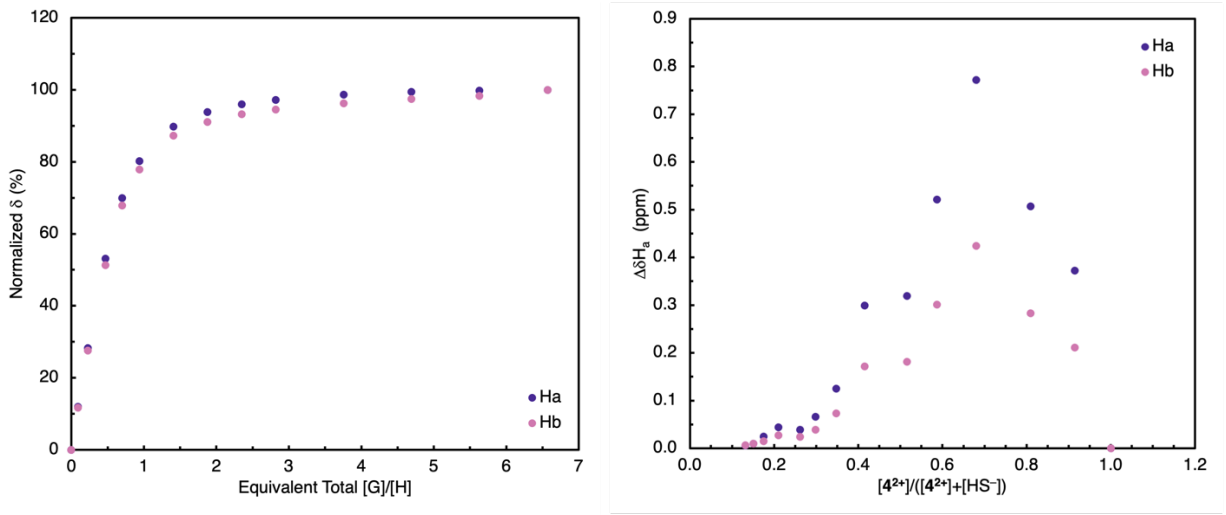

Figure B29. Normalized change in chemical shift of bound protons and Job Plot of HS^- titration of $\mathbf{4^{2+}}$.

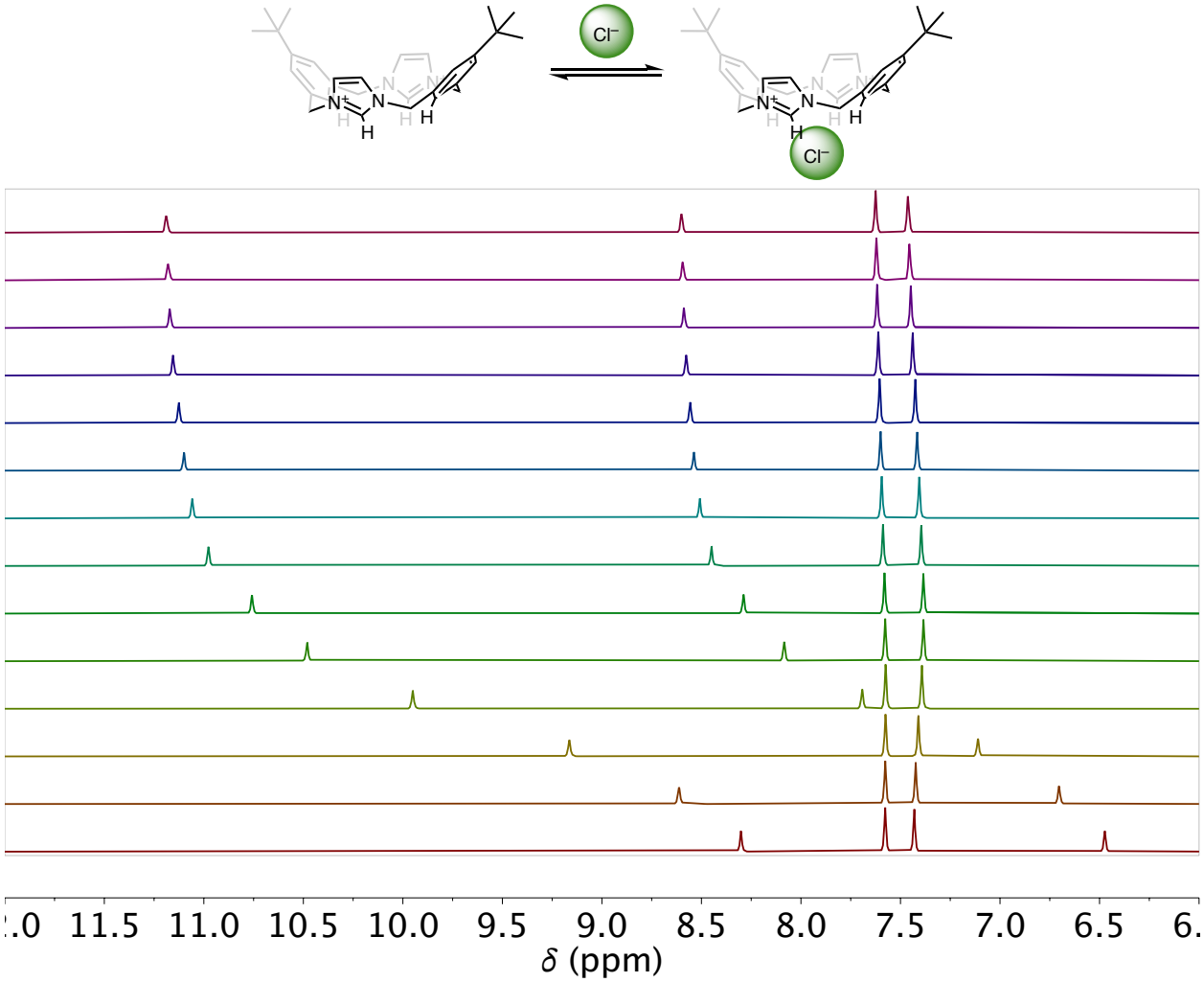

Figure B30. Titration scheme of receptor $\mathbf{4}^{2+}$ with Cl^- and representative ^1H NMR spectra.

Table B8. Representative titration of receptor $\mathbf{4}^{2+}$ with Cl^- in CD_3CN at room temperature.

Entry	V_{guest} (μL)	[Receptor] (M)	[Guest] (M)	Anion Equiv.	CH_a (ppm)	CH_b (ppm)
1	0	1.42E-03	0.00E+00	0.00	8.309	6.479
2	5	1.41E-03	9.72E-05	0.07	8.435	6.572
3	5	1.39E-03	1.92E-04	0.14	8.601	6.694
4	15	1.35E-03	4.67E-04	0.35	9.139	7.092
5	25	1.29E-03	8.92E-04	0.69	9.919	7.669
6	25	1.24E-03	1.28E-03	1.04	10.451	8.062
7	25	1.19E-03	1.64E-03	1.38	10.736	8.273
8	25	1.14E-03	1.96E-03	1.73	10.882	8.38
9	25	1.09E-03	2.26E-03	2.07	10.963	8.439
10	25	1.05E-03	2.54E-03	2.42	11.014	8.476
11	25	1.02E-03	2.80E-03	2.76	11.048	8.501
12	25	9.81E-04	3.05E-03	3.11	11.073	8.513
13	25	9.48E-04	3.27E-03	3.45	11.091	8.532
14	25	9.17E-04	3.48E-03	3.80	11.106	8.542
15	25	8.89E-04	3.68E-03	4.14	11.117	8.551

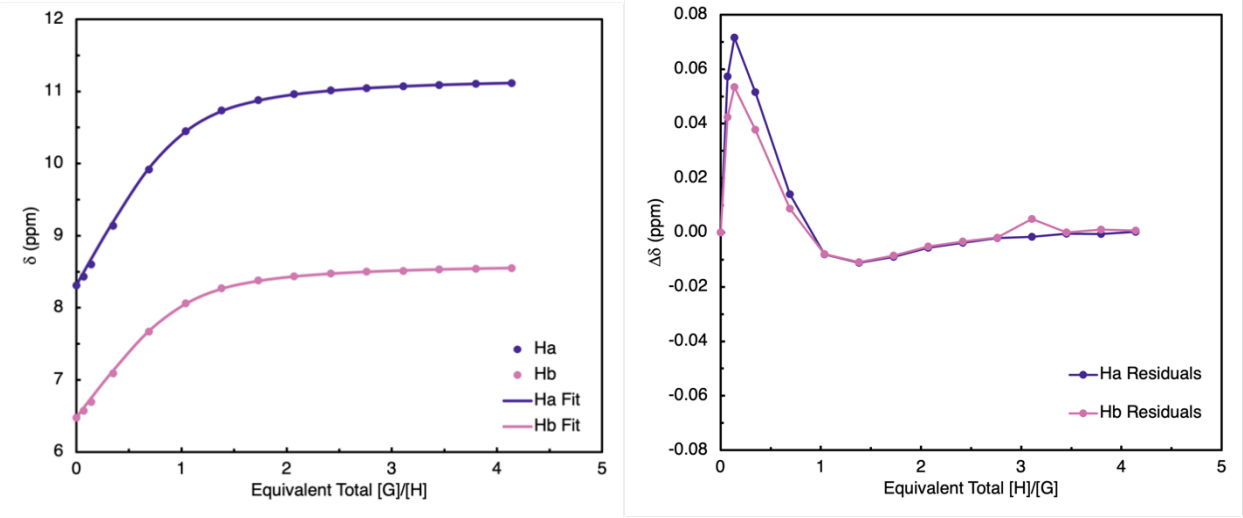

Figure B31. Representative 1:1 binding isotherm and residuals of Cl^- titration of $\mathbf{4}^{2+}$ in CD_3CN at room temperature determined via ^1H NMR spectroscopy.

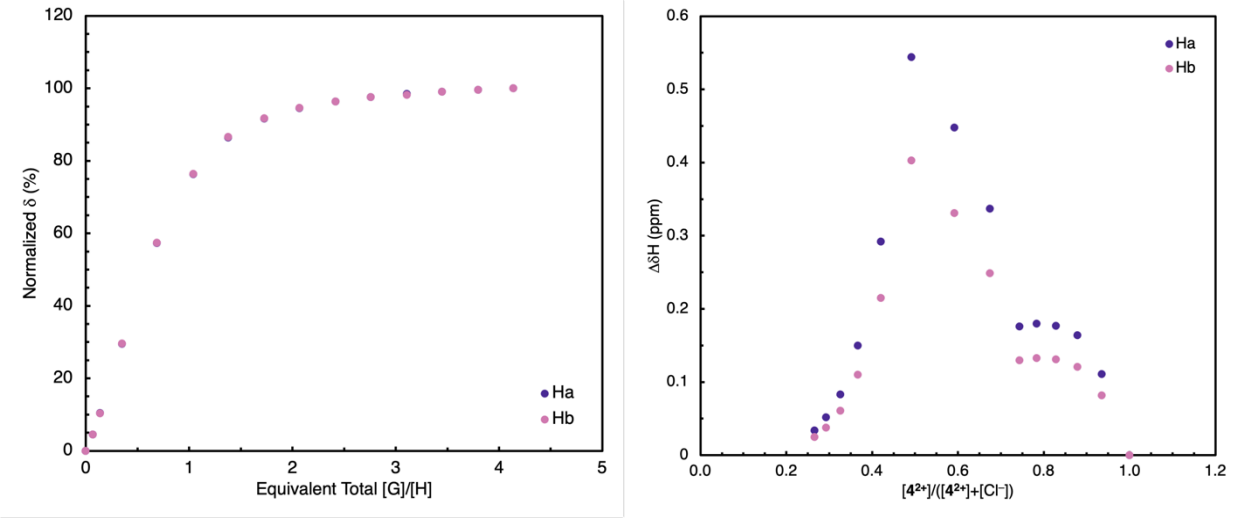

Figure B32. Normalized change in chemical shift of bound protons and Job Plot of Cl^- titration of $\mathbf{4}^{2+}$.

B3. X-RAY CRYSTALLOGRAPHIC DATA

X-ray Crystallography. Diffraction intensities for $[(\mathbf{4}^{2+})_2 \cdot HS^-][PF_6]_3$ were collected at 173 K on a Bruker Apex2 CCD diffractometer using a *Incoatec* Cu *IμS* source, CuK_α radiation, 1.54178 Å. Space groups were determined based on systematic absences. Absorption corrections were applied by SADABS.[256] The structure was solved by direct methods and Fourier techniques and refined on F^2 using full matrix least-squares procedures. All non-H atoms were refined with anisotropic thermal parameters. The H atoms were refined in calculated positions in a rigid group model. The space groups symmetry options P2/m, P2/c, and Pc were all checked. The structure

was solved in two possible space groups: P2/c and Pc. The structural data in both groups are comparable and the structure in P2/c is given as the final data. In the crystal there were MeCN and Et_2O solvent molecules. The Et_2O was highly disordered and was treated by SQUEEZE. The terminal -CMe_3 group including the C27, C27a, C28, C28a, C29, C29a, and C30, C30a atoms is highly disordered. All H atoms were treated in calculated positions. The H atom at the S atom was not found from the XRD data. All calculations were performed by the Bruker SHELXL-2014/7 package.[257]

Table B9. X-Ray crystallographic parameters for $[(\mathbf{4}^{2+})_2 \cdot HS^-][PF_6]_3$

	$[(\mathbf{4}^{2+})_2 \cdot HS^-][PF_6]_3$
formula	$C_{68}H_{93}F_{18}N_{10}OP_3S$
formula weight	1533.49
temperature (K)	173(2)
crystal system	Monoclinic
space group	P 2/c
a (Å)	14.1026(7)
b (Å)	10.6885(6)
c (Å)	26.0478(14)
α (deg)	90
β (deg)	93.740(4)
γ (deg)	90
V (Å^3)	3918.0(4)
Z	2
ρ (mm^{-1})	1.724
F(000)	1604
crystal size (mm^3)	0.17 × 0.09 × 0.02
θ range (deg)	3.40 – 66.56
completeness to θ (%)	99.4
total reflns	27133
indep reflns	6900
restraints / param	6 / 466
R1 (wR2) [I > 2σ(I)]	0.0565 (0.1730)
R1 (wR2)	0.0776 (0.1916)
GOF (F^2)	1.056
max, min peaks (e Å^{-3})	0.848, –0.472

B4. CCDC DATABASE SEARCH PARAMETERS

The CCDC Conquest Program was used to compare our crystal structure to those in the Cambridge Structural Database up to April 2023. The search was done in a similar yet more restrictive method to our previously published method.[206] C–H···S---NM contacts were identified when S was bound (by any bond order) to 1, 2, and 3 other non-metal (NM) elements. The draw function of Conquest allows the user to restrict contact angles and distances. Intermolecular C···S contacts were defined between 0 and 4 Å. Intermolecular H···S contacts were defined between 0 and 3 Å. Both C–H···S and H···S---NM bond angles were defined between and including 90° and 180°. Both organic and organometallic structures were allowed. Structures with poor R factors (<= 0.05) were excluded. No further filters were applied. After the search was completed, contact distances and angles were downloaded into Microsoft Excel spreadsheets. The smallest H···S contact distance within our structure (2.525 Å) was placed at 259 of 76,146 entries.

APPENDIX C

CHAPTER IV SUPPLEMENTARY INFORMATION

C1: EXPERIMENTAL METHODS

General Methods: All drybox manipulations were performed in an Innovative Atmospheres N_2-filled glove box. All NMR spectra for compound characterization were acquired at room temperature unless otherwise noted on a Bruker Avance III-HD 500 NMR spectrometer equipped with a multinuclear Prodigy™ CryoProbe (^{1}H: 500 MHz, ^{13}C: 126 MHz, ^{19}F: 471 MHz, ^{31}P: 202 MHz). All NMR titration spectra were acquired at room temperature on a Bruker Avance III-HD 600 NMR Spectrometer equipped with a multinuclear Prodigy CryoProbe (^{1}H: 600 MHz) or on a Varian INOVA-500 NMR Spectrometer (^{1}H: 500 MHz). ^{1}H and ^{13}C chemical shifts (δ) are reported in ppm relative to residual CD_3CN (^{1}H: 1.94 ppm, ^{13}C: 118.26 ppm). Anhydrous and deoxygenated CD_3CN was obtained by sparging with N_2, distilling over K_2CO_3, and storing over 4 Å molecular sieves in an inert atmosphere glovebox. Tetrabutylammonium hydrosulfide (TBASH),[211] intermediate **1** (I1),[253] and receptors **5** & **6**[210] were all synthesized according to previous reports. All other reagents were used as received from commercial suppliers.

RECEPTOR SYNTHESES

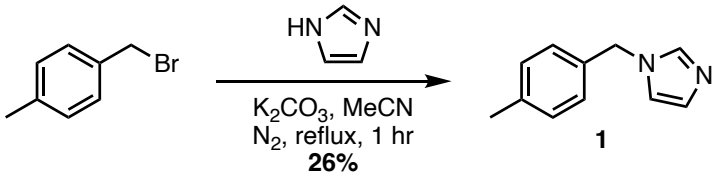

Scheme C1. Synthetic scheme for receptor **1**.

Synthesis of **1**: 4-Methylbenzyl bromide (244.8 mg, 1.323 mmol), imidazole (110.4 mg, 1.622 mmol), and K_2CO_3 (281.4 mg, 2.036 mmol) were dissolved in anhydrous MeCN (25 mL) in a round bottom flask. The solution was brought to reflux and stirred for 1 hour under N_2. The reaction mixture was then concentrated under vacuum before extracting the crude material into CH_2Cl_2 (20 mL) and washing with a saturated $NaHCO_3$ solution (3 x 20 mL). The organic layer was dried over Na_2SO_4, filtered, and concentrated under vacuum. The crude material was suspended in a 20% EtOAc/hexanes solution and passed through a silica plug to remove

impurities. The pure product was isolated by flushing the plug with EtOAc to afford 60.9 mg, 26% yield. ^{1}H NMR (500 MHz, Acetonitrile-d_3) δ: 7.55 (s, 1H), 7.22 – 7.08 (m, 4H), 7.00 (d, J = 1.4 Hz, 1H), 6.92 (s, 1H), 5.09 (s, 2H), 2.31 (s, 3H). ^{13}C{^{1}H} NMR (126 MHz, Acetonitrile-d_3) δ: 138.8, 138.3, 135.6, 130.3, 129.9, 128.5, 120.2, 50.8, 21.1. The NMR data matches previously reported data.[254]

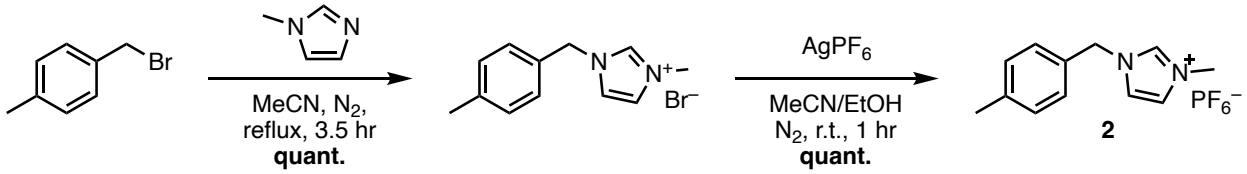

Scheme C2. Synthetic scheme for receptor **2**$^{+}$.

Synthesis of **2**$^{+}$: 4-Methylbenzyl bromide (0.224 g, 1.21 mmol) was dissolved in anhydrous MeCN (7 mL) in a round bottom flask, after which 1-methylimidazole (0.105 mL, 1.33 mmol) was added dropwise. The solution was blanketed with Ar and heated to 40 °C for 3.5 hrs. The solution was concentrated under vacuum to yield the bromide precursor in quantitative yield, 0.315 g. ^{1}H NMR (500 MHz, DMSO-d_6) δ: 9.23 (t, J = 1.7 Hz, 1H), 7.78 (t, J = 1.8 Hz, 1H), 7.71 (t, J = 1.8 Hz, 1H), 7.33 (d, 8.8 Hz, 2H), 7.23 (d, 7.94 Hz, 2H), 5.37 (s, 2H), 3.85 (s, 3H), 2.30 (s, 3H). The NMR data matches previously reported data.[255]

The the bromide precursor (106.9 mg, 0.4001 mmol) was dissolved in a 1:1 MeCN/EtOH mixture (20 mL) in a scintillation vial in a glovebox. $AgPF_6$ (121.3 mg, 0.4801 mmol) was dissolved in minimal MeCN and then added to a stirred solution of the bromide precursor. The reaction mixture was stirred for 1 hour before being filtered through celite and concentrated under vacuum. The resulting solid was triturated with Et_2O to yield receptor **2** in quantitative yield, 0.133 g. ^{1}H NMR (500 MHz, Acetonitrile-d_3) δ: 8.41 (t, J = 1.8 Hz, 1H), 7.33 (dt, J = 9.1, 1.9 Hz, 2H), 7.26 (m, 4H), 5.25 (s, 2H), 2.35 (s, 3H). ^{13}C{^{1}H} NMR (126 MHz, Acetonitrile-d_3) δ 140.4, 136.9, 131.7, 130.8, 129.6, 125.0, 123.2, 53.6, 36.9, 21.1.^{19}F NMR (471 MHz, Acetonitrile-d_3) δ: -73.0 (d, J = 706 Hz).^{31}P{^{1}H} NMR (202 MHz, Acetonitrile-d_3) δ: -144.6 (hept, J = 706.3 Hz).

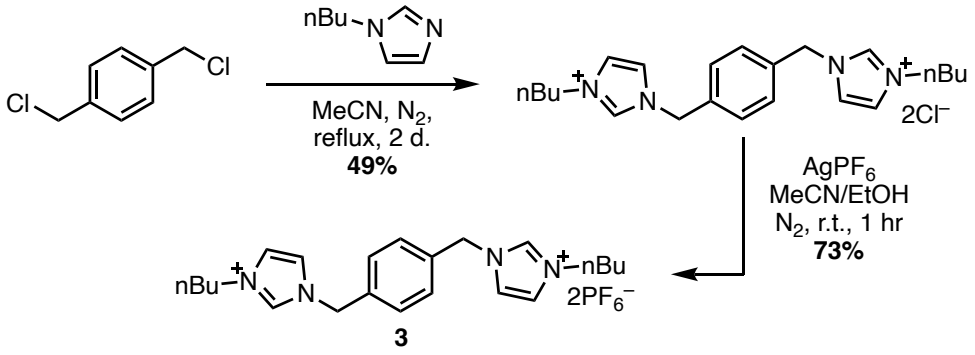

3

Scheme C3. Synthetic scheme for receptor $\mathbf{3}^{2+}$.

Synthesis of receptor $\mathbf{3}^{2+}$: 1,4-bis(Chloromethyl)benzene (0.2508 mg, 1.428 mmol) was dissolved in anhydrous MeCN (25 mL) in a round bottom flask, after which 1-butylimidazole (0.4 mL, 3 mmol) was added slowly. A reflux condenser was attached and the reaction mixture was refluxed for 3 days under an Ar balloon. The reaction mixture was then cooled to room temperature and then further in an ice bath to precipitate the chloride precursor product, 0.2951 g, 49% yield. ^{1}H NMR (500 MHz, DMSO-d_6) δ: 9.40 (t, J = 1.6 Hz, 2H), 7.79 (d, J = 1.6 Hz, 4H), 7.47 (s, 4H), 5.43 (s, 4H), 4.16 (t, J = 7.2 Hz, 4H), 1.76 (p, J = 7.5 Hz, 4H), 1.23 (h, J = 7.5 Hz, 4H), 0.88 (t, J = 7.4 Hz, 6H).

The chloride precursor (108.8 mg, 0.2123 mmol) was dissolved in a MeCN/EtOH solution in a scintillation vial and $AgPF_6$ (110 mg, 0.435 mmol) added to the solution. The reaction solution was stirred for 1 hr. The resulting suspension was filtered over celite, and the filtrate concentrated under vacuum. The resultant solid was extracted into acetone and concentrated to yield a white powder, 73.1 mg, 58% yield. ^{1}H NMR (500 MHz, Acetonitrile-d_3) δ: 8.59 (s, 2H), 7.42 (s, 4H), 7.40 (t, J = 1.9 Hz, 2H), 7.36 (t, J = 1.9 Hz, 2H), 5.33 (s, 4H), 4.13 (t, J = 7.3 Hz, 4H), 1.81 (p, J = 7.4 Hz, 4H), 1.33 (h, J = 7.4 Hz, 4H), 0.94 (t, J = 7.4 Hz, 6H). ^{13}C{^{1}H} NMR (126 MHz, Acetonitrile-d_3) δ: 136.6, 135.8, 130.3, 123.9, 123.4, 53.2, 50.5, 32.4, 12.0, 13.6. ^{19}F NMR (471 MHz, Acetonitrile-d_3) δ: -72.9 (d, J = 707 Hz). ^{31}P{^{1}H} NMR (202 MHz, Acetonitrile-d_3) δ: -144.6 (hept, J = 706 Hz). The NMR data matches previously reported data.[258]

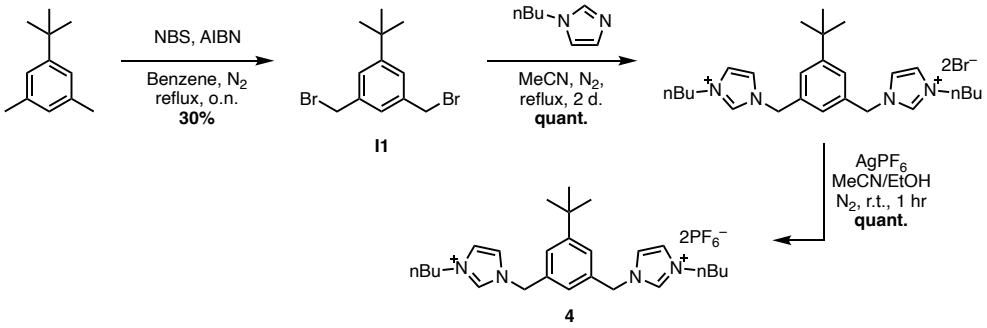

Scheme C4. Synthetic scheme for receptor $\mathbf{4^{2+}}$.

Synthesis of **I1**: Intermediate **1** (**I1**) was synthesized according to published procedure.[253] A 250 mL 3-neck round bottom flask was evacuated and refilled with N_2 3x. Under a positive flow of N_2, *N*-bromosuccinimide (5.864 g, 32.17 mmol) and 5-tert-butyl-m-xylene (3.0 mL, 16.1 mmol) was added to the 3-neck flask. Sparged benzene was cannula transferred to the 3-neck flask and the reaction mixture was brought to reflux. Azobisisobutyronitrile (AIBN, 0.0263 g, 0.1608 mmol) was added to a separate 25 mL round bottom flask and dissolved in additional sparged benzene. The AIBN solution was cannula transferred into the hot, stirring reaction mixture in the 3-neck round bottom flask before letting stir at reflux overnight under low flow of N_2. The reaction mixture was then concentrated under vacuum and the resulting solid was purified by column chromatography. The product was isolated via column chromatography (0-5% EtOAc/hexanes) to afford a white solid, 1.5952 g, 30% yield. ^{1}H NMR (500 MHz, DMSO-d_6) δ: 7.42 (d, J = 1.6 Hz, 2H), 7.34 (t, J = 1.8 Hz, 1H), 4.69 (s, 4H), 1.28 (s, 9H). The NMR data matches previously reported data.[253]

Synthesis of receptor $\mathbf{4^{2+}}$: Under a positive flow of N_2, **I1** (0.2508 g, 0.7811 mmol) was dissolved in anhydrous MeCN (50 mL) in a round bottom flask and 1-Butylimidazole (225 μL, 1.72 mmol) was added to stirring solution via an N_2 purged syringe. The reaction mixture was then refluxed for 2 days under N_2. The reaction mixture was concentrated under vacuum and the resulting solid was washed with Et_2O (3 x 20 mL) to yield pure bromide precursor in quantitative yield, 0.444 g. ^{1}H NMR (500 MHz, DMSO-d_6) δ: 9.40 (t, J = 1.6 Hz, 2H), 7.83 (d, J = 1.7 Hz, 4H), 7.45 (d, J = 1.6 Hz, 2H), 7.31 (t, J = 1.6 Hz, 1H), 5.42 (s, 4H), 4.20 (t, J = 7.1 Hz, 4H), 1.78 (p, J = 7.5 Hz, 4H), 1.26 (s, 9H), 1.24 (sxt, J = 7.6 Hz, 4H), 0.89 (t, J = 7.4 Hz, 6H).

In a drybox, the bromide precursor (104.1 mg, 0.1831 mmol) was dissolved in a 1:1 MeCN/EtOH mixture (20 mL) in a scintillation vial. $AgPF_6$ (97.9 mg, 0.387 mmol) was dissolved in minimal MeCN and then added to the stirring bromide precursor solution. The

reaction mixture was stirred for 1 hour before being filtered through celite and concentrated under vacuum. The resulting solid was triturated with Et_2O to yield receptor **4** in quantitative yield, 123 mg. ^{1}H NMR (500 MHz, Acetonitrile-d_3) δ: 8.48 (t, J = 1.4 Hz, 2H), 7.46 (d, J = 1.7 Hz, 2H), 7.40 (t, J = 1.9 Hz, 2H), 7.34 (t, J = 1.9 Hz, 2H), 7.16 (t, J = 1.9 Hz, 1H), 5.28 (s, 4H), 4.13 (t, J = 7.3 Hz, 4H), 1.81 (p, J = 7.4 Hz, 4H), 1.31 (h, J = 7.5 Hz, 4H), 1.30 (s, 9H), 0.94 (t, J = 7.4 Hz, 6H). ^{13}C{^{1}H} NMR (126 MHz, Acetonitrile-d_3) δ: 154.7, 136.4, 135.5, 127.6, 127.0, 123.8, 123.4, 53.6, 50.5, 35.6, 32.4, 31.3, 20.0, 13.6. ^{19}F NMR (471 MHz, Acetonitrile-d_3) δ: -72.9 (d, J = 707 Hz). ^{31}P{^{1}H} NMR (202 MHz, Acetonitrile-d_3) δ: -144.6 (hept, J = 706 Hz). TOF MS (ES$^+$, *m/z*): exact mass calc. for [**4**·PF_6]$^+$, $C_{26}H_{40}N_4PF_6$, 553.2889; found, 553.2889

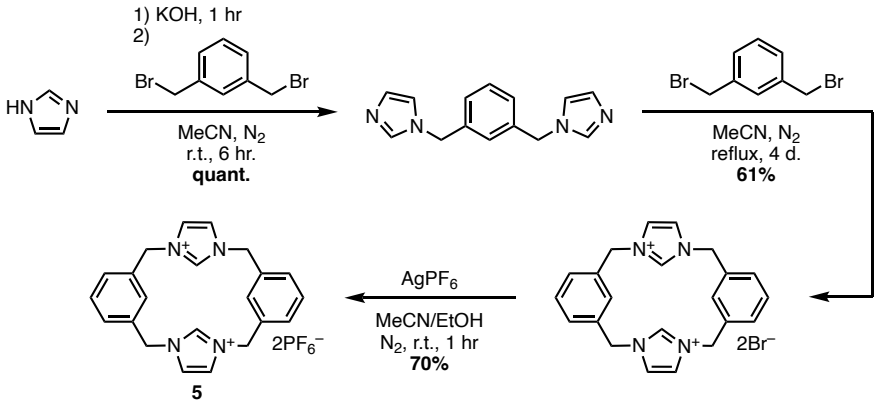

Scheme C5. Synthetic scheme for receptor $\mathbf{5}^{2+}$.

Synthesis of H-Protophane: The protophane was synthesized according to published procedure.[210] Imidazole (0.5164 g, 7.578 mmol) was dissolved in anhydrous MeCN (50 mL) in a round bottom flask, and KOH pellets (~1 g, ~20 mmol) were ground in a mortar and pestle and added to the flask. The resultant reaction mixture was stirred at room temperature under an Ar balloon for 1 hr, after which 1,3-bis(bromomethy)benzene (1.0048 g, 3.788 mmol) was dissolved in MeCN (5 mL) and added dropwise via N_2 purged syringe. The reaction mixture was stirred for an additional 6 hours at room temperature. The resulting insoluble salts formed over the course of the reaction were removed by filtration, and the resultant filtrate was concentrated under vacuum. The crude solid was extracted into CH_2Cl_2 (50 mL), washed with DI H_2O (3 x 50 mL), dried over Na_2SO_4, filtered, and concentrated under vacuum to yield a white solid in quantitative yield, 0.9038 g. ^{1}H NMR (500 MHz, DMSO-d_6) δ: 7.73 (t, J = 1.2 Hz, 2H), 7.33 (t, J = 7.6 Hz, 1H), 7.21 (t, J = 1.9 Hz, 1H), 7.15 (m, 4H), 6.89 (t, J = 1.2, 2H), 5.16 (s, 4H). The NMR data matches previously reported data.[210]

Synthesis of receptor $\mathbf{5}^{2+}$: The macrocycle was synthesized according to published procedure.[210] The H-protophane (276 mg, 1.16 mmol) was dissolved in anhydrous MeCN (500 mL) in a round bottom flask. 1, 3-bis(Bromomethyl) benzene (305.9 mg, 1.159 mmol) was dissolved in a small amount of MeCN and then added dropwise to the stirred reaction mixture via a N_2 purged syringe. The reaction mixture was then refluxed and stirred for 4 days under N_2. The reaction mixture was then concentrated under vacuum yielding a beige solid, which was then triturated with acetone (3 x 20 mL) to afford the bromide macrocycle, 489.9 mg, 84% yield. ^{1}H NMR (500 MHz, DMSO-d_6) δ: 9.32 (t, J = 1.5 2H), 7.83 (d, J = 1.5 Hz, 4H), 7.58 (m, 4H), 7.52 (m, 2H), 7.01 (t, J = 1.8, 2H), 5.44 (s, 8H). The NMR data matches previously reported data.[210]

In a drybox, the bromide precursor (489.9 mg, 0.9745 mmol) was dissolved in a 1:1 MeCN/EtOH mixture (20 mL) in a scintillation vial. $AgPF_6$ (532.9 mg, 2.108 mmol) was dissolved in minimal MeCN before being added to the stirring bromide precursor solution. The reaction mixture was stirred for 1 hour before being filtered through celite and concentrated under vacuum. The resulting solid was triturated with acetone (3 x 10 mL) to yield receptor **5**, 429.9 mg, 70% yield. ^{1}H NMR (500 MHz, Acetonitrile-d_3) δ: 8.37 (t, J = 1.7 Hz, 2H), 7.54 (d, J = 1.3 Hz, 6H), 7.43 (d, J = 1.6 Hz, 4H), 6.75 (s, 2H), 5.31 (s, 8H). ^{13}C{^{1}H} NMR (126 MHz, Acetonitrile-d_3) δ: 136.5, 136.5, 130.9, 130.5, 126.9, 124.3, 53.5.^{19}F NMR (471 MHz, Acetonitrile-d_3) δ: -72.8 (d, J = 707 Hz).^{31}P{^{1}H} NMR (202 MHz, Acetonitrile-d_3) δ: -144.6 (hept, J = 706 Hz). The NMR data matches previously reported data.[210]

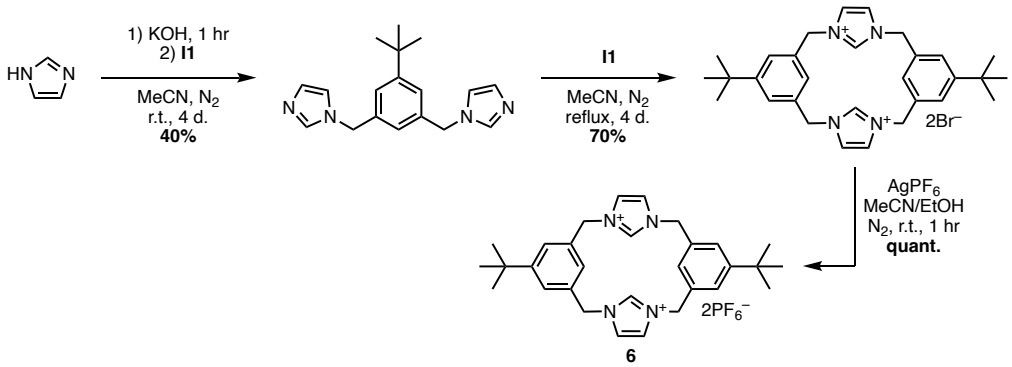

Scheme C6. Synthetic scheme for receptor $\mathbf{6}^{2+}$.

Synthesis of tBu-protophane: The protophane was synthesized according to published procedure.[210] Imidazole (0.3826 g, 5.720 mmol) was dissolved in anhydrous MeCN (80 mL) in a

round bottom flask. KOH pellets (0.44 g, 7.4 mmol) were ground in a mortar and pestle and added to the flask. The reaction mixture was stirred for 1 hour under an Ar balloon. **I1** (0.9152 g, 2.859 mmol) was dissolved in anhydrous MeCN (20 mL) and then slowly added to the reaction mixture via N_2 purged syringe. The reaction mixture was stirred at room temperature for 4 days under an Ar balloon. The solution was then filtered and concentrated under vacuum. The resulting oil was diluted with CH_2Cl_2 (20 mL) and then washed with DI H_2O (3 x 20 mL). The organic layer was dried with Na_2SO_4, filtered, and concentrated under vacuum. The oil was then purified via column chromatography (0–10% MeOH/EtOAc) to yield the product as a viscous yellow oil, 0.5459 g, 65% yield. ^{1}H NMR (500 MHz, DMSO-d_6) δ: 7.71 (t, J = 1.5, 2H), 7.22 (d, J = 1.5 Hz, 2H), 7.15 (t, J = 1.7 Hz, 2H), 6.95 (t, J = 1.7 Hz, 1H), 6.89 (d, J = 1.5 Hz, 2H), 5.14 (s, 4H), 1.22 (s, 9H). The NMR data matches previously reported data.[210]

Synthesis of receptor $\mathbf{6}^{2+}$: The macrocycle was synthesized according to published procedure.[210] tBu-protophane (545.9 mg, 1.854 mmol) was dissolved in anhydrous MeCN (400 mL) in a round bottom flask. **I1** (645.4 mg, 2.016 mmol) was dissolved in anhydrous MeCN (100 mL) and then added dropwise to the protophane solution via N_2 purged syringe. The reaction mixture was refluxed for 4 days under an Ar balloon. The solution was then concentrated under vacuum and the resulting solid was triturated with acetone (3 x 10 mL) to yield an off-white solid, 988.2 mg, 87% yield. ^{1}H NMR (500 MHz, DMSO-d_6) δ: 9.34 (t, J = 1.6 Hz, 2H), 7.82 (d, J = 1.6 Hz, 4H), 7.61 (d, J = 1.6 Hz, 4H), 6.68 (t, J = 1.6 Hz, 2H), 5.44 (s, 8H), 1.33 (s, 18H). NMR data matches previously reported. The NMR data matches previously reported data.[210]

In a drybox, the bromide precursor (499.8 mg, 0.8134 mmol) was dissolved in a 1:1 MeCN/EtOH mixture (50 mL) in a round bottom flask. $AgPF_6$ (457.6 mg, 1.810 mmol) was dissolved in minimal MeCN and then added to bromide precursor solution. The reaction mixture was stirred for 1 hour before being filtered through celite and concentrated under vacuum. The resulting solid was triturated with acetone to afford receptor **6**, 550.7 mg, 91% yield. ^{1}H NMR (500 MHz, Acetonitrile-d_3) δ: 8.32 (t, J = 1.7 Hz, 2H), 7.58 (d, J = 1.6 Hz, 4H), 7.43 (d, J = 1.7 Hz, 4H), 6.49 (s, 2H), 5.30 (s, 8H), 1.36 (s, 18H). ^{13}C{^{1}H} NMR (126 MHz, Acetonitrile-d_3) δ: 154.4, 136.3, 136.3, 127.5, 124.4, 123.4, 53.8, 35.7, 31.3. ^{19}F NMR (471 MHz, Acetonitrile-d_3) δ: -72.9 (d, J = 707 Hz).^{31}P{^{1}H} NMR (202 MHz, Acetonitrile-d_3) δ: -144.6, (hept, J = 707 Hz). The NMR data matches previously reported data.[210]

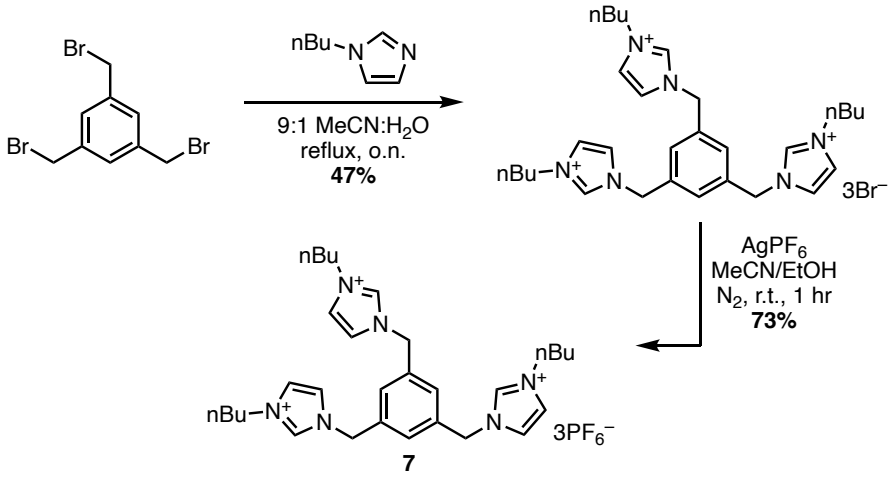

Scheme C7. Synthetic scheme for receptor $\mathbf{7}^{3+}$.

Synthesis of receptor $\mathbf{7}^{3+}$: 1,3,5-tris(Bromomethyl)benzene (254.5 mg, 0.7005 mmol) was dissolved in a 9:1 MeCN/H_2O solution (50 mL) in a round bottom flask, under N_2. 1-Butylimidazole (0.31 mL, 2.311 mmol) was added to the stirring solution via a N_2 purged syringe. The reaction mixture was refluxed overnight under N_2. The reaction mixture was then concentrated under vacuum and the resulting solid was triturated with acetone (3 x 10 mL) to yield pure precursor, 241.6 mg, 47% yield. ^{1}H NMR (500 MHz, DMSO-d_6) δ: 9.49 (t, J = 1.7 3H), 7.84 (t, J = 1.9 Hz, 6H), 7.57 (s, 3H), 5.47 (s, 6H), 4.21 (t, J = 7.3 Hz, 6H), 1.79 (p, J = 7.5 6H), 1.27 (h, J = 7.5, 6H), 0.90 (t, J = 7.4, 9H).

In a drybox, the bromide precursor (208 mg, 0.285 mmol) was dissolved in a 1:1 MeCN/EtOH solution (20 mL) in a scintillation vial. $AgPF_6$ (237.1 mg, 0.9410 mmol) was dissolved in minimal MeCN and then added to the bromide precursor solution. The reaction mixture was allowed to stir for 1 hour before being filtered through celite and concentrated under vacuum. The resulting solid was triturated with acetone to yield receptor **7**, 192.5 mg, 73% yield. ^{1}H NMR (500 MHz, Acetonitrile-d_3) δ: 8.46 (t, J = 1.8 Hz, 3H), 7.42 (t, J = 1.9 Hz, 3H), 7.35 (s, 3H), 7.32 (t, J = 1.9 Hz, 3H), 5.30 (s, 6H), 4.14 (t, J = 7.4 Hz, 6H), 1.82 (p, J = 7.5 Hz, 6H), 1.34 (h, J = 7.4 Hz, 6H), 0.95 (t, J = 7.4 Hz, 9H). ^{13}C{^{1}H} NMR (126 MHz, Acetonitrile-d_3) δ: 136.7, 136.5, 130.5, 123.9, 123.5, 53.0, 50.5, 32.5, 20.0, 13.6. ^{19}F NMR (471 MHz, Acetonitrile-d_3) δ: -72.7 (d, J = 707 Hz). ^{31}P{^{1}H} NMR (202 MHz, Acetonitrile-d_3) δ: -144.6 (hept, J = 708 Hz). TOF MS (ES$^+$, *m/z*): exact mass calc. for $[\mathbf{7}\cdot 2PF_6]^+$, $C_{30}H_{45}N_6P_2F_{12}$, 779.2989; found, 779.2957.

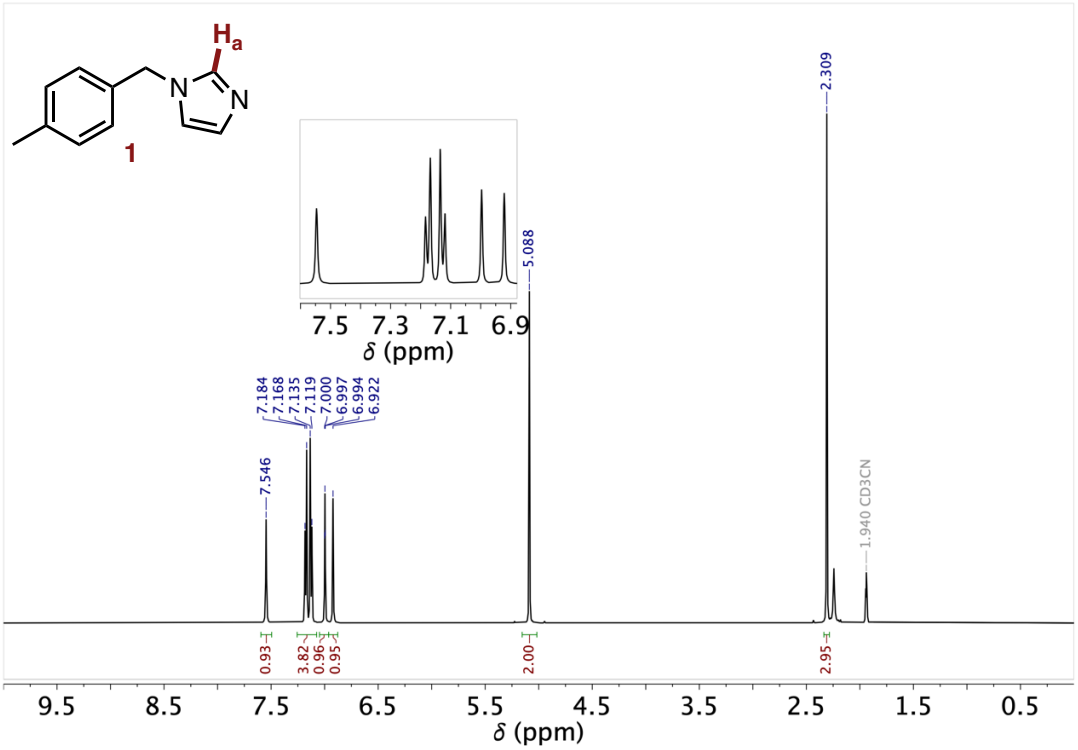

Figure C1. ^{1}H NMR spectrum (500 MHz, CD_3CN) of receptor **1**.

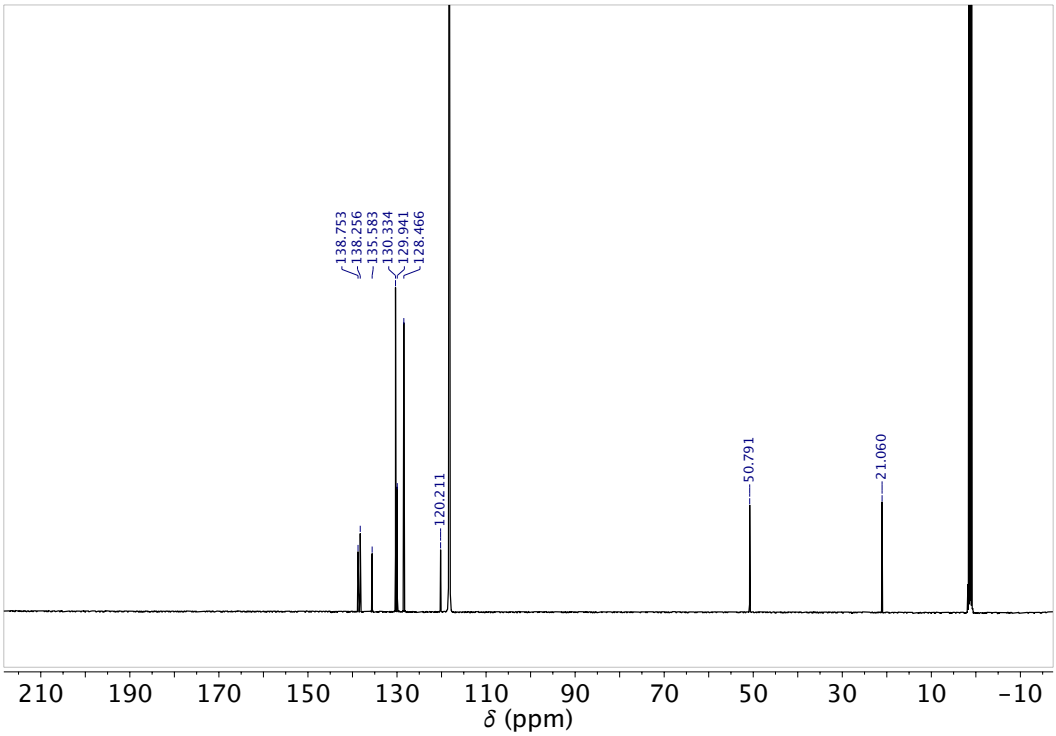

Figure C2. $^{13}C\{^{1}H\}$ NMR spectrum (126 MHz, CD_3CN) of receptor **1**.

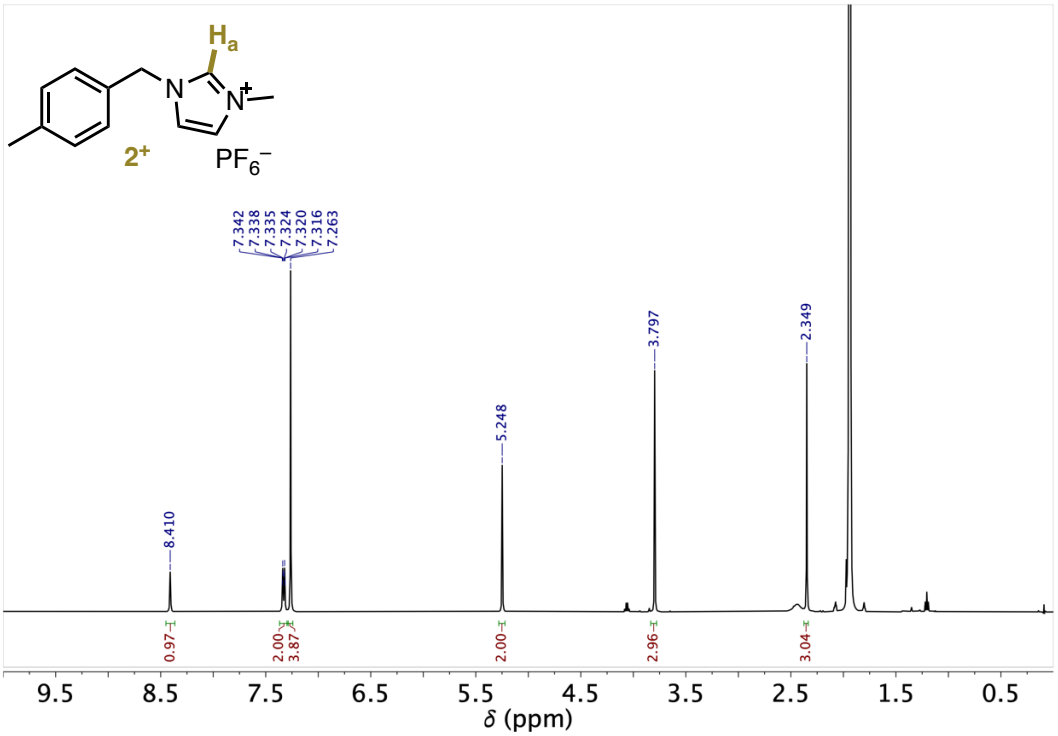

Figure C3. ^{1}H NMR spectrum (500 MHz, CD_3CN) of receptor $\mathbf{2}^{+}$.

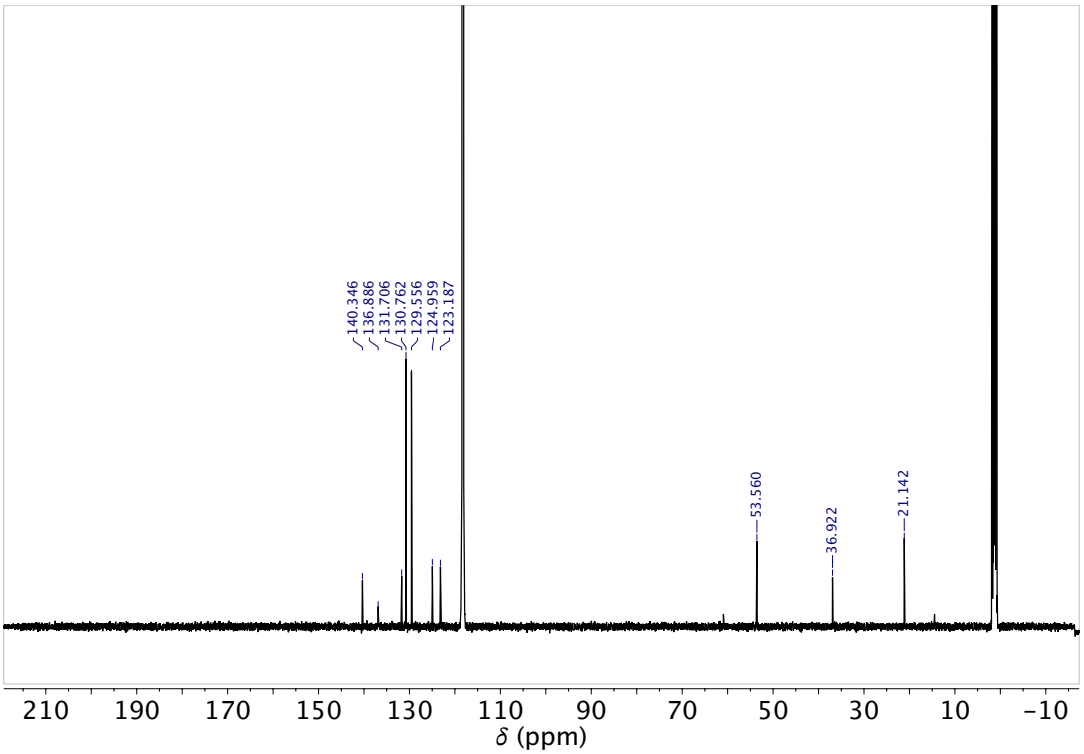

Figure C4: $^{13}C\{^{1}H\}$ NMR spectrum (126 MHz, CD_3CN) of receptor $\mathbf{2}^{+}$.

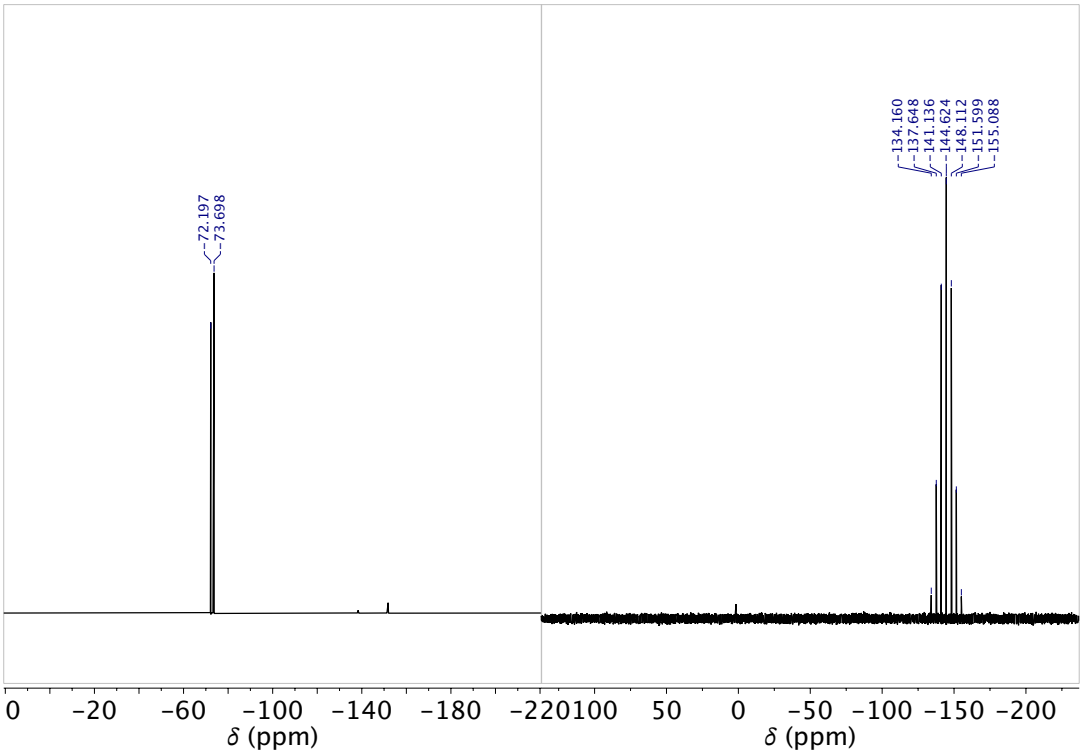

Figure C5. $^{19}F\{^{1}H\}$ NMR spectrum (471 MHz, CD_3CN) and $^{31}P\{^{1}H\}$ NMR spectrum (202 MHz, CD_3CN) of receptor $\mathbf{2}^{+}$.

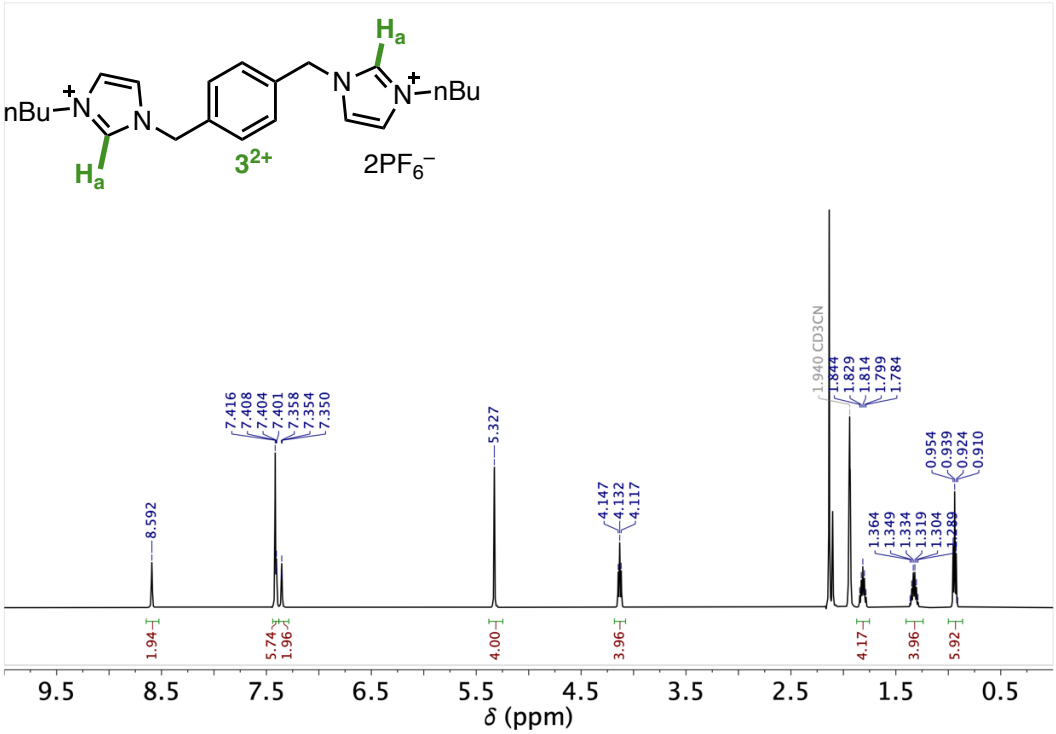

Figure C6. ^{1}H NMR spectrum (500 MHz, CD_3CN) of receptor $\mathbf{3}^{2+}$.

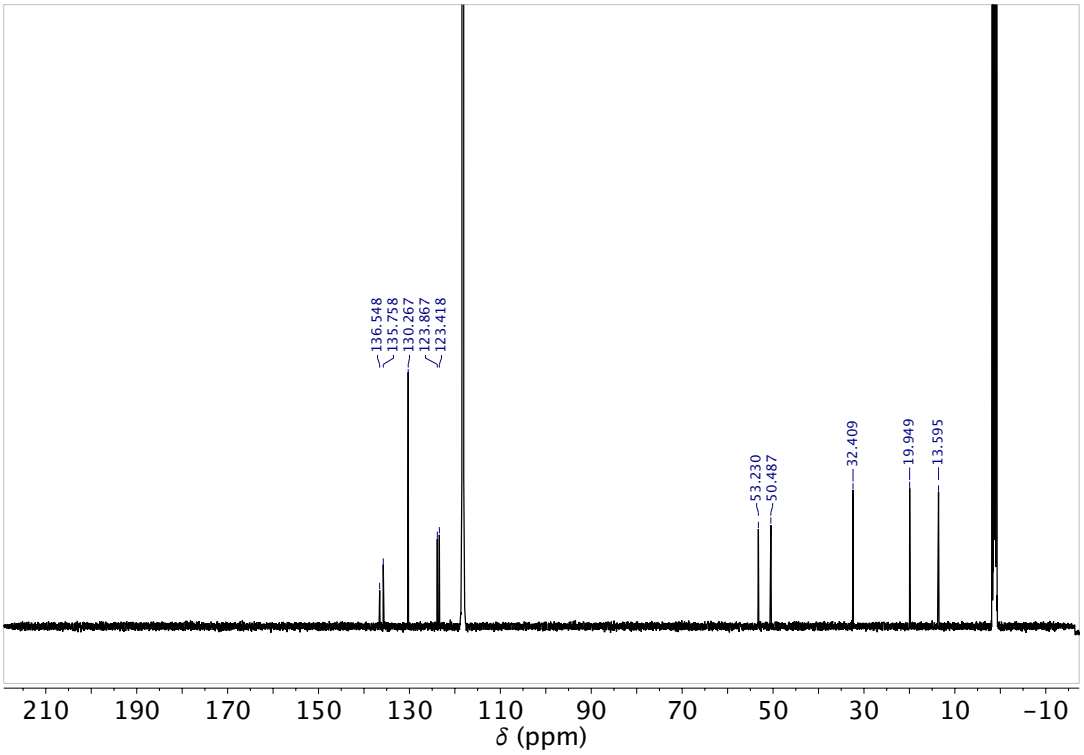

Figure C7. $^{13}C\{^{1}H\}$ NMR spectrum (126 MHz, CD_3CN) of receptor $\mathbf{3}^{2+}$.

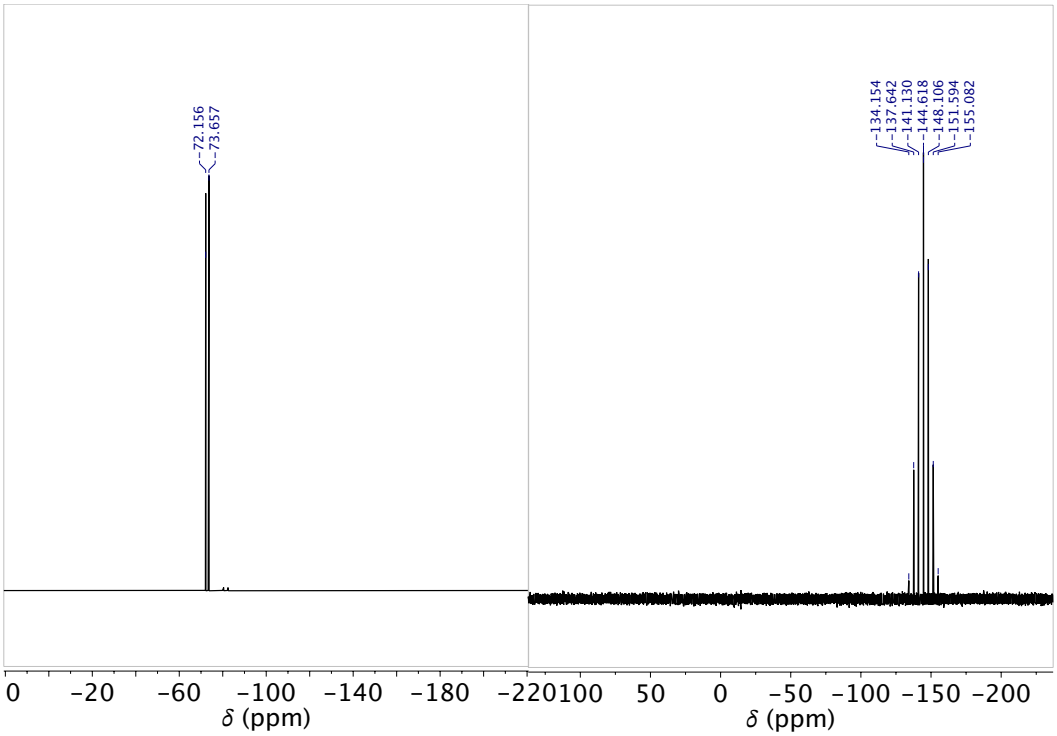

Figure C8. $^{19}F\{^{1}H\}$ NMR spectrum (471 MHz, CD_3CN) and $^{31}P\{^{1}H\}$ NMR spectrum (202 MHz, CD_3CN) of receptor $\mathbf{3}^{2+}$.

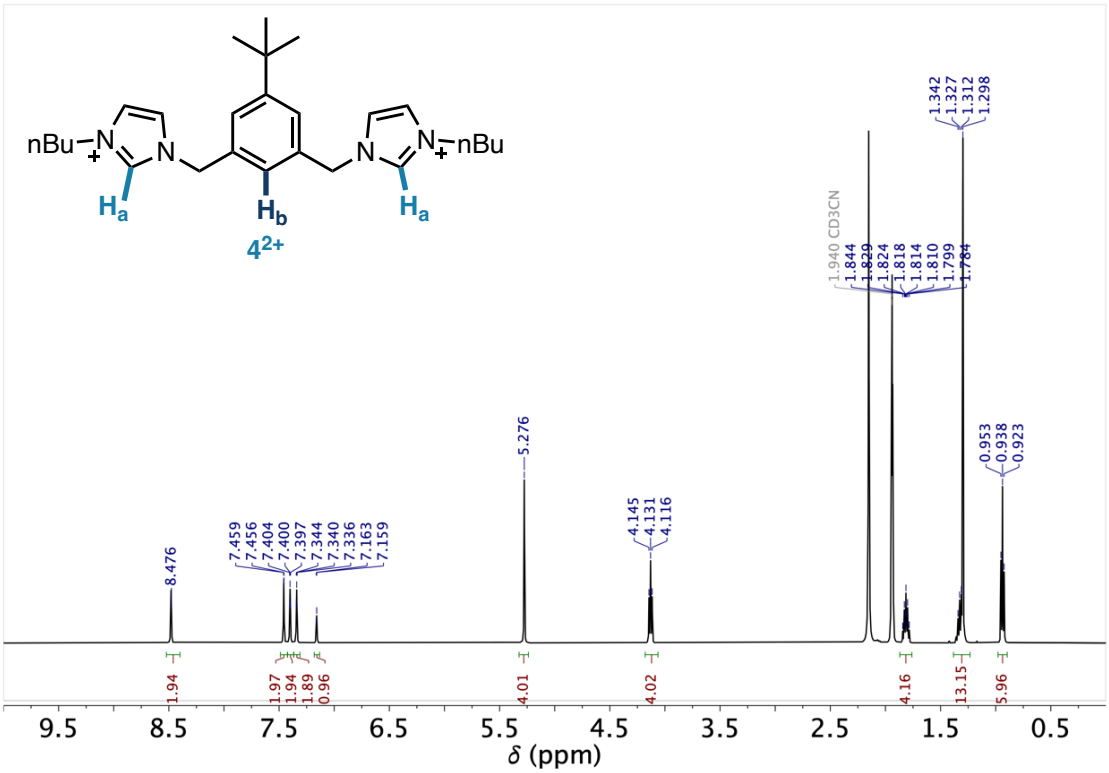

Figure C9. ^{1}H NMR spectrum of receptor $\mathbf{4}^{2+}$ in CD_3CN.

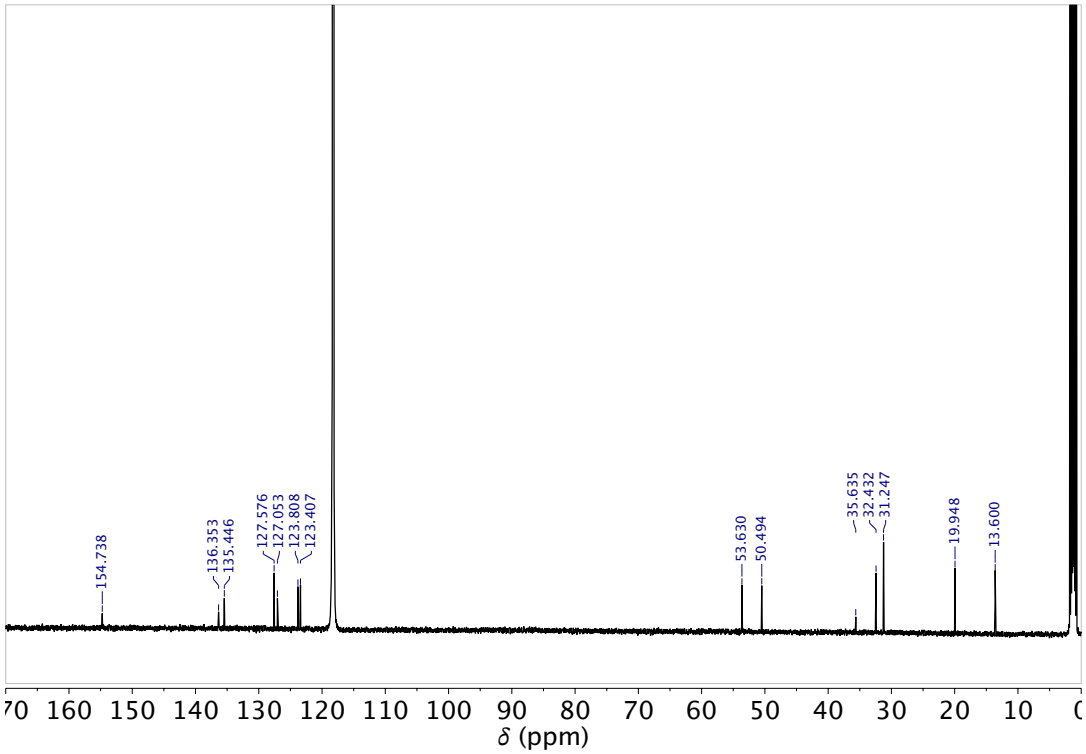

Figure C10. $^{13}C\{^{1}H\}$ NMR spectrum (126 MHz, CD_3CN) of receptor $\mathbf{4}^{2+}$.

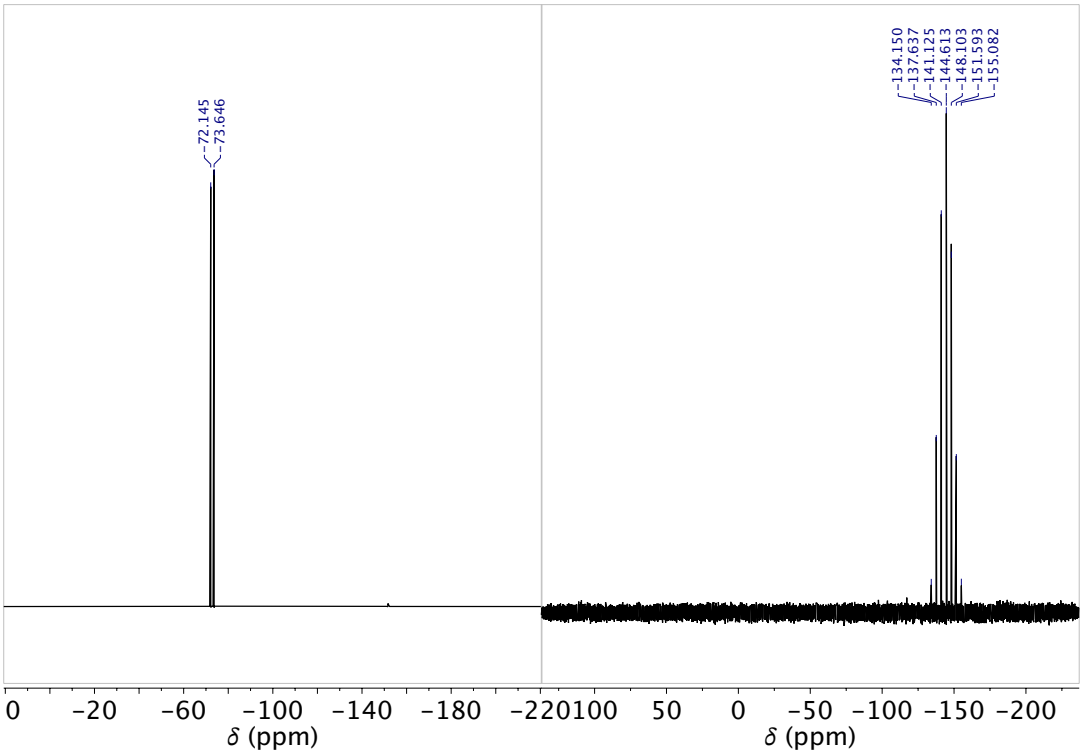

Figure C11. $^{19}F\{^{1}H\}$ NMR spectrum (471 MHz, CD_3CN) and $^{31}P\{^{1}H\}$ NMR spectrum (202 MHz, CD_3CN) of receptor $\mathbf{4}^{2+}$.

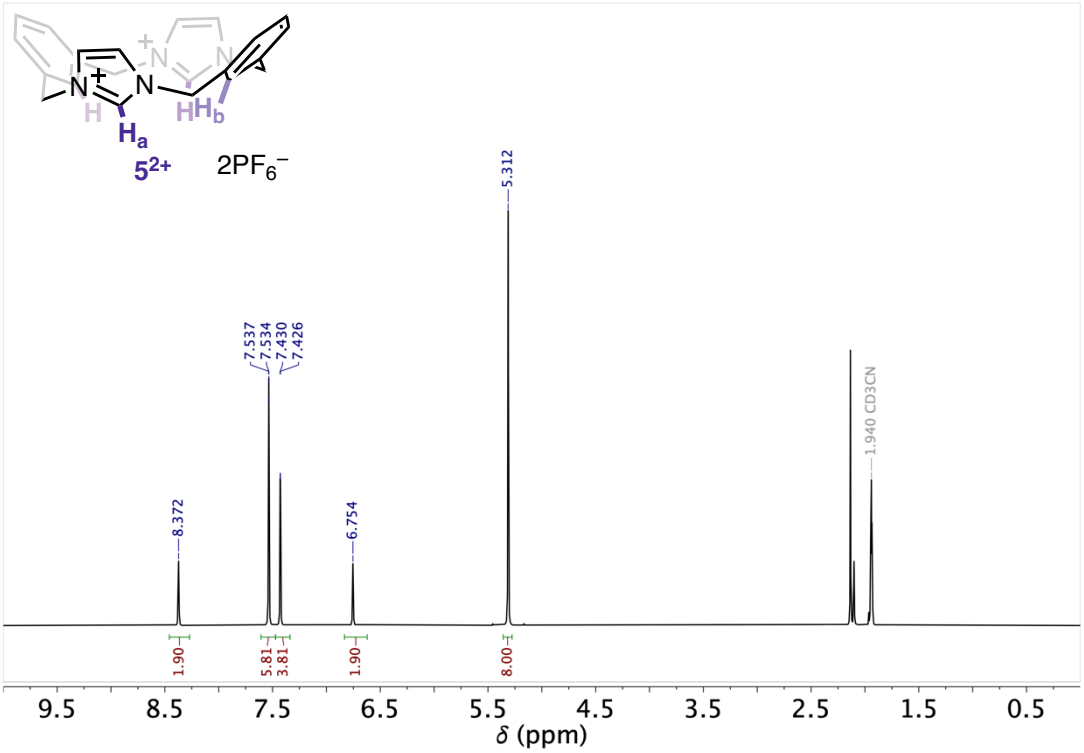

Figure C12. ^{1}H NMR spectrum of receptor $\mathbf{5}^{2+}$ in CD_3CN.

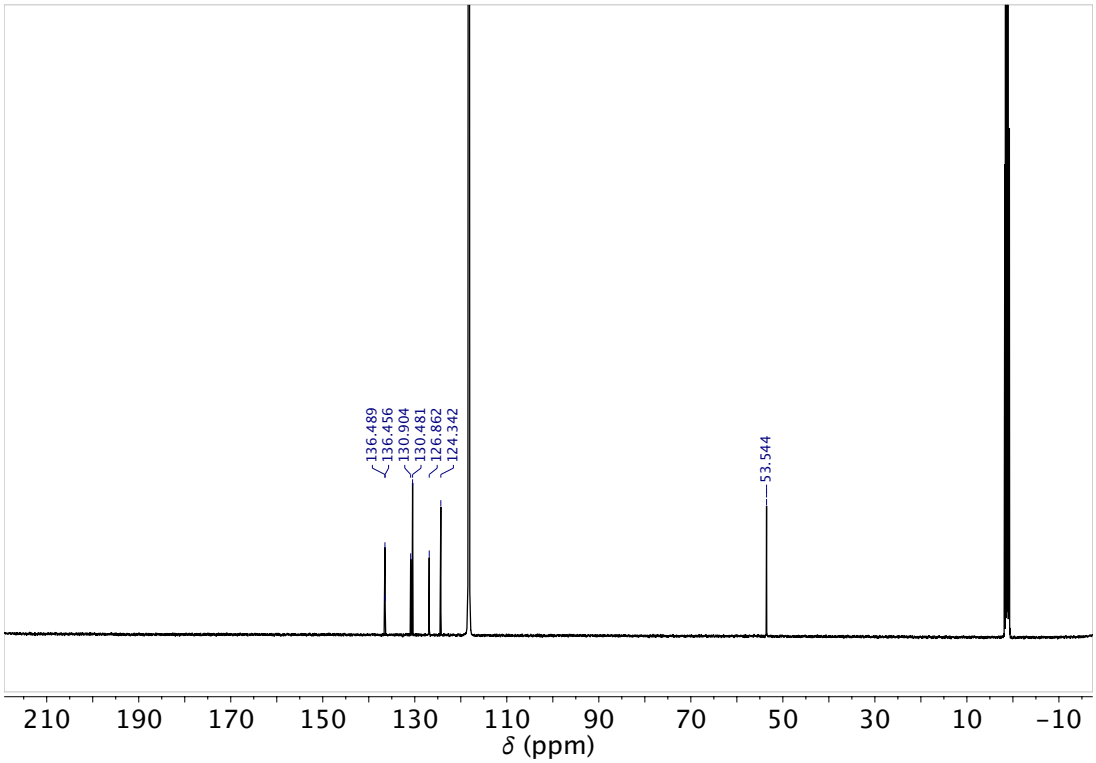

Figure C13. $^{13}C\{^{1}H\}$ NMR spectrum (126 MHz, CD_3CN) of receptor $\mathbf{5}^{2+}$.

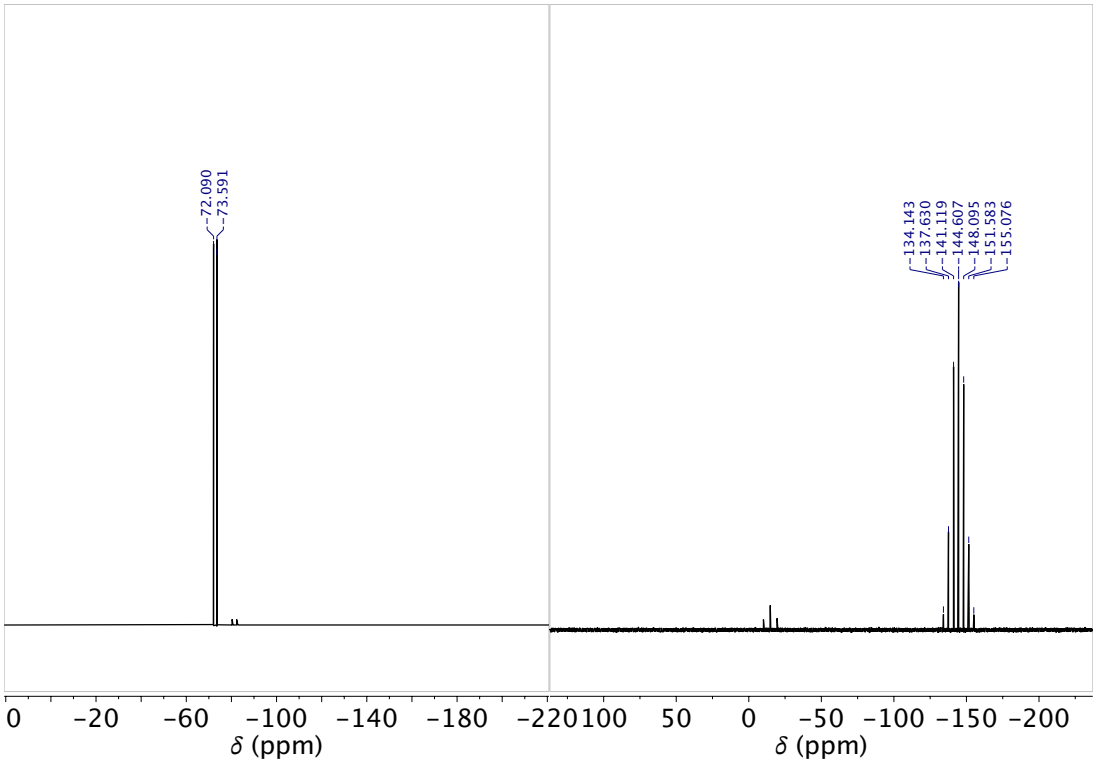

Figure C14. $^{19}F\{^{1}H\}$ NMR spectrum (471 MHz, CD_3CN) and $^{31}P\{^{1}H\}$ NMR spectrum (202 MHz, CD_3CN) of receptor $\mathbf{5}^{2+}$.

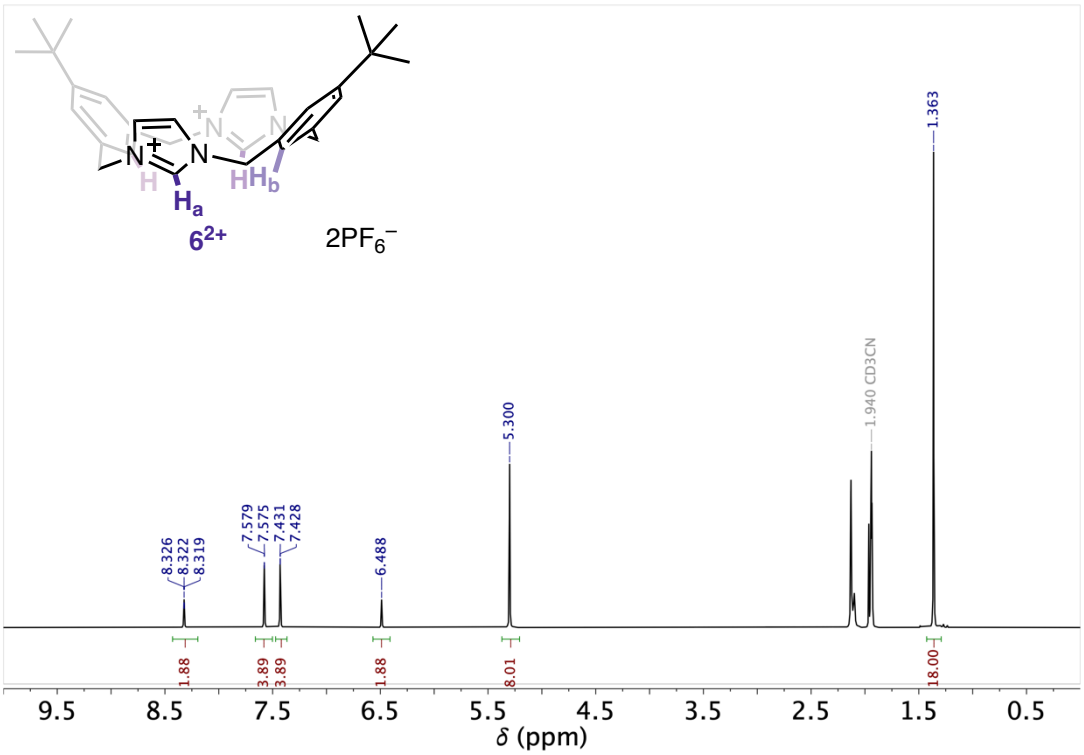

Figure C15. ^{1}H NMR spectrum of receptor $\mathbf{6}^{2+}$ in CD_3CN.

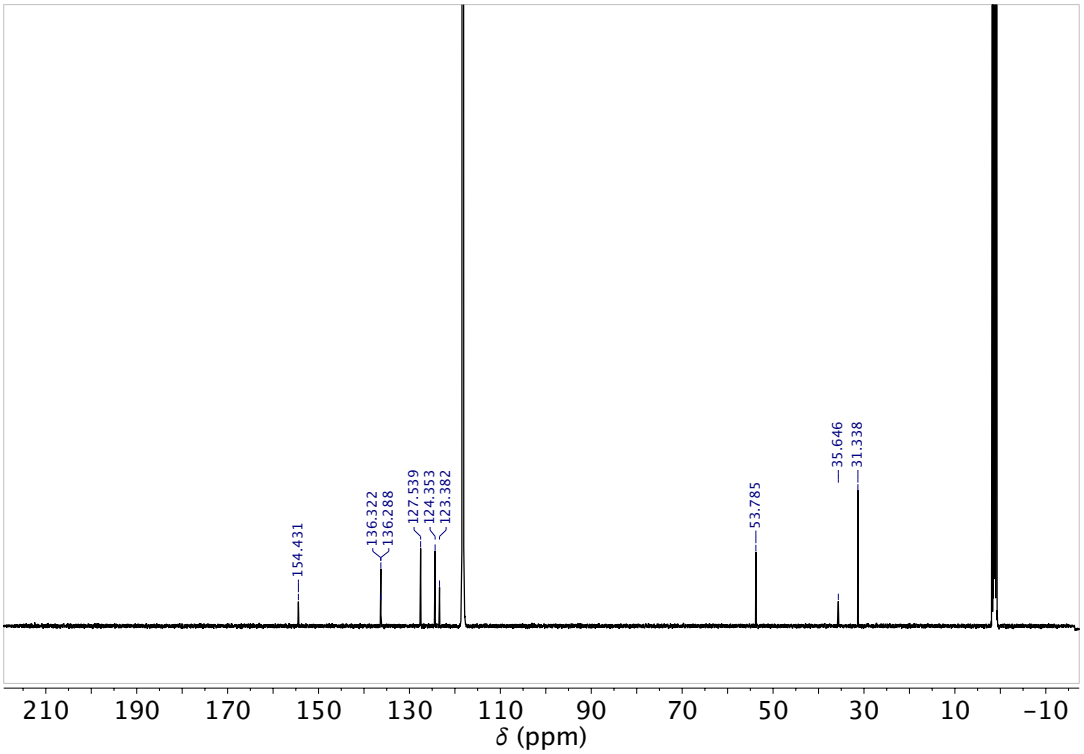

Figure C16. $^{13}C\{^{1}H\}$ NMR spectrum (126 MHz, CD_3CN) of receptor $\mathbf{6}^{2+}$.

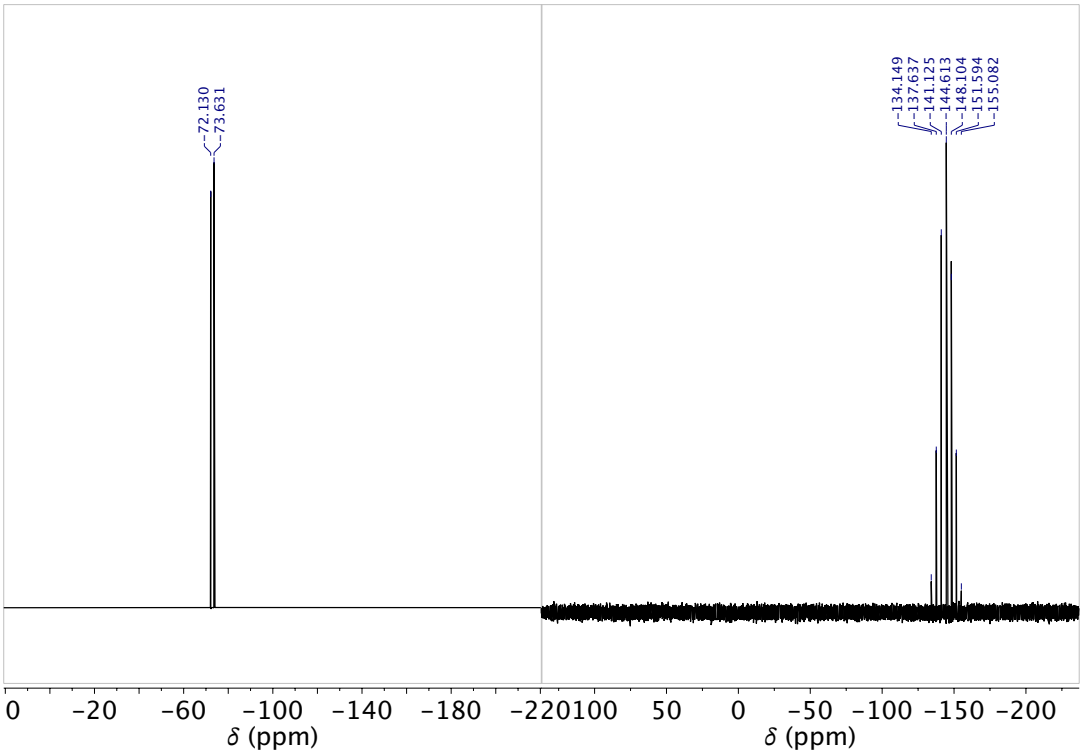

Figure C17. $^{19}F\{^{1}H\}$ NMR spectrum (471 MHz, CD_3CN) and $^{31}P\{^{1}H\}$ NMR spectrum (202 MHz, CD_3CN) of receptor $\mathbf{6}^{2+}$.

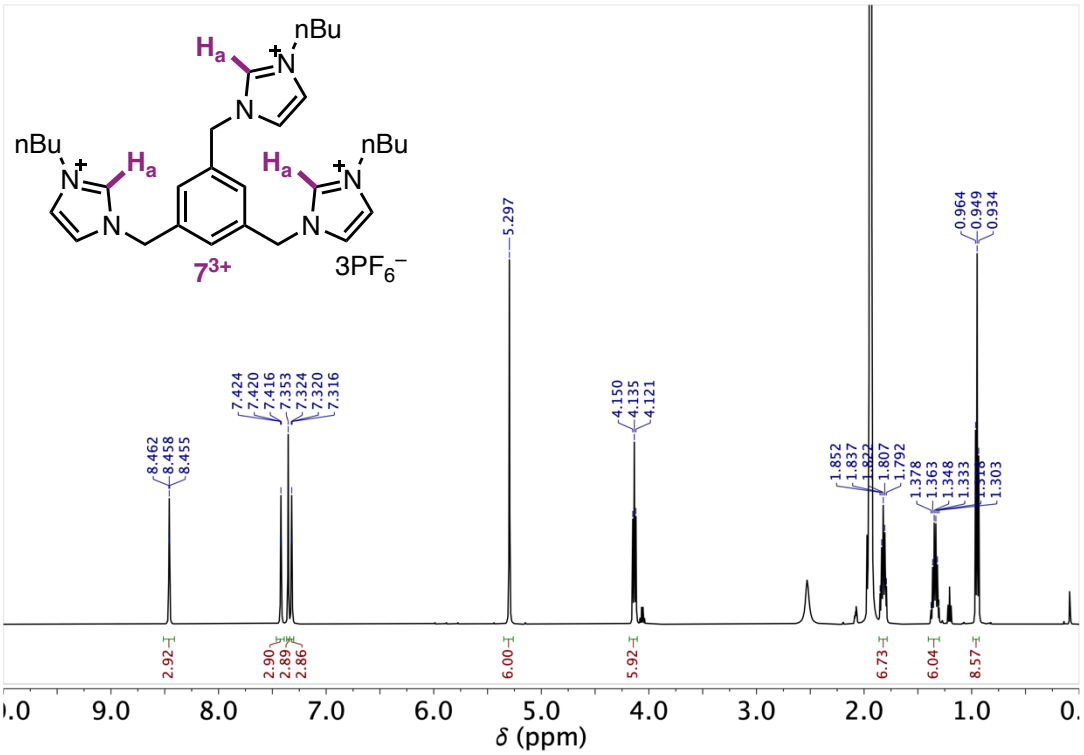

Figure C18. ^{1}H NMR spectrum of receptor $\mathbf{7}^{3+}$ in CD_3CN.

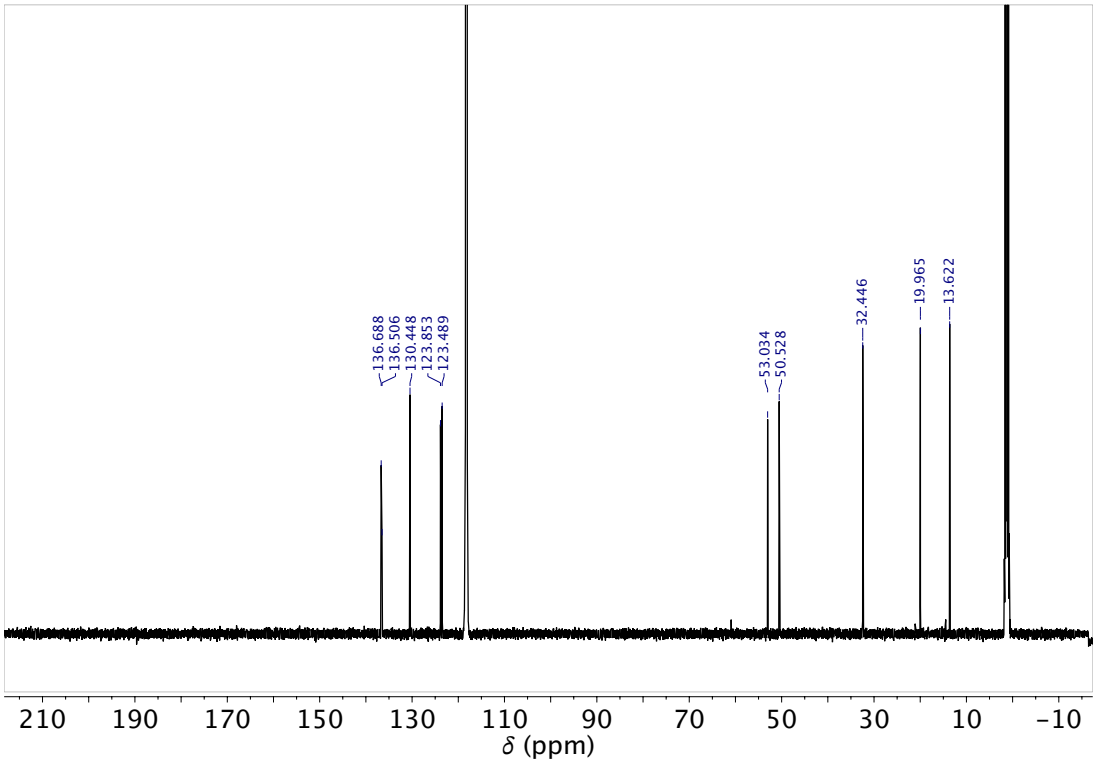

Figure C19. $^{13}C\{^{1}H\}$ NMR spectrum (126 MHz, CD_3CN) of receptor $\mathbf{7^{3+}}$.

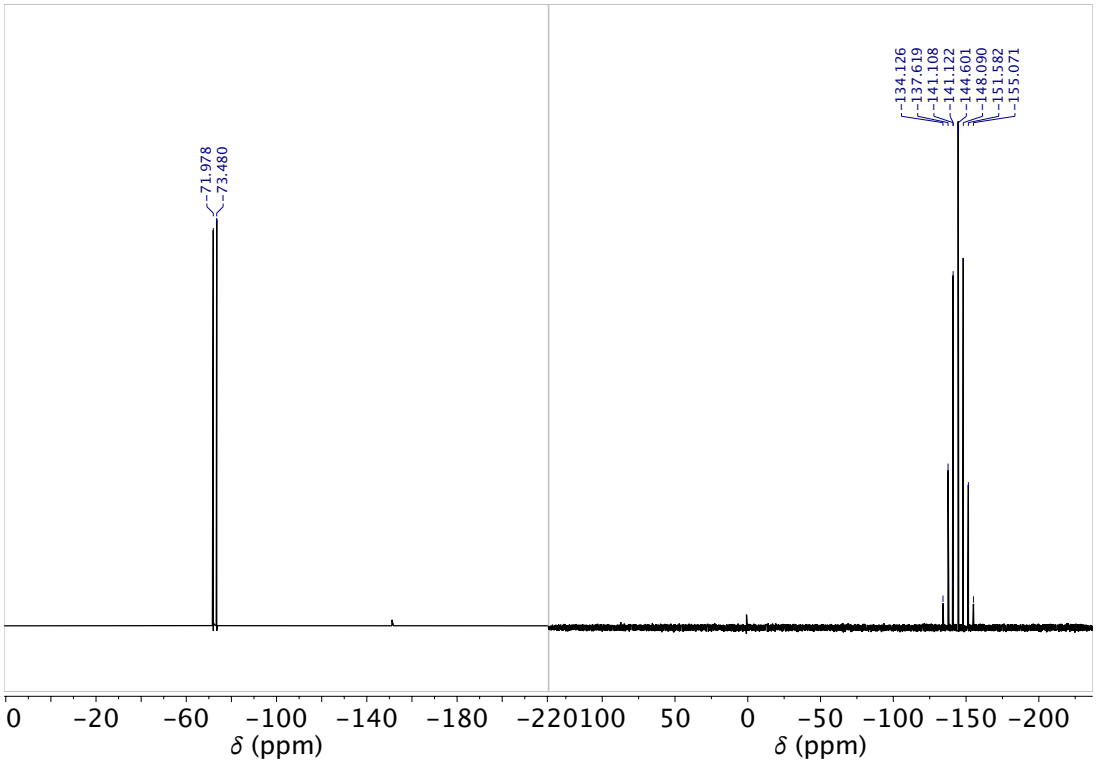

Figure C20. $^{19}F\{^{1}H\}$ NMR spectrum (471 MHz, CD_3CN) and $^{31}P\{^{1}H\}$ NMR spectrum (202 MHz, CD_3CN) of receptor $\mathbf{7^{3+}}$.

C2. ^{1}H NMR TITRATIONS

General Methods:All NMR titration spectra were acquired at room temperature on a Bruker Avance III-HD 600 NMR Spectrometer equipped with a multinuclear Prodigy CryoProbe (^{1}H: 600 MHz) or on a Varian INOVA-500 NMR Spectrometer (^{1}H: 500 MHz). All chemical shifts (δ) are reported in ppm relative to residue CD_3CN (^{1}H: 1.940 ppm).

General Procedure A: In a drybox, the desired receptor was dissolved in 1.7–1.8 mL of anhydrous CD_3CN (0.87 mM – 5.8 mM), divided between three NMR tubes (500 μL in each), and sealed with a rubber septum and parafilm. The guest salt was dissolved in 2.4–2.6 mL of anhydrous CD_3CN (3.7 mM – 47.7 mM) and divided between three individual vials (~800 μL each). Aliquots of guest stock solution were added to the receptor solution via gas tight Hamilton syringes. ^{1}H NMR spectra were recorded at room temperature after each addition of the guest. The change in chemical shift (Δδ) of the C–H imidazolium proton and various C–H aromatic protons were used to follow the progress of the titration. The association constants were determined using the Nedler-Mead method in Bindfit.

General Procedure B: In a drybox, the desired receptor was dissolved in 1.7 mL of anhydrous CD_3CN (0.91 mM – 1.56 mM), added to an NMR tube (600 μL), and sealed with a rubber septum and parafilm. The remaining receptor solution was used to prepare a receptor-guest (47.4 mM – 71.3 mM) stock solution. Aliquots of receptor-guest stock solution were added to the receptor solution via gas tight Hamilton syringes. ^{1}H NMR spectra were recorded at room temperature after each addition of the guest. The change in chemical shift (Δδ) of the C–H imidazolium proton and various C–H aromatic protons were used to follow the progress of the titration. The association constants were determined using the Nedler-Mead method in Bindfit.

Representative ^{1}H NMR Titration Data

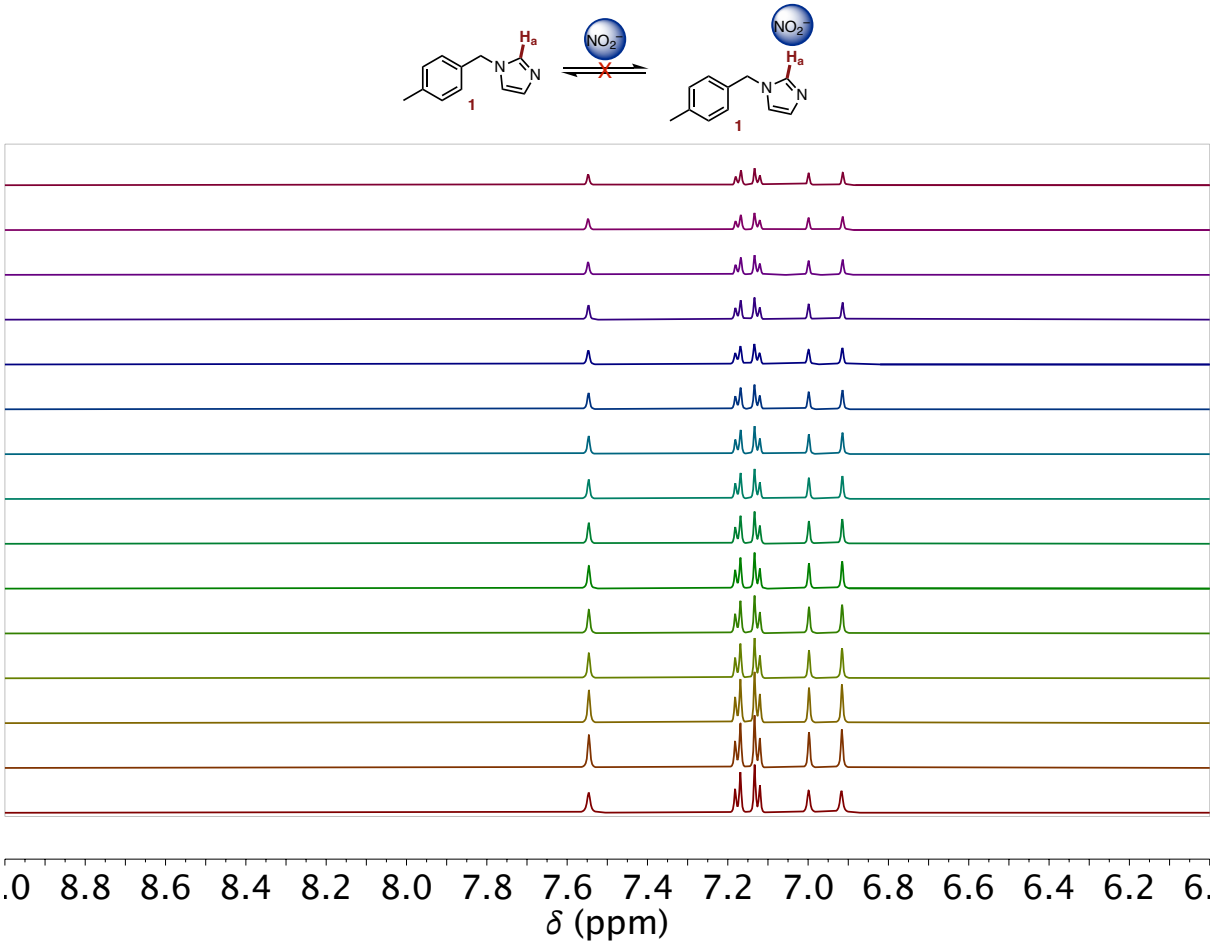

Figure C21. Titration scheme of receptor **1** with NO_2^- and representative ^{1}H NMR spectra.

Table C1. Representative titration of receptor **1** with NO_2^- in CD_3CN at room temperature.

Entry	$V_{total,\ guest}$ (μL)	[Receptor] (M)	[Guest] (M)	Anion Equiv.	CH_a (ppm)
1	0	5.81E-03	0.00E+00	0.00	7.547
2	10	5.69E-03	8.75E-04	0.15	7.546
3	25	5.53E-03	2.13E-03	0.38	7.546
4	50	5.28E-03	4.06E-03	0.77	7.546
5	75	5.05E-03	5.82E-03	1.15	7.546
6	100	4.84E-03	7.44E-03	1.54	7.546
7	150	4.47E-03	1.03E-02	2.31	7.546
8	200	4.15E-03	1.28E-02	3.07	7.547
9	250	3.87E-03	1.49E-02	3.84	7.547
10	300	3.63E-03	1.67E-02	4.61	7.547
11	350	3.42E-03	1.84E-02	5.38	7.547
12	400	3.23E-03	1.98E-02	6.15	7.547
13	500	2.90E-03	2.23E-02	7.69	7.548
14	600	2.64E-03	2.43E-02	9.22	7.548

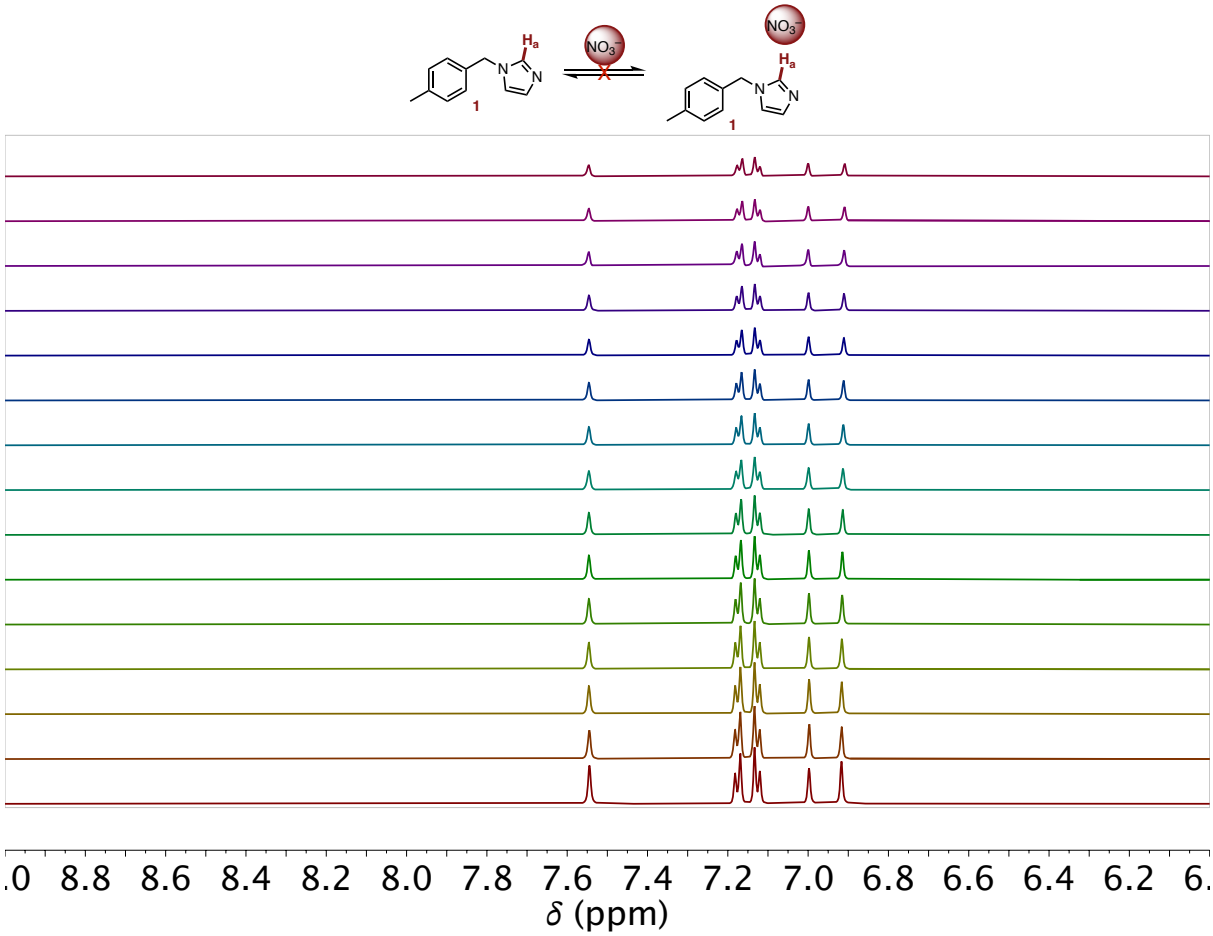

Figure C22. Titration scheme of receptor **1** with NO_3^- and representative ^1H NMR spectra.

Table C2. Representative titration of receptor **1** with NO_3^- in CD_3CN at room temperature.

Entry	$V_{total,\ guest}$ (μL)	[Receptor] (M)	[Guest] (M)	Anion Equiv.	CH_a (ppm)
1	0	9.68E-03	0.00E+00	0.00	7.545
2	10	9.49E-03	3.16E-03	0.33	7.545
3	25	9.22E-03	7.66E-03	0.83	7.546
4	50	8.80E-03	1.46E-02	1.66	7.546
5	75	8.41E-03	2.10E-02	2.49	7.546
6	100	8.06E-03	2.68E-02	3.33	7.546
7	150	7.44E-03	3.71E-02	4.99	7.546
8	200	6.91E-03	4.60E-02	6.65	7.546
9	250	6.45E-03	5.36E-02	8.32	7.546
10	300	6.05E-03	6.03E-02	9.98	7.546
11	350	5.69E-03	6.63E-02	11.64	7.546
12	400	5.38E-03	7.15E-02	13.30	7.546
13	500	4.84E-03	8.05E-02	16.63	7.546
14	600	4.40E-03	8.78E-02	19.96	7.546
15	700	4.03E-03	9.39E-02	23.28	7.546

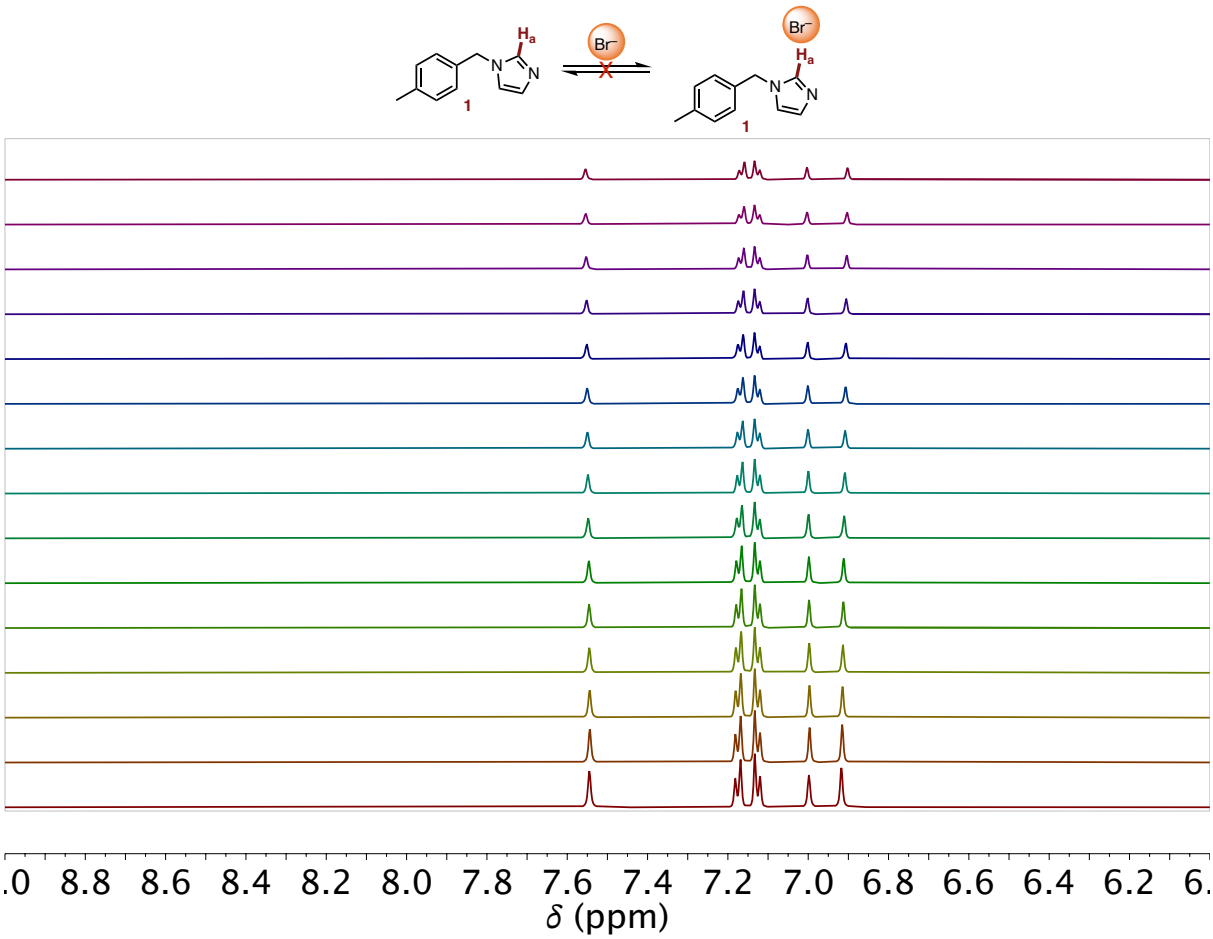

Figure C23. Titration scheme of receptor **1** with Br^- and representative ^1H NMR spectra.

Table C3. Representative titration of receptor **1** with Br^- in CD_3CN at room temperature.

Entry	$V_{total,\ guest}$ (μL)	[Receptor] (M)	[Guest] (M)	Anion Equiv.	CH_a (ppm)
1	0	9.68E-03	0.00E+00	0.00	7.545
2	10	9.49E-03	3.00E-03	0.32	7.544
3	25	9.22E-03	7.30E-03	0.79	7.544
4	50	8.80E-03	1.39E-02	1.58	7.545
5	75	8.41E-03	2.00E-02	2.38	7.546
6	100	8.06E-03	2.55E-02	3.17	7.546
7	150	7.44E-03	3.54E-02	4.75	7.548
8	200	6.91E-03	4.38E-02	6.33	7.549
9	250	6.45E-03	5.11E-02	7.92	7.550
10	300	6.05E-03	5.75E-02	9.50	7.550
11	350	5.69E-03	6.31E-02	11.08	7.551
12	400	5.38E-03	6.81E-02	12.67	7.552
13	500	4.84E-03	7.66E-02	15.84	7.553
14	600	4.40E-03	8.36E-02	19.00	7.554
15	700	4.03E-03	8.94E-02	22.17	7.555

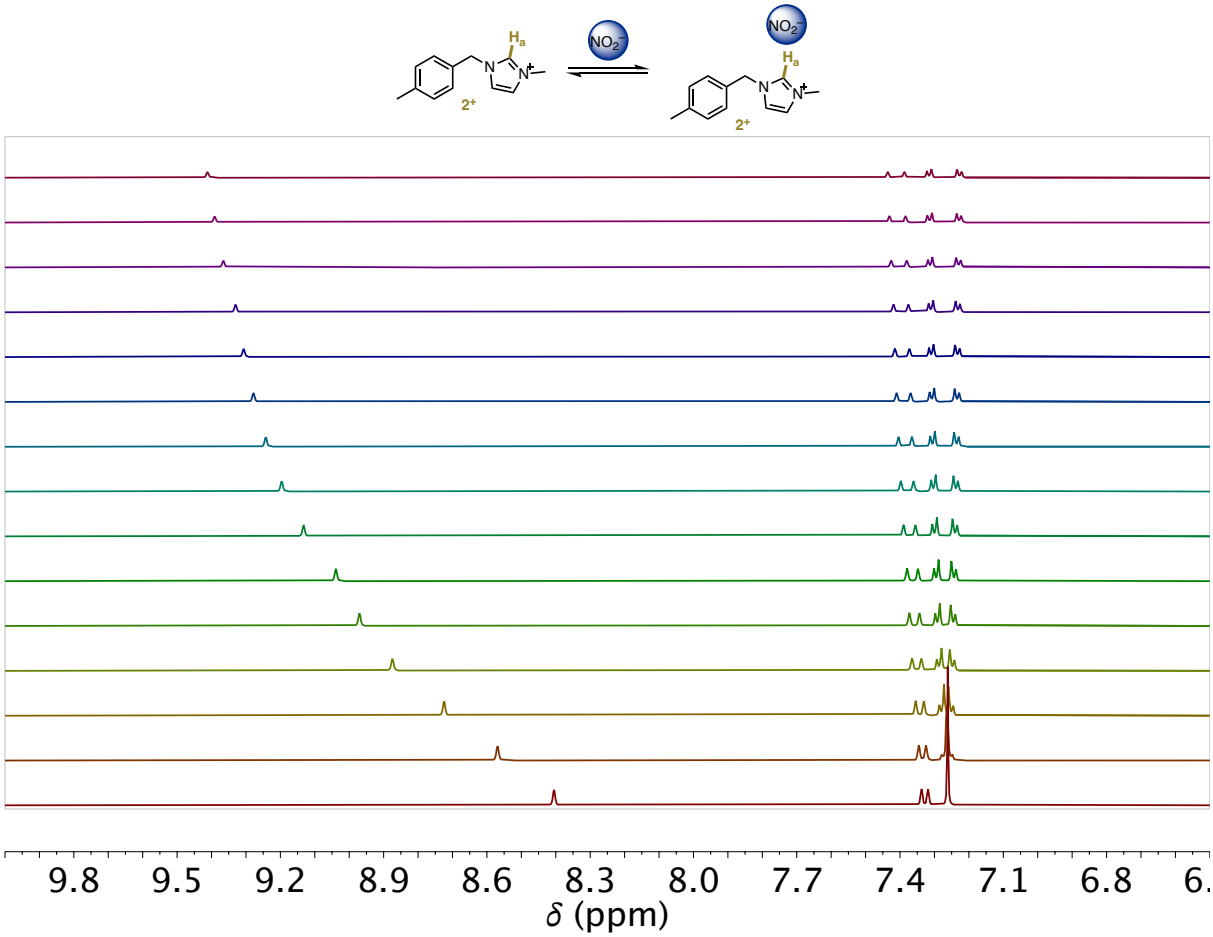

Figure C24. Titration scheme of receptor $\mathbf{2}^{+}$ with NO_2^- and representative ^1H NMR spectra.

Table C4. Representative titration of receptor $\mathbf{2}^{+}$ with NO_2^- in CD_3CN at room temperature.

Entry	$V_{total,\ guest}$ (μL)	[Receptor] (M)	[Guest] (M)	Anion Equiv.	CH_a (ppm)
1	0	3.19E-03	0.00E+00	0.00	8.405
2	10	3.12E-03	4.83E-03	1.55	8.568
3	25	3.04E-03	1.17E-02	3.86	8.723
4	50	2.90E-03	2.24E-02	7.73	8.872
5	75	2.77E-03	3.21E-02	11.59	8.967
6	100	2.66E-03	4.10E-02	15.46	9.036
7	150	2.45E-03	5.68E-02	23.18	9.131
8	200	2.28E-03	7.04E-02	30.91	9.195
9	250	2.12E-03	8.21E-02	38.64	9.241
10	300	1.99E-03	9.24E-02	46.37	9.277
11	350	1.87E-03	1.01E-01	54.10	9.305
12	400	1.77E-03	1.09E-01	61.82	9.328
13	500	1.59E-03	1.23E-01	77.28	9.364
14	600	1.45E-03	1.34E-01	92.73	9.390
15	700	1.33E-03	1.44E-01	108.19	9.410

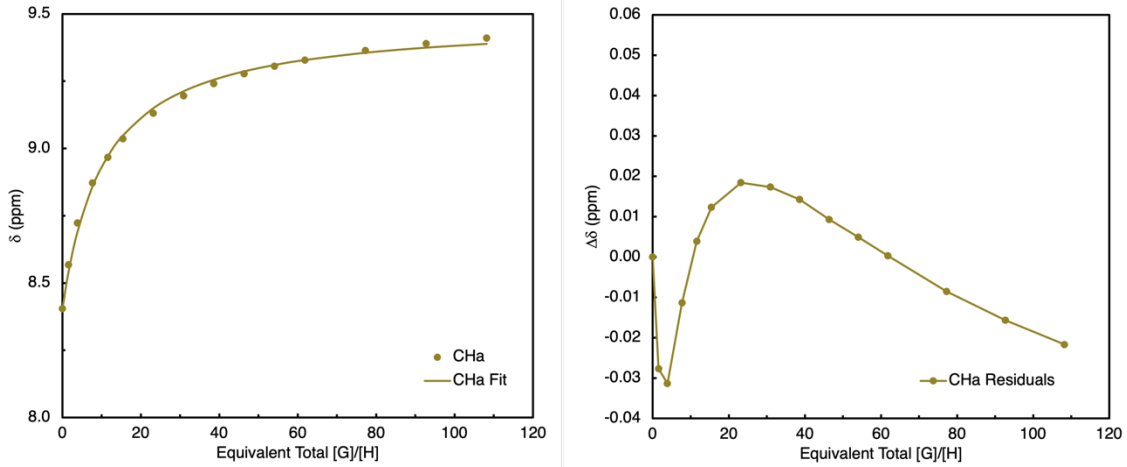

Figure C25. Representative 1:1 binding isotherm and residuals of NO_2^- titration of $\mathbf{2}^+$ in CD_3CN at room temperature determined via ^1H NMR spectroscopy.

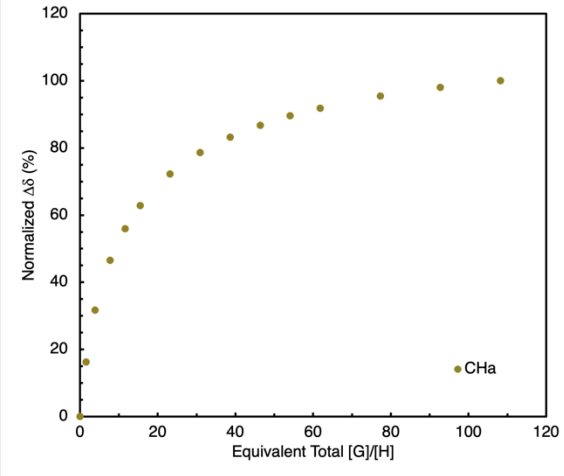

Figure C26. Normalized change in chemical shift of bound protons for NO_2^- titration of $\mathbf{2}^+$.

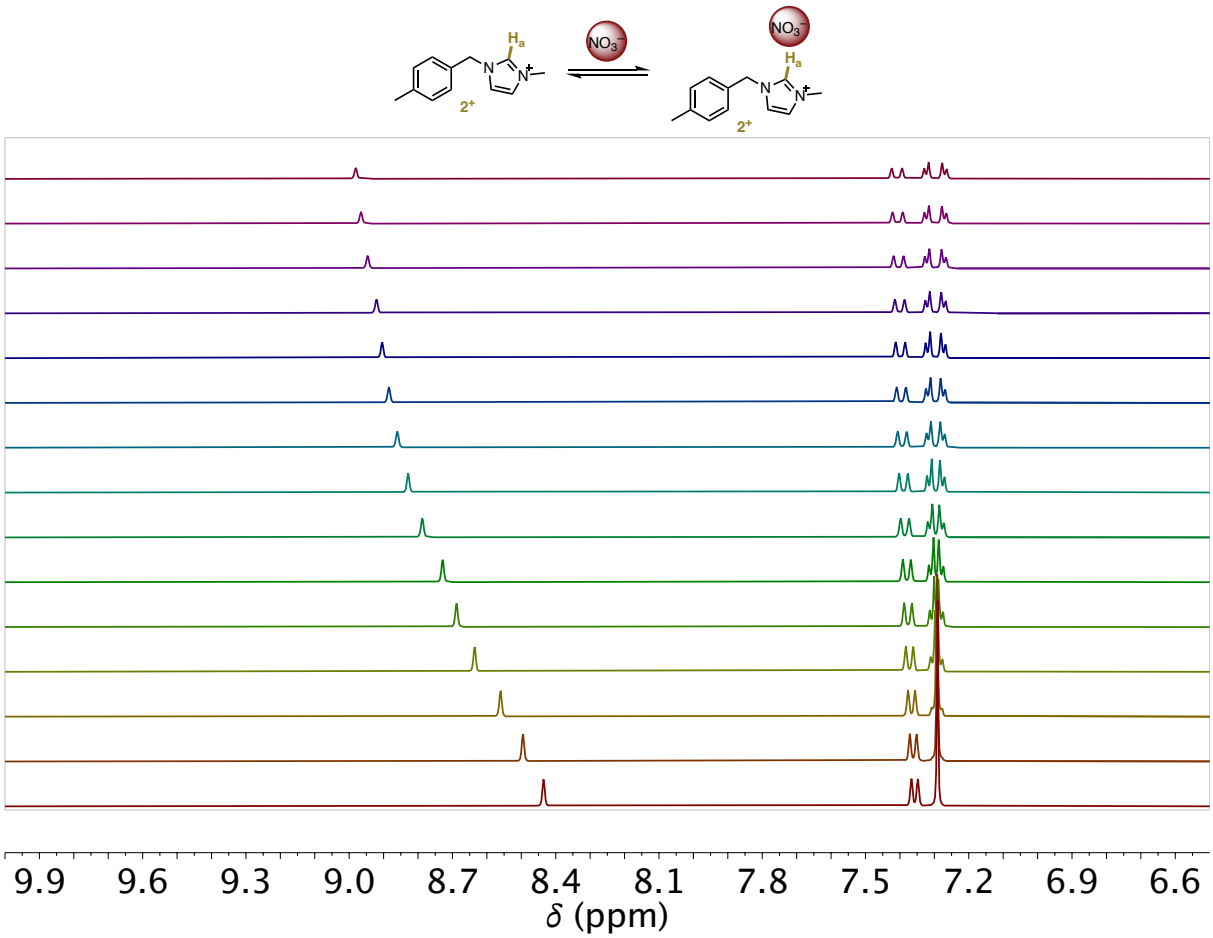

Figure C27. Titration scheme of receptor $\mathbf{2}^{+}$ with NO_3^- and representative ^1H NMR spectra.

Table C5. Representative titration of receptor $\mathbf{2}^{+}$ with NO_3^- in CD_3CN at room temperature.

Entry	$V_{total,\ guest}$ (μL)	[Receptor] (M)	[Guest] (M)	Anion Equiv.	CH_a (ppm)
1	0	3.36E-03	0.00E+00	0.00	8.406
2	10	3.30E-03	2.78E-03	0.84	8.466
3	25	3.20E-03	6.75E-03	2.11	8.532
4	50	3.06E-03	1.29E-02	4.21	8.607
5	75	2.93E-03	1.85E-02	6.32	8.659
6	100	2.80E-03	2.36E-02	8.43	8.700
7	150	2.59E-03	3.27E-02	12.64	8.759
8	200	2.40E-03	4.05E-02	16.85	8.800
9	250	2.24E-03	4.72E-02	21.07	8.831
10	300	2.10E-03	5.32E-02	25.28	8.856
11	350	1.98E-03	5.84E-02	29.50	8.875
12	400	1.87E-03	6.30E-02	33.71	8.892
13	500	1.68E-03	7.09E-02	42.14	8.918
14	600	1.53E-03	7.73E-02	50.56	8.937
15	700	1.40E-03	8.27E-02	58.99	8.952

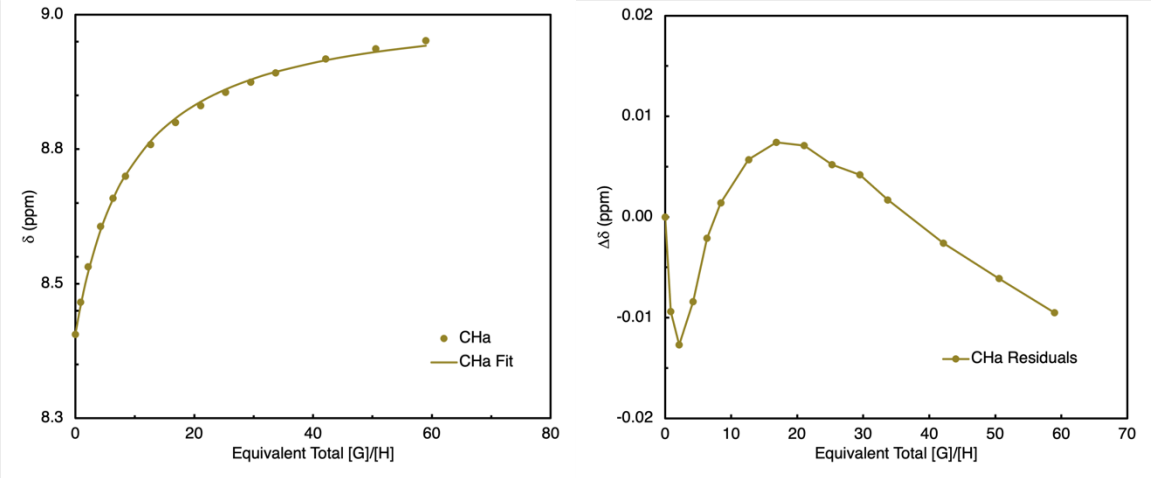

Figure C28. Representative 1:1 binding isotherm and residuals of NO_3^- titration of $\mathbf{2}^+$ in CD_3CN at room temperature determined via ^1H NMR spectroscopy.

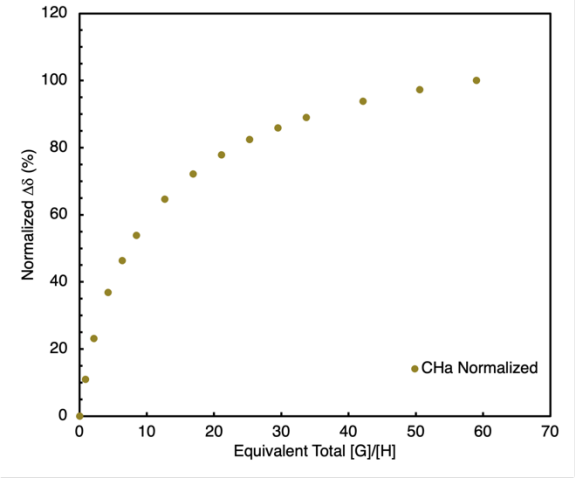

Figure C29. Normalized change in chemical shift of bound protons for NO_3^- titration of $\mathbf{2}^+$.

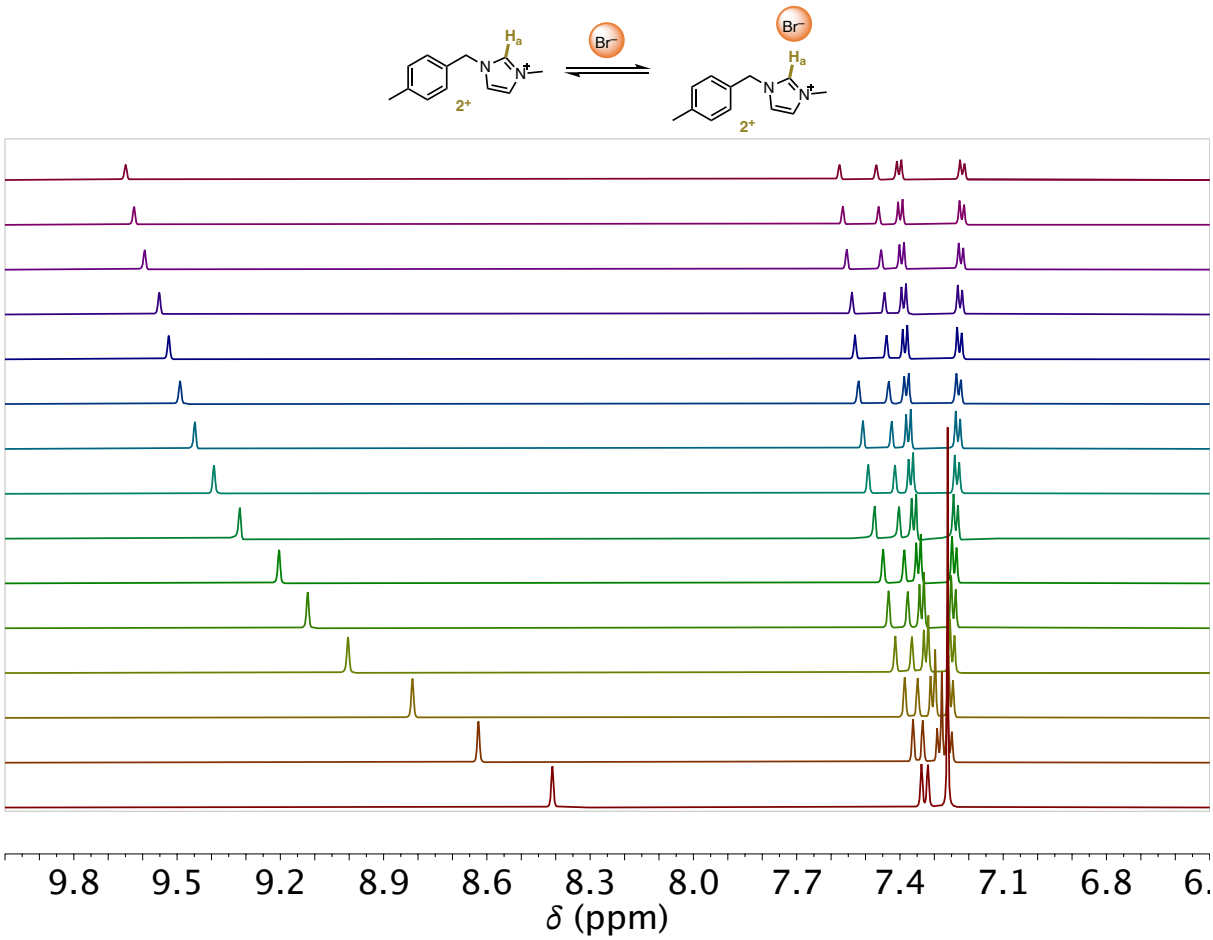

Figure C30. Titration scheme of receptor $\mathbf{2}^{+}$ with Br^{-} and representative ^{1}H NMR spectra.

Table C6. Representative titration of receptor $\mathbf{2}^{+}$ with Br^{-} in CD_3CN at room temperature.

Entry	$V_{total,\ guest}$ (μL)	[Receptor] (M)	[Guest] (M)	Anion Equiv.	CH_a (ppm)
1	0	4.60E-03	0.00E+00	0.00	8.411
2	10	4.51E-03	6.39E-03	1.42	8.625
3	25	4.38E-03	1.55E-02	3.54	8.817
4	50	4.18E-03	2.96E-02	7.08	9.004
5	75	4.00E-03	4.25E-02	10.62	9.121
6	100	3.84E-03	5.43E-02	14.16	9.204
7	150	3.54E-03	7.52E-02	21.23	9.318
8	200	3.29E-03	9.31E-02	28.31	9.394
9	250	3.07E-03	1.09E-01	35.39	9.449
10	300	2.88E-03	1.22E-01	42.47	9.492
11	350	2.71E-03	1.34E-01	49.54	9.525
12	400	2.56E-03	1.45E-01	56.62	9.552
13	500	2.30E-03	1.63E-01	70.78	9.595
14	600	2.09E-03	1.78E-01	84.93	9.626
15	700	1.92E-03	1.90E-01	99.09	9.650

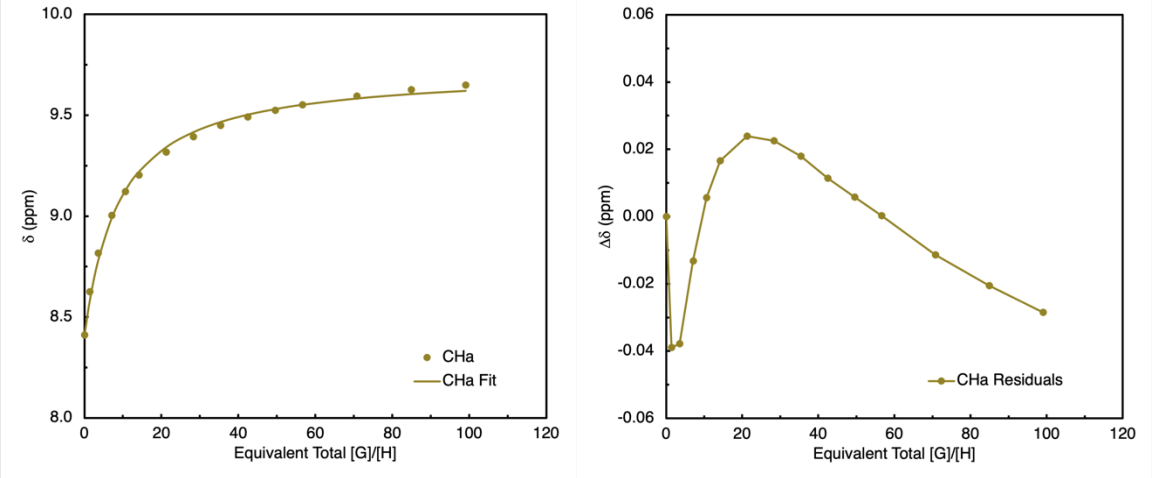

Figure C31. Representative 1:1 binding isotherm and residuals of Cl^- titration of $\mathbf{2}^+$ in CD_3CN at room temperature determined via ^1H NMR spectroscopy.

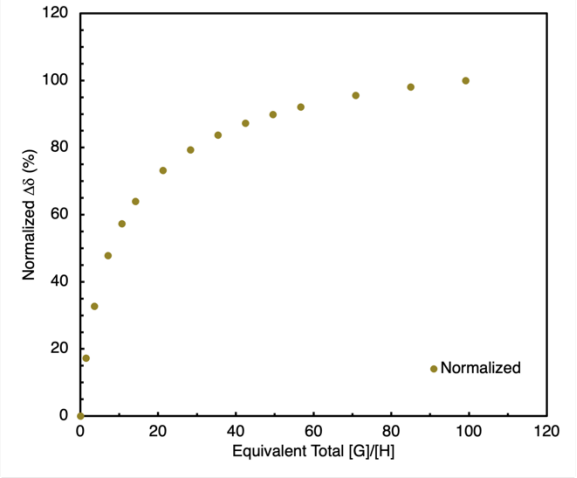

Figure C32. Normalized change in chemical shift of bound protons for Cl^- titration of $\mathbf{2}^+$.

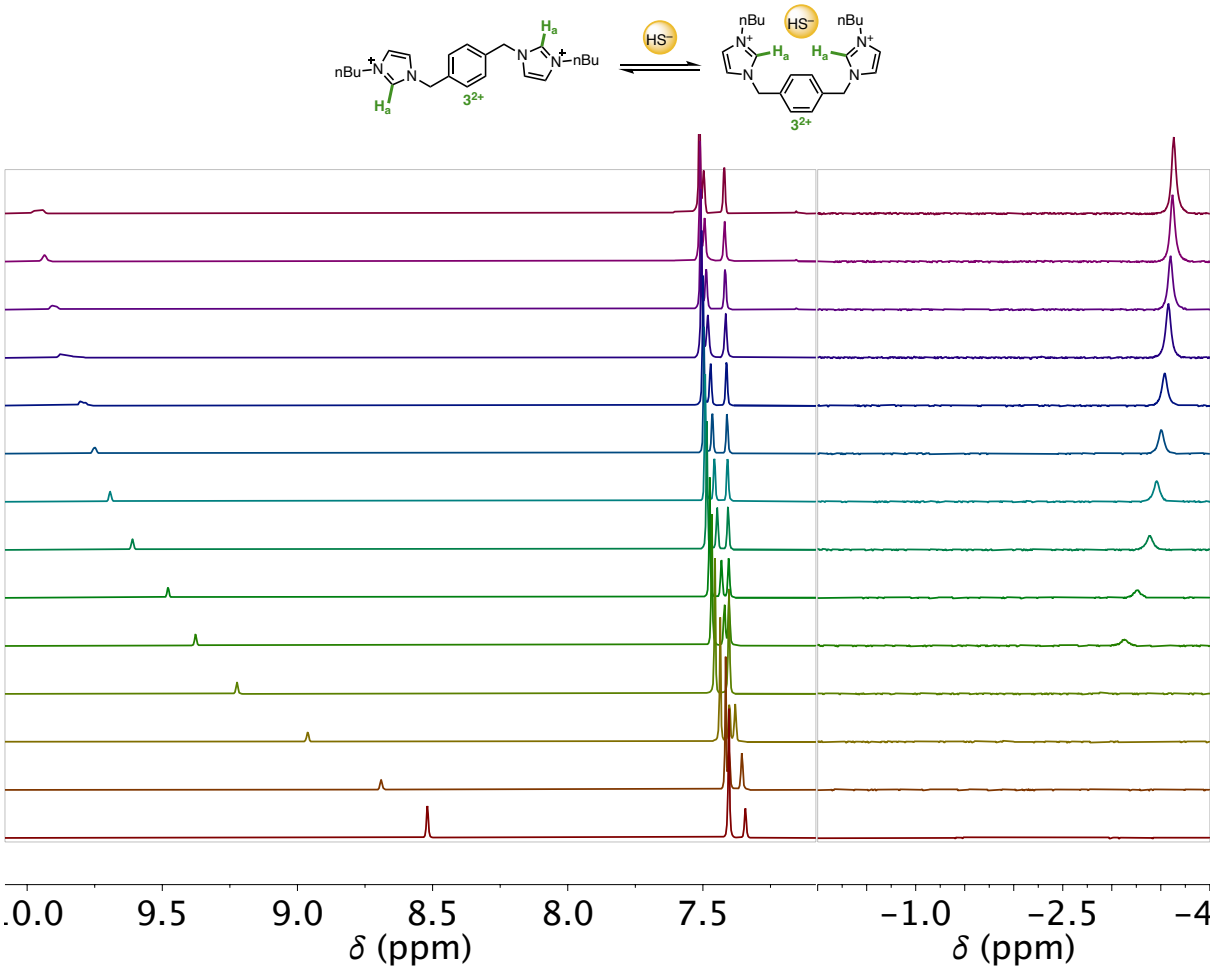

Figure C33. Titration scheme of receptor $\mathbf{3}^{2+}$ with HS^- and representative ^1H NMR spectra.

Table C7. Representative titration of receptor $\mathbf{3}^{2+}$ with HS^- in CD_3CN at room temperature.

Entry	$V_{total,\ guest}$ (μL)	[Receptor] (M)	[Guest] (M)	Anion Equiv.	CH_a (ppm)
1	0	1.01E-03	0.00E+00	0.00	8.519
2	10	1.01E-03	7.90E-04	0.78	8.691
3	25	1.01E-03	1.93E-03	1.91	8.962
4	50	1.01E-03	3.70E-03	3.68	9.223
5	75	1.01E-03	5.35E-03	5.31	9.377
6	100	1.01E-03	6.88E-03	6.83	9.479
7	150	1.01E-03	9.63E-03	9.56	9.610
8	200	1.01E-03	1.20E-02	11.96	9.694
9	250	1.01E-03	1.42E-02	14.06	9.752
10	300	1.01E-03	1.61E-02	15.94	9.801
11	400	1.01E-03	1.93E-02	19.13	9.873
12	500	1.01E-03	2.19E-02	21.74	9.902
13	600	1.01E-03	2.41E-02	23.91	9.936
14	700	1.01E-03	2.59E-02	25.75	9.957

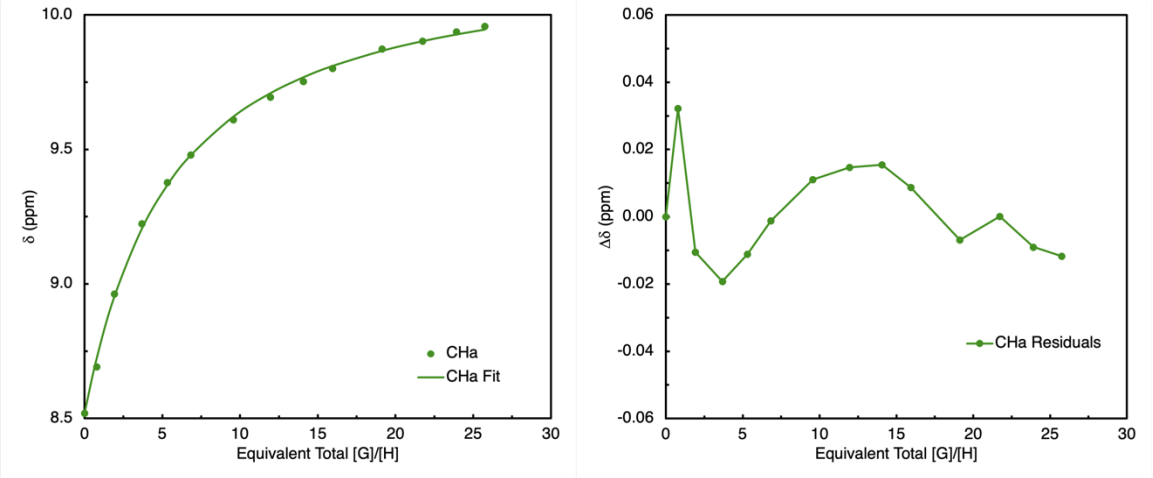

Figure C34. Representative binding isotherm and residuals of HS^- titration of $\mathbf{3}^+$ in CD_3CN at room temperature determined via ^1H NMR spectroscopy.

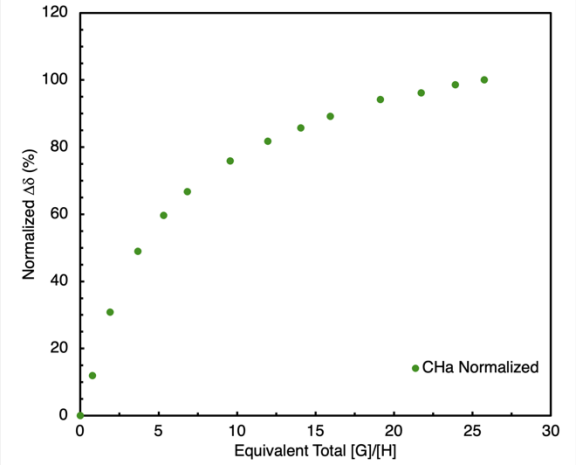

Figure C35. Normalized change in chemical shift of bound protons for HS^- titration of $\mathbf{3}^+$.

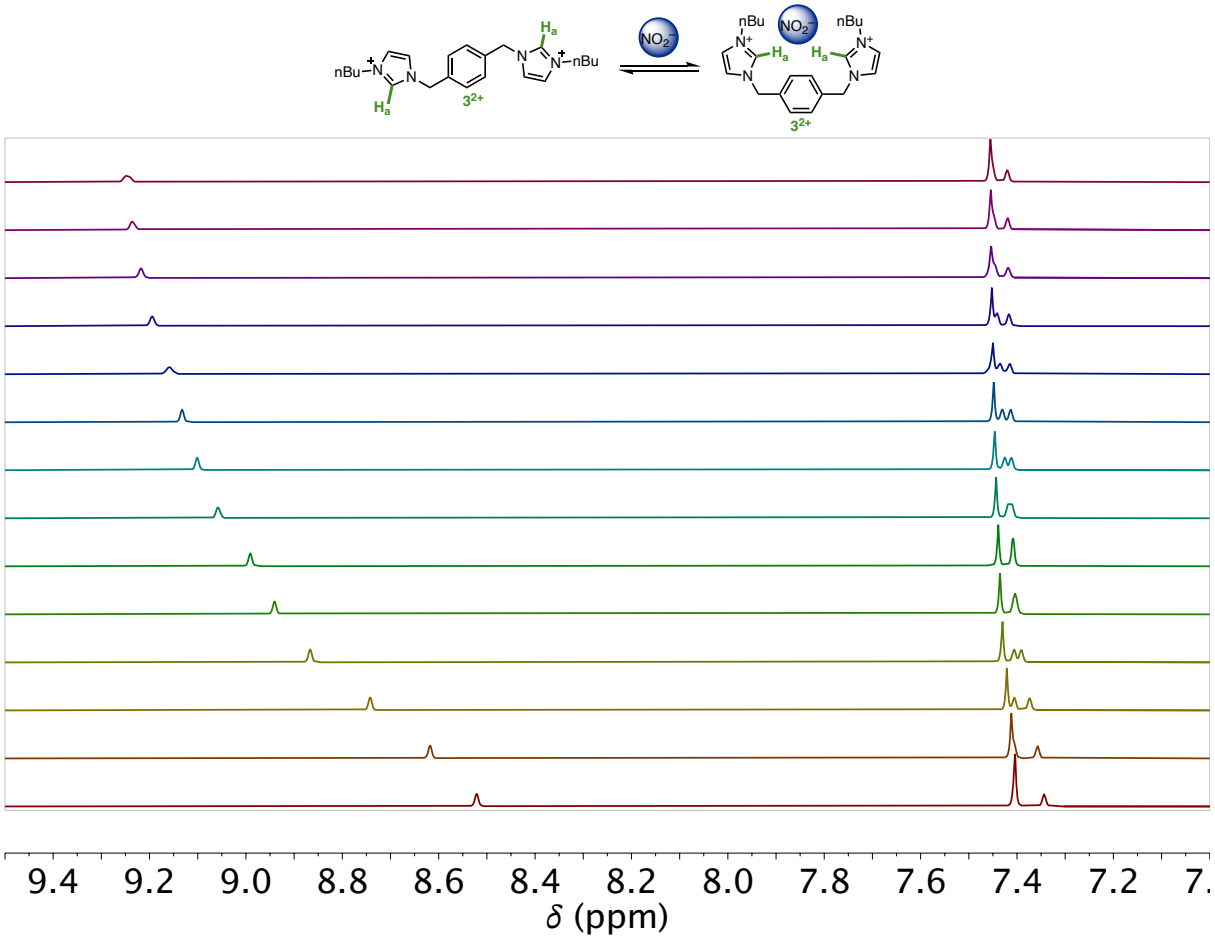

Figure C36. Titration scheme of receptor $\mathbf{3}^{2+}$ with NO_2^- and representative ^1H NMR spectra.

Table C8. Representative titration of receptor $\mathbf{3}^{2+}$ with NO_2^- in CD_3CN at room temperature.

Entry	$V_{total,\ guest}$ (μL)	[Receptor] (M)	[Guest] (M)	Anion Equiv.	CH_a (ppm)
1	0	1.52E-03	0.00E+00	0.00	8.478
2	10	1.49E-03	2.15E-04	0.14	8.534
3	25	1.44E-03	5.22E-04	0.36	8.614
4	50	1.38E-03	9.96E-04	0.72	8.725
5	75	1.32E-03	1.43E-03	1.08	8.813
6	100	1.26E-03	1.83E-03	1.44	8.881
7	150	1.17E-03	2.53E-03	2.17	8.980
8	200	1.08E-03	3.13E-03	2.89	9.045
9	250	1.01E-03	3.65E-03	3.61	9.092
10	300	9.48E-04	4.11E-03	4.33	9.126
11	350	8.92E-04	4.51E-03	5.06	9.153
12	400	8.42E-04	4.87E-03	5.78	9.174
13	500	7.58E-04	5.48E-03	7.22	9.205
14	600	6.89E-04	5.97E-03	8.67	9.227
15	700	6.32E-04	6.39E-03	10.11	9.243

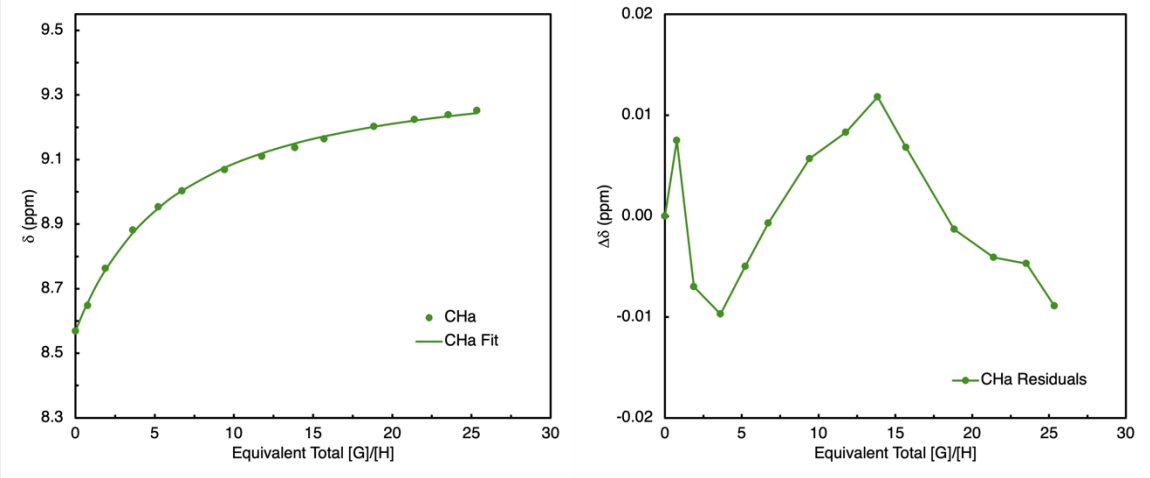

Figure C37. Representative binding isotherm and residuals of NO_2^- titration of $\mathbf{3}^{2+}$ in CD_3CN at room temperature determined via ^1H NMR spectroscopy.

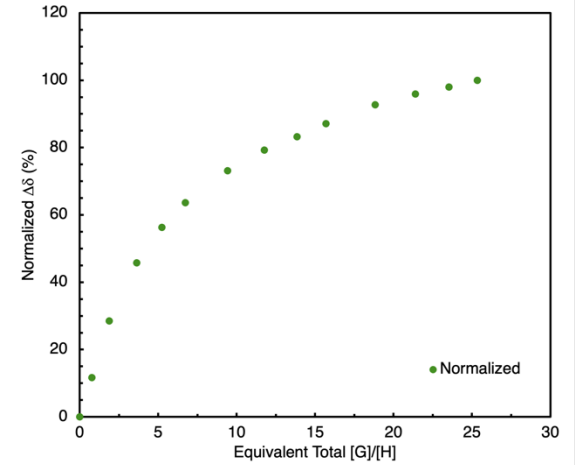

Figure C38. Normalized change in chemical shift of bound protons for NO_2^- titration of $\mathbf{3}^{2+}$.

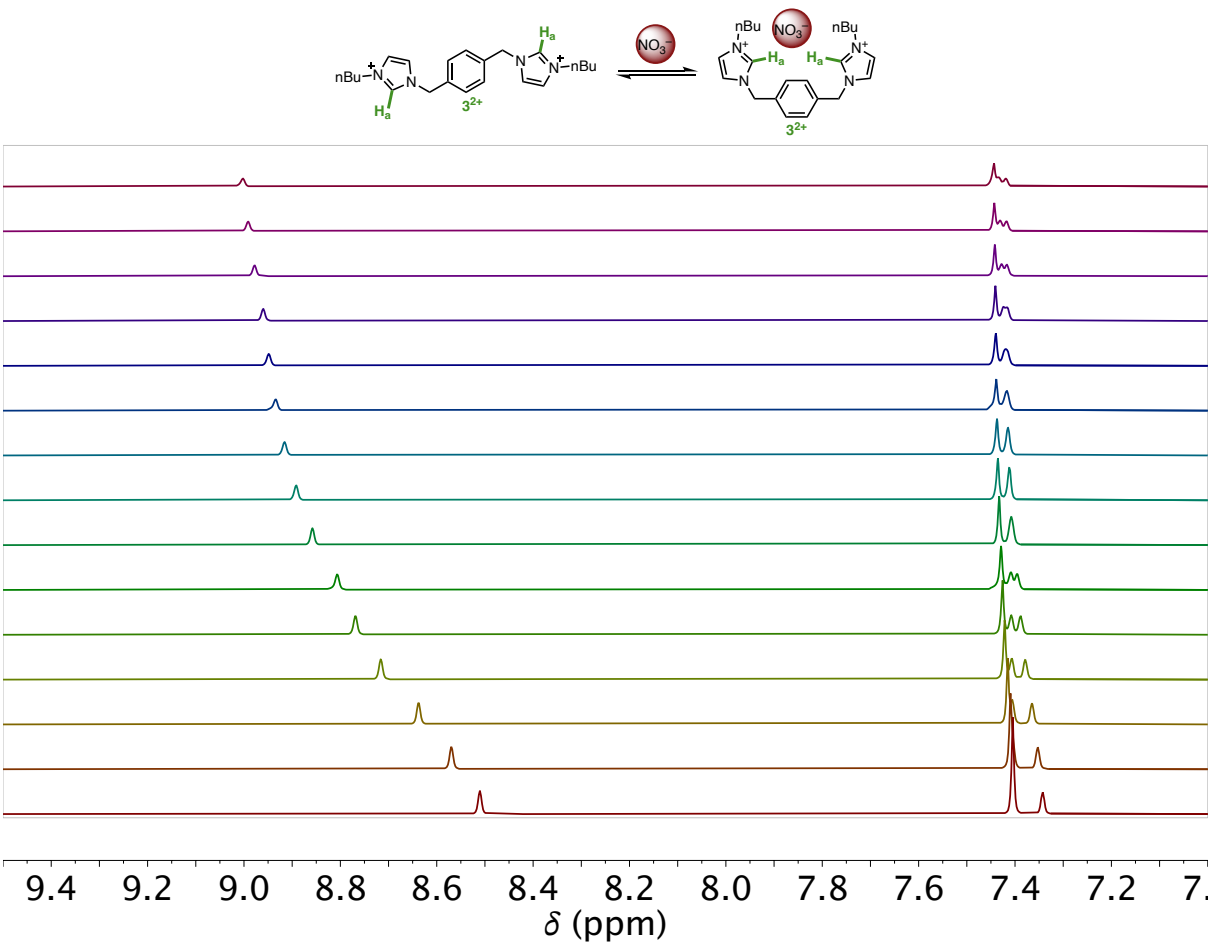

Figure C39. Titration scheme of receptor $\mathbf{3}^{2+}$ with NO_3^- and representative ^1H NMR spectra.

Table C9. Representative titration of receptor $\mathbf{3}^{2+}$ with NO_3^- in CD_3CN at room temperature.

Entry	$V_{total,\ guest}$ (μL)	[Receptor] (M)	[Guest] (M)	Anion Equiv.	CH_a (ppm)
1	0	1.92E-03	0.00E+00	0.00	8.511
2	10	1.89E-03	7.19E-04	0.38	8.570
3	25	1.83E-03	1.75E-03	0.95	8.638
4	50	1.75E-03	3.33E-03	1.91	8.716
5	75	1.67E-03	4.78E-03	2.86	8.769
6	100	1.60E-03	6.11E-03	3.81	8.807
7	150	1.48E-03	8.46E-03	5.72	8.858
8	200	1.37E-03	1.05E-02	7.62	8.892
9	250	1.28E-03	1.22E-02	9.53	8.916
10	300	1.20E-03	1.37E-02	11.44	8.934
11	350	1.13E-03	1.51E-02	13.34	8.949
12	400	1.07E-03	1.63E-02	15.25	8.960
13	500	9.61E-04	1.83E-02	19.06	8.978
14	600	8.74E-04	2.00E-02	22.87	8.991
15	700	8.01E-04	2.14E-02	26.69	9.002

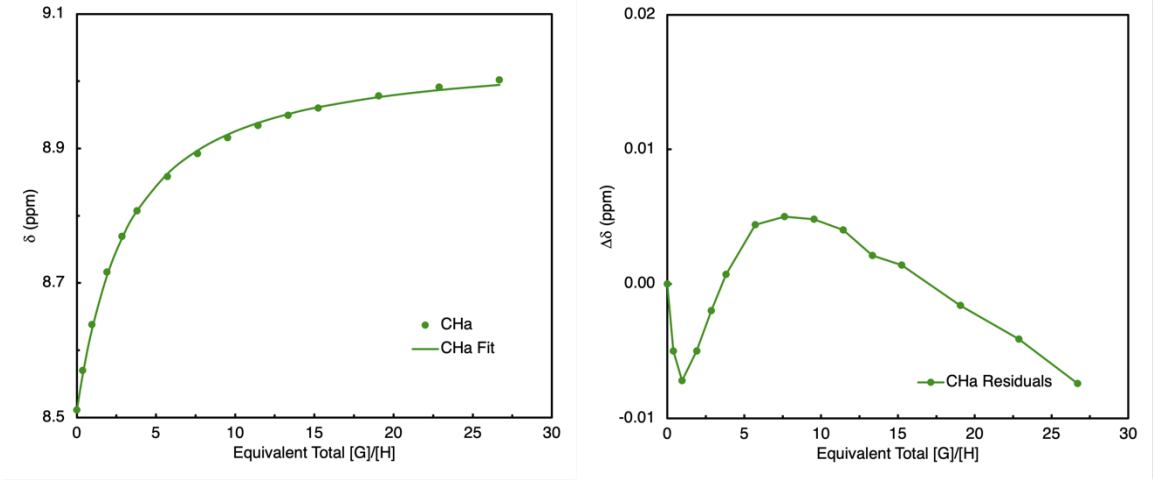

Figure C40. Representative binding isotherm and residuals of NO_3^- titration of $\mathbf{3}^{2+}$ in CD_3CN at room temperature determined via ^1H NMR spectroscopy.

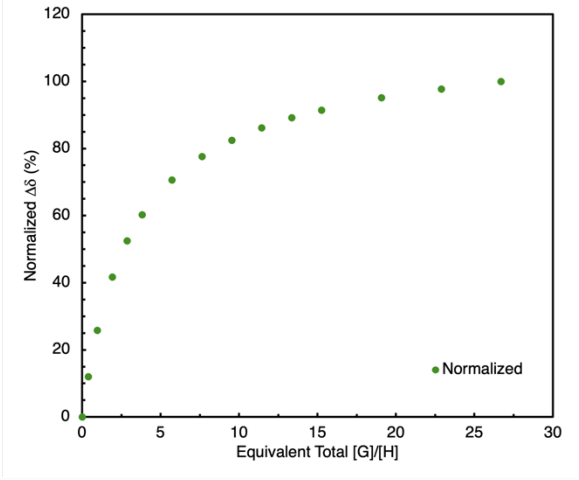

Figure C41. Normalized change in chemical shift of bound protons for NO_3^- titration of $\mathbf{3}^{2+}$.

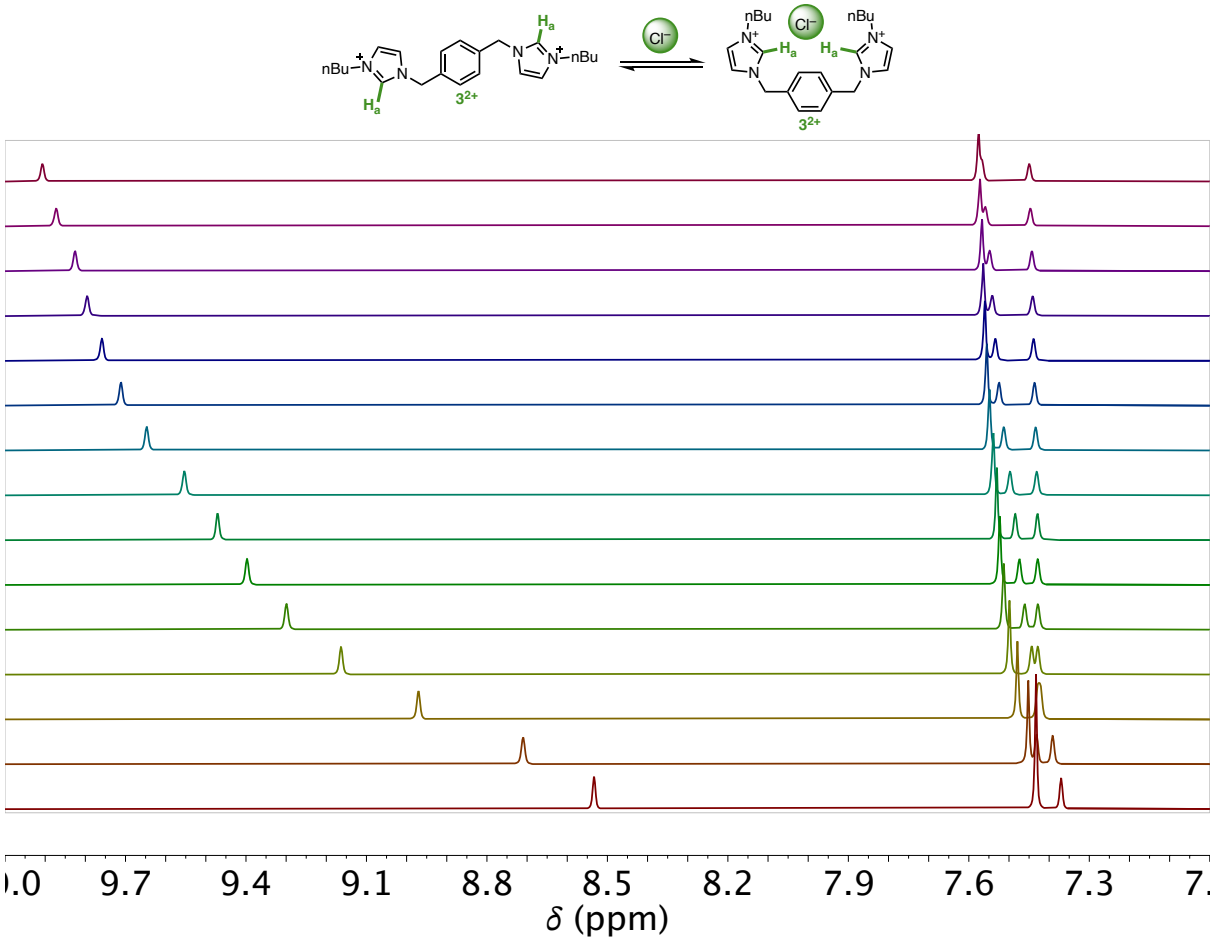

Figure C42. Titration scheme of receptor $\mathbf{3}^{2+}$ with Cl^- and representative ^1H NMR spectra.

Table C10. Representative titration of receptor $\mathbf{3}^{2+}$ with Cl^- in CD_3CN at room temperature.

Entry	$V_{total,\ guest}$ (μL)	[Receptor] (M)	[Guest] (M)	Anion Equiv.	CH_a (ppm)
1	0	1.83E-03	0.00E+00	0.00	8.505
2	10	1.80E-03	8.49E-04	0.47	8.681
3	20	1.76E-03	1.67E-03	0.95	8.942
4	30	1.73E-03	2.45E-03	1.42	9.134
5	40	1.70E-03	3.21E-03	1.89	9.270
6	50	1.66E-03	3.94E-03	2.37	9.368
7	60	1.64E-03	4.64E-03	2.84	9.442
8	75	1.59E-03	5.65E-03	3.55	9.525
9	100	1.53E-03	7.22E-03	4.73	9.618
10	125	1.46E-03	8.66E-03	5.91	9.683
11	150	1.41E-03	1.00E-02	7.10	9.730
12	175	1.36E-03	1.12E-02	8.28	9.767
13	200	1.31E-03	1.24E-02	9.46	9.797
14	250	1.22E-03	1.44E-02	11.83	9.844
15	300	1.14E-03	1.62E-02	14.19	9.879

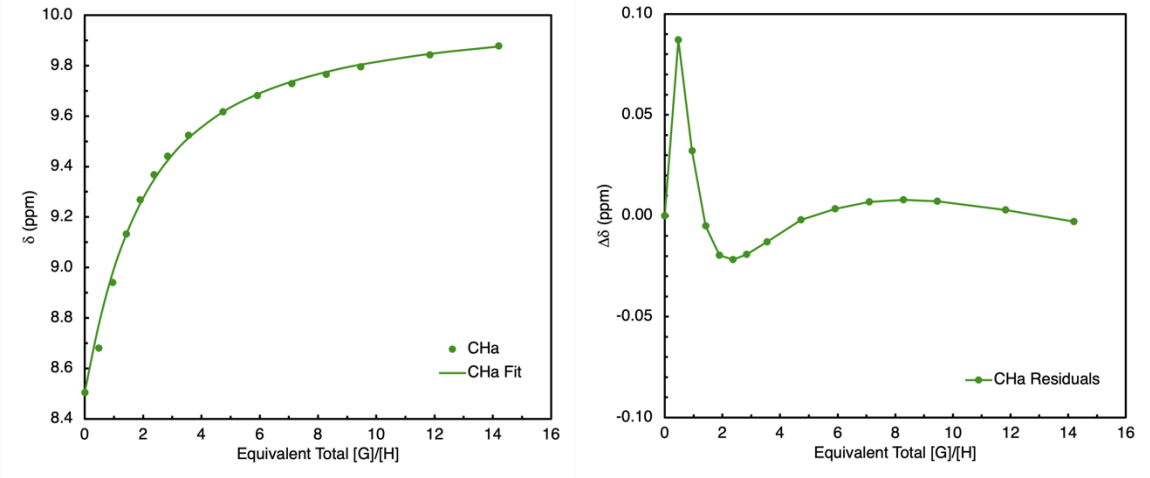

Figure C43. Representative binding isotherm and residuals of Cl^- titration of $\mathbf{3}^{2+}$ in CD_3CN at room temperature determined via ^1H NMR spectroscopy.

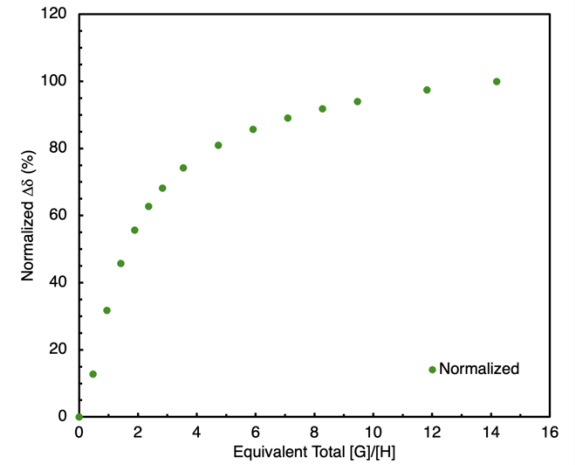

Figure C44. Normalized change in chemical shift of bound protons for Cl^- titration of $\mathbf{3}^{2+}$.

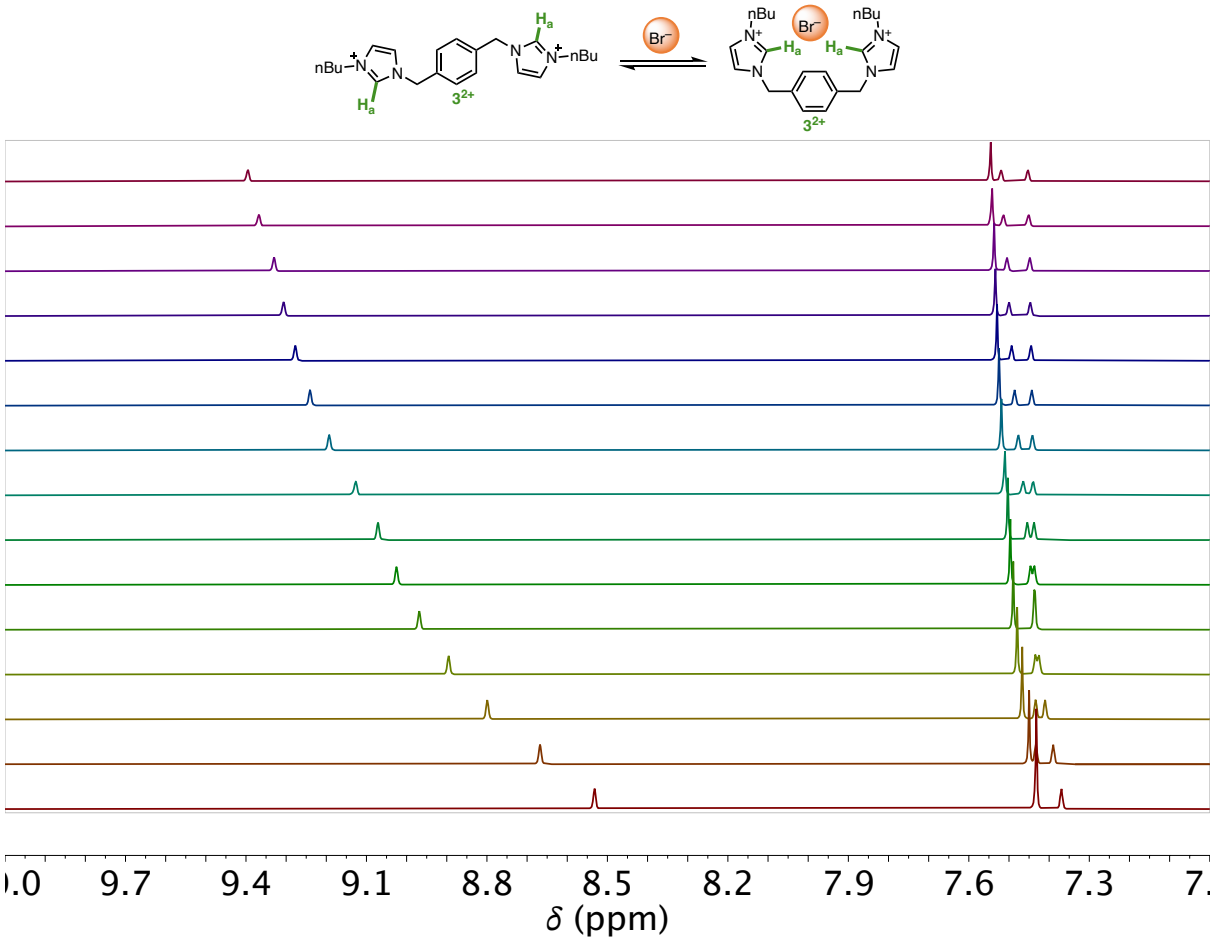

Figure C45. Titration scheme of receptor $\mathbf{3}^{2+}$ with Br^- and representative ^1H NMR spectra.

Table C11. Representative titration of receptor $\mathbf{3}^{2+}$ with Br^- in CD_3CN at room temperature.

Entry	$V_{total,\ guest}$ (μL)	[Receptor] (M)	[Guest] (M)	Anion Equiv.	CH_a (ppm)
1	0	1.65E-03	0.00E+00	0.00	8.503
2	10	1.62E-03	7.44E-04	0.46	8.639
3	20	1.58E-03	1.46E-03	0.92	8.770
4	30	1.55E-03	2.15E-03	1.38	8.867
5	40	1.53E-03	2.81E-03	1.84	8.940
6	50	1.50E-03	3.45E-03	2.30	8.996
7	60	1.47E-03	4.07E-03	2.76	9.043
8	75	1.43E-03	4.95E-03	3.46	9.098
9	100	1.37E-03	6.33E-03	4.61	9.164
10	125	1.32E-03	7.59E-03	5.76	9.212
11	150	1.27E-03	8.76E-03	6.91	9.248
12	175	1.22E-03	9.84E-03	8.06	9.277
13	200	1.18E-03	1.08E-02	9.21	9.301
14	250	1.10E-03	1.27E-02	11.52	9.339
15	300	1.03E-03	1.42E-02	13.82	9.366

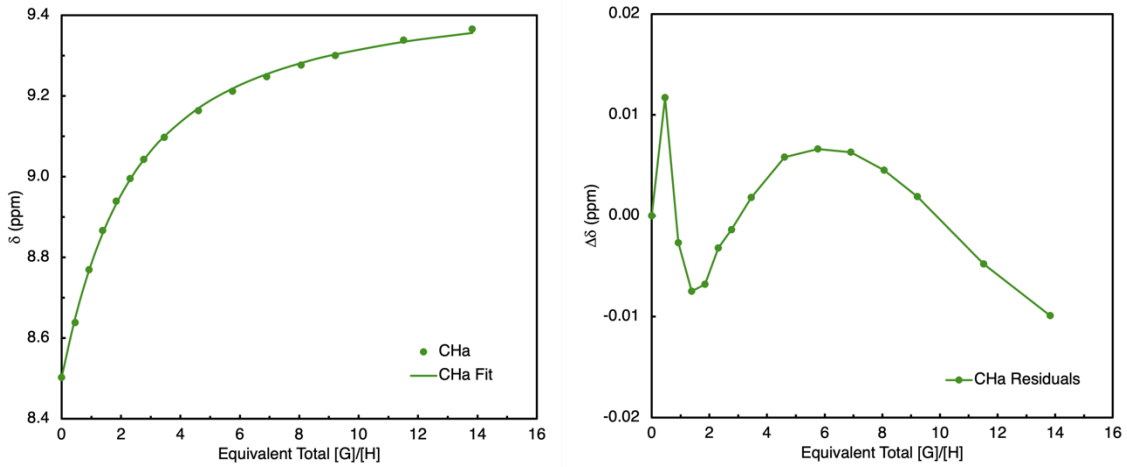

Figure C46. Representative binding isotherm and residuals of Br^- titration of $\mathbf{3}^{2+}$ in CD_3CN at room temperature determined via ^1H NMR spectroscopy.

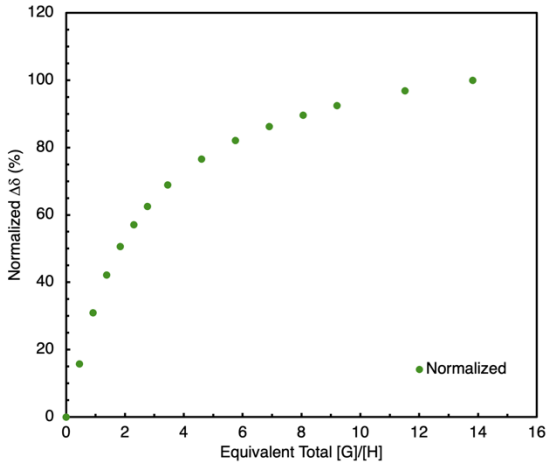

Figure C47. Normalized change in chemical shift of bound protons for Br^- titration of $\mathbf{3}^{2+}$.

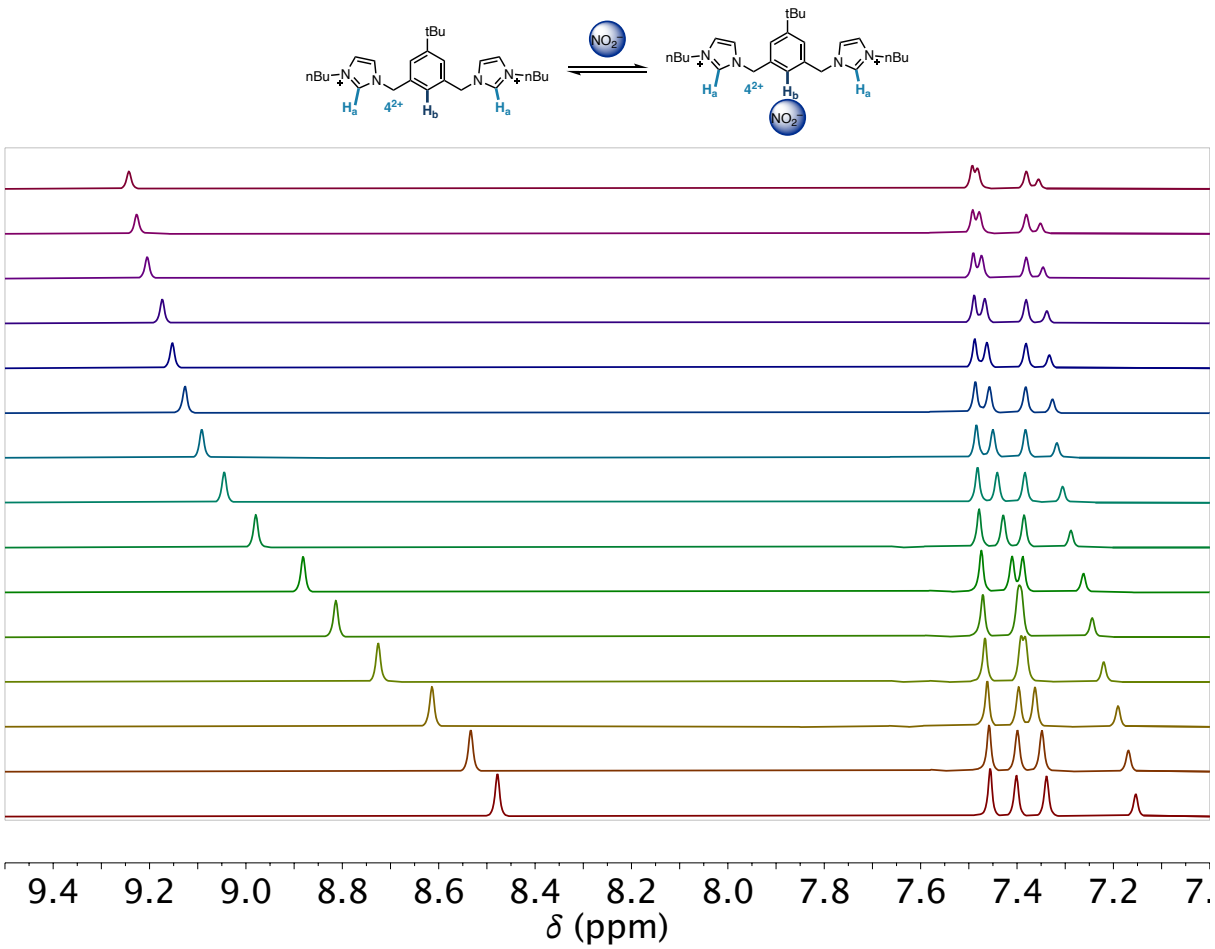

Figure C48. Titration scheme of receptor $\mathbf{4}^{2+}$ with NO_2^- and representative ^1H NMR spectra.

Table C12. Representative titration of receptor $\mathbf{4}^{2+}$ with NO_2^- in CD_3CN at room temperature.

Entry	$V_{total,\ guest}$ (μL)	[Receptor] (M)	[Guest] (M)	Anion Equiv.	CH_a (ppm)	CH_b (ppm)
1	0	1.52E-03	0.00E+00	0.00	8.478	7.154
2	10	1.49E-03	2.15E-04	0.14	8.534	7.169
3	25	1.44E-03	5.22E-04	0.36	8.614	7.190
4	50	1.38E-03	9.96E-04	0.72	8.725	7.220
5	75	1.32E-03	1.43E-03	1.08	8.813	7.244
6	100	1.26E-03	1.83E-03	1.44	8.881	7.262
7	150	1.17E-03	2.53E-03	2.17	8.980	7.288
8	200	1.08E-03	3.13E-03	2.89	9.045	7.305
9	250	1.01E-03	3.65E-03	3.61	9.092	7.317
10	300	9.48E-04	4.11E-03	4.33	9.126	7.326
11	350	8.92E-04	4.51E-03	5.06	9.153	7.333
12	400	8.42E-04	4.87E-03	5.78	9.174	7.338
13	500	7.58E-04	5.48E-03	7.22	9.205	7.346
14	600	6.89E-04	5.97E-03	8.67	9.227	7.351
15	700	6.32E-04	6.39E-03	10.11	9.243	7.355

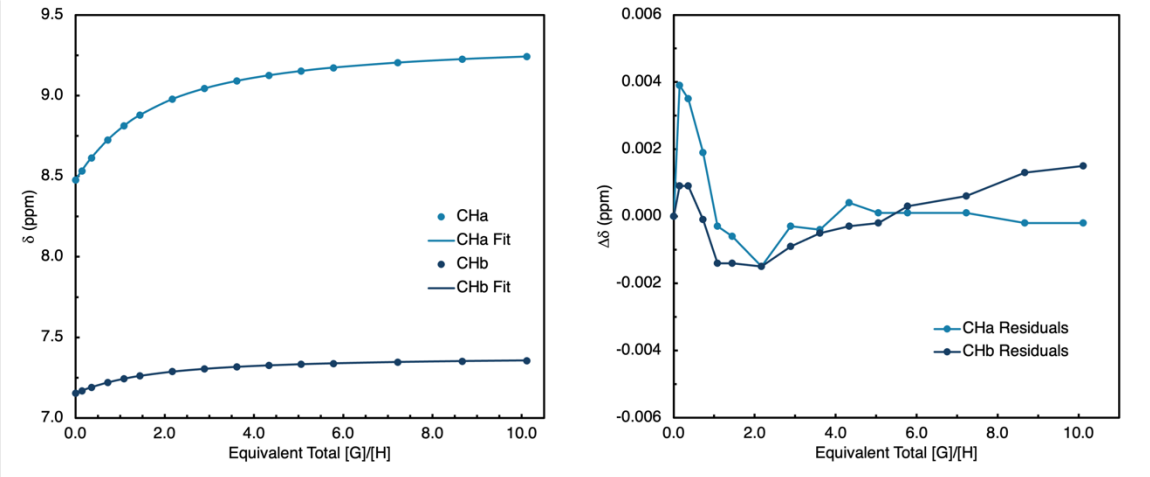

Figure C49. Representative binding isotherm and residuals of NO_2^- titration of $\mathbf{4}^{2+}$ in CD_3CN at room temperature determined via ^1H NMR spectroscopy.

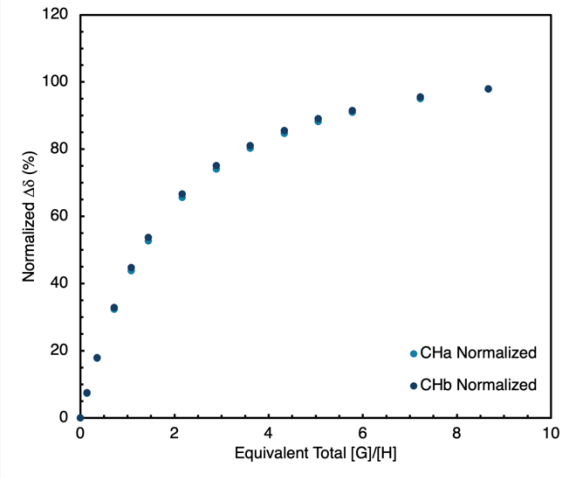

Figure C50. Normalized change in chemical shift of bound protons for NO_2^- titration of $\mathbf{4}^{2+}$.

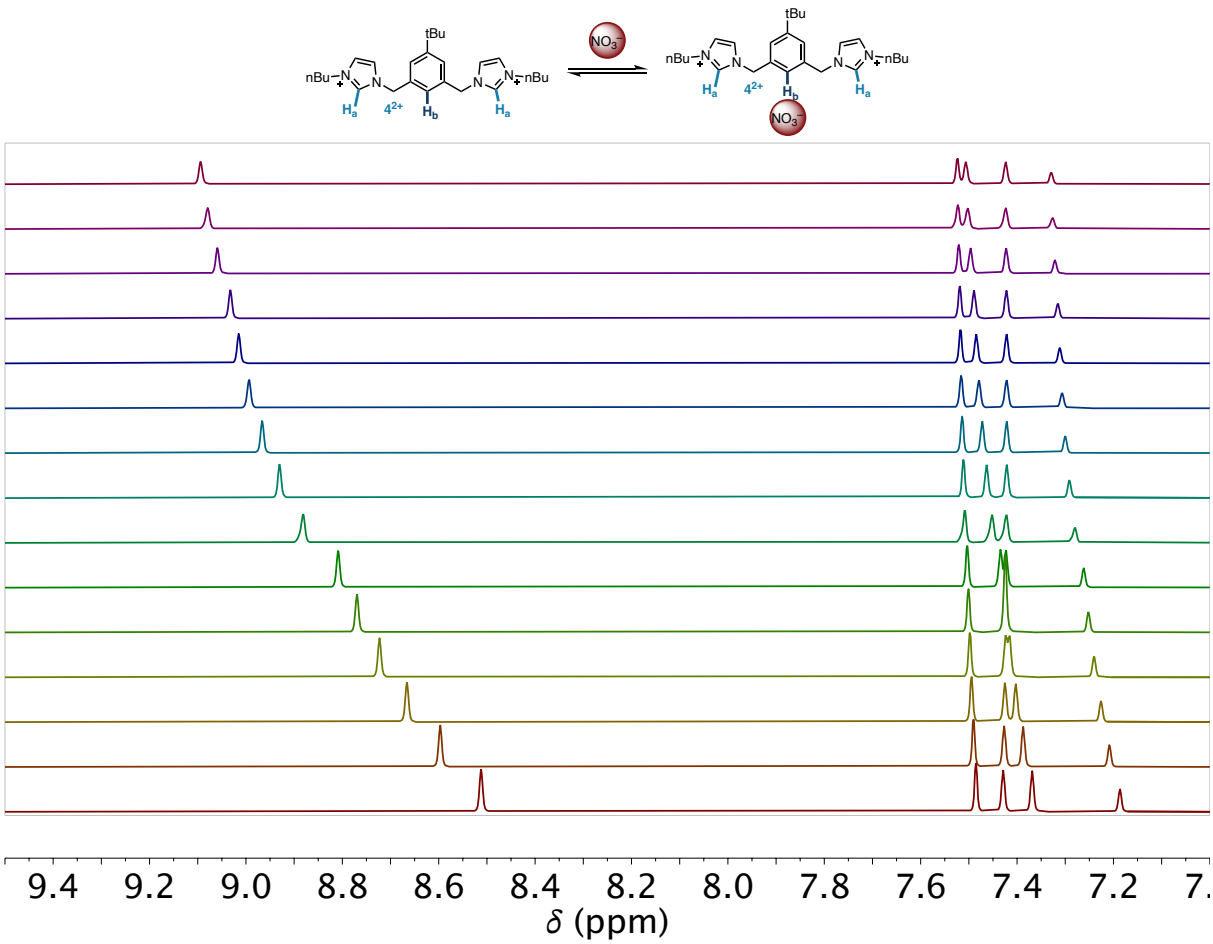

Figure C51. Titration scheme of receptor $\mathbf{4}^{2+}$ with NO_3^- and representative ^1H NMR spectra.

Table C13. Representative titration of receptor $\mathbf{4}^{2+}$ with NO_3^- in CD_3CN at room temperature.

Entry	$V_{total, guest}$ (μL)	[Receptor] (M)	[Guest] (M)	Anion Equiv.	CH_a (ppm)	CH_b (ppm)
1	0	2.02E-03	0.00E+00	0.00	8.483	7.158
2	10	1.98E-03	5.62E-04	0.28	8.568	7.180
3	20	1.94E-03	1.10E-03	0.57	8.637	7.194
4	30	1.91E-03	1.62E-03	0.85	8.694	7.211
5	40	1.87E-03	2.12E-03	1.13	8.741	7.223
6	50	1.84E-03	2.60E-03	1.42	8.780	7.233
7	75	1.76E-03	3.74E-03	2.13	8.853	7.251
8	100	1.68E-03	4.77E-03	2.83	8.902	7.263
9	125	1.62E-03	5.73E-03	3.54	8.938	7.271
10	150	1.55E-03	6.61E-03	4.25	8.965	7.278
11	175	1.50E-03	7.42E-03	4.96	8.986	7.280
12	200	1.44E-03	8.18E-03	5.67	9.004	7.283
13	250	1.35E-03	9.55E-03	7.09	9.030	7.292
14	300	1.26E-03	1.07E-02	8.50	9.051	7.298
15	350	1.19E-03	1.18E-02	9.92	9.065	7.301

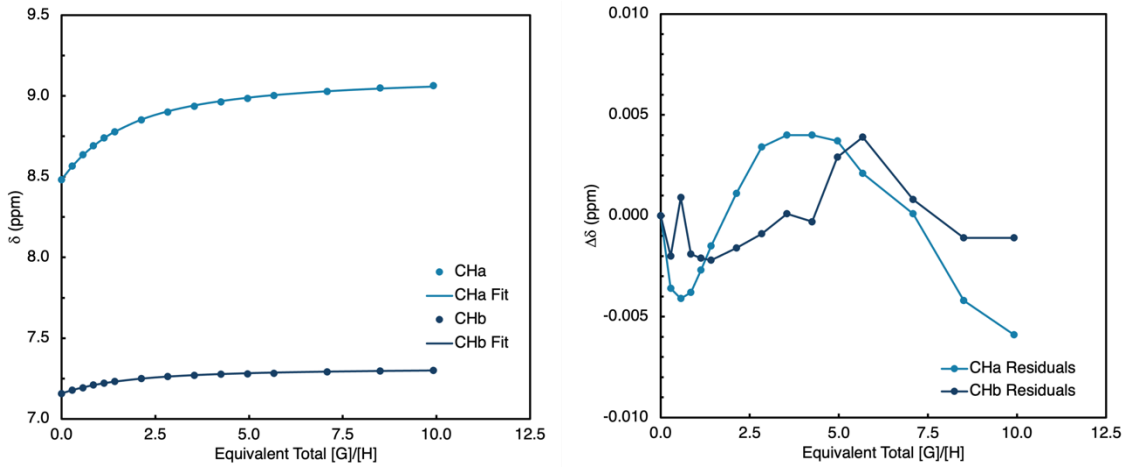

Figure C52. Representative binding isotherm and residuals of NO_3^- titration of $\mathbf{4}^{2+}$ in CD_3CN at room temperature determined via ^1H NMR spectroscopy.

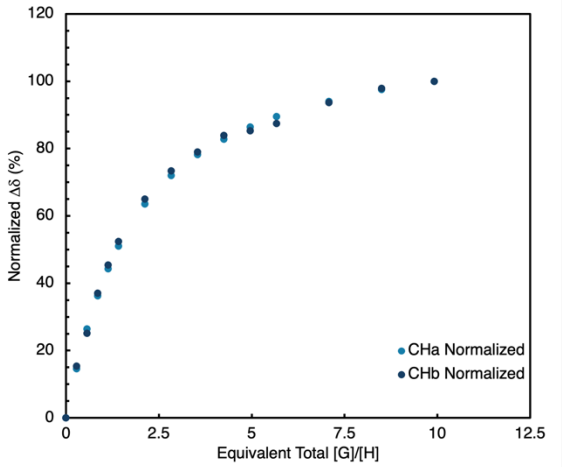

Figure C53. Normalized change in chemical shift of bound protons for NO_3^- titration of $\mathbf{4}^{2+}$.

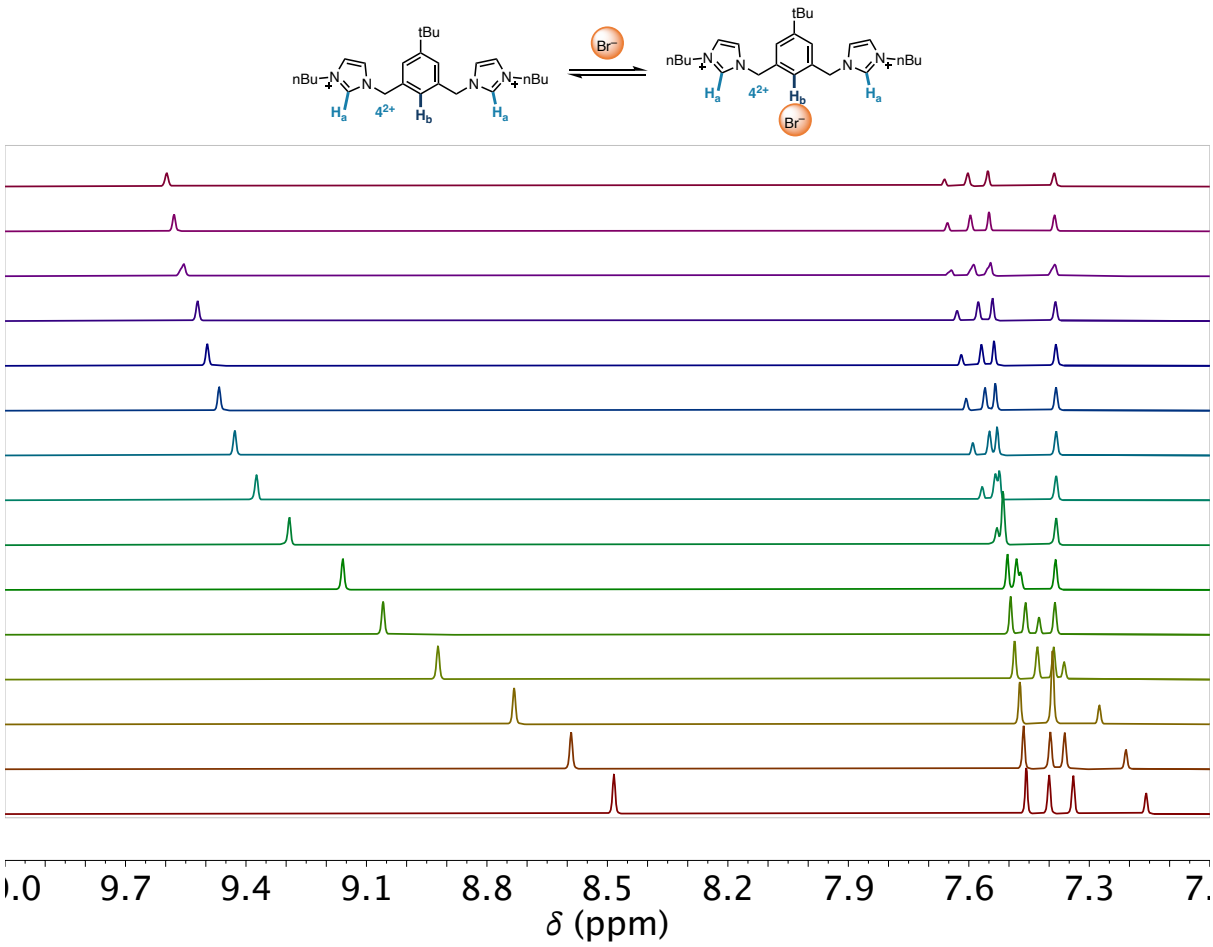

Figure C54. Titration scheme of receptor $\mathbf{4}^{2+}$ with Br^- and representative ^1H NMR spectra.

Table C14. Representative titration of receptor $\mathbf{4}^{2+}$ with Br^- in CD_3CN at room temperature.

Entry	$V_{total,\ guest}$ (μL)	[Receptor] (M)	[Guest] (M)	Anion Equiv.	CH_a (ppm)	CH_b (ppm)
1	0	1.85E-03	0.00E+00	0.00	8.484	7.159
2	10	1.82E-03	3.19E-04	0.18	8.591	7.209
3	25	1.76E-03	7.74E-04	0.44	8.733	7.275
4	50	1.68E-03	1.48E-03	0.88	8.922	7.363
5	75	1.61E-03	2.12E-03	1.32	9.059	7.425
6	100	1.54E-03	2.71E-03	1.75	9.159	7.471
7	150	1.43E-03	3.75E-03	2.63	9.292	7.530
8	200	1.32E-03	4.64E-03	3.51	9.374	7.567
9	250	1.24E-03	5.42E-03	4.39	9.429	7.591
10	300	1.16E-03	6.10E-03	5.26	9.468	7.607
11	350	1.09E-03	6.69E-03	6.14	9.497	7.619
12	400	1.03E-03	7.22E-03	7.02	9.520	7.629
13	500	9.26E-04	8.13E-03	8.77	9.554	7.643
14	600	8.42E-04	8.87E-03	10.53	9.580	7.654
15	700	7.72E-04	9.48E-03	12.28	9.598	7.661

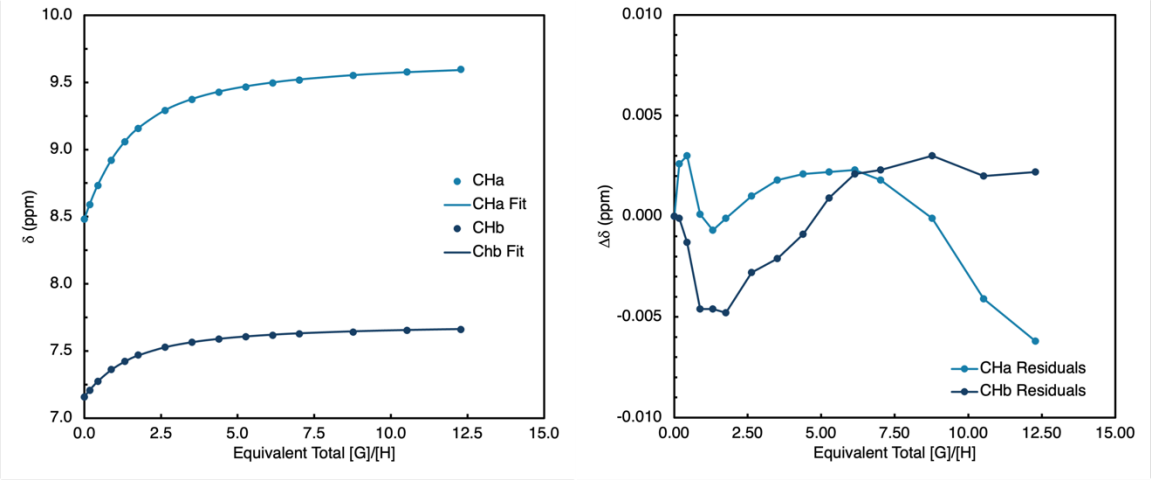

Figure C55. Representative binding isotherm and residuals of Br^- titration of $\mathbf{4}^{2+}$ in CD_3CN at room temperature determined via ^1H NMR spectroscopy.

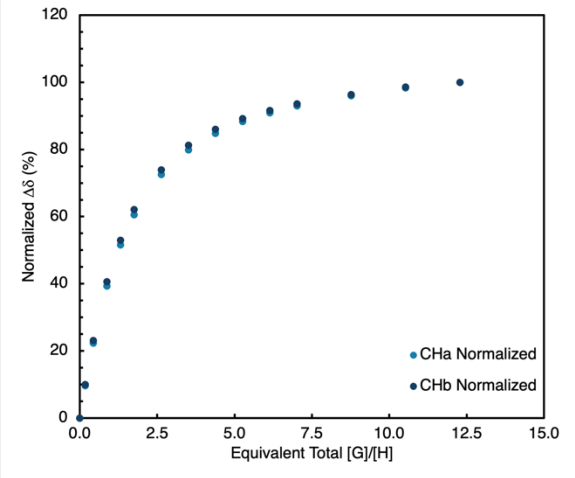

Figure C56. Normalized change in chemical shift of bound protons for Br^- titration of $\mathbf{4}^{2+}$.

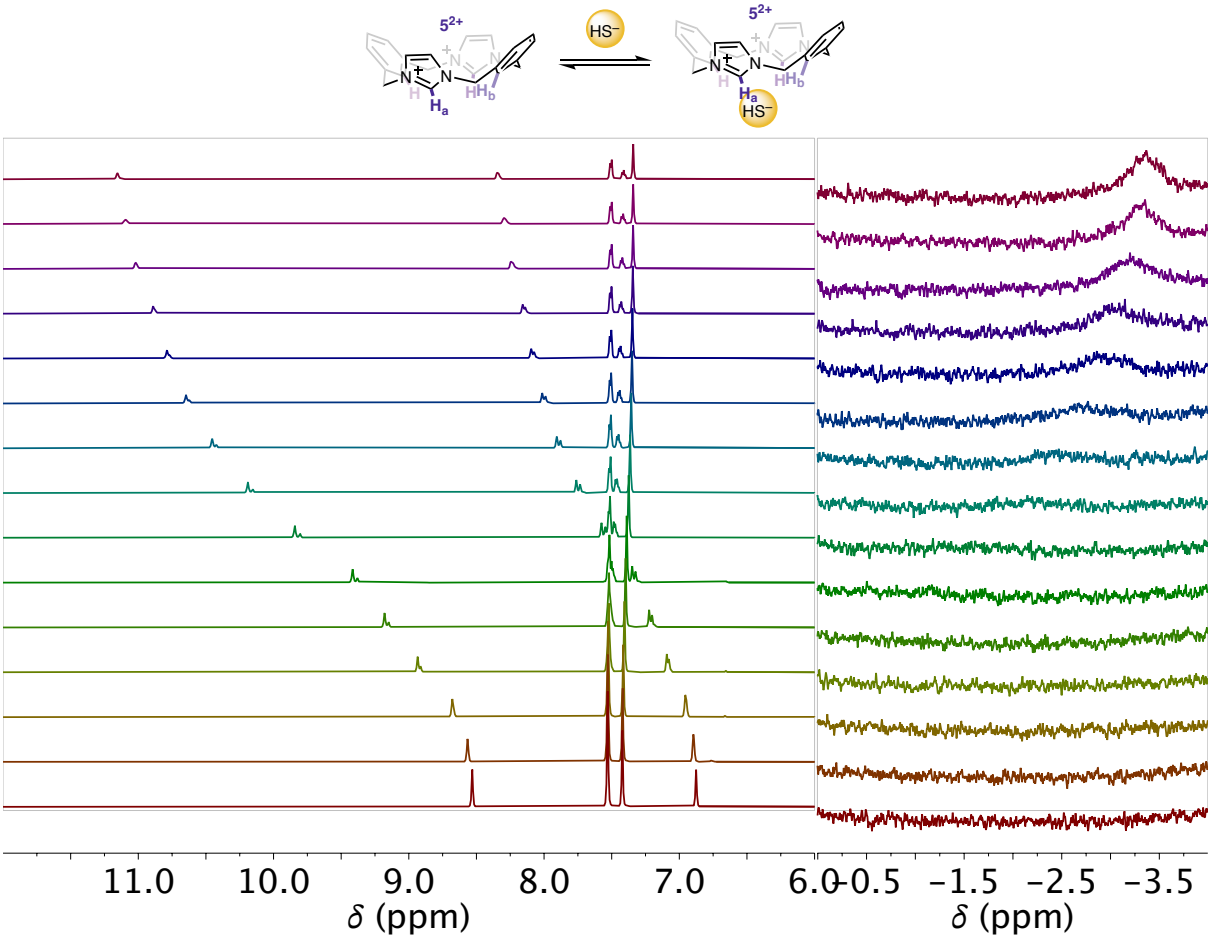

Figure C57. Titration scheme of receptor $\mathbf{5}^{2+}$ with HS^- and representative ^1H NMR spectra.

Table C15. Representative titration of receptor $\mathbf{5}^{2+}$ with HS^- in CD_3CN at room temperature.

Entry	$V_{total,\ guest}$ (μL)	[Receptor] (M)	[Guest] (M)	Anion Equiv.	CH_a (ppm)	CH_b (ppm)
1	0	1.58E-03	0.00E+00	0.00	8.531	6.876
2	10	1.55E-03	5.61E-05	0.04	8.566	6.896
3	25	1.51E-03	1.36E-04	0.09	8.678	6.957
4	50	1.44E-03	2.60E-04	0.18	8.934	7.093
5	75	1.38E-03	3.73E-04	0.27	9.179	7.223
6	100	1.32E-03	4.77E-04	0.36	9.415	7.348
7	150	1.22E-03	6.60E-04	0.54	9.842	7.575
8	200	1.13E-03	8.18E-04	0.72	10.190	7.762
9	250	1.05E-03	9.54E-04	0.90	10.454	7.906
10	300	9.88E-04	1.07E-03	1.09	10.647	8.014
11	350	9.30E-04	1.18E-03	1.27	10.787	8.095
12	400	8.79E-04	1.27E-03	1.45	10.890	8.158
13	500	7.91E-04	1.43E-03	1.81	11.020	8.246
14	600	7.19E-04	1.56E-03	2.17	11.094	8.293
15	700	6.59E-04	1.67E-03	2.53	11.154	8.347

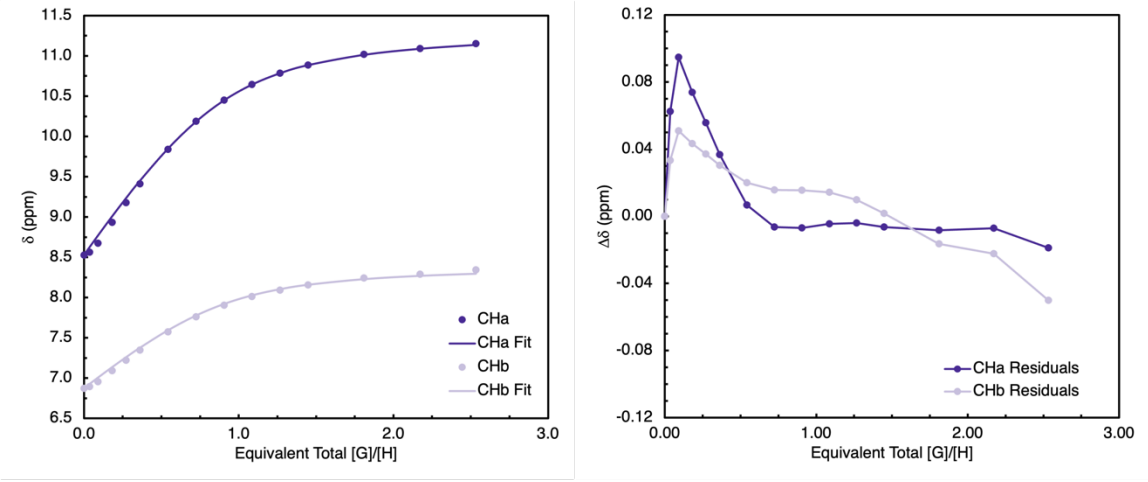

Figure C58. Representative binding isotherm and residuals of HS^- titration of $\mathbf{5}^{2+}$ in CD_3CN at room temperature determined via ^1H NMR spectroscopy.

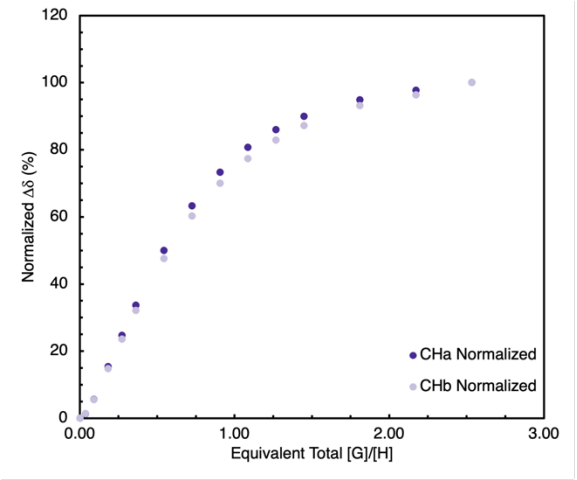

Figure C59. Normalized change in chemical shift of bound protons for HS^- titration of $\mathbf{5}^{2+}$.

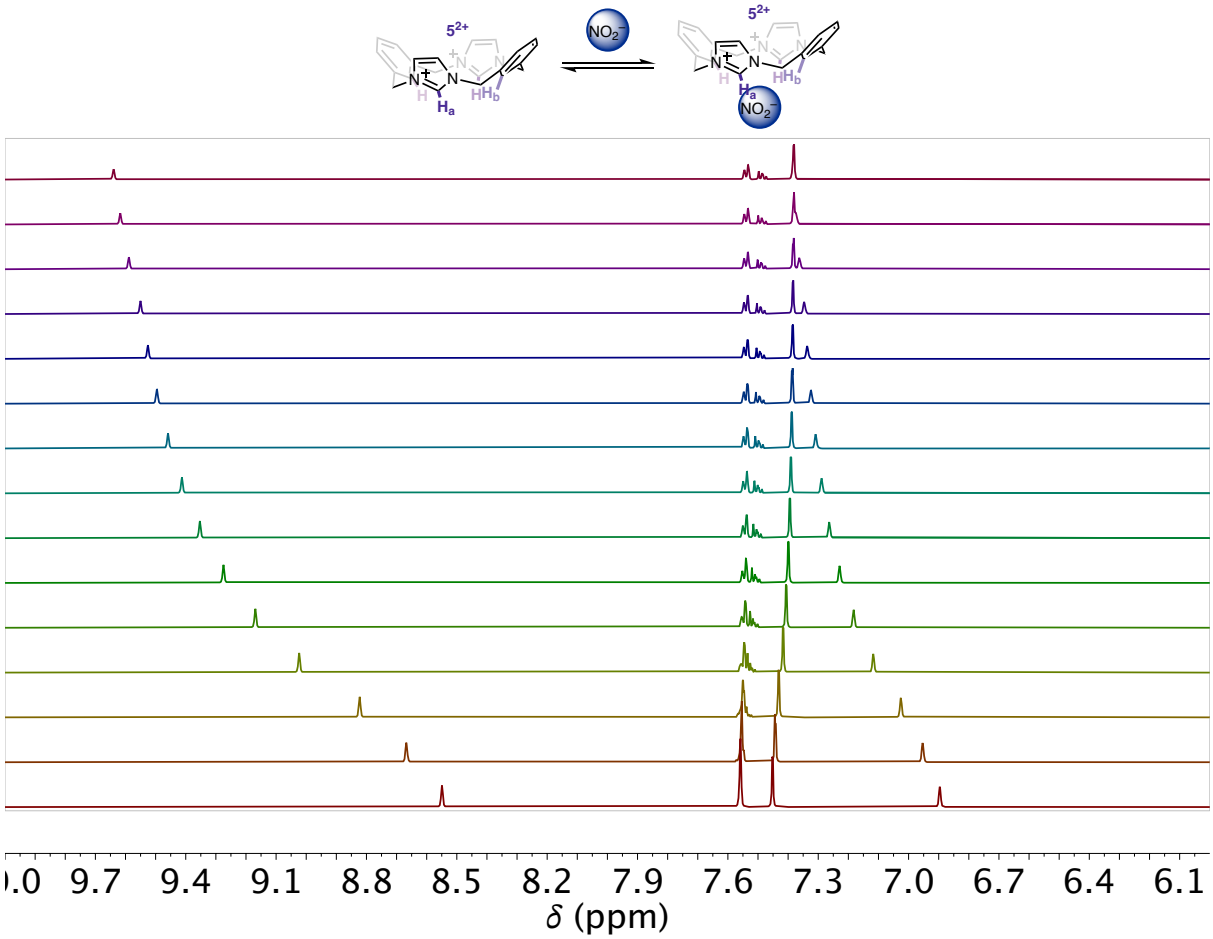

Figure C60. Titration scheme of receptor $\mathbf{5}^{2+}$ with NO_2^- and representative ^1H NMR spectra.

Table C16. Representative titration of receptor $\mathbf{5}^{2+}$ with NO_2^- in CD_3CN at room temperature.

Entry	$V_{total,\ guest}$ (μL)	[Receptor] (M)	[Guest] (M)	Anion Equiv.	CH_a (ppm)	CH_b (ppm)
1	0	1.58E-03	0.00E+00	0.00	8.521	6.868
2	10	1.55E-03	1.99E-04	0.13	8.632	6.920
3	25	1.51E-03	4.83E-04	0.32	8.790	6.995
4	50	1.44E-03	9.21E-04	0.64	8.995	7.089
5	75	1.38E-03	1.32E-03	0.96	9.140	7.154
6	100	1.32E-03	1.69E-03	1.28	9.246	7.201
7	125	1.27E-03	2.03E-03	1.60	9.325	7.235
8	150	1.22E-03	2.34E-03	1.92	9.384	7.261
9	175	1.17E-03	2.63E-03	2.24	9.430	7.280
10	200	1.13E-03	2.90E-03	2.56	9.467	7.296
11	225	1.09E-03	3.14E-03	2.88	9.497	7.308
12	250	1.05E-03	3.38E-03	3.20	9.522	7.318
13	300	9.88E-04	3.80E-03	3.84	9.560	7.334
14	350	9.30E-04	4.17E-03	4.49	9.589	7.347
15	400	8.79E-04	4.50E-03	5.13	9.611	7.356

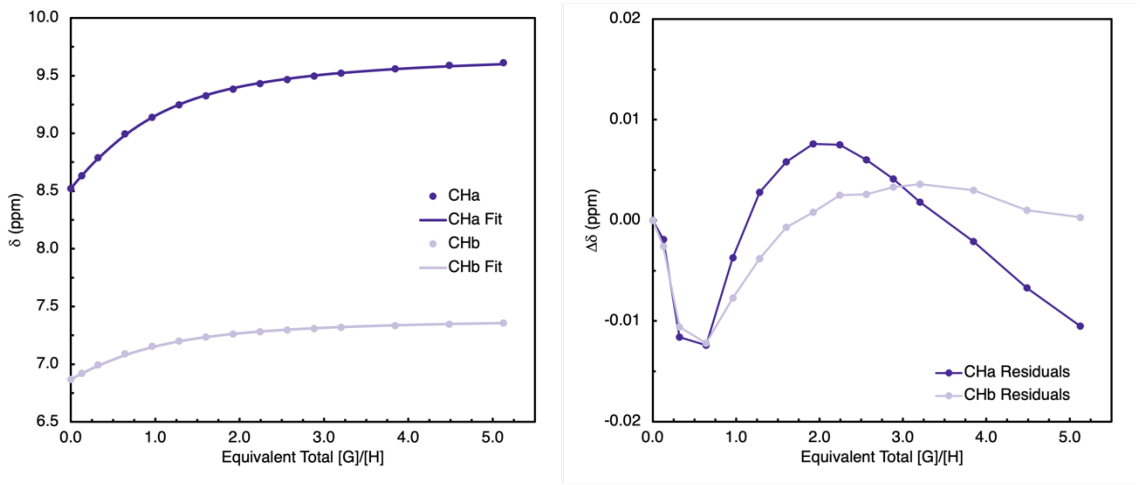

Figure C61. Representative binding isotherm and residuals of NO_2^- titration of $\mathbf{5}^{2+}$ in CD_3CN at room temperature determined via ^1H NMR spectroscopy.

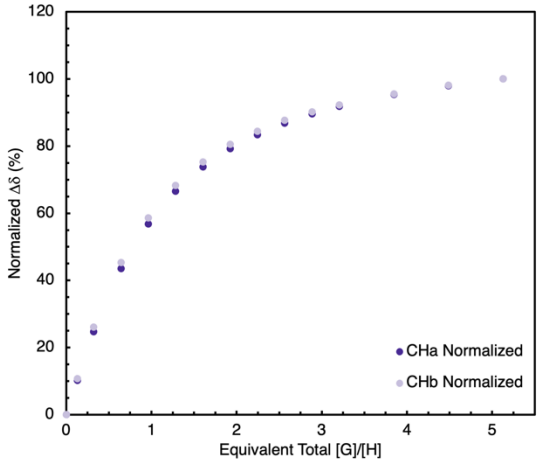

Figure C62. Normalized change in chemical shift of bound protons for NO_2^- titration of $\mathbf{5}^{2+}$.

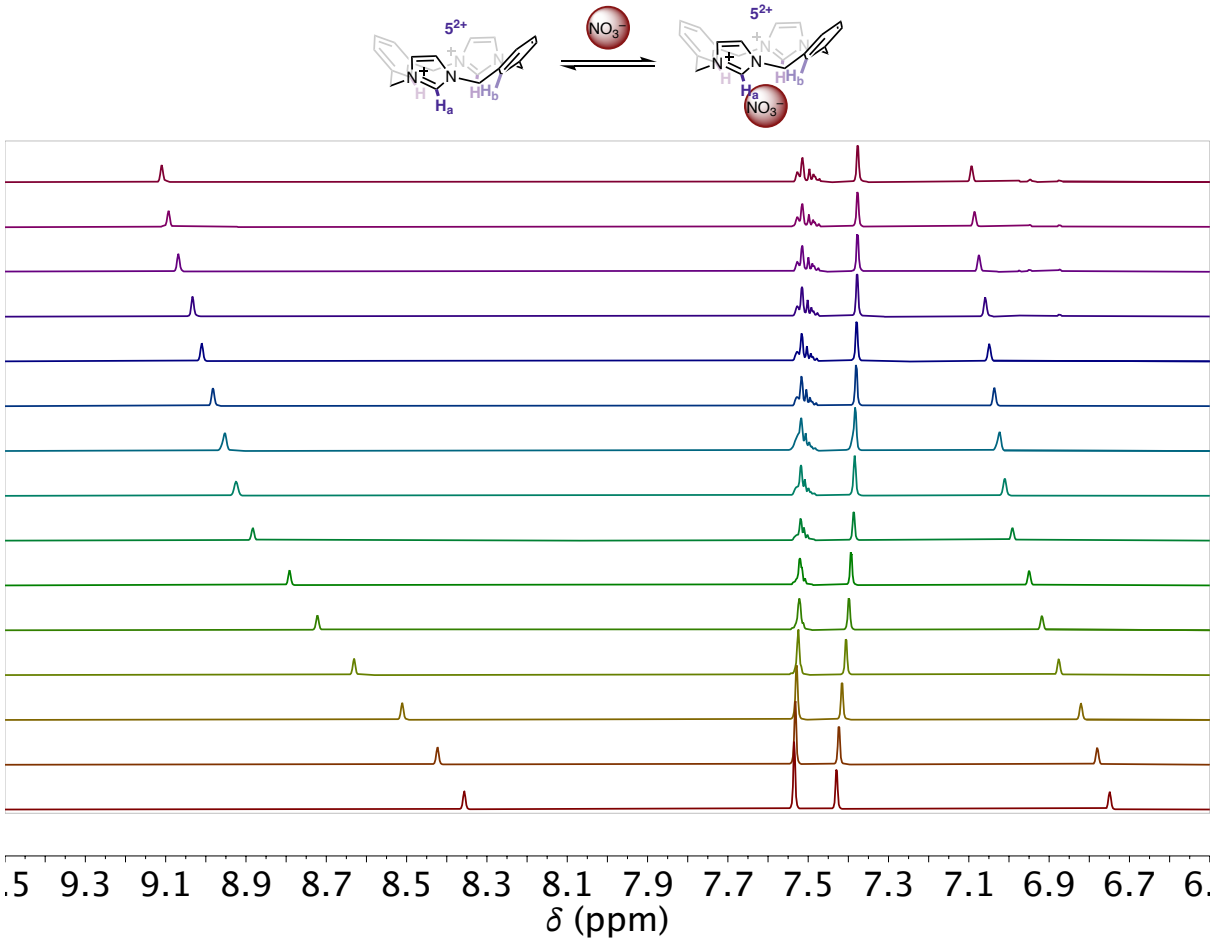

Figure C63. Titration scheme of receptor $\mathbf{5}^{2+}$ with NO_3^- and representative ^1H NMR spectra.

Table C17. Representative titration of receptor $\mathbf{5}^{2+}$ with NO_3^- in CD_3CN at room temperature.

Entry	$V_{total,\ guest}$ (μL)	[Receptor] (M)	[Guest] (M)	Anion Equiv.	CH_a (ppm)	CH_b (ppm)
1	0	1.95E-03	0.00E+00	0.00	8.356	6.749
2	10	1.92E-03	2.40E-04	0.13	8.423	6.780
3	25	1.86E-03	5.82E-04	0.31	8.511	6.821
4	50	1.78E-03	1.11E-03	0.63	8.631	6.876
5	75	1.70E-03	1.59E-03	0.94	8.722	6.918
6	100	1.63E-03	2.04E-03	1.25	8.791	6.950
7	150	1.50E-03	2.82E-03	1.88	8.883	6.991
8	200	1.40E-03	3.49E-03	2.50	8.925	7.010
9	250	1.30E-03	4.07E-03	3.13	8.953	7.024
10	300	1.22E-03	4.58E-03	3.75	8.982	7.036
11	350	1.15E-03	5.03E-03	4.38	9.010	7.049
12	400	1.09E-03	5.43E-03	5.00	9.033	7.059
13	500	9.77E-04	6.11E-03	6.25	9.068	7.075
14	600	8.88E-04	6.66E-03	7.51	9.093	7.085
15	700	8.14E-04	7.13E-03	8.76	9.110	7.093

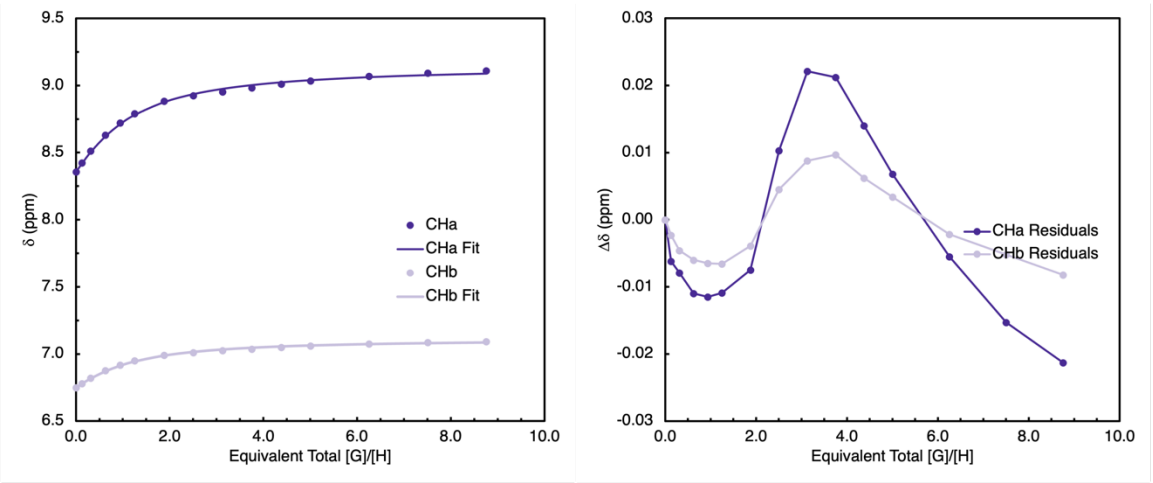

Figure C64. Representative binding isotherm and residuals of NO_3^- titration of $\mathbf{5}^{2+}$ in CD_3CN at room temperature determined via ^1H NMR spectroscopy.

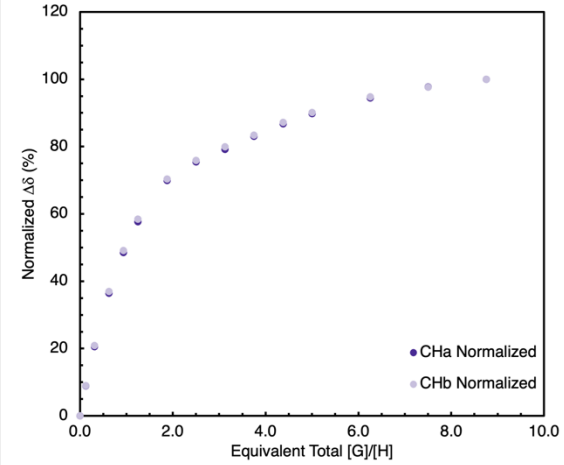

Figure C65. Normalized change in chemical shift of bound protons for NO_3^- titration of $\mathbf{5}^{2+}$.

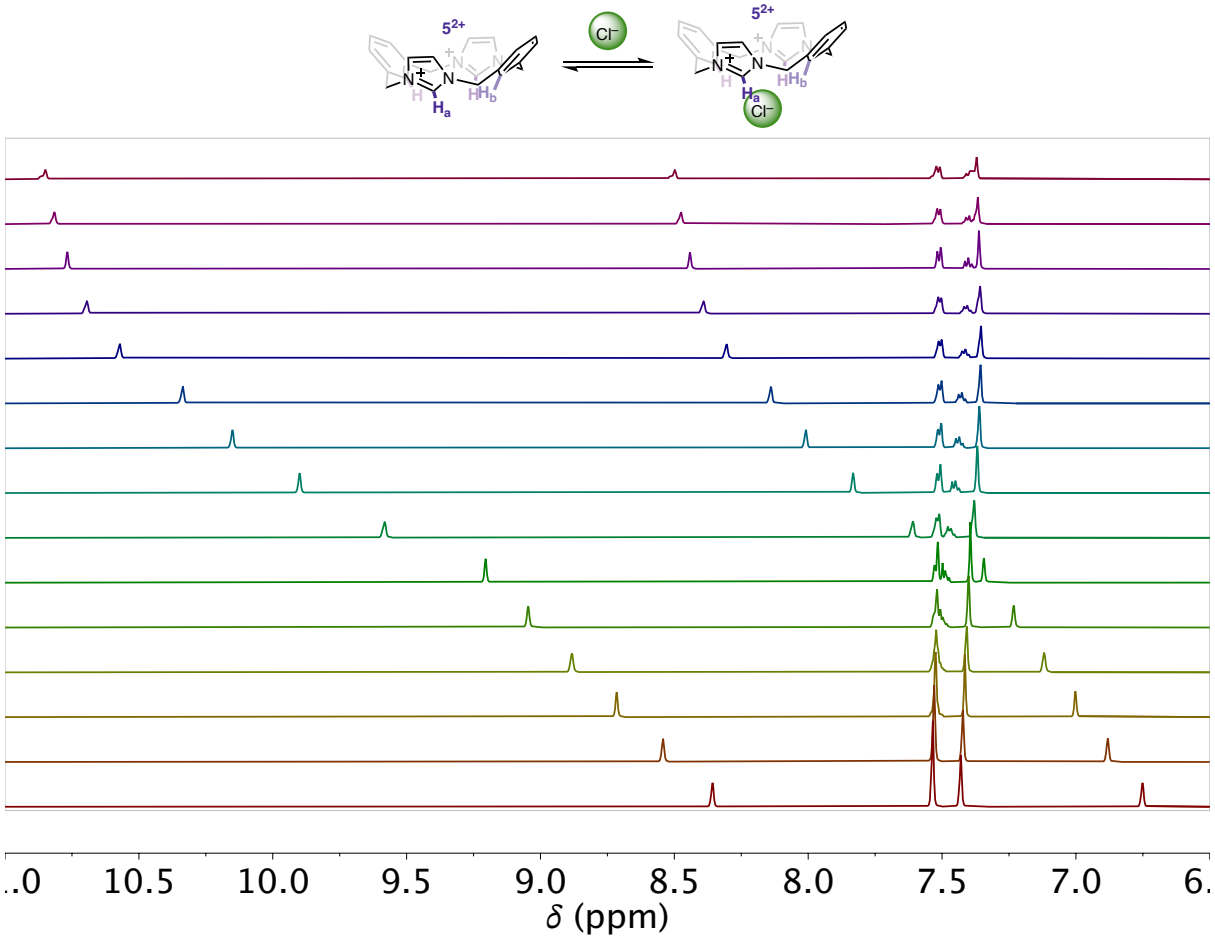

Figure C66. Titration scheme of receptor $\mathbf{5}^{2+}$ with Cl^- and representative ^1H NMR spectra.

Table C18. Representative titration of receptor $\mathbf{5}^{2+}$ with Cl^- in CD_3CN at room temperature.

Entry	$V_{total,\ guest}$ (μL)	[Receptor] (M)	[Guest] (M)	Anion Equiv.	CH_a (ppm)	CH_b (ppm)
1	0	1.95E-03	0.00E+00	0.00	8.357	6.751
2	10	1.92E-03	1.36E-04	0.07	8.542	6.881
3	20	1.88E-03	2.67E-04	0.14	8.716	7.002
4	30	1.84E-03	3.93E-04	0.21	8.883	7.119
5	40	1.81E-03	5.15E-04	0.28	9.046	7.233
6	50	1.78E-03	6.32E-04	0.36	9.205	7.344
7	75	1.70E-03	9.06E-04	0.53	9.586	7.613
8	100	1.63E-03	1.16E-03	0.71	9.900	7.832
9	125	1.56E-03	1.39E-03	0.89	10.151	8.009
10	150	1.50E-03	1.60E-03	1.07	10.336	8.139
11	200	1.40E-03	1.99E-03	1.42	10.571	8.304
12	250	1.30E-03	2.32E-03	1.78	10.694	8.390
13	300	1.22E-03	2.61E-03	2.13	10.768	8.442
14	350	1.15E-03	2.86E-03	2.49	10.815	8.475
15	400	1.09E-03	3.09E-03	2.85	10.849	8.498

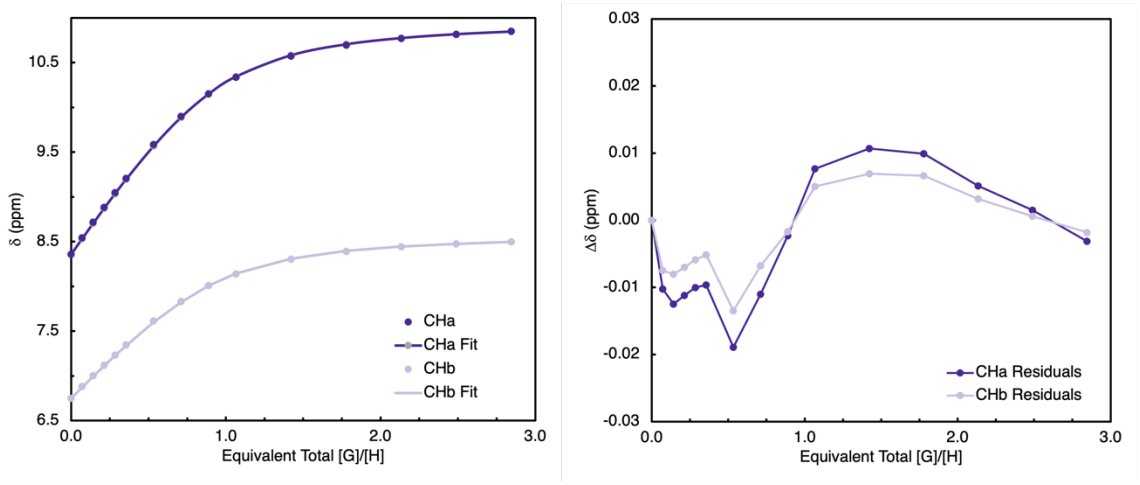

Figure C67. Representative binding isotherm and residuals of Cl^- titration of $\mathbf{5}^{2+}$ in CD_3CN at room temperature determined via ^1H NMR spectroscopy.

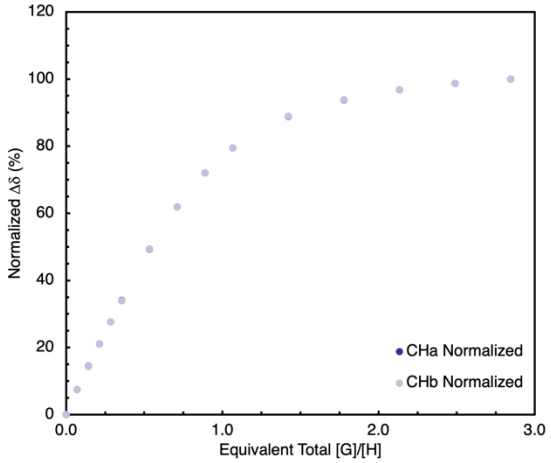

Figure C68. Normalized change in chemical shift of bound protons for Cl^- titration of $\mathbf{5}^{2+}$.

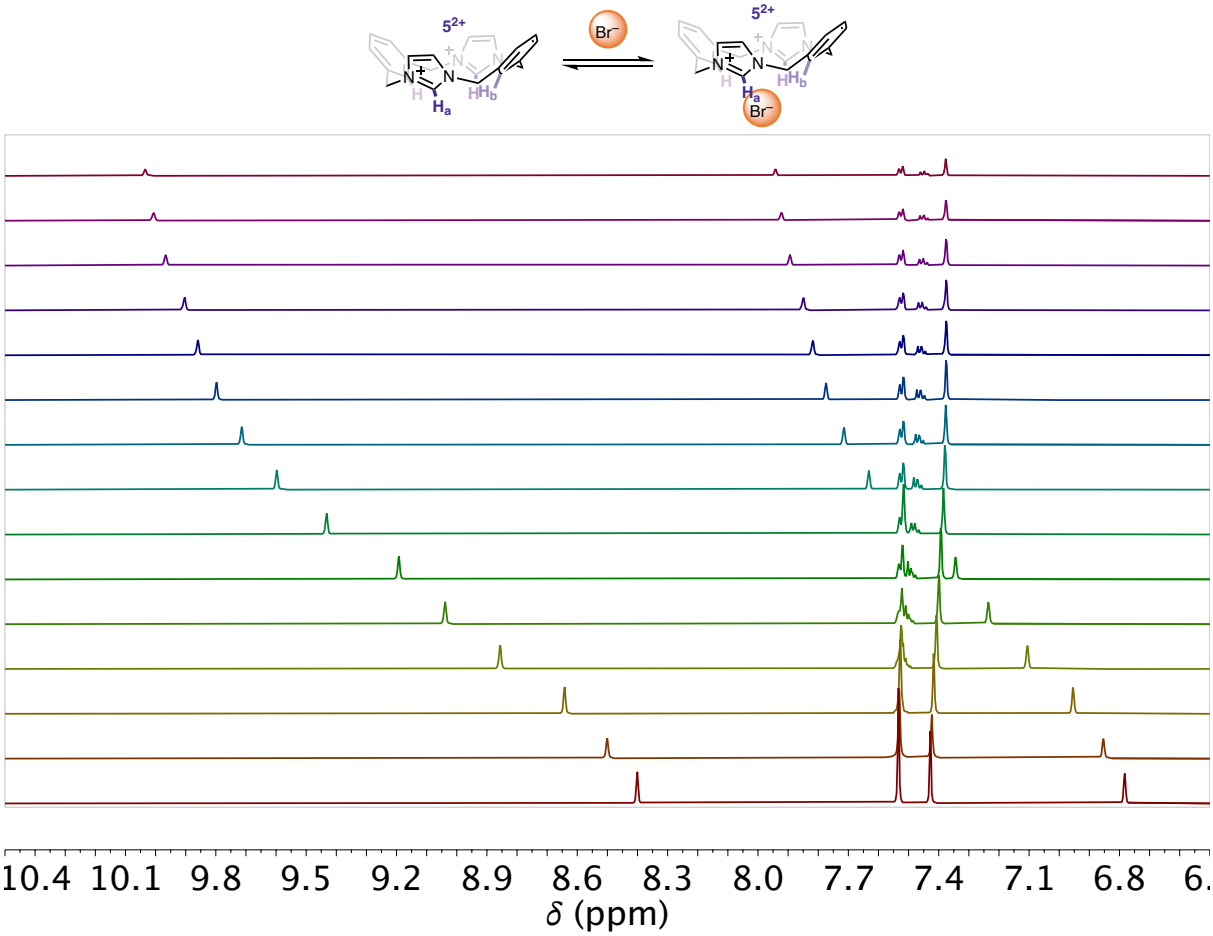

Figure C69. Titration scheme of receptor $\mathbf{5}^{2+}$ with Br^- and representative ^1H NMR spectra.

Table C19. Representative titration of receptor $\mathbf{5}^{2+}$ with Br^- in CD_3CN at room temperature.

Entry	$V_{total,\ guest}$ (μL)	[Receptor] (M)	[Guest] (M)	Anion Equiv.	CH_a (ppm)	CH_b (ppm)
1	0	1.40E-03	0.00E+00	0.00	8.401	6.783
2	10	1.37E-03	1.12E-04	0.08	8.501	6.854
3	25	1.33E-03	2.72E-04	0.20	8.642	6.954
4	50	1.27E-03	5.19E-04	0.41	8.856	7.106
5	75	1.21E-03	7.44E-04	0.61	9.039	7.235
6	100	1.16E-03	9.51E-04	0.82	9.192	7.344
7	150	1.07E-03	1.32E-03	1.23	9.432	7.530
8	200	9.97E-04	1.63E-03	1.64	9.598	7.632
9	250	9.30E-04	1.90E-03	2.05	9.714	7.715
10	300	8.72E-04	2.14E-03	2.45	9.798	7.774
11	350	8.21E-04	2.35E-03	2.86	9.859	7.818
12	400	7.75E-04	2.54E-03	3.27	9.903	7.849
13	500	6.98E-04	2.85E-03	4.09	9.967	7.894
14	600	6.34E-04	3.11E-03	4.91	10.007	7.922
15	700	5.81E-04	3.33E-03	5.73	10.034	7.942

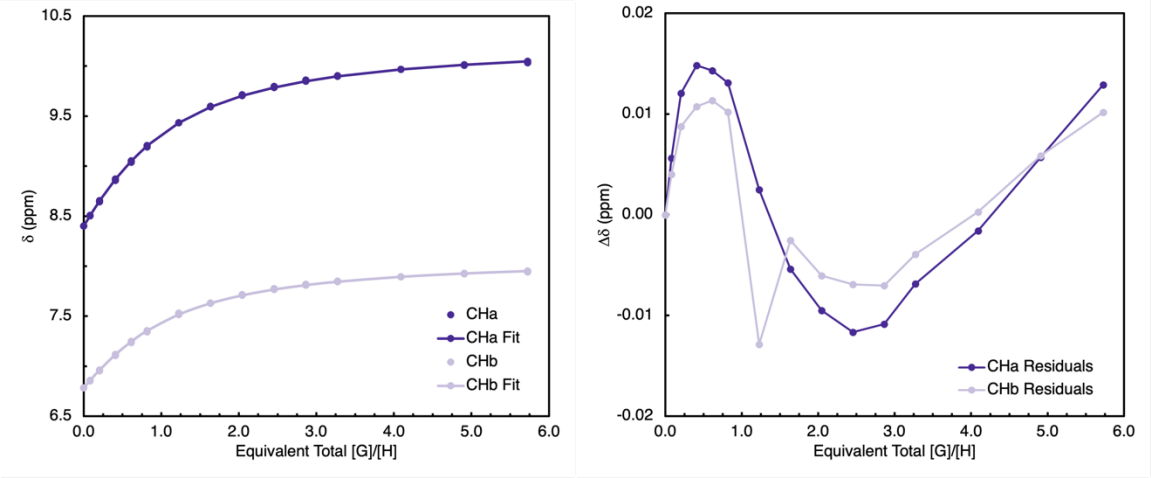

Figure C70. Representative binding isotherm and residuals of Br^- titration of $\mathbf{5}^{2+}$ in CD_3CN at room temperature determined via ^1H NMR spectroscopy.

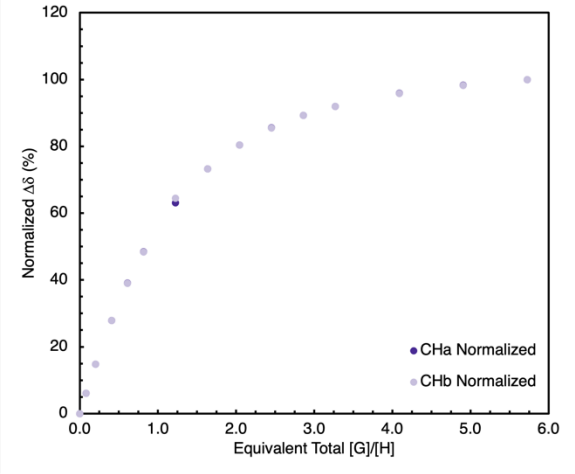

Figure C71. Normalized change in chemical shift of bound protons for Br^- titration of $\mathbf{5}^{2+}$.

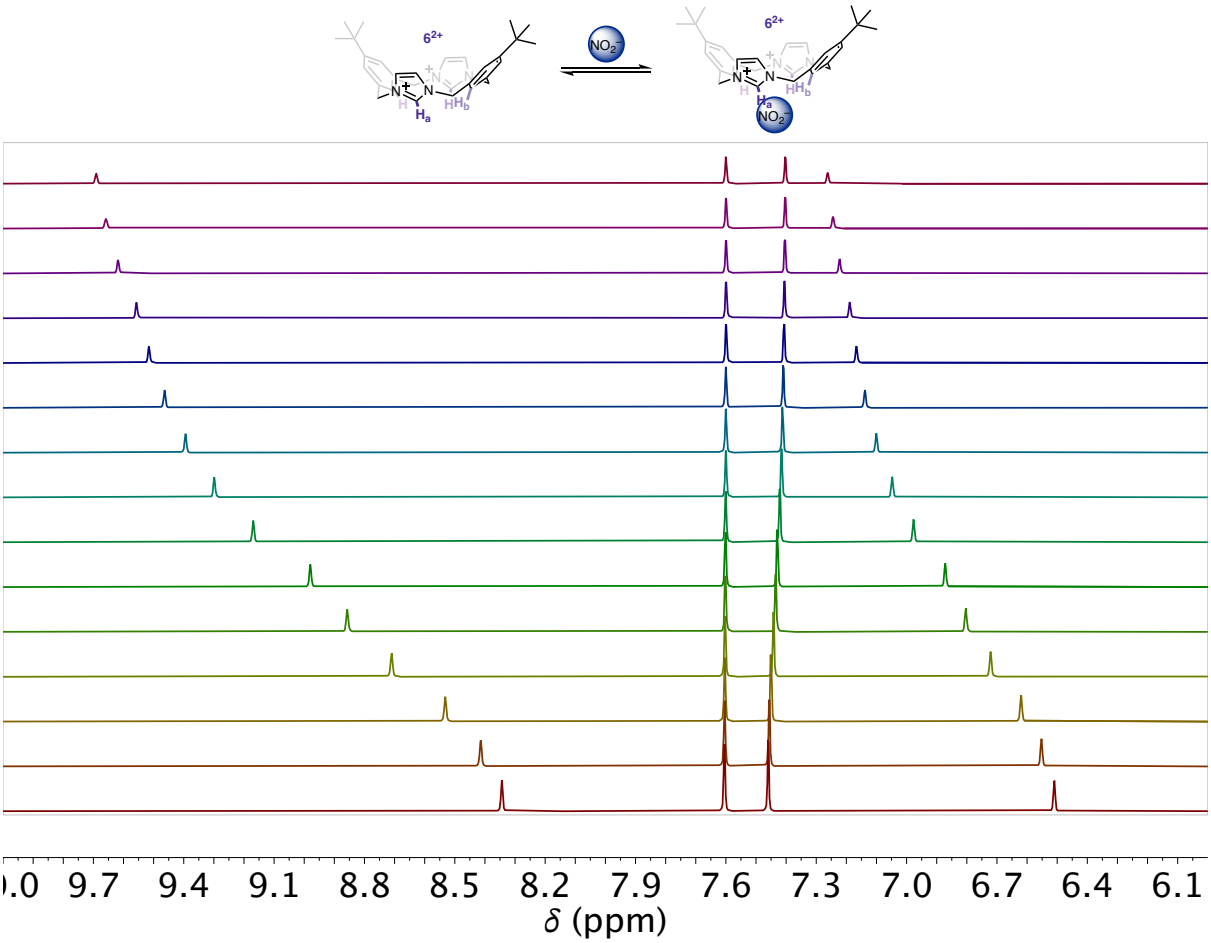

Figure C72. Titration scheme of receptor $\mathbf{6}^{2+}$ with NO_2^- and representative ^1H NMR spectra.

Table C20. Representative titration of receptor **6** with NO_2^- in CD_3CN at room temperature.

Entry	$V_{total,\ guest}$ (μL)	[Receptor] (M)	[Guest] (M)	Anion Equiv.	CH_a (ppm)	CH_b (ppm)
1	0	8.69E-04	0.00E+00	0.00	8.315	6.481
2	10	8.52E-04	7.34E-05	0.09	8.386	6.524
3	25	8.28E-04	1.78E-04	0.22	8.503	6.592
4	50	7.90E-04	3.40E-04	0.43	8.682	6.693
5	75	7.56E-04	4.88E-04	0.65	8.829	6.775
6	100	7.24E-04	6.24E-04	0.86	8.952	6.843
7	150	6.68E-04	8.64E-04	1.29	9.141	6.948
8	200	6.21E-04	1.07E-03	1.72	9.271	7.020
9	250	5.79E-04	1.25E-03	2.15	9.366	7.072
10	300	5.43E-04	1.40E-03	2.58	9.435	7.110
11	350	5.11E-04	1.54E-03	3.02	9.487	7.138
12	400	4.83E-04	1.66E-03	3.45	9.529	7.161
13	500	4.35E-04	1.87E-03	4.31	9.590	7.194
14	600	3.95E-04	2.04E-03	5.17	9.630	7.216
15	700	3.62E-04	2.18E-03	6.03	9.662	7.234

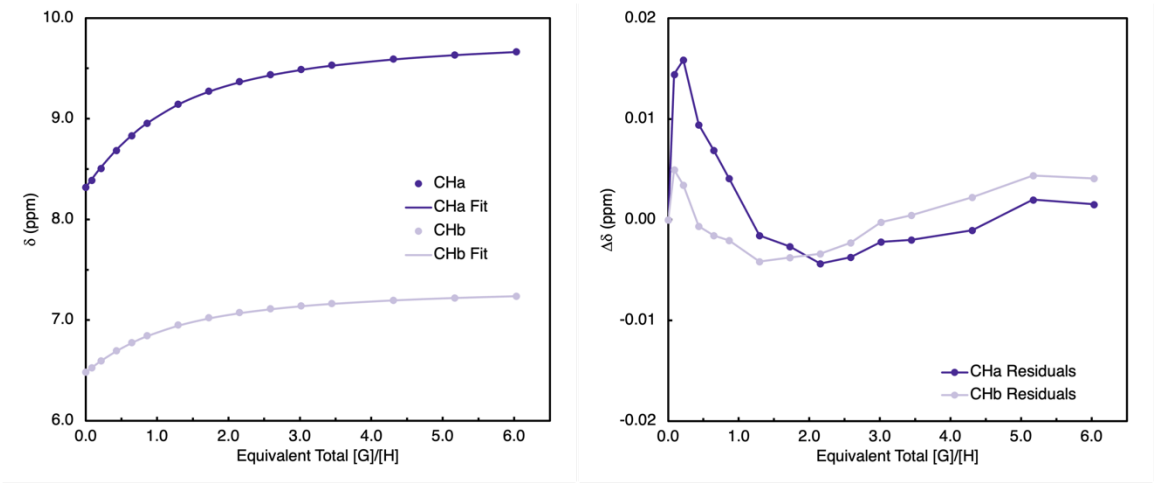

Figure C73. Representative binding isotherm and residuals of NO_2^- titration of $\mathbf{6}^{2+}$ in CD_3CN at room temperature determined via ^1H NMR spectroscopy.

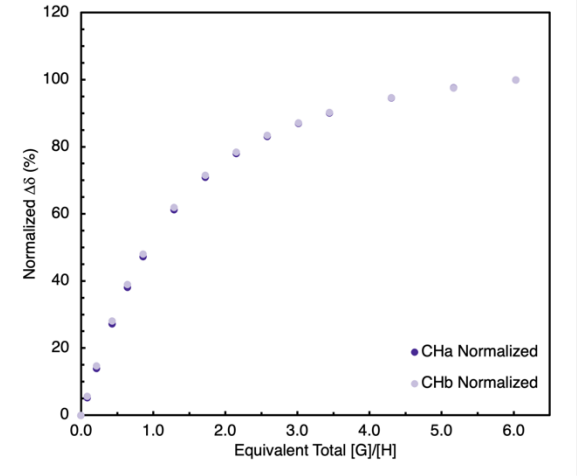

Figure C74. Normalized change in chemical shift of bound protons for NO_2^- titration of $\mathbf{6}^{2+}$.

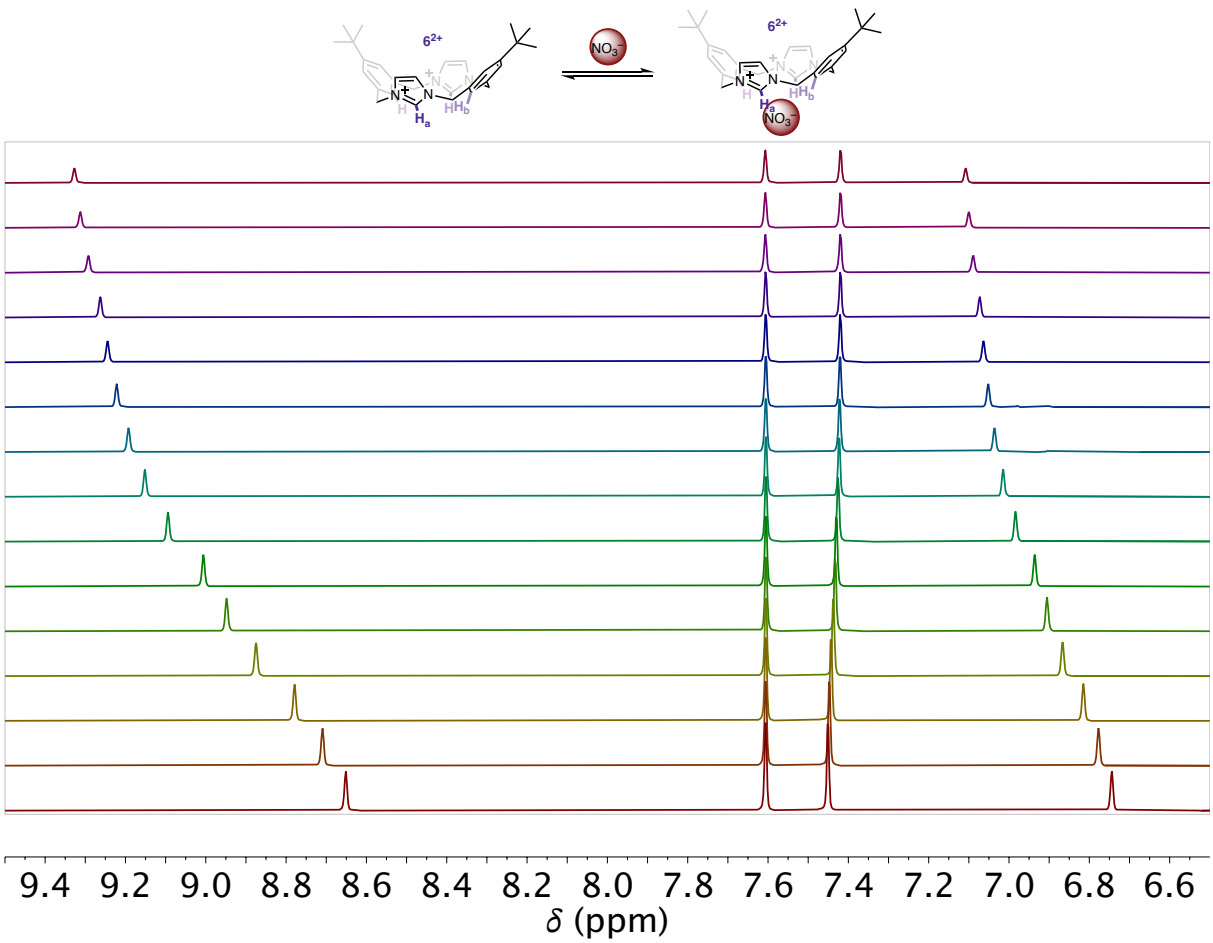

Figure C75. Titration scheme of receptor $\mathbf{6}^{2+}$ with NO_3^- and representative ^1H NMR spectra.

Table C21. Representative titration of receptor $\mathbf{6}^{2+}$ with NO_3^- in CD_3CN at room temperature.

Entry	$V_{total,\ guest}$ (μL)	[Receptor] (M)	[Guest] (M)	Anion Equiv.	CH_a (ppm)	CH_b (ppm)
1	0	1.11E-03	0.00E+00	0.00	8.623	6.715
2	10	1.08E-03	1.24E-04	0.11	8.618	6.749
3	25	1.05E-03	3.00E-04	0.29	8.750	6.786
4	50	1.01E-03	5.73E-04	0.57	8.846	6.838
5	75	9.62E-04	8.22E-04	0.86	8.920	6.877
6	100	9.22E-04	1.05E-03	1.14	8.977	6.907
7	150	8.51E-04	1.46E-03	1.71	9.066	6.955
8	200	7.90E-04	1.80E-03	2.28	9.123	6.986
9	250	7.37E-04	2.10E-03	2.85	9.164	7.008
10	300	6.91E-04	2.36E-03	3.42	9.193	7.023
11	350	6.51E-04	2.60E-03	3.99	9.216	7.035
12	400	6.14E-04	2.80E-03	4.56	9.234	7.044
13	500	5.53E-04	3.15E-03	5.70	9.264	7.061
14	600	5.03E-04	3.44E-03	6.84	9.284	7.071
15	700	4.61E-04	3.68E-03	7.98	9.299	7.080

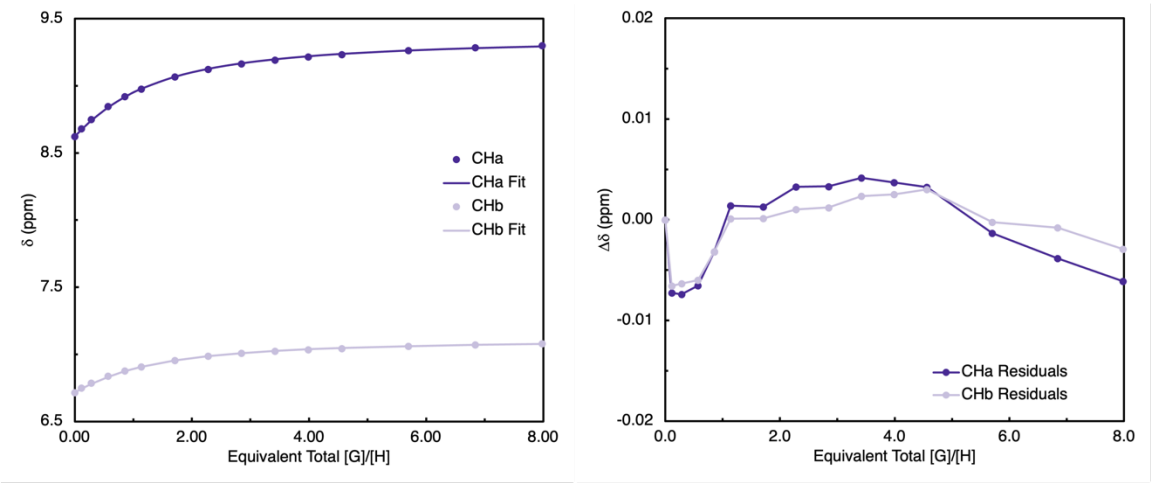

Figure C76. Representative binding isotherm and residuals of NO_3^- titration of $\mathbf{6}^{2+}$ in CD_3CN at room temperature determined via ^1H NMR spectroscopy.

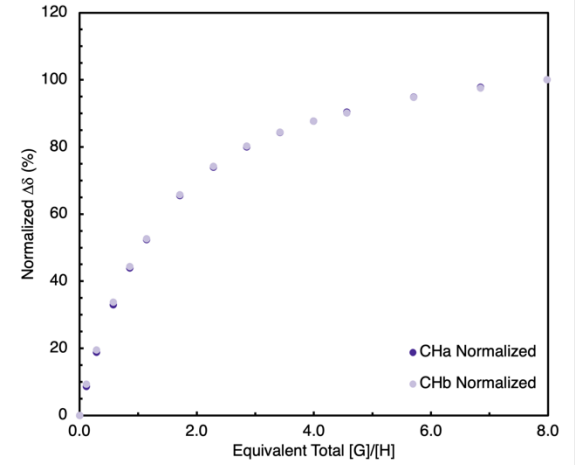

Figure C77. Normalized change in chemical shift of bound protons for NO_3^- titration of $\mathbf{6}^{2+}$.

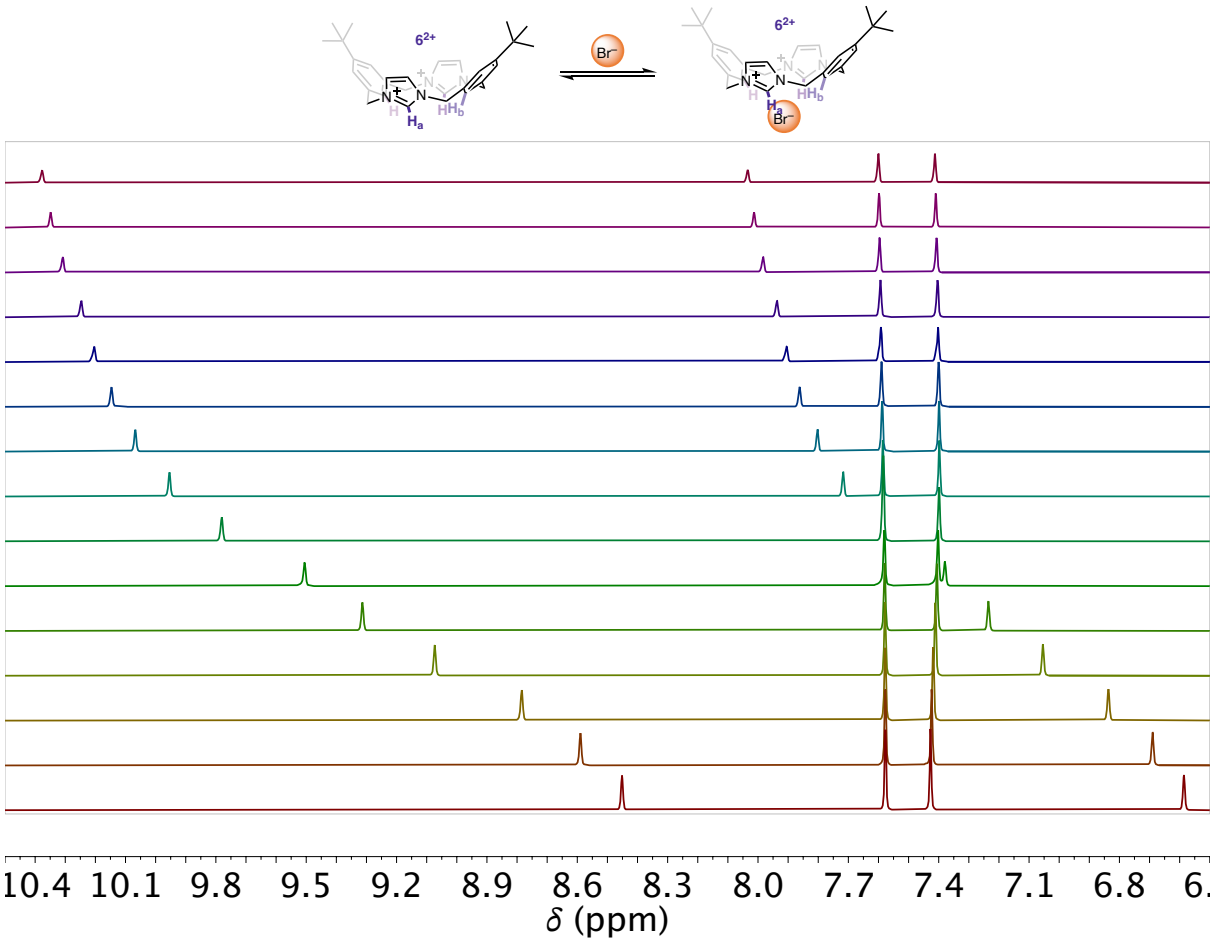

Figure C78. Titration scheme of receptor $\mathbf{6}^{2+}$ with Br^- and representative ^1H NMR spectra.

Table C22. Representative titration of receptor $\mathbf{6}^{2+}$ with Br^- in CD_3CN at room temperature.

Entry	$V_{total,\ guest}$ (μL)	[Receptor] (M)	[Guest] (M)	Anion Equiv.	CH_a (ppm)	CH_b (ppm)
1	0	1.26E-03	0.00E+00	0.00	8.452	6.586
2	10	1.24E-03	1.17E-04	0.09	8.590	6.690
3	25	1.20E-03	2.84E-04	0.24	8.785	6.837
4	50	1.15E-03	5.41E-04	0.47	9.073	7.054
5	75	1.10E-03	7.77E-04	0.71	9.313	7.235
6	100	1.05E-03	9.93E-04	0.94	9.505	7.379
7	150	9.72E-04	1.37E-03	1.41	9.781	7.584
8	200	9.03E-04	1.70E-03	1.88	9.954	7.717
9	250	8.43E-04	1.99E-03	2.36	10.068	7.803
10	300	7.90E-04	2.23E-03	2.83	10.147	7.862
11	350	7.44E-04	2.45E-03	3.30	10.203	7.905
12	400	7.02E-04	2.65E-03	3.77	10.247	7.937
13	500	6.32E-04	2.98E-03	4.71	10.308	7.983
14	600	5.75E-04	3.25E-03	5.65	10.349	8.013
15	700	5.27E-04	3.47E-03	6.60	10.377	8.034

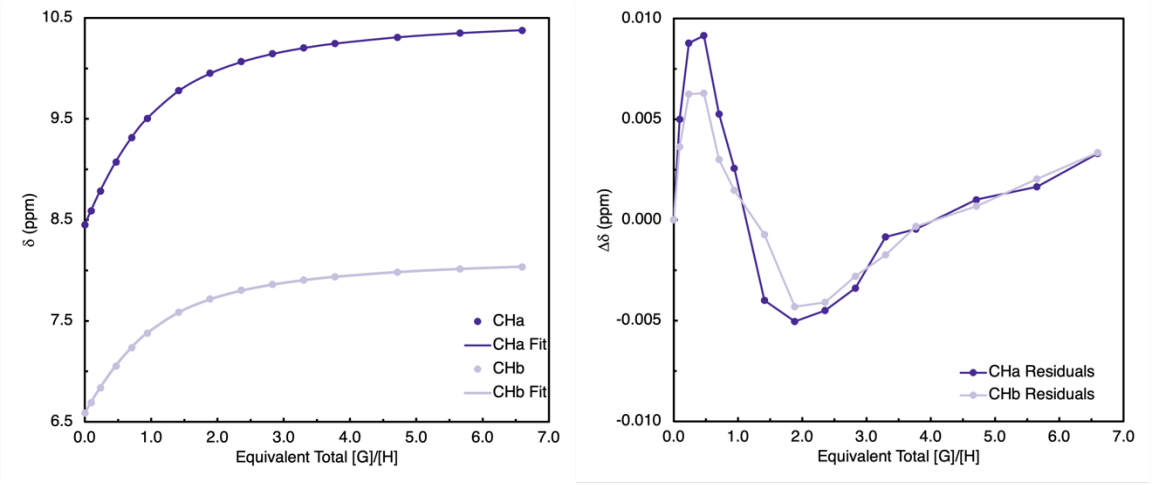

Figure C79. Representative binding isotherm and residuals of Br^- titration of $\mathbf{6}^{2+}$ in CD_3CN at room temperature determined via ^1H NMR spectroscopy.

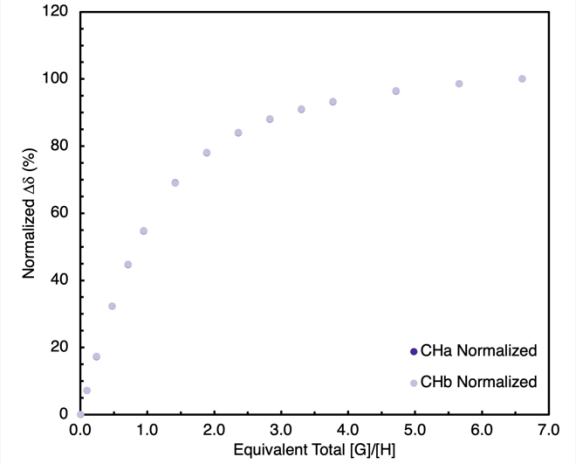

Figure C80. Normalized change in chemical shift of bound protons for Br^- titration of $\mathbf{6}^{2+}$.

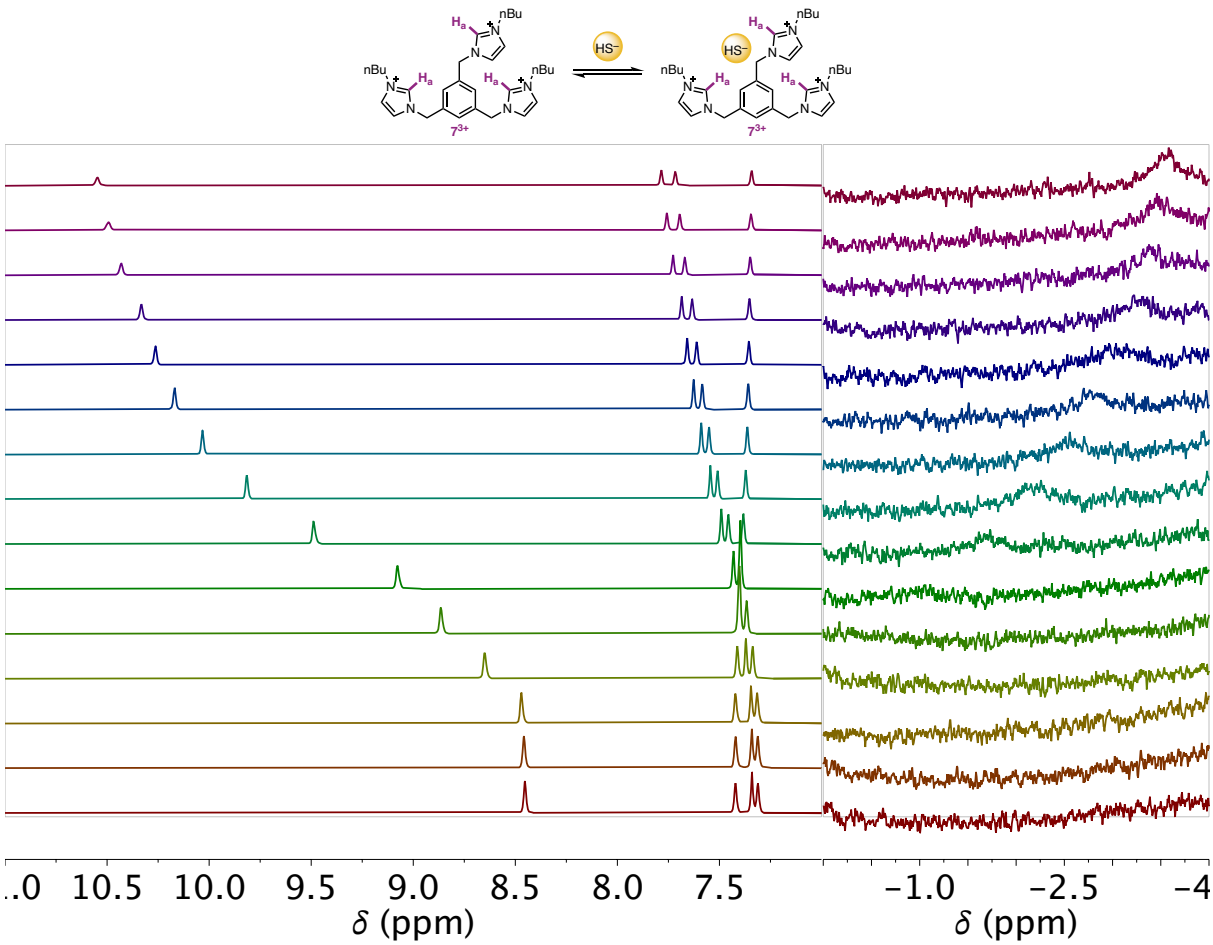

Figure C81. Titration scheme of receptor $\mathbf{7}^{3+}$ with HS^- and representative ^1H NMR spectra.

Table C23. Representative titration of receptor $\mathbf{7}^{3+}$ with HS^- in CD_3CN at room temperature.

Entry	$V_{total,\ guest}$ (μL)	[Receptor] (M)	[Guest] (M)	Anion Equiv.	CH_a (ppm)
1	0	2.29E-03	0.00E+00	0.00	8.454
2	10	2.25E-03	1.21E-04	0.05	8.483
3	25	2.18E-03	2.94E-04	0.13	8.496
4	50	2.08E-03	5.62E-04	0.27	8.664
5	75	1.99E-03	8.06E-04	0.40	8.879
6	100	1.91E-03	1.03E-03	0.54	9.092
7	150	1.76E-03	1.43E-03	0.81	9.498
8	200	1.64E-03	1.77E-03	1.08	9.817
9	250	1.53E-03	2.06E-03	1.35	10.024
10	300	1.43E-03	2.32E-03	1.62	10.155
11	350	1.35E-03	2.55E-03	1.89	10.243
12	400	1.27E-03	2.75E-03	2.16	10.309
13	500	1.15E-03	3.09E-03	2.70	10.400
14	600	1.04E-03	3.37E-03	3.24	10.461
15	700	9.54E-04	3.61E-03	3.78	10.500

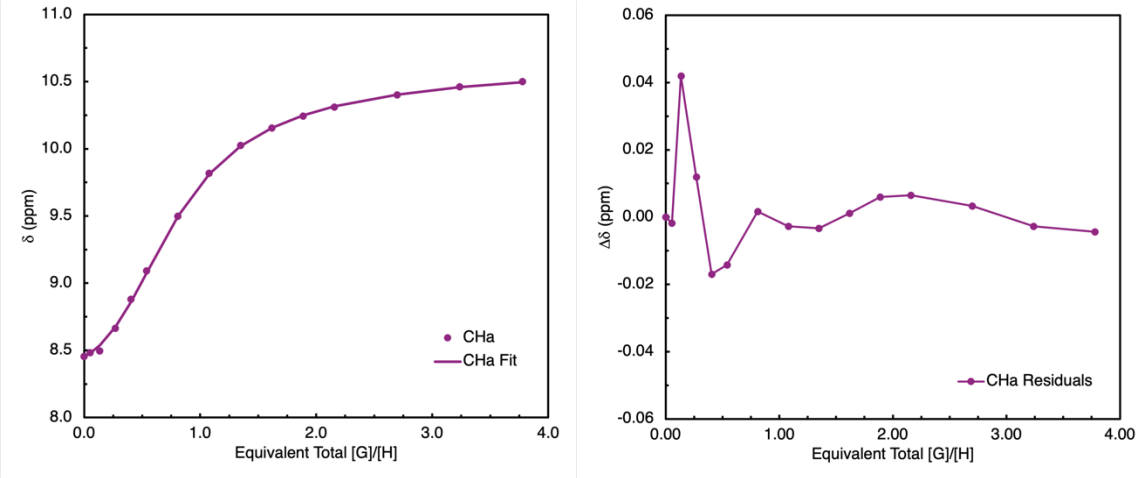

Figure C82. Representative binding isotherm and residuals of HS^- titration of $\mathbf{7}^{3+}$ in CD_3CN at room temperature determined via ^1H NMR spectroscopy.

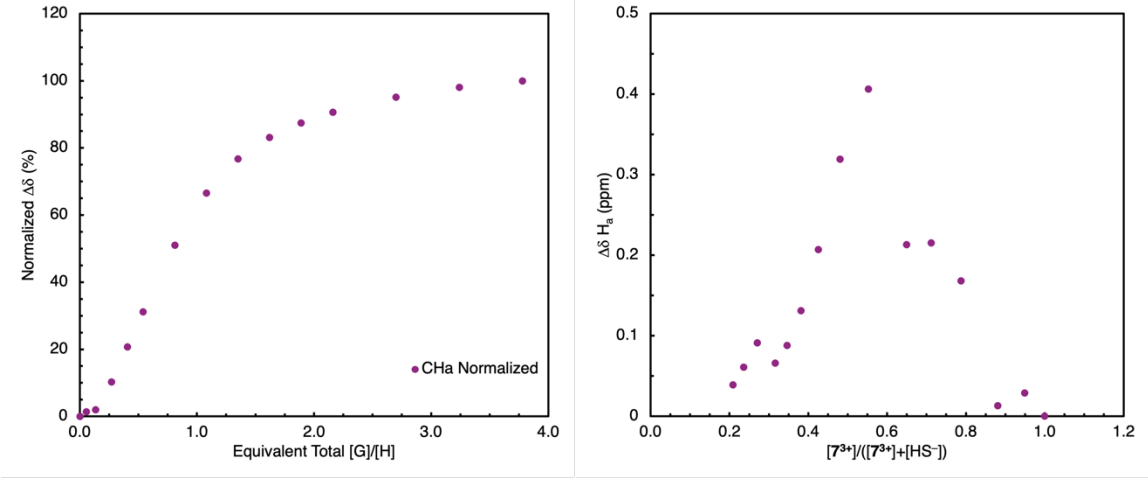

Figure C83. Normalized change in chemical shift of bound protons and Job Plot for HS^- titration of $\mathbf{7}^{3+}$.

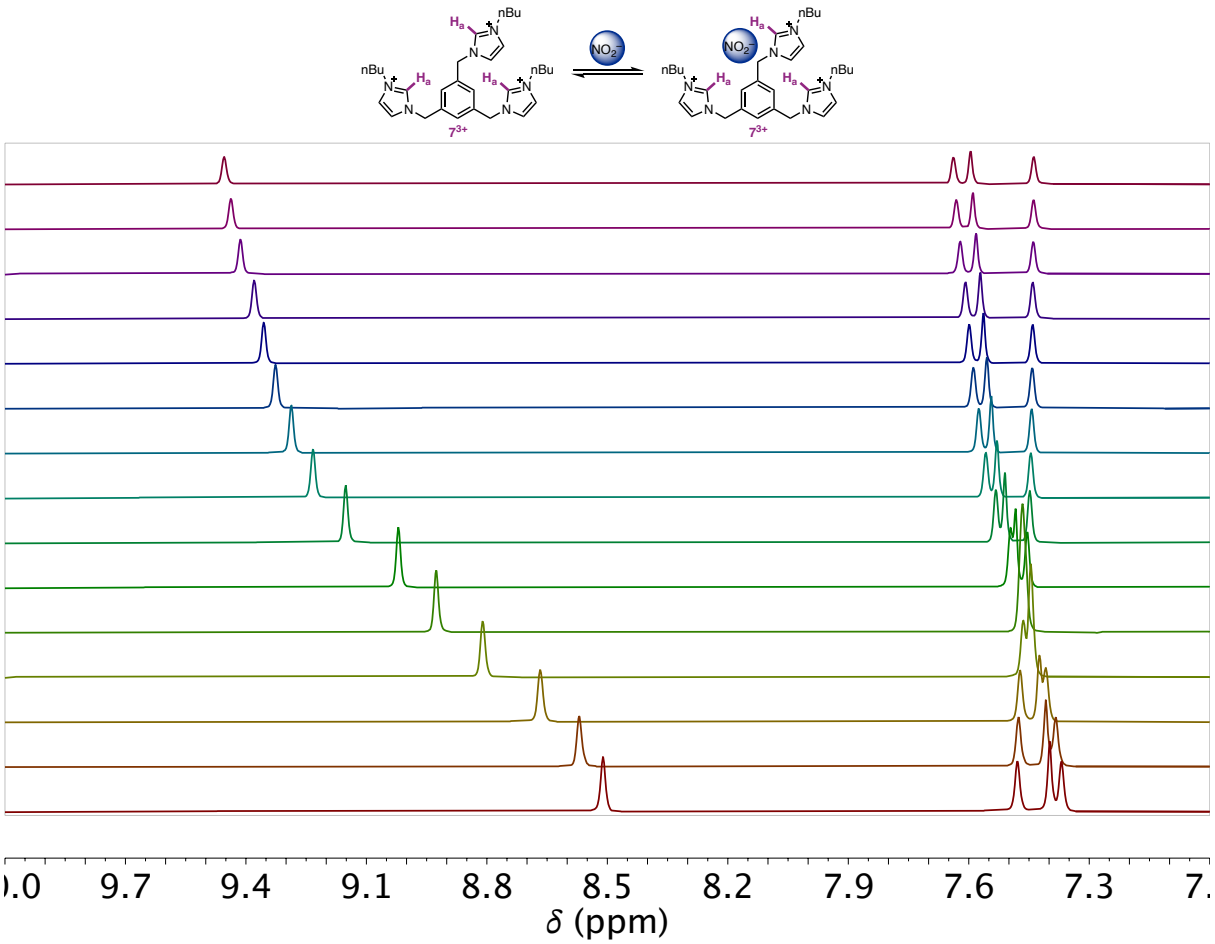

Figure C84. Titration scheme of receptor $\mathbf{7}^{3+}$ with NO_2^- and representative ^1H NMR spectra.

Table C24. Representative titration of receptor $\mathbf{7}^{3+}$ with NO_2^- in CD_3CN at room temperature.

Entry	$V_{total,\ guest}$ (μL)	[Receptor] (M)	[Guest] (M)	Anion Equiv.	CH_a (ppm)
1	0	2.29E-03	0.00E+00	0.00	8.453
2	10	2.25E-03	2.45E-04	0.11	8.513
3	25	2.18E-03	5.94E-04	0.27	8.610
4	50	2.08E-03	1.13E-03	0.54	8.753
5	75	1.99E-03	1.63E-03	0.82	8.870
6	100	1.91E-03	2.08E-03	1.09	8.964
7	150	1.76E-03	2.88E-03	1.63	9.095
8	200	1.64E-03	3.57E-03	2.18	9.176
9	250	1.53E-03	4.16E-03	2.72	9.229
10	300	1.43E-03	4.68E-03	3.27	9.268
11	350	1.35E-03	5.14E-03	3.81	9.297
12	400	1.27E-03	5.55E-03	4.36	9.321
13	500	1.15E-03	6.24E-03	5.45	9.355
14	600	1.04E-03	6.81E-03	6.54	9.381
15	700	9.54E-04	7.28E-03	7.63	9.397

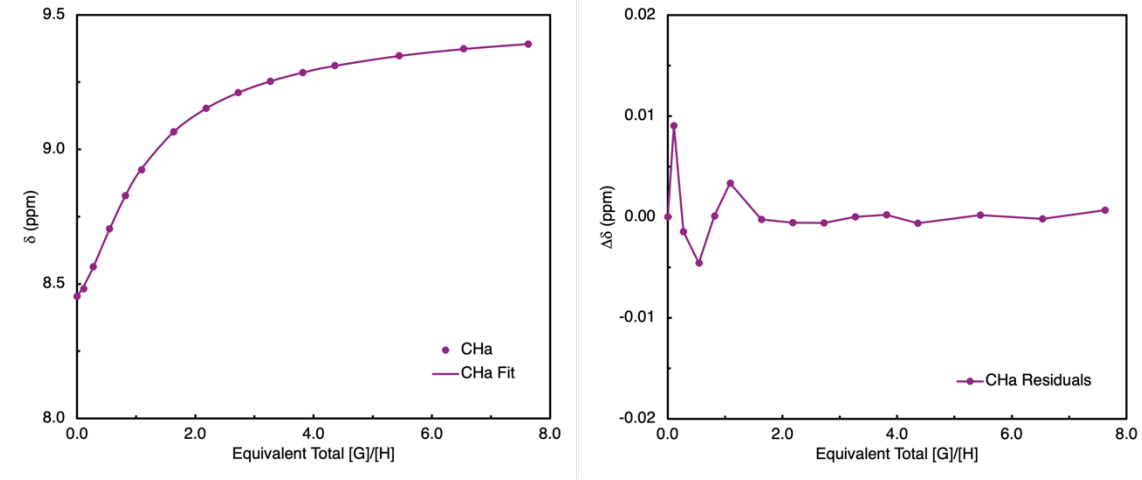

Figure C85. Representative binding isotherm and residuals of NO_2^- titration of $\mathbf{7}^{3+}$ in CD_3CN at room temperature determined via ^1H NMR spectroscopy.

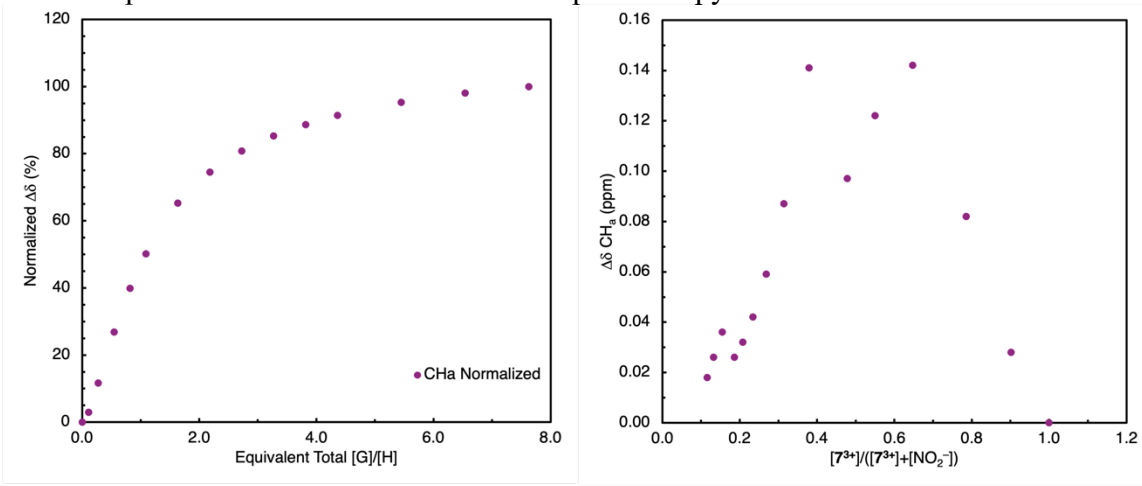

Figure C86. Normalized change in chemical shift of bound protons and Job Plot for NO_2^- titration of $\mathbf{7}^{3+}$.

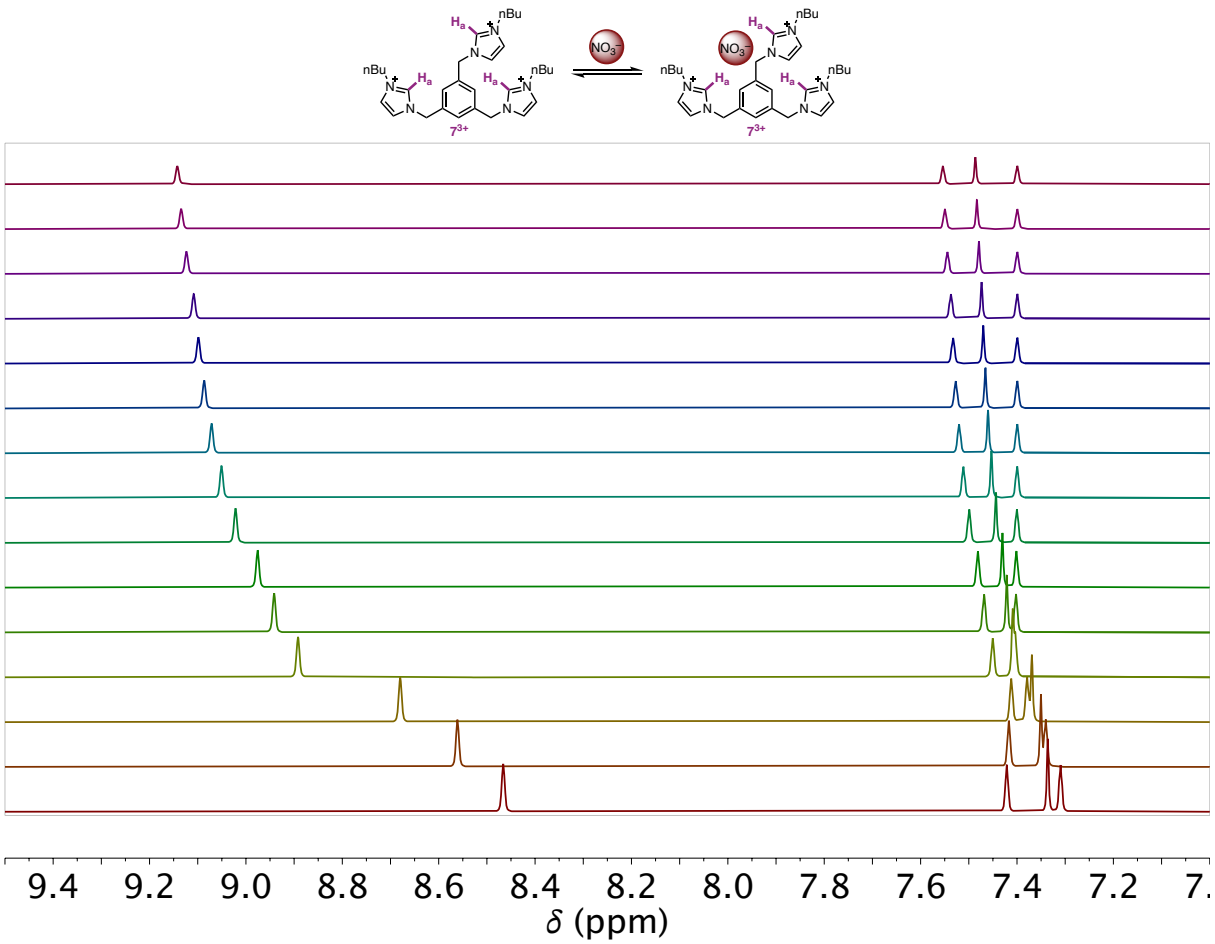

Figure C87. Titration scheme of receptor $\mathbf{7}^{3+}$ with NO_3^- and representative ^1H NMR spectra.

Table C25. Representative titration of receptor $\mathbf{7}^{3+}$ with NO_3^- in CD_3CN at room temperature.

Entry	$V_{total,\ guest}$ (μL)	[Receptor] (M)	[Guest] (M)	Anion Equiv.	CH_a (ppm)
1	0	1.27E-03	0.00E+00	0.00	8.464
2	10	1.25E-03	2.60E-04	0.21	8.557
3	25	1.21E-03	6.32E-04	0.52	8.676
4	50	1.16E-03	1.21E-03	1.04	8.810
5	75	1.11E-03	1.73E-03	1.56	8.890
6	100	1.06E-03	2.21E-03	2.09	8.939
7	150	9.79E-04	3.06E-03	3.13	8.999
8	200	9.09E-04	3.79E-03	4.17	9.036
9	250	8.48E-04	4.42E-03	5.21	9.060
10	300	7.95E-04	4.98E-03	6.26	9.078
11	350	7.48E-04	5.46E-03	7.30	9.091
12	400	7.07E-04	5.90E-03	8.34	9.103
13	500	6.36E-04	6.63E-03	10.43	9.119
14	600	5.78E-04	7.24E-03	12.51	9.130
15	700	5.30E-04	7.74E-03	14.60	9.139

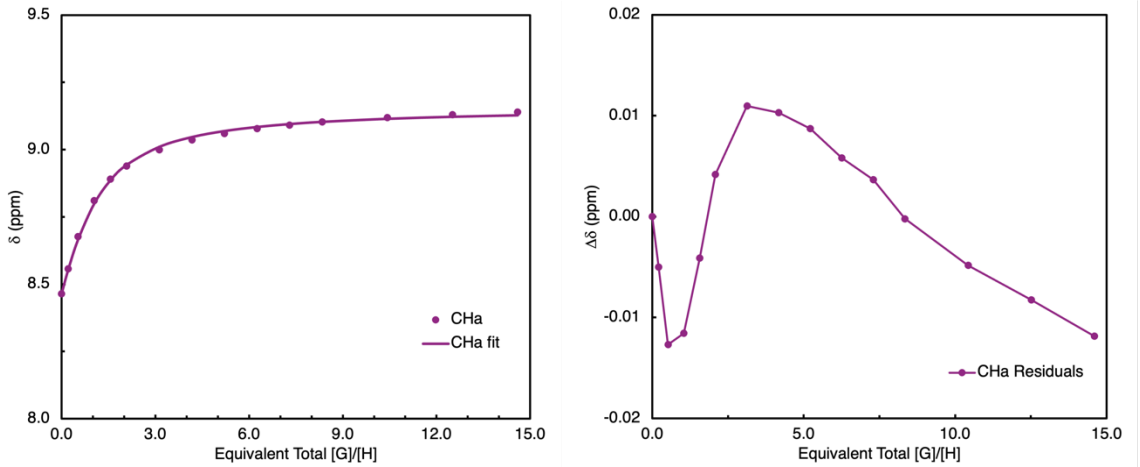

Figure C88. Representative binding isotherm and residuals of NO_3^- titration of 7^{3+} in CD_3CN at room temperature determined via ^1H NMR spectroscopy.

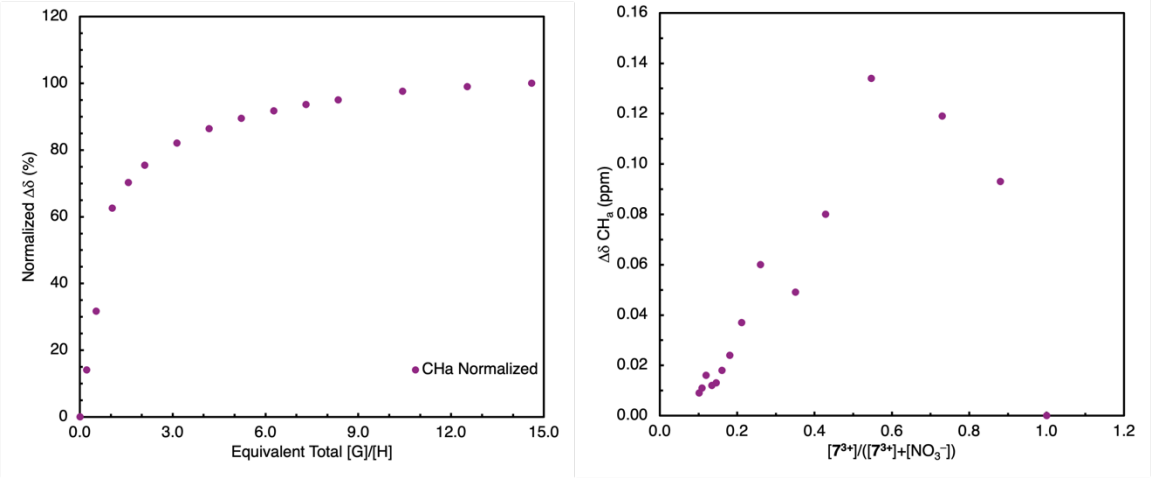

Figure C89. Normalized change in chemical shift of bound protons and Job Plot for NO_3^- titration of 7^{3+}.

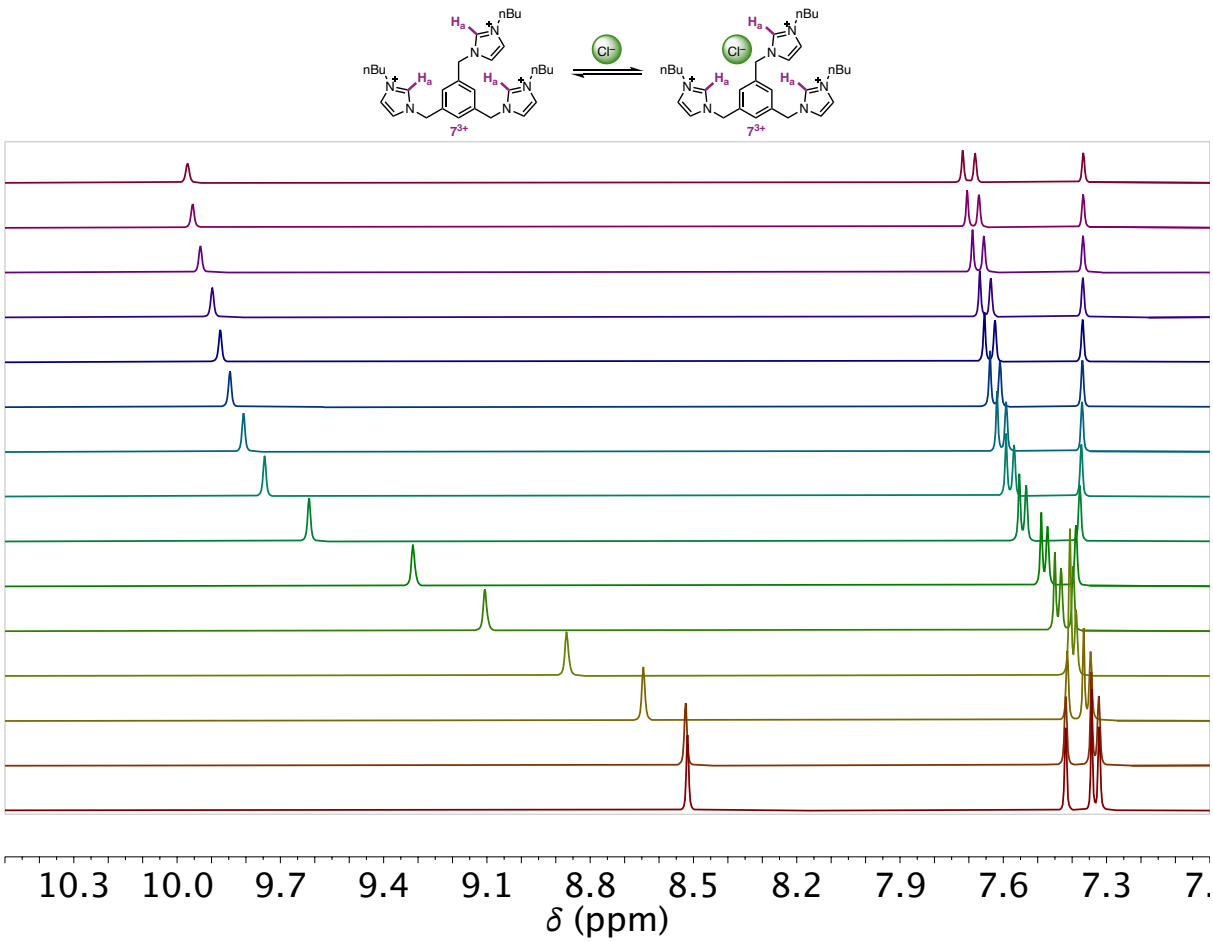

Figure C90. Titration scheme of receptor $\mathbf{7}^{3+}$ with Cl^- and representative ^1H NMR spectra.

Table C26. Representative titration of receptor $\mathbf{7}^{3+}$ with Cl^- in CD_3CN at room temperature.

Entry	$V_{total,\ guest}$ (μL)	[Receptor] (M)	[Guest] (M)	Anion Equiv.	CH_a (ppm)
1	0	1.07E-03	0.00E+00	0.00	8.517
2	10	1.05E-03	6.21E-05	0.06	8.523
3	25	1.02E-03	1.51E-04	0.15	8.646
4	50	9.72E-04	2.88E-04	0.30	8.869
5	75	9.29E-04	4.13E-04	0.44	9.106
6	100	8.91E-04	5.28E-04	0.59	9.315
7	150	8.22E-04	7.31E-04	0.89	9.617
8	200	7.63E-04	9.05E-04	1.19	9.746
9	250	7.13E-04	1.06E-03	1.48	9.807
10	300	6.68E-04	1.19E-03	1.78	9.847
11	350	6.29E-04	1.30E-03	2.07	9.875
12	400	5.94E-04	1.41E-03	2.37	9.898
13	500	5.34E-04	1.58E-03	2.96	9.933
14	600	4.86E-04	1.73E-03	3.56	9.955
15	700	4.45E-04	1.85E-03	4.15	9.970

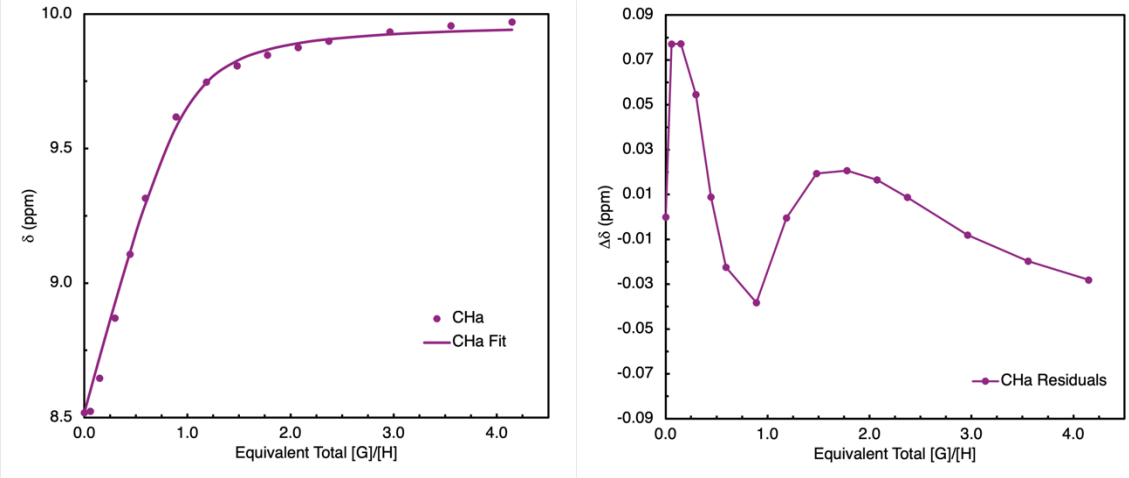

Figure C91. Representative binding isotherm and residuals of Cl^- titration of 7^{3+} in CD3CN at room temperature determined via ^1H NMR spectroscopy.

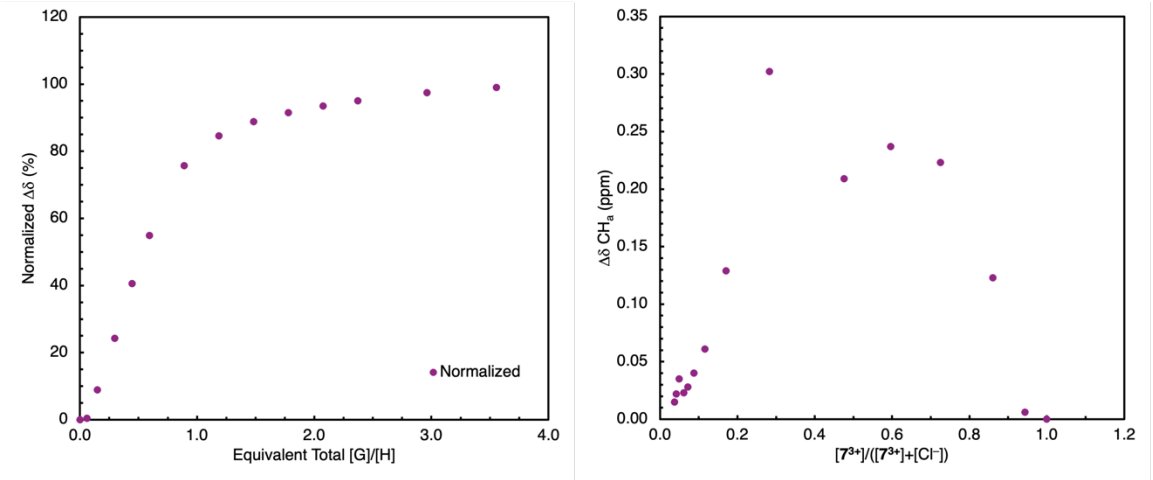

Figure C92. Normalized change in chemical shift of bound protons and Job Plot for Cl^- titration of 7^{3+}.

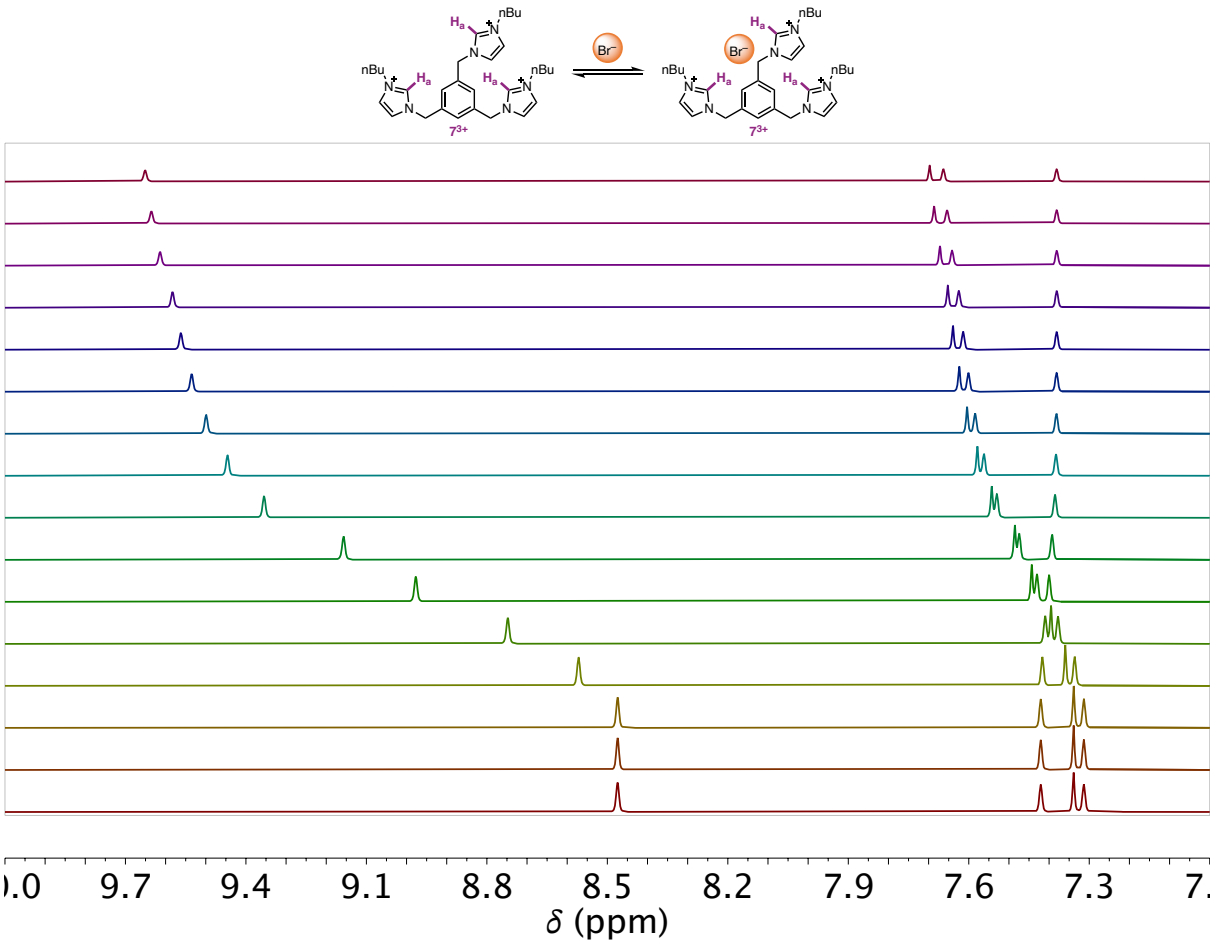

Figure C93. Titration scheme of receptor $\mathbf{7}^{3+}$ with Br^- and representative ^1H NMR spectra.

Table C27. Representative titration of receptor $\mathbf{7}^{3+}$ with Br^- in CD_3CN at room temperature.

Entry	$V_{total,\ guest}$ (μL)	[Receptor] (M)	[Guest] (M)	Anion Equiv.	CH_a (ppm)
1	0	1.05E-03	0.00E+00	0.00	8.464
2	10	1.03E-03	1.27E-04	0.12	8.474
3	25	1.00E-03	3.07E-04	0.31	8.572
4	50	9.54E-04	5.87E-04	0.61	8.748
5	75	9.13E-04	8.42E-04	0.92	8.977
6	100	8.75E-04	1.08E-03	1.23	9.157
7	150	8.07E-04	1.49E-03	1.84	9.355
8	200	7.50E-04	1.84E-03	2.46	9.446
9	250	7.00E-04	2.15E-03	3.07	9.499
10	300	6.56E-04	2.42E-03	3.69	9.535
11	350	6.17E-04	2.66E-03	4.30	9.562
12	400	5.83E-04	2.87E-03	4.92	9.583
13	500	5.25E-04	3.23E-03	6.15	9.614
14	600	4.77E-04	3.52E-03	7.38	9.635
15	700	4.37E-04	3.76E-03	8.61	9.651

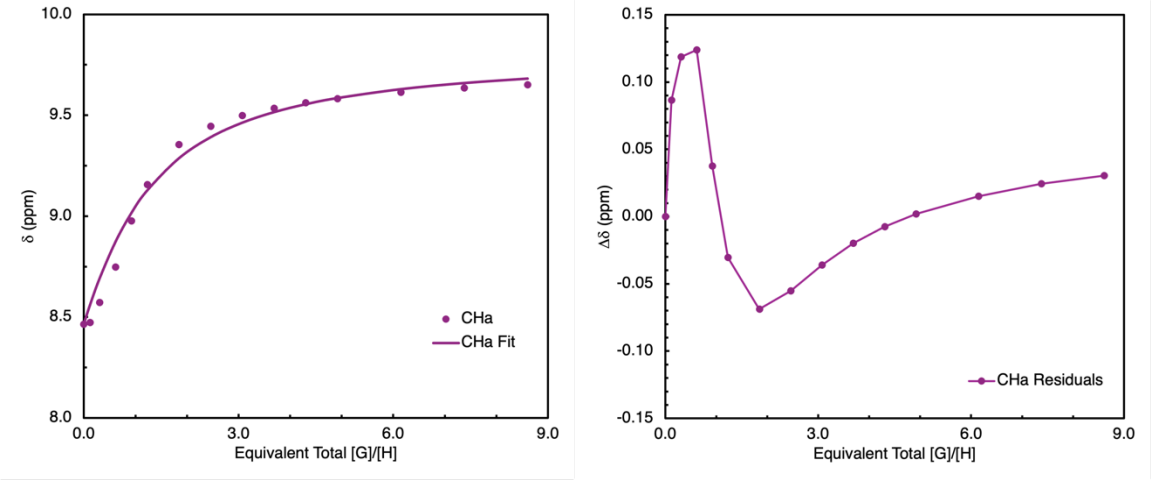

Figure C94. Representative binding isotherm and residuals of Br^- titration of 7^{3+} in CD3CN at room temperature determined via ^1H NMR spectroscopy.

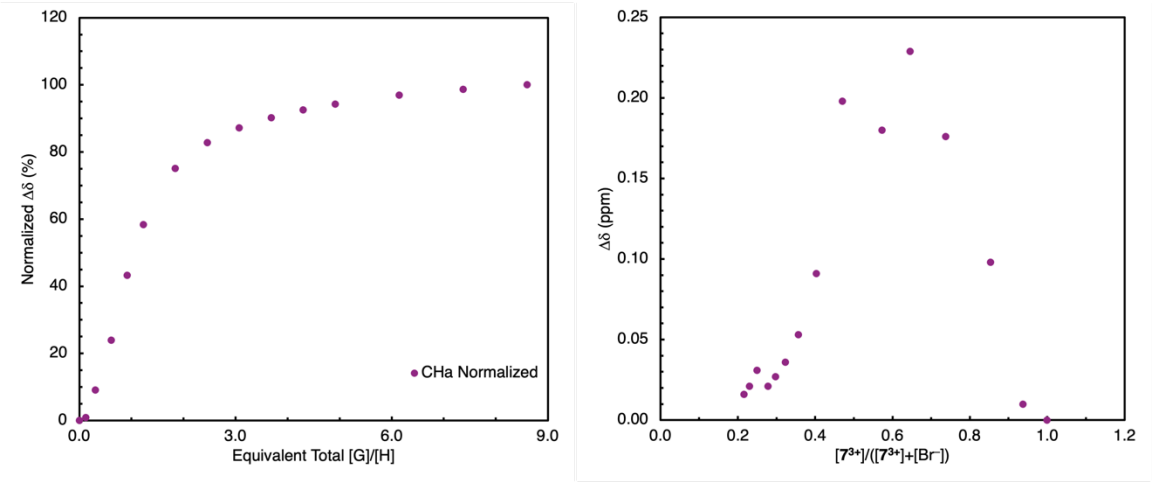

Figure C95. Normalized change in chemical shift of bound protons and Job Plot for Br^- titration of 7^{3+}.

C3. X-RAY CRYSTALLOGRAPHY

Additional Structures

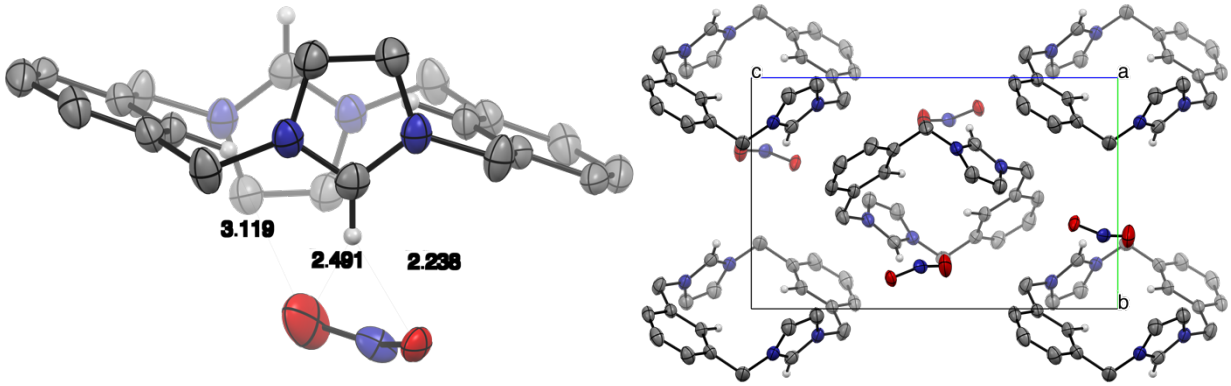

Figure C96. Crystal structure of $\mathbf{5}^{2+}\bullet 2NO_2^-$. Left: Structure of $\mathbf{5}^{2+}$ bound to NO_2^- anions showing C–H···O H-bonding distances (Å). Right: Extended packing structure of $\mathbf{5}^{2+}\bullet 2NO_2^-$.

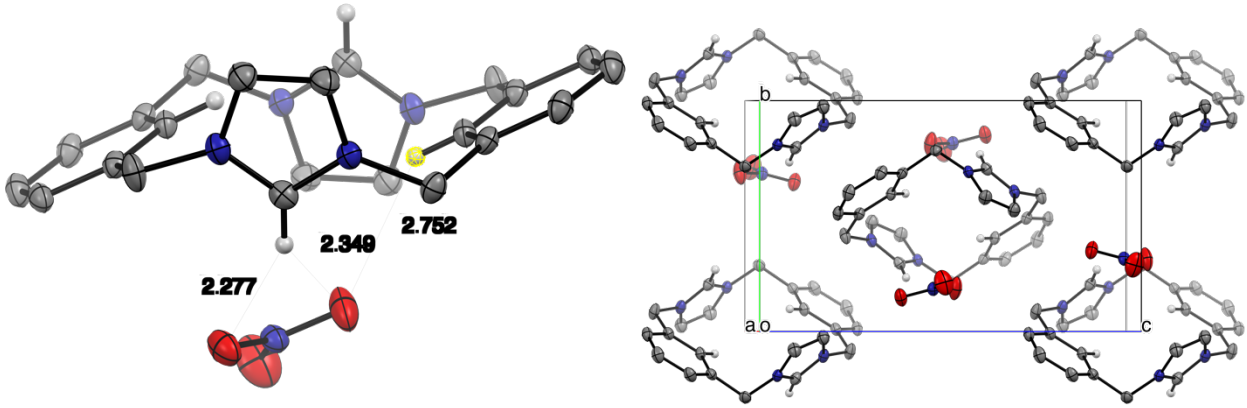

Figure C97. Crystal structure of $\mathbf{5}^{2+}\bullet 2NO_3^-$. Left: Structure of $\mathbf{5}^{2+}$ bound to NO_3^- anions showing C–H···O H-bonding distances (Å). Right: Extended packing structure of $\mathbf{5}^{2+}\bullet 2NO_3^-$.

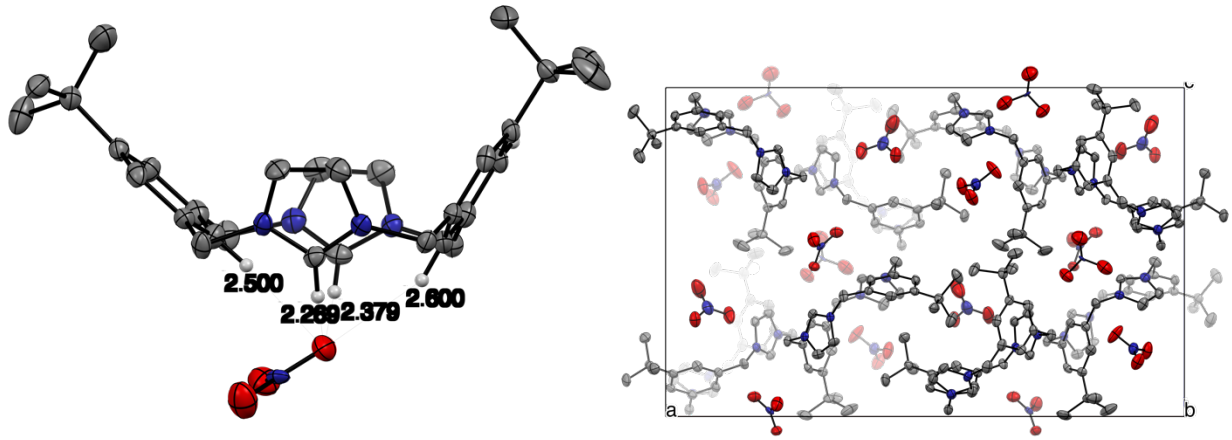

Figure C98. Crystal structure of $\mathbf{6}^{2+}\bullet 2NO_3^-$. Left: Structure of $\mathbf{6}^{2+}$ bound to NO_3^- anions showing C–H···O H-bonding distances (Å). Right: Extended packing structure of $\mathbf{6}^{2+}\bullet 2NO_3^-$.

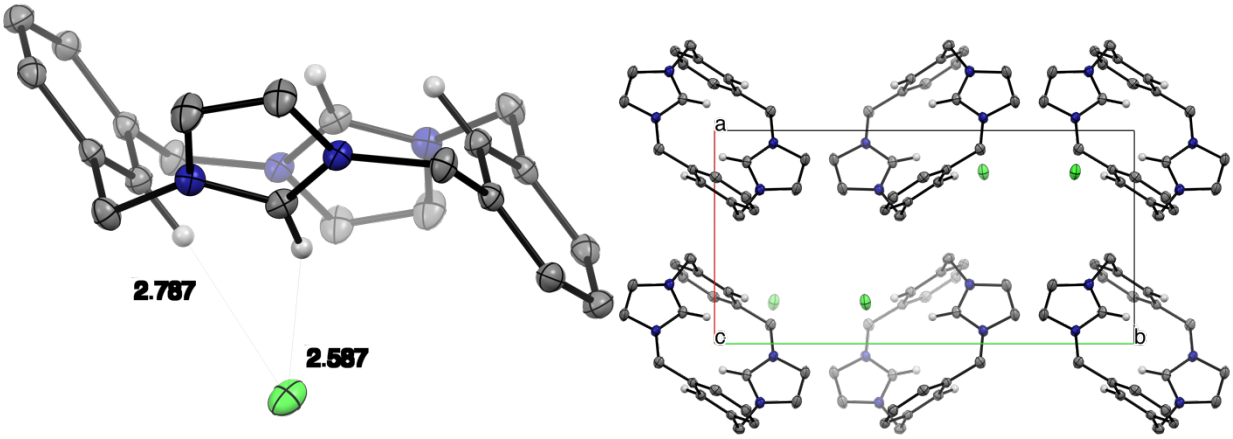

Figure C99. Crystal structure of $\mathbf{5}^{2+}$•2Cl⁻. Left: Structure of $\mathbf{5}^{2+}$ bound to Cl⁻ anions showing C–H···Cl H-bonding distances (Å). Right: Extended packing structure of $\mathbf{5}^{2+}$•2Cl⁻.

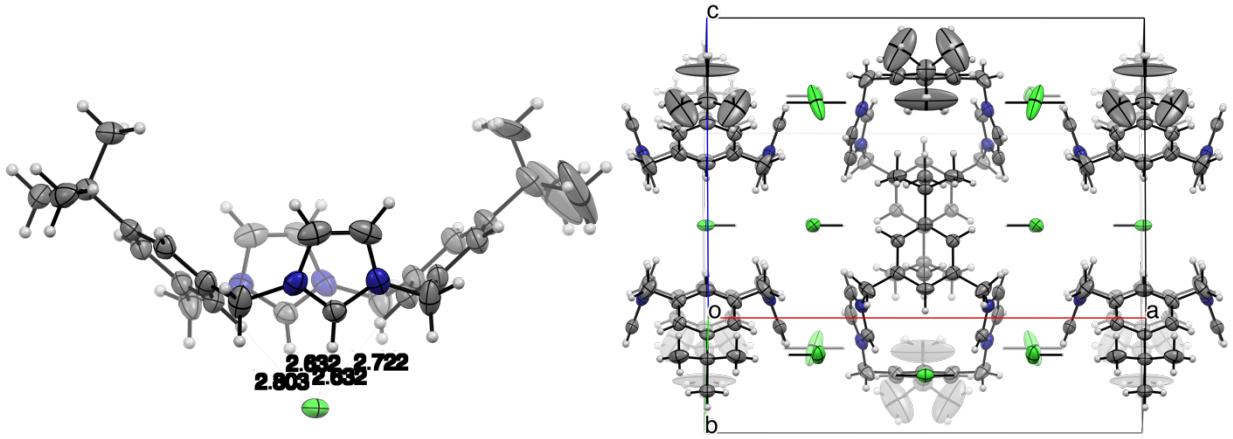

Figure C100. Crystal structure of $\mathbf{6}^{2+}$•2Cl⁻. Left: Structure of $\mathbf{6}^{2+}$ bound to Cl⁻ anions showing C–H···Cl H-bonding distances (Å). Right: Extended packing structure of $\mathbf{6}^{2+}$•2Cl⁻.

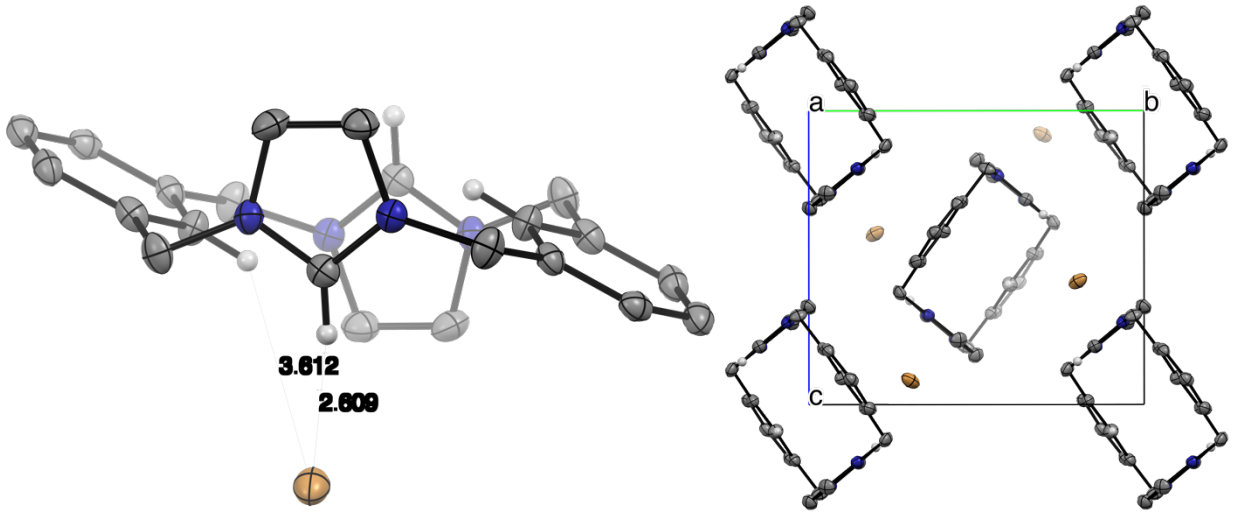

Figure C101. Crystal structure of $\mathbf{5}^{2+}$•2Br⁻. Left: Structure of $\mathbf{5}^{2+}$ bound to Br⁻ anions showing C–H···Br H-bonding distances (Å). Right: Extended packing structure of $\mathbf{5}^{2+}$•2Br⁻.

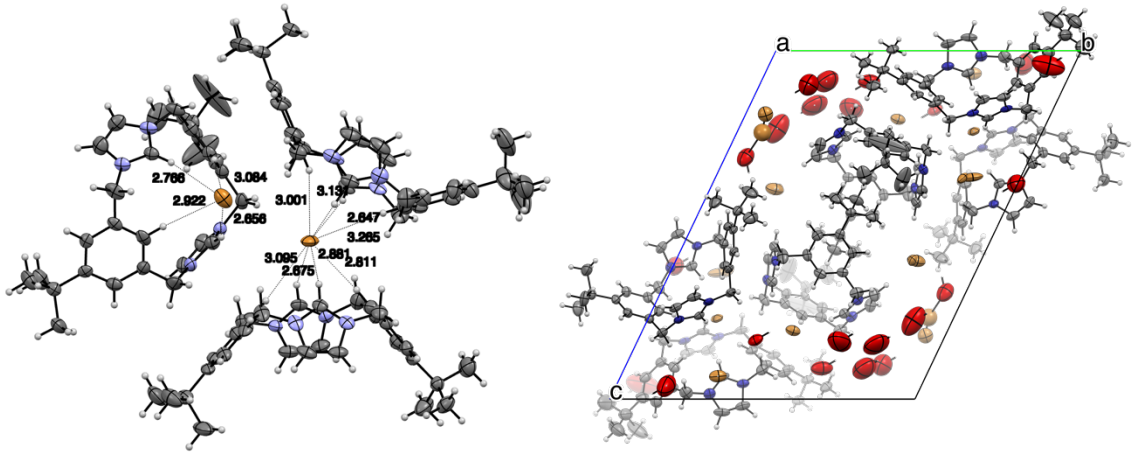

Figure C102. Crystal structure of $\mathbf{6}^{2+}$•2Br⁻. Left: Structure of $\mathbf{6}^{2+}$ bound to Br⁻ anions showing C–H···Br H-bonding distances (Å). Right: Extended packing structure of $\mathbf{6}^{2+}$•2Br⁻.

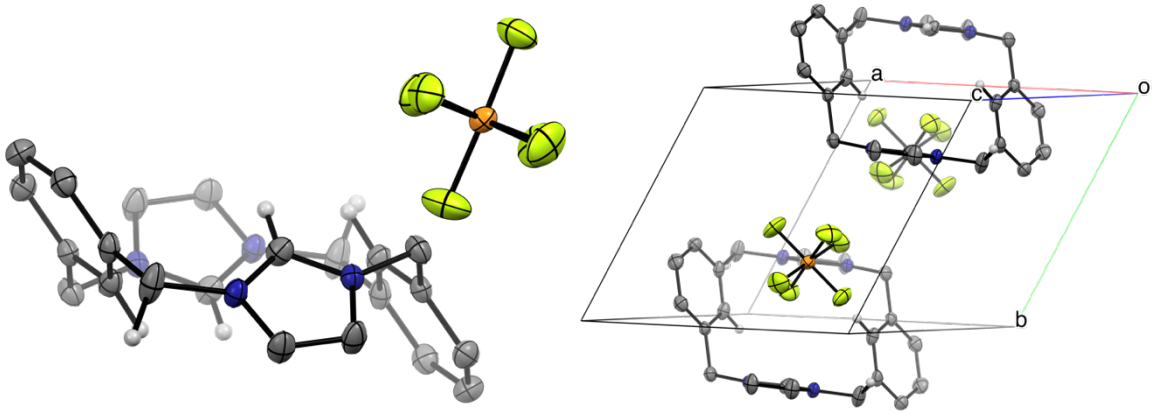

Figure C103. Crystal structure of $\mathbf{5}^{2+}$•2PF_6^-. Left: Structure of $\mathbf{5}^{2+}$ with PF_6^- counter anions. Right: Extended packing structure of $\mathbf{5}^{2+}$•2PF_6^-.

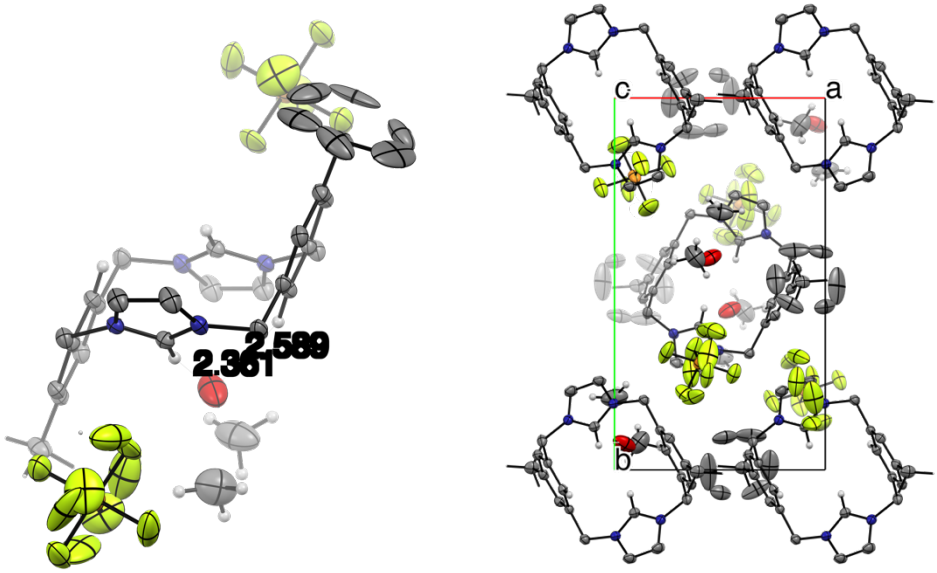

Figure C104. Crystal structure of $\mathbf{6}^{2+}$•2PF_6^-. Left: Structure of $\mathbf{6}^{2+}$•2PF_6^- bound to cocrystallized acetone molecule showing C–H···O H-bonding distances (Å). Right: Extended packing structure of $\mathbf{6}^{2+}$•2PF_6^-.

XRD Parameters

Table C28. X-Ray crystallographic parameters for 5^{2+}•X^- complexes.

	5^{2+}•NO_2^-	5^{2+}•NO_3^-	5^{2+}•Cl^-	5^{2+}•Br^-	5^{2+}•PF_6^-
formula	$C_{22}H_{22}N_6O_4$	$C_{22}H_{22}N_6O_6$	$C_{22}H_{26}Cl_2N_4O_2$	$C_{22}H_{20}Br_2N_4$	$C_{22}H_{22}F_{12}N_4P_2$
formula weight	434.45	466.45	449.37	500.24	632.37
temperature (K)	173(2)	173(2)	173(2)	173(2)	213(2)
crystal system	monoclinic	monoclinic	monoclinic	monoclinic	triclinic
space group	P 2_1/c	P 2_1/c	P 2_1/c	P 2_1/n	P -1
a (Å)	8.4235(15)	8.8817(8)	8.7220(7)	9.7282(19)	8.763(3)
b (Å)	8.8563(15)	8.4779(7)	15.7694(13)	11.146(2)	8.776(3)
c (Å)	14.035(3)	14.0492(12)	8.6267(7)	10.0099(19)	9.677(4)
a (deg)	90	90	90	90	85.868(8)
b (deg)	90.582(5)	93.568(2)	113.298(2)	103.019(3)	66.126(7)
g (deg)	90	90	90	90	63.579(7)
V (Å^3)	1047.0(3)	1055.83(16)	1089.77(15)	1057.4(4)	604.1(4)
Z	2	2	2	2	1
r (mm^{-1})	1.378	1.467	1.369	1.571	1.738
F(000)	456	488	472	500	320
crystal size (mm^3)	0.08 x 0.18 x 0.21	0.12 x 0.14 x 0.18	0.06 x 0.15 x 0.23	0.01 x 0.05 x 0.15	0.09 x 0.14 x 0.16
q range (deg)	2.42 – 28.26	2.30 – 28.22	2.54 – 28.09	2.64 – 23.85	2.61 – 27.59
completeness to q (%)	99.7	100	99.9	100	100
total reflns	7031	9133	6761	8804	7020
indep reflns	2532	2615	2668	2599	2936
restraints / param	4 / 205	0 / 198	0 / 188	0 / 167	0 / 225
R1 (wR2) [I > 2s(*I*)]	0.18 (0.098)	0.041 (0.1033)	0.0361 (0.0903)	0.0382 (0.0733)	0.0456 (0.1052)
R1 (wR2)	0.21 (0.080)	0.0542 (0.1118)	0.0468 (0.0971)	0.072 (0.0830)	0.0716 (0.1183)
GOF (F^2)	1.009	1.027	0.997	1.005	1.009
max, min peaks (e Å^{-3})	0.540, -0.252	0.321, -0.208	0.339, -0.314	0.812, -0.411	0.304, -0.295

Table C29. X-Ray crystallographic parameters for $6^{2+}\bullet X^-$ complexes.

	$6^{2+}\bullet NO_3^-$	$6^{2+}\bullet Cl^-$	$6^{2+}\bullet Br^-$	$6^{2+}\bullet PF_6^-$
formula	$C_{30}H_{38}N_6O_6$	$C_{33}H_{44}Cl_2N_{4.5}O_{0.5}$	$C_{30}H_{45.26}Br_2N_4O_{3.63}$	$C_{36}H_{50}F_{12}N_4O_2P_2$
formula weight	578.66	582.62	679.86	860.74
temperature (K)	173(2)	173(2)	173(2)	173(2)
crystal system	orthorhombic	orthorhombic	triclinic	monoclinic
space group	$Pca2_1$	Pmna	P -1	P $2_1/n$
a (Å)	27.619(6)	18.889(4)	12.319(6)	9.2483(7)
b (Å)	12.238(3)	13.201(2)	19.040(8)	16.2608(11)
c (Å)	17.514(4	14.009(3)	23.542(11)	13.6467(11)
a (deg)	90	90	113.584(7)	90
b (deg)	90	90	94.624(7)	94.988(2)
g (deg)	90	90	102.952(7)	90
V (Å^3)	5920(2)	3493.4(12)	4841(4)	2044.5(3)
Z	8	4	6	2
r (mm^{-1})	0.092	0.214	2.549	0.198
F(000)	2464	1246	2114	896
crystal size (mm^3)	0.06 x 0.12 x 0.16	0.09 x 0.16 x 0.18	0.02 x 0.07 x 0.23	0.19 x 0.22 x 0.23
q range (deg)	2.75 – 19.38	2.38 – 24.72	2.60 – 26.30	2.51 – 27.88
completeness to q (%)	99.5	100	99.8	99.4
total reflns	36466	23255	61671	22534
indep reflns	12812	3182	19943	5047
restraints / param	1 / 757	0 / 184	0 / 1096	0 / 318
R1 (wR2) [I > 2s(*l*)]	0.0745 (0.1196)	0.0848 (0.2694)	0.0783 (0.1803)	0.051 (0.1379)
R1 (wR2)	0.218 (0.1625)	0.1003 (0.2870)	0.1857 (0.2224)	0.0708 (0.1529)
GOF (F^2)	1.002	1.061	0.974	1.034
max, min peaks (e Å^{-3})	0.301, -0.323	1.124, -0.416	0.968, -0.902	0.352, -0.299

REFERENCES CITED

(1) Borquez, E.; Cleaves, H. J.; Lazcano, A.; Miller, S. L. An Investigation of Prebiotic Purine Synthesis from the Hydrolysis of HCN Polymers. *Orig. Life Evol. Biospheres* **2005**, *35* (2), 79–90. https://doi.org/10.1007/s11084-005-5945-9.

(2) Sutherland, J. D. The Origin of Life—Out of the Blue. *Angew. Chem. Int. Ed.* **2016**, *55* (1), 104–121. https://doi.org/10.1002/anie.201506585.

(3) Sanchez, R. A.; Ferbis, J. P.; Orgel, L. E. Studies in Prebiodc Synthesis: II. Synthesis of Purine Precursors and Amino Acids from Aqueous Hydrogen Cyanide. *J. Mol. Biol.* **1967**, *30* (2), 223–253. https://doi.org/10.1016/S0022-2836(67)80037-8.

(4) Oró, J. Mechanism of Synthesis of Adenine from Hydrogen Cyanide under Possible Primitive Earth Conditions. *Nature* **1961**, *191* (4794), 1193–1194. https://doi.org/10.1038/1911193a0.

(5) Miller, S. L. A Production of Amino Acids Under Possible Primitive Earth Conditions. *Science* **1953**, *117* (3046), 528–529. https://doi.org/10.1126/science.117.3046.528.

(6) Miller, S. L.; Urey, H. C. Organic Compound Synthesis on the Primitive Earth. *Science* **1959**, *130* (3370), 245–251. https://doi.org/10.1126/science.130.3370.245.

(7) Miller, S. L. Production of Some Organic Compounds under Possible Primitive Earth Conditions1. *J. Am. Chem. Soc.* **1955**, *77* (9), 2351–2361. https://doi.org/10.1021/ja01614a001.

(8) Green, N. J.; Xu, J.; Sutherland, J. D. Illuminating Life's Origins: UV Photochemistry in Abiotic Synthesis of Biomolecules. *J. Am. Chem. Soc.* **2021**, *143* (19), 7219–7236. https://doi.org/10.1021/jacs.1c01839.

(9) Valer, L.; Hu, Y. J.; Cini, A.; Lantieri, M.; Walton, C. R.; Shorttle, O.; Fittipaldi, M.; Mansy, S. S. Prebiotic Environmental Conditions Impact the Type of Iron-Sulfur Cluster Formed. *ChemSystemsChem* **2025**, *7* (1), e202400051. https://doi.org/10.1002/syst.202400051.

(10) Todd, Z. R. Sources of Nitrogen-, Sulfur-, and Phosphorus-Containing Feedstocks for Prebiotic Chemistry in the Planetary Environment. *Life* **2022**, *12* (8), 1268. https://doi.org/10.3390/life12081268.

(11) Heinen, W.; Lauwers, A. M. Organic Sulfur Compounds Resulting from the Interaction of Iron Sulfide, Hydrogen Sulfide and Carbon Dioxide in an Anaerobic Aqueous Environment. *Orig. Life Evol. Biosph.* **1996**, *26* (2), 131–150. https://doi.org/10.1007/BF01809852.

(12) Camprubi, E.; Jordan, S. F.; Vasiliadou, R.; Lane, N. Iron Catalysis at the Origin of Life. *IUBMB Life* **2017**, *69* (6), 373–381. https://doi.org/10.1002/iub.1632.

(13) Goldman, A. D.; Kacar, B. Cofactors Are Remnants of Life's Origin and Early Evolution. *J. Mol. Evol.* **2021**, *89* (3), 127–133. https://doi.org/10.1007/s00239-020-09988-4.

(14) Kopp, R. E.; Kirschvink, J. L.; Hilburn, I. A.; Nash, C. Z. The Paleoproterozoic Snowball Earth: A Climate Disaster Triggered by the Evolution of Oxygenic Photosynthesis. *Proc. Natl. Acad. Sci.* **2005**, *102* (32), 11131–11136. https://doi.org/10.1073/pnas.0504878102.

(15) Canfield, D. E. THE EARLY HISTORY OF ATMOSPHERIC OXYGEN: Homage to Robert M. Garrels. *Annu. Rev. Earth Planet. Sci.* **2005**, *33* (Volume 33, 2005), 1–36. https://doi.org/10.1146/annurev.earth.33.092203.122711.

(16) Falkowski, P. G. Tracing Oxygen's Imprint on Earth's Metabolic Evolution. *Science* **2006**, *311* (5768), 1724–1725. https://doi.org/10.1126/science.1125937.

(17) Raymond, J.; Segrè, D. The Effect of Oxygen on Biochemical Networks and the Evolution of Complex Life. *Science* **2006**, *311* (5768), 1764–1767. https://doi.org/10.1126/science.1118439.

(18) Hendriks, K. D.; Maassen, H.; van Dijk, P. R.; Henning, R. H.; van Goor, H.; Hillebrands, J.-L. Gasotransmitters in Health and Disease: A Mitochondria-Centered View. *Curr. Opin. Pharmacol.* **2019**, *45*, 87–93. https://doi.org/10.1016/j.coph.2019.07.001.

(19) Fukuto, J. M.; Carrington, S. J.; Tantillo, D. J.; Harrison, J. G.; Ignarro, L. J.; Freeman, B. A.; Chen, A.; Wink, D. A. Small Molecule Signaling Agents: The Integrated Chemistry and Biochemistry of Nitrogen Oxides, Oxides of Carbon, Dioxygen, Hydrogen Sulfide, and Their Derived Species. *Chem. Res. Toxicol.* **2012**, *25* (4), 769–793. https://doi.org/10.1021/tx2005234.

(20) Pacher, P. Cyanide Emerges as an Endogenous Mammalian Gasotransmitter. *Proc. Natl. Acad. Sci. U. S. A.* **2021**, *118* (25), e2108040118. https://doi.org/10.1073/pnas.2108040118.

(21) Zuhra, K.; Szabo, C. The Two Faces of Cyanide: An Environmental Toxin and a Potential Novel Mammalian Gasotransmitter. *FEBS J.* **2022**, *289* (9), 2481–2515. https://doi.org/10.1111/febs.16135.

(22) Boros, M.; Tuboly, E.; Mészáros, A.; Amann, A. The Role of Methane in Mammalian Physiology—Is It a Gasotransmitter? *J. Breath Res.* **2015**, *9* (1), 014001. https://doi.org/10.1088/1752-7155/9/1/014001.

(23) Steiger, A. K.; Zhao, Y.; Pluth, M. D. Emerging Roles of Carbonyl Sulfide in Chemical Biology: Sulfide Transporter or Gasotransmitter? *Antioxid. Redox Signal.* **2018**, *28* (16), 1516–1532. https://doi.org/10.1089/ars.2017.7119.

(24) Kuganesan, M.; Samra, K.; Evans, E.; Singer, M.; Dyson, A. Selenium and Hydrogen Selenide: Essential Micronutrient and the Fourth Gasotransmitter? *Intensive Care Med. Exp.* **2019**, *7* (1), 71. https://doi.org/10.1186/s40635-019-0281-y.

(25) Poole, L. B. The Basics of Thiols and Cysteines in Redox Biology and Chemistry. *Free Radic. Biol. Med.* **2015**, *0*, 148–157. https://doi.org/10.1016/j.freeradbiomed.2014.11.013.

(26) Etzkorn, F. A. Appendix C: pKa Tables. In *Green Chemistry: Principles and Case Studies*; Royal Society of Chemistry, 2020; pp 409–415.

(27) Rosselli, M.; Keller, R.; Dubey, R. Role of Nitric Oxide in the Biology, Physiology and Pathophysiology of Reproduction. *Hum. Reprod. Update* **1998**, *4* (1), 3–24. https://doi.org/10.1093/humupd/4.1.3.

(28) McCleverty, J. A. Chemistry of Nitric Oxide Relevant to Biology. *Chem. Rev.* **2004**, *104* (2), 403–418. https://doi.org/10.1021/cr020623q.

(29) Bryan, N. S. Nitrite in Nitric Oxide Biology: Cause or Consequence?: A Systems-Based Review. *Free Radic. Biol. Med.* **2006**, *41* (5), 691–701. https://doi.org/10.1016/j.freeradbiomed.2006.05.019.

(30) Stamler, J. S.; Singel, D. J.; Loscalzo, J. Biochemistry of Nitric Oxide and Its Redox-Activated Forms. *Science* **1992**, *258* (5090), 1898–1902. https://doi.org/10.1126/science.1281928.

(31) Walford, G.; Loscalzo, J. Nitric Oxide in Vascular Biology. *J. Thromb. Haemost.* **2003**, *1* (10), 2112–2118. https://doi.org/10.1046/j.1538-7836.2003.00345.x.

(32) Lundberg, J. O.; Weitzberg, E.; Gladwin, M. T. The Nitrate–Nitrite–Nitric Oxide Pathway in Physiology and Therapeutics. *Nat. Rev. Drug Discov.* **2008**, *7* (2), 156–167. https://doi.org/10.1038/nrd2466.

(33) Förstermann, U.; Sessa, W. C. Nitric Oxide Synthases: Regulation and Function. *Eur. Heart J.* **2012**, *33* (7), 829–837. https://doi.org/10.1093/eurheartj/ehr304.

(34) Chatzianastasiou, A.; Bibli, S.-I.; Andreadou, I.; Efentakis, P.; Kaludercic, N.; Wood, M. E.; Whiteman, M.; Lisa, F. D.; Daiber, A.; Manolopoulos, V. G.; Szabó, C.; Papapetropoulos, A. Cardioprotection by H2S Donors: Nitric Oxide-Dependent and -Independent Mechanisms. *J. Pharmacol. Exp. Ther.* **2016**, *358* (3), 431–440. https://doi.org/10.1124/jpet.116.235119.

(35) Gladwin, M. T.; Schechter, A. N.; Kim-Shapiro, D. B.; Patel, R. P.; Hogg, N.; Shiva, S.; Cannon, R. O.; Kelm, M.; Wink, D. A.; Espey, M. G.; Oldfield, E. H.; Pluta, R. M.; Freeman, B. A.; Lancaster, J. R.; Feelisch, M.; Lundberg, J. O. The Emerging Biology of the Nitrite Anion. *Nat. Chem. Biol.* **2005**, *1* (6), 308–314. https://doi.org/10.1038/nchembio1105-308.

(36) Bryan, N. S.; Fernandez, B. O.; Bauer, S. M.; Garcia-Saura, M. F.; Milsom, A. B.; Rassaf, T.; Maloney, R. E.; Bharti, A.; Rodriguez, J.; Feelisch, M. Nitrite Is a Signaling Molecule and Regulator of Gene Expression in Mammalian Tissues. *Nat. Chem. Biol.* **2005**, *1* (5), 290–297. https://doi.org/10.1038/nchembio734.

(37) Jansson, E. Å.; Huang, L.; Malkey, R.; Govoni, M.; Nihlén, C.; Olsson, A.; Stensdotter, M.; Petersson, J.; Holm, L.; Weitzberg, E.; Lundberg, J. O. A Mammalian Functional Nitrate Reductase That Regulates Nitrite and Nitric Oxide Homeostasis. *Nat. Chem. Biol.* **2008**, *4* (7), 411–417. https://doi.org/10.1038/nchembio.92.

(38) DeMartino, A. W.; Kim-Shapiro, D. B.; Patel, R. P.; Gladwin, M. T. Nitrite and Nitrate Chemical Biology and Signalling. *Br. J. Pharmacol.* **2019**, *176* (2), 228–245. https://doi.org/10.1111/bph.14484.

(39) Maia, L. B.; Moura, J. J. G. How Biology Handles Nitrite. *Chem. Rev.* **2014**, *114* (10), 5273–5357. https://doi.org/10.1021/cr400518y.

(40) Doyle, M. P.; Hoekstra, J. W. Oxidation of Nitrogen Oxides by Bound Dioxygen in Hemoproteins. *J. Inorg. Biochem.* **1981**, *14* (4), 351–358. https://doi.org/10.1016/S0162-0134(00)80291-3.

(41) Mishra, S.; Meuwly, M. Atomistic Simulation of NO Dioxygenation in Group I Truncated Hemoglobin. *J. Am. Chem. Soc.* **2010**, *132* (9), 2968–2982. https://doi.org/10.1021/ja9078144.

(42) Shafirovich, V.; Lymar, S. V. Spin-Forbidden Deprotonation of Aqueous Nitroxyl (HNO). *J. Am. Chem. Soc.* **2003**, *125* (21), 6547–6552. https://doi.org/10.1021/ja034378j.

(43) Fukuto, J. M.; Hobbs, A. J.; Ignarro, L. J. Conversion of Nitroxyl (HNO) to Nitric Oxide (NO) in Biological Systems: The Role of Physiological Oxidants and Relevance to the Biological Activity of HNO. *Biochem. Biophys. Res. Commun.* **1993**, *196* (2), 707–713. https://doi.org/10.1006/bbrc.1993.2307.

(44) Tocchetti, C. G.; Stanley, B. A.; Murray, C. I.; Sivakumaran, V.; Donzelli, S.; Mancardi, D.; Pagliaro, P.; Gao, W. D.; van Eyk, J.; Kass, D. A.; Wink, D. A.; Paolocci, N. Playing with Cardiac "Redox Switches": The "HNO Way" to Modulate Cardiac Function. *Antioxid. Redox Signal.* **2011**, *14* (9), 1687–1698. https://doi.org/10.1089/ars.2010.3859.

(45) Sabbah, H. N.; Tocchetti, C. G.; Wang, M.; Daya, S.; Gupta, R. C.; Tunin, R. S.; Mazhari, R.; Takimoto, E.; Paolocci, N.; Cowart, D.; Colucci, W. S.; Kass, D. A. Nitroxyl (HNO). *Circ. Heart Fail.* **2013**, *6* (6), 1250–1258. https://doi.org/10.1161/CIRCHEARTFAILURE.113.000632.

(46) Bonner, F. T.; Dzelzkalns, L. S.; Bonucci, J. A. Properties of Nitroxyl as Intermediate in the Nitric Oxide-Hydroxylamine Reaction and in Trioxodinitrate Decomposition. *Inorg. Chem.* **1978**, *17* (9), 2487–2494. https://doi.org/10.1021/ic50187a030.

(47) Yoo, J.; Fukuto, J. M. Oxidation of N-Hydroxyguanidine by Nitric Oxide and the Possible Generation of Vasoactive Species. *Biochem. Pharmacol.* **1995**, *50* (12), 1995–2000. https://doi.org/10.1016/0006-2952(95)02098-5.

(48) Poderoso, J. J.; Carreras, M. C.; Schöpfer, F.; Lisdero, C. L.; Riobó, N. A.; Giulivi, C.; Boveris, A. D.; Boveris, A.; Cadenas, E. The Reaction of Nitric Oxide with Ubiquinol: Kinetic Properties and Biological Significance. *Free Radic. Biol. Med.* **1999**, *26* (7), 925–935. https://doi.org/10.1016/S0891-5849(98)00277-9.

(49) Bonner, F. T.; Pearsall, K. A. Aqueous Nitrosyliron(II) Chemistry. 1. Reduction of Nitrite and Nitric Oxide by Iron(II) and (Trioxodinitrato)Iron(II) in Acetate Buffer. Intermediacy of Nitrosyl Hydride. *Inorg. Chem.* **1982**, *21* (5), 1973–1978. https://doi.org/10.1021/ic00135a053.

(50) Doyle, M. P.; Mahapatro, S. N.; Broene, R. D.; Guy, J. K. Oxidation and Reduction of Hemoproteins by Trioxodinitrate(II). The Role of Nitrosyl Hydride and Nitrite. *J. Am. Chem. Soc.* **1988**, *110* (2), 593–599. https://doi.org/10.1021/ja00210a047.

(51) Turk, T.; Hollocher, T. C. Oxidation of Dithiothreitol during Turnover of Nitric Oxide Reductase: Evidence for Generation of Nitroxyl with the Enzyme from *Paracoccus Denitrificans*. *Biochem. Biophys. Res. Commun.* **1992**, *183* (3), 983–988. https://doi.org/10.1016/S0006-291X(05)80287-6.

(52) Beckman, J. S.; Koppenol, W. H. Nitric Oxide, Superoxide, and Peroxynitrite: The Good, the Bad, and Ugly. *Am. J. Physiol.-Cell Physiol.* **1996**, *271* (5), C1424–C1437. https://doi.org/10.1152/ajpcell.1996.271.5.C1424.

(53) Muyzer, G.; Stams, A. J. M. The Ecology and Biotechnology of Sulphate-Reducing Bacteria. *Nat. Rev. Microbiol.* **2008**, *6* (6), 441–454. https://doi.org/10.1038/nrmicro1892.

(54) Bak, F.; Pfennig, N. Chemolithotrophic Growth of Desulfovibrio Sulfodismutans Sp. Nov. by Disproportionation of Inorganic Sulfur Compounds. *Arch. Microbiol.* **1987**, *147* (2), 184–189. https://doi.org/10.1007/BF00415282.

(55) Markovich, D. Physiological Roles and Regulation of Mammalian Sulfate Transporters. *Physiol. Rev.* **2001**, *81* (4), 1499–1533. https://doi.org/10.1152/physrev.2001.81.4.1499.

(56) Wang, R. Two's Company, Three's a Crowd: Can H2S Be the Third Endogenous Gaseous Transmitter? *FASEB J.* **2002**, *16* (13), 1792–1798. https://doi.org/10.1096/fj.02-0211hyp.

(57) Zhao, K.; Li, H.; Li, S.; Yang, G. Regulation of Cystathionine Gamma-Lyase/H_2S System and Its Pathological Implication. *Front. Biosci.-Landmark* **2014**, *19* (8), 1355–1369. https://doi.org/10.2741/4286.

(58) Chen, X.; Jhee, K.-H.; Kruger, W. D. Production of the Neuromodulator H2S by Cystathionine β-Synthase via the Condensation of Cysteine and Homocysteine *. *J. Biol. Chem.* **2004**, *279* (50), 52082–52086. https://doi.org/10.1074/jbc.C400481200.

(59) Shibuya, N.; Tanaka, M.; Yoshida, M.; Ogasawara, Y.; Togawa, T.; Ishii, K.; Kimura, H. 3-Mercaptopyruvate Sulfurtransferase Produces Hydrogen Sulfide and Bound Sulfane Sulfur in the Brain. *Antioxid. Redox Signal.* **2009**, *11* (4), 703–714. https://doi.org/10.1089/ars.2008.2253.

(60) Akaike, T.; Ida, T.; Wei, F.-Y.; Nishida, M.; Kumagai, Y.; Alam, M. M.; Ihara, H.; Sawa, T.; Matsunaga, T.; Kasamatsu, S.; Nishimura, A.; Morita, M.; Tomizawa, K.; Nishimura, A.; Watanabe, S.; Inaba, K.; Shima, H.; Tanuma, N.; Jung, M.; Fujii, S.; Watanabe, Y.; Ohmuraya, M.; Nagy, P.; Feelisch, M.; Fukuto, J. M.; Motohashi, H. Cysteinyl-tRNA Synthetase Governs

Cysteine Polysulfidation and Mitochondrial Bioenergetics. *Nat. Commun.* **2017**, *8* (1), 1177. https://doi.org/10.1038/s41467-017-01311-y.

(61) Shen, Y.; Shen, Z.; Luo, S.; Guo, W.; Zhu, Y. Z. The Cardioprotective Effects of Hydrogen Sulfide in Heart Diseases: From Molecular Mechanisms to Therapeutic Potential. *Oxid. Med. Cell. Longev.* **2015**, *2015*, 925167. https://doi.org/10.1155/2015/925167.

(62) Osipov, R. M.; Robich, M. P.; Feng, J.; Liu, Y.; Clements, R. T.; Glazer, H. P.; Sodha, N. R.; Szabo, C.; Bianchi, C.; Sellke, F. W. Effect of Hydrogen Sulfide in a Porcine Model of Myocardial Ischemia-Reperfusion: Comparison of Different Administration Regimens and Characterization of the Cellular Mechanisms of Protection. *J. Cardiovasc. Pharmacol.* **2009**, *54* (4), 287. https://doi.org/10.1097/FJC.0b013e3181b2b72b.

(63) Hildebrandt, T. M.; Grieshaber, M. K. Three Enzymatic Activities Catalyze the Oxidation of Sulfide to Thiosulfate in Mammalian and Invertebrate Mitochondria. *FEBS J.* **2008**, *275* (13), 3352–3361. https://doi.org/10.1111/j.1742-4658.2008.06482.x.

(64) Olson, K. R.; DeLeon, E. R.; Gao, Y.; Hurley, K.; Sadauskas, V.; Batz, C.; Stoy, G. F. Thiosulfate: A Readily Accessible Source of Hydrogen Sulfide in Oxygen Sensing. *Am. J. Physiol.-Regul. Integr. Comp. Physiol.* **2013**, *305* (6), R592–R603. https://doi.org/10.1152/ajpregu.00421.2012.

(65) Wang, M.; Tang, J.; Zhang, S.; Pang, K.; Zhao, Y.; Liu, N.; Huang, J.; Kang, J.; Dong, S.; Li, H.; Tian, Z.; Duan, B.; Lu, F.; Zhang, W. Exogenous H2S Initiating Nrf2/GPx4/GSH Pathway through Promoting Syvn1-Keap1 Interaction in Diabetic Hearts. *Cell Death Discov.* **2023**, *9* (1), 1–14. https://doi.org/10.1038/s41420-023-01690-w.

(66) Elrod, J. W.; Calvert, J. W.; Morrison, J.; Doeller, J. E.; Kraus, D. W.; Tao, L.; Jiao, X.; Scalia, R.; Kiss, L.; Szabo, C.; Kimura, H.; Chow, C.-W.; Lefer, D. J. Hydrogen Sulfide Attenuates Myocardial Ischemia-Reperfusion Injury by Preservation of Mitochondrial Function. *Proc. Natl. Acad. Sci.* **2007**, *104* (39), 15560–15565. https://doi.org/10.1073/pnas.0705891104.

(67) Tang, G.; Wu, L.; Wang, R. Interaction of Hydrogen Sulfide with Ion Channels. *Clin. Exp. Pharmacol. Physiol.* **2010**, *37* (7), 753–763. https://doi.org/10.1111/j.1440-1681.2010.05351.x.

(68) Bian, J.-S.; Yong, Q. C.; Pan, T.-T.; Feng, Z.-N.; Ali, M. Y.; Zhou, S.; Moore, P. K. Role of Hydrogen Sulfide in the Cardioprotection Caused by Ischemic Preconditioning in the Rat Heart and Cardiac Myocytes. *J. Pharmacol. Exp. Ther.* **2006**, *316* (2), 670–678. https://doi.org/10.1124/jpet.105.092023.

(69) Papapetropoulos, A.; Pyriochou, A.; Altaany, Z.; Yang, G.; Marazioti, A.; Zhou, Z.; Jeschke, M. G.; Branski, L. K.; Herndon, D. N.; Wang, R.; Szabó, C. Hydrogen Sulfide Is an Endogenous Stimulator of Angiogenesis. *Proc. Natl. Acad. Sci.* **2009**, *106* (51), 21972–21977. https://doi.org/10.1073/pnas.0908047106.

(70) Qipshidze, N.; Metreveli, N.; Mishra, P. K.; Lominadze, D.; Tyagi, S. C. Hydrogen Sulfide Mitigates Cardiac Remodeling During Myocardial Infarction via Improvement of Angiogenesis. *Int. J. Biol. Sci.* **2012**, *8* (4), 430–441. https://doi.org/10.7150/ijbs.3632.

(71) Coletta, C.; Papapetropoulos, A.; Erdelyi, K.; Olah, G.; Módis, K.; Panopoulos, P.; Asimakopoulou, A.; Gerö, D.; Sharina, I.; Martin, E.; Szabo, C. Hydrogen Sulfide and Nitric Oxide Are Mutually Dependent in the Regulation of Angiogenesis and Endothelium-Dependent Vasorelaxation. *Proc. Natl. Acad. Sci.* **2012**, *109* (23), 9161–9166. https://doi.org/10.1073/pnas.1202916109.

(72) Whiteman, M.; Moore, P. K. Hydrogen Sulfide and the Vasculature: A Novel Vasculoprotective Entity and Regulator of Nitric Oxide Bioavailability? *J. Cell. Mol. Med.* **2009**, *13* (3), 488–507. https://doi.org/10.1111/j.1582-4934.2009.00645.x.

(73) Altaany, Z.; Yang, G.; Wang, R. Crosstalk between Hydrogen Sulfide and Nitric Oxide in Endothelial Cells. *J. Cell. Mol. Med.* **2013**, *17* (7), 879–888. https://doi.org/10.1111/jcmm.12077.

(74) Marcolongo, J. P.; Zeida, A.; Slep, L. D.; Olabe, J. A. Thionitrous Acid/Thionitrite and Perthionitrite Intermediates in the "Crosstalk" of NO and H2S. In *Advances in Inorganic Chemistry*; van Eldik, R., Hubbard, C. D., Eds.; Inorganic Reaction Mechanisms; Academic Press, 2017; Vol. 70, pp 277–309. https://doi.org/10.1016/bs.adioch.2017.02.002.

(75) Ivanovic-Burmazovic, I.; Filipovic, M. R. Saying NO to H_2S: A Story of HNO, HSNO, and $SSNO^-$. *Inorg. Chem.* **2019**, *58* (7), 4039–4051. https://doi.org/10.1021/acs.inorgchem.8b02592.

(76) Dent, M. R.; DeMartino, A. W. Nitric Oxide and Thiols: Chemical Biology, Signalling Paradigms and Vascular Therapeutic Potential. *Br. J. Pharmacol.* **2023**. https://doi.org/10.1111/bph.16274.

(77) Marcolongo, J. P.; Venâncio, M. F.; Rocha, W. R.; Doctorovich, F.; Olabe, J. A. NO/H_2S "Crosstalk" Reactions. The Role of Thionitrites (SNO^-) and Perthionitrites ($SSNO^-$). *Inorg. Chem.* **2019**, *58* (22), 14981–14997. https://doi.org/10.1021/acs.inorgchem.9b01978.

(78) Gao, Y.; Toubaei, A.; Kong, X.; Wu, G. Solving the 170-Year-Old Mystery About Red-Violet and Blue Transient Intermediates in the Gmelin Reaction. *Chem. – Eur. J.* **2015**, *21* (48), 17172–17177. https://doi.org/10.1002/chem.201503353.

(79) Ondrias, K.; Stasko, A.; Cacanyiova, S.; Sulova, Z.; Krizanova, O.; Kristek, F.; Malekova, L.; Knezl, V.; Breier, A. H2S and HS− Donor NaHS Releases Nitric Oxide from Nitrosothiols, Metal Nitrosyl Complex, Brain Homogenate and Murine L1210 Leukaemia Cells. *Pflüg. Arch. - Eur. J. Physiol.* **2008**, *457* (2), 271–279. https://doi.org/10.1007/s00424-008-0519-0.

(80) Filipovic, M. R.; Miljkovic, J. Lj.; Nauser, T.; Royzen, M.; Klos, K.; Shubina, T.; Koppenol, W. H.; Lippard, S. J.; Ivanović-Burmazović, I. Chemical Characterization of the

Smallest S-Nitrosothiol, HSNO; Cellular Cross-Talk of H2S and S-Nitrosothiols. *J. Am. Chem. Soc.* **2012**, *134* (29), 12016–12027. https://doi.org/10.1021/ja3009693.

(81) Whiteman, M.; Li, L.; Kostetski, I.; Chu, S. H.; Siau, J. L.; Bhatia, M.; Moore, P. K. Evidence for the Formation of a Novel Nitrosothiol from the Gaseous Mediators Nitric Oxide and Hydrogen Sulphide. *Biochem. Biophys. Res. Commun.* **2006**, *343* (1), 303–310. https://doi.org/10.1016/j.bbrc.2006.02.154.

(82) Cortese-Krott, M. M.; Fernandez, B. O.; Santos, J. L. T.; Mergia, E.; Grman, M.; Nagy, P.; Kelm, M.; Butler, A.; Feelisch, M. Nitrosopersulfide (SSNO−) Accounts for Sustained NO Bioactivity of S-Nitrosothiols Following Reaction with Sulfide. *Redox Biol.* **2014**, *2*, 234–244. https://doi.org/10.1016/j.redox.2013.12.031.

(83) Cortese-Krott, M. M.; Fernandez, B. O.; Kelm, M.; Butler, A. R.; Feelisch, M. On the Chemical Biology of the Nitrite/Sulfide Interaction. *Nitric Oxide* **2015**, *46*, 14–24. https://doi.org/10.1016/j.niox.2014.12.009.

(84) Cortese-Krott, M. M.; Pullmann, D.; Feelisch, M. Nitrosopersulfide (SSNO−) Targets the Keap-1/Nrf2 Redox System. *Pharmacol. Res.* **2016**, *113*, 490–499. https://doi.org/10.1016/j.phrs.2016.09.022.

(85) Wedmann, R.; Zahl, A.; Shubina, T. E.; Dürr, M.; Heinemann, F. W.; Bugenhagen, B. E. C.; Burger, P.; Ivanovic-Burmazovic, I.; Filipovic, M. R. Does Perthionitrite ($SSNO^-$) Account for Sustained Bioactivity of NO? A (Bio)Chemical Characterization. *Inorg. Chem.* **2015**, *54* (19), 9367–9380. https://doi.org/10.1021/acs.inorgchem.5b00831.

(86) Davis, A. G.; Pluth, M. D. Experimental Insights into the Formation, Reactivity, and Crosstalk of Thionitrite (SNO−) and Perthionitrite (SSNO−). *Angew. Chem. Int. Ed.* **2025**, *64* (1), e202413092. https://doi.org/10.1002/anie.202413092.

(87) Wedmann, R.; Ivanovic-Burmazovic, I.; Filipovic, M. R. Nitrosopersulfide (SSNO−) Decomposes in the Presence of Sulfide, Cyanide or Glutathione to Give HSNO/SNO−: Consequences for the Assumed Role in Cell Signalling. *Interface Focus* **2017**, *7* (2), 20160139. https://doi.org/10.1098/rsfs.2016.0139.

(88) Rossi, F. The O2−-Forming NADPH Oxidase of the Phagocytes: Nature, Mechanisms of Activation and Function. *Biochim. Biophys. Acta BBA - Rev. Bioenerg.* **1986**, *853* (1), 65–89. https://doi.org/10.1016/0304-4173(86)90005-4.

(89) Fridovich, I. SUPEROXIDE RADICAL AND SUPEROXIDE DISMUTASES. *Annu. Rev. Biochem.* **1995**, *64* (Volume 64, 1995), 97–112. https://doi.org/10.1146/annurev.bi.64.070195.000525.

(90) Hausladen, A.; Fridovich, I. Superoxide and Peroxynitrite Inactivate Aconitases, but Nitric Oxide Does Not. *J. Biol. Chem.* **1994**, *269* (47), 29405–29408. https://doi.org/10.1016/S0021-9258(18)43893-8.

(91) Huie, R. E.; and Padmaja, S. The Reaction of No With Superoxide. *Free Radic. Res. Commun.* **1993**, *18* (4), 195–199. https://doi.org/10.3109/10715769309145868.

(92) Goldstein, S.; Merényi, G. Chapter Four - The Chemistry of Peroxynitrite: Implications for Biological Activity. In *Methods in Enzymology*; Poole, R. K., Ed.; Academic Press, 2008; Vol. 436, pp 49–61. https://doi.org/10.1016/S0076-6879(08)36004-2.

(93) Crow, J. P.; Beckman, J. S.; McCord, J. M. Sensitivity of the Essential Zinc-Thiolate Moiety of Yeast Alcohol Dehydrogenase to Hypochlorite and Peroxynitrite. *Biochemistry* **1995**, *34* (11), 3544–3552. https://doi.org/10.1021/bi00011a008.

(94) Radi, R.; Rodriguez, M.; Castro, L.; Telleri, R. Inhibition of Mitochondrial Electron Transport by Peroxynitrite. *Arch. Biochem. Biophys.* **1994**, *308* (1), 89–95. https://doi.org/10.1006/abbi.1994.1013.

(95) Estévez, A. G.; Crow, J. P.; Sampson, J. B.; Reiter, C.; Zhuang, Y.; Richardson, G. J.; Tarpey, M. M.; Barbeito, L.; Beckman, J. S. Induction of Nitric Oxide-Dependent Apoptosis in Motor Neurons by Zinc-Deficient Superoxide Dismutase. *Science* **1999**, *286* (5449), 2498–2500. https://doi.org/10.1126/science.286.5449.2498.

(96) Bandookwala, M.; Sengupta, P. 3-Nitrotyrosine: A Versatile Oxidative Stress Biomarker for Major Neurodegenerative Diseases. *Int. J. Neurosci.* **2020**.

(97) Wong, H.-S.; Dighe, P. A.; Mezera, V.; Monternier, P.-A.; Brand, M. D. Production of Superoxide and Hydrogen Peroxide from Specific Mitochondrial Sites under Different Bioenergetic Conditions. *J. Biol. Chem.* **2017**, *292* (41), 16804–16809. https://doi.org/10.1074/jbc.R117.789271.

(98) Herrmann, J. M.; Dick, T. P. Redox Biology on the Rise. *Biol. Chem.* **2012**, *393* (9), 999–1004. https://doi.org/10.1515/hsz-2012-0111.

(99) Miller, E. W.; Dickinson, B. C.; Chang, C. J. Aquaporin-3 Mediates Hydrogen Peroxide Uptake to Regulate Downstream Intracellular Signaling. *Proc. Natl. Acad. Sci.* **2010**, *107* (36), 15681–15686. https://doi.org/10.1073/pnas.1005776107.

(100) Marinho, H. S.; Real, C.; Cyrne, L.; Soares, H.; Antunes, F. Hydrogen Peroxide Sensing, Signaling and Regulation of Transcription Factors. *Redox Biol.* **2014**, *2*, 535–562. https://doi.org/10.1016/j.redox.2014.02.006.

(101) Cho, S.-H.; Lee, C.-H.; Ahn, Y.; Kim, H.; Kim, H.; Ahn, C.-Y.; Yang, K.-S.; Lee, S.-R. Redox Regulation of PTEN and Protein Tyrosine Phosphatases in H2O2-Mediated Cell Signaling. *FEBS Lett.* **2004**, *560* (1–3), 7–13. https://doi.org/10.1016/S0014-5793(04)00112-7.

(102) Sobotta, M. C.; Liou, W.; Stöcker, S.; Talwar, D.; Oehler, M.; Ruppert, T.; Scharf, A. N. D.; Dick, T. P. Peroxiredoxin-2 and STAT3 Form a Redox Relay for H2O2 Signaling. *Nat. Chem. Biol.* **2015**, *11* (1), 64–70. https://doi.org/10.1038/nchembio.1695.

(103) Andrés, C. M. C.; Pérez de la Lastra, J. M.; Juan, C. A.; Plou, F. J.; Pérez-Lebeña, E. Hypochlorous Acid Chemistry in Mammalian Cells—Influence on Infection and Role in Various Pathologies. *Int. J. Mol. Sci.* **2022**, *23* (18), 10735. https://doi.org/10.3390/ijms231810735.

(104) Storkey, C.; Davies, M. J.; Pattison, D. I. Reevaluation of the Rate Constants for the Reaction of Hypochlorous Acid (HOCl) with Cysteine, Methionine, and Peptide Derivatives Using a New Competition Kinetic Approach. *Free Radic. Biol. Med.* **2014**, *73*, 60–66. https://doi.org/10.1016/j.freeradbiomed.2014.04.024.

(105) Sies, H. Hydrogen Peroxide as a Central Redox Signaling Molecule in Physiological Oxidative Stress: Oxidative Eustress. *Redox Biol.* **2017**, *11*, 613–619. https://doi.org/10.1016/j.redox.2016.12.035.

(106) Griendling, K. K.; Sorescu, D.; Ushio-Fukai, M. NAD(P)H Oxidase. *Circ. Res.* **2000**, *86* (5), 494–501. https://doi.org/10.1161/01.RES.86.5.494.

(107) Sies, H.; Berndt, C.; Jones, D. P. Oxidative Stress. *Annu. Rev. Biochem.* **2017**, *86* (Volume 86, 2017), 715–748. https://doi.org/10.1146/annurev-biochem-061516-045037.

(108) Huber, R. E.; Criddle, R. S. Comparison of the Chemical Properties of Selenocysteine and Selenocystine with Their Sulfur Analogs. *Arch. Biochem. Biophys.* **1967**, *122* (1), 164–173. https://doi.org/10.1016/0003-9861(67)90136-1.

(109) Steinmann, D.; Nauser, T.; Koppenol, W. H. Selenium and Sulfur in Exchange Reactions: A Comparative Study. *J. Org. Chem.* **2010**, *75* (19), 6696–6699. https://doi.org/10.1021/jo1011569.

(110) Cupp-Sutton, K. A.; Ashby, M. T. Biological Chemistry of Hydrogen Selenide. *Antioxidants* **2016**, *5* (4), 42. https://doi.org/10.3390/antiox5040042.

(111) Maia, L. B.; Maiti, B. K.; Moura, I.; Moura, J. J. G. Selenium—More than Just a Fortuitous Sulfur Substitute in Redox Biology. *Molecules* **2024**, *29* (1), 120. https://doi.org/10.3390/molecules29010120.

(112) Vinceti, M.; Burlingame, B.; Filippini, T.; Naska, A.; Bargellini, A.; Borella, P. The Epidemiology of Selenium and Human Health. In *Selenium: Its Molecular Biology and Role in Human Health*; Hatfield, D. L., Schweizer, U., Tsuji, P. A., Gladyshev, V. N., Eds.; Springer International Publishing: Cham, 2016; pp 365–376. https://doi.org/10.1007/978-3-319-41283-2_31.

(113) Gilbert, A. K.; Newton, T. D.; Hettiaratchi, M. H.; Pluth, M. D. Reactive Sulfur and Selenium Species in the Regulation of Bone Homeostasis. *Free Radic. Biol. Med.* **2022**, *190*, 148–157. https://doi.org/10.1016/j.freeradbiomed.2022.08.002.

(114) Combs, G. F.; Yan, L. Status of Dietary Selenium in Cancer Prevention. In *Selenium: Its Molecular Biology and Role in Human Health*; Hatfield, D. L., Schweizer, U., Tsuji, P. A.,

Gladyshev, V. N., Eds.; Springer International Publishing: Cham, 2016; pp 321–332. https://doi.org/10.1007/978-3-319-41283-2_27.

(115) Stolwijk, J. M.; Garje, R.; Sieren, J. C.; Buettner, G. R.; Zakharia, Y. Understanding the Redox Biology of Selenium in the Search of Targeted Cancer Therapies. *Antioxidants* **2020**, *9* (5), 420. https://doi.org/10.3390/antiox9050420.

(116) Xie, C.; Zeng, M.; Shi, Z.; Li, S.; Jiang, K.; Zhao, Y. Association between Selenium Status and Chronic Kidney Disease in Middle-Aged and Older Chinese Based on CHNS Data. *Nutrients* **2022**, *14* (13), 2695. https://doi.org/10.3390/nu14132695.

(117) Bella, S. D.; Grilli, E.; Cataldo, M. A.; Petrosillo, N. Selenium Deficiency and HIV Infection. *Infect. Dis. Rep.* **2010**, *2* (2), e18. https://doi.org/10.4081/idr.2010.e18.

(118) Ju, W.; Li, X.; Li, Z.; Wu, G. R.; Fu, X. F.; Yang, X. M.; Zhang, X. Q.; Gao, X. B. The Effect of Selenium Supplementation on Coronary Heart Disease: A Systematic Review and Meta-Analysis of Randomized Controlled Trials. *J. Trace Elem. Med. Biol. Organ Soc. Miner. Trace Elem. GMS* **2017**, *44*, 8–16. https://doi.org/10.1016/j.jtemb.2017.04.009.

(119) *Selenium: Its Molecular Biology and Role in Human Health*; Hatfield, D. L., Schweizer, U., Tsuji, P. A., Gladyshev, V. N., Eds.; Springer International Publishing: Cham, 2016. https://doi.org/10.1007/978-3-319-41283-2.

(120) Reich, H. J.; Hondal, R. J. Why Nature Chose Selenium. *ACS Chem. Biol.* **2016**, *11* (4), 821–841. https://doi.org/10.1021/acschembio.6b00031.

(121) Hatfield, D. L.; Tsuji, P. A.; Carlson, B. A.; Gladyshev, V. N. Selenium and Selenocysteine: Roles in Cancer, Health, and Development. *Trends Biochem. Sci.* **2014**, *39* (3), 112–120. https://doi.org/10.1016/j.tibs.2013.12.007.

(122) Lazard, M.; Dauplais, M.; Blanquet, S.; Plateau, P. Trans-Sulfuration Pathway Seleno-Amino Acids Are Mediators of Selenomethionine Toxicity in Saccharomyces Cerevisiae*. *J. Biol. Chem.* **2015**, *290* (17), 10741–10750. https://doi.org/10.1074/jbc.M115.640375.

(123) Hsieh, H. S.; Ganther, H. E. Acid-Volatile Selenium Formation Catalyzed by Glutathione Reductase. *Biochemistry* **1975**, *14* (8), 1632–1636. https://doi.org/10.1021/bi00679a014.

(124) Kessi, J.; Hanselmann, K. W. Similarities between the Abiotic Reduction of Selenite with Glutathione and the Dissimilatory Reaction Mediated by Rhodospirillum Rubrum and Escherichia Coli. *J. Biol. Chem.* **2004**, *279* (49), 50662–50669. https://doi.org/10.1074/jbc.M405887200.

(125) Lacourciere, G. M. Biosynthesis of Selenophosphate. *BioFactors* **1999**, *10* (2–3), 237–244. https://doi.org/10.1002/biof.5520100222.

(126) Stadtman, T. C. SELENOCYSTEINE. *Annu. Rev. Biochem.* **1996**, *65* (Volume 65, 1996), 83–100. https://doi.org/10.1146/annurev.bi.65.070196.000503.

(127) Holben, D. H.; Smith, A. M. The Diverse Role of Selenium within Selenoproteins: A Review. *J. Am. Diet. Assoc.* **1999**, *99* (7), 836–843. https://doi.org/10.1016/S0002-8223(99)00198-4.

(128) Köhrle, J.; Brigelius-Flohé, R.; Böck, A.; Gärtner, R.; Meyer, O.; Flohé, L. Selenium in Biology: Facts and Medical Perspectives. **2000**, *381* (9–10), 849–864. https://doi.org/10.1515/BC.2000.107.

(129) Vetter, J. Plant Cyanogenic Glycosides. *Toxicon Off. J. Int. Soc. Toxinology* **2000**, *38* (1), 11–36. https://doi.org/10.1016/s0041-0101(99)00128-2.

(130) Yulvianti, M.; Zidorn, C. Chemical Diversity of Plant Cyanogenic Glycosides: An Overview of Reported Natural Products. *Molecules* **2021**, *26* (3), 719. https://doi.org/10.3390/molecules26030719.

(131) Stelmaszynska, T. Formation of HCN by Human Phagocytosing Neutrophils — 1. Chlorination of *Staphylococcus Epidermidis* as a Source of HCN. *Int. J. Biochem.* **1985**, *17* (3), 373–379. https://doi.org/10.1016/0020-711X(85)90213-7.

(132) Gunasekar, P. g.; Borowitz, J. l.; Turek, J. j.; Van Horn, D. a.; Isom, G. e. Endogenous Generation of Cyanide in Neuronal Tissue: Involvement of a Peroxidase System. *J. Neurosci. Res.* **2000**, *61* (5), 570–575. https://doi.org/10.1002/1097-4547(20000901)61:5<570::AID-JNR12>3.0.CO;2-V.

(133) Borowitz, J. L.; Gunasekar, P. G.; Isom, G. E. Hydrogen Cyanide Generation by μ-Opiate Receptor Activation: Possible Neuromodulatory Role of Endogenous Cyanide. *Brain Res.* **1997**, *768* (1), 294–300. https://doi.org/10.1016/S0006-8993(97)00659-8.

(134) Eiserich, J. P.; Ott, S. P.; Kadir, T.; Morrissey, B. M.; Hayakawa, K. A.; La Merrill, M. A.; Cross, C. E. Quantitative Assessment of Cyanide in Cystic Fibrosis Sputum and Its Oxidative Catabolism by Hypochlorous Acid. *Free Radic. Biol. Med.* **2018**, *129*, 146–154. https://doi.org/10.1016/j.freeradbiomed.2018.09.007.

(135) Delporte, C.; Zouaoui Boudjeltia, K.; Furtmüller, P. G.; Maki, R. A.; Dieu, M.; Noyon, C.; Soudi, M.; Dufour, D.; Coremans, C.; Nuyens, V.; Reye, F.; Rousseau, A.; Raes, M.; Moguilevsky, N.; Vanhaeverbeek, M.; Ducobu, J.; Nève, J.; Robaye, B.; Vanhamme, L.; Reynolds, W. F.; Obinger, C.; Van Antwerpen, P. Myeloperoxidase-Catalyzed Oxidation of Cyanide to Cyanate: A Potential Carbamylation Route Involved in the Formation of Atherosclerotic Plaques? *J. Biol. Chem.* **2018**, *293* (17), 6374–6386. https://doi.org/10.1074/jbc.M117.801076.

(136) Gupta, N.; Balomajumder, C.; Agarwal, V. K. Enzymatic Mechanism and Biochemistry for Cyanide Degradation: A Review. *J. Hazard. Mater.* **2010**, *176* (1), 1–13. https://doi.org/10.1016/j.jhazmat.2009.11.038.

(137) Keilin, D. Cytochrome and Respiratory Enzymes. *Proc. R. Soc. Lond.* **1929**, *104* (730), 206–252. https://doi.org/10.1098/rspb.1929.0009.

(138) Fosslien, E. Mitochondrial Medicine – Molecular Pathology of Defective Oxidative Phosphorylation. *Ann. Clin. Lab. Sci.* **2001**, *31* (1), 25–67.

(139) Younes, M.; Strubelt, O. Cyanide-Induced Injury to the Isolated Perfused Rat Liver. *Pharmacol. Toxicol.* **1988**, *63* (5), 382–385. https://doi.org/10.1111/j.1600-0773.1988.tb00972.x.

(140) Bhattacharya, R.; Lakshmana Rao, P. V. Cyanide Induced DNA Fragmentation in Mammalian Cell Cultures. *Toxicology* **1997**, *123* (3), 207–215. https://doi.org/10.1016/S0300-483X(97)00130-3.

(141) Yamamoto, H.; Mohanan, P. V. Melatonin Attenuates Brain Mitochondria DNA Damage Induced by Potassium Cyanide in Vivo and in Vitro. *Toxicology* **2002**, *179* (1), 29–36. https://doi.org/10.1016/S0300-483X(02)00244-5.

(142) Zemlyak, I.; Sapolsky, R.; Gozes, I. NAP Protects against Cyanide-Related Microtubule Destruction. *J. Neural Transm.* **2009**, *116* (11), 1411–1416. https://doi.org/10.1007/s00702-009-0252-7.

(143) Shou, Y.; Gunasekar, P. G.; Borowitz, J. L.; Isom, G. E. Cyanide-Induced Apoptosis Involves Oxidative-Stress-Activated NF-kappaB in Cortical Neurons. *Toxicol. Appl. Pharmacol.* **2000**, *164* (2), 196–205. https://doi.org/10.1006/taap.2000.8900.

(144) Shou, Y.; Li, N.; Li, L.; Borowitz, J. L.; Isom, G. E. NF-kappaB-Mediated up-Regulation of Bcl-X(S) and Bax Contributes to Cytochrome c Release in Cyanide-Induced Apoptosis. *J. Neurochem.* **2002**, *81* (4), 842–852. https://doi.org/10.1046/j.1471-4159.2002.00880.x.

(145) Prabhakaran, K.; Li, L.; Borowitz, J. L.; Isom, G. E. Caspase Inhibition Switches the Mode of Cell Death Induced by Cyanide by Enhancing Reactive Oxygen Species Generation and PARP-1 Activation. *Toxicol. Appl. Pharmacol.* **2004**, *195* (2), 194–202. https://doi.org/10.1016/j.taap.2003.11.012.

(146) Maduh, E. U.; Borowitz, J. L.; Isom, G. E. Cyanide-Induced Alteration of Cytosolic pH: Involvement of Cellular Hydrogen Ion Handling Processes. *Toxicol. Appl. Pharmacol.* **1990**, *106* (2), 201–208. https://doi.org/10.1016/0041-008x(90)90240-u.

(147) Persson, S.-Å.; Cassel, G.; Sellström, Å. Acute Cyanide Intoxication and Central Transmitter Systems. *Fundam. Appl. Toxicol.* **1985**, *5* (6, Part 2), S150–S159. https://doi.org/10.1016/0272-0590(85)90124-1.

(148) Patel, M. N.; Ardelt, B. K.; Yim, G. K. W.; Isom, G. E. Cyanide Induces Ca2+-Dependent and -Independent Release of Glutamate from Mouse Brain Slices. *Neurosci. Lett.* **1991**, *131* (1), 42–44. https://doi.org/10.1016/0304-3940(91)90332-N.

(149) Correia, S. C.; Santos, R. X.; Cardoso, S. M.; Santos, M. S.; Oliveira, C. R.; Moreira, P. I. Cyanide Preconditioning Protects Brain Endothelial and NT2 Neuron-like Cells against Glucotoxicity: Role of Mitochondrial Reactive Oxygen Species and HIF-1α. *Neurobiol. Dis.* **2012**, *45* (1), 206–218. https://doi.org/10.1016/j.nbd.2011.08.005.

(150) Zuhra, K.; Petrosino, M.; Janickova, L.; Petric, J.; Ascenção, K.; Vignane, T.; Khalaf, M.; Philipp, T. M.; Ravani, S.; Anand, A.; Martins, V.; Santos, S.; Erdemir, S.; Malkondu, S.; Sitek, B.; Kelestemur, T.; Kieronska-Rudek, A.; Majtan, T.; Filgueira, L.; Maric, D.; Chlopicki, S.; Hoogewijs, D.; Haskó, G.; Papapetropoulos, A.; Logue, B. A.; Boss, G. R.; Filipovic, M. R.; Szabo, C. Regulation of Mammalian Cellular Metabolism by Endogenous Cyanide Production. *Nat. Metab.* **2025**, 1–25. https://doi.org/10.1038/s42255-025-01225-w.

(151) Randi, E. B.; Zuhra, K.; Pecze, L.; Panagaki, T.; Szabo, C. Physiological Concentrations of Cyanide Stimulate Mitochondrial Complex IV and Enhance Cellular Bioenergetics. *Proc. Natl. Acad. Sci.* **2021**, *118* (20), e2026245118. https://doi.org/10.1073/pnas.2026245118.

(152) Motl, N.; Yadav, P.; Banerjee, R. Enzymology of Hydrogen Sulfide Turnover. In *Hydrogen Sulfide and its Therapeutic Applications*; Kimura, H., Ed.; Springer: Vienna, 2013; pp 1–35. https://doi.org/10.1007/978-3-7091-1550-3_1.

(153) Mooshammer, M.; Wanek, W.; Jones, S. H.; Richter, A.; Wagner, M. Cyanate Is a Low Abundance but Actively Cycled Nitrogen Compound in Soil. *Commun. Earth Environ.* **2021**, *2* (1), 1–10. https://doi.org/10.1038/s43247-021-00235-2.

(154) Staicu, L. C.; van Hullebusch, E. D.; Lens, P. N. L. Industrial Selenium Pollution: Wastewaters and Physical–Chemical Treatment Technologies. In *Bioremediation of Selenium Contaminated Wastewater*; van Hullebusch, E. D., Ed.; Springer International Publishing: Cham, 2017; pp 103–130. https://doi.org/10.1007/978-3-319-57831-6_5.

(155) Filipovic, M. R.; Zivanovic, J.; Alvarez, B.; Banerjee, R. Chemical Biology of H_2S Signaling through Persulfidation. *Chem. Rev.* **2018**, *118* (3), 1253–1337. https://doi.org/10.1021/acs.chemrev.7b00205.

(156) Hoiland, R. L.; MacLeod, D. B.; Stacey, B. S.; Caldwell, H. G.; Howe, C. A.; Nowak-Flück, D.; Carr, J. M.; Tymko, M. M.; Coombs, G. B.; Patrician, A.; Tremblay, J. C.; Van Mierlo, M.; Gasho, C.; Stembridge, M.; Sekhon, M. S.; Bailey, D. M.; Ainslie, P. N. Hemoglobin and Cerebral Hypoxic Vasodilation in Humans: Evidence for Nitric Oxide-Dependent and S-Nitrosothiol Mediated Signal Transduction. *J. Cereb. Blood Flow Metab.* **2023**, *43* (9), 1519–1531. https://doi.org/10.1177/0271678X231169579.

(157) Wang, K.; Moore, A.; Grayson, C.; Mailloux, R. J. S-Nitroso-Glutathione (GSNO) Inhibits Hydrogen Peroxide Production by Alpha-Ketoglutarate Dehydrogenase: An Investigation into Sex and Diet Effects. *Free Radic. Biol. Med.* **2023**, *204*, 287–300. https://doi.org/10.1016/j.freeradbiomed.2023.05.010.

(158) Müller, R. P.; Nonella, M.; Russegger, P.; Huber, J. R. UV-, VIS- and IR-Light-Induced Isomerization of HSNO in a Low-Temperature Matrix. *Chem. Phys.* **1984**, *87* (3), 351–361. https://doi.org/10.1016/0301-0104(84)85116-2.

(159) Nonella, M.; Huber, J. Robert.; Ha, T. Kyu. Photolytic Preparation and Isomerization of Thionyl Imide, Thiocyanic Acid, Thionitrous Acid, and Nitrogen Hydroxide Sulfide in an Argon

Matrix: An Experimental and Theoretical Study. *J. Phys. Chem.* **1987**, *91* (20), 5203–5209. https://doi.org/10.1021/j100304a014.

(160) Kolliyedath, G.; Sahana, T.; Johnson, S. M.; Kundu, S. Synergistic Activation of Nitrite and Thiocarbonyl Compounds Affords NO and Sulfane Sulfur via (Per)Thionitrite (SNO−/SSNO−). *Angew. Chem. Int. Ed.* **2023**, *62* (50), e202313187. https://doi.org/10.1002/anie.202313187.

(161) Ghosh, P.; Stauffer, M.; Ahmed, M. E.; Bertke, J. A.; Staples, R. J.; Warren, T. H. Thiol and H2S-Mediated NO Generation from Nitrate at Copper(II). *J. Am. Chem. Soc.* **2023**, *145* (22), 12007–12012. https://doi.org/10.1021/jacs.3c00394.

(162) Kundu, S.; Kim, W. Y.; Bertke, J. A.; Warren, T. H. Copper(II) Activation of Nitrite: Nitrosation of Nucleophiles and Generation of NO by Thiols. *J. Am. Chem. Soc.* **2017**, *139* (3), 1045–1048. https://doi.org/10.1021/jacs.6b11332.

(163) Nava, M.; Martin-Drumel, M.-A.; Lopez, C. A.; Crabtree, K. N.; Womack, C. C.; Nguyen, T. L.; Thorwirth, S.; Cummins, C. C.; Stanton, J. F.; McCarthy, M. C. Spontaneous and Selective Formation of HSNO, a Crucial Intermediate Linking H2S and Nitroso Chemistries. *J. Am. Chem. Soc.* **2016**, *138* (36), 11441–11444. https://doi.org/10.1021/jacs.6b05886.

(164) Bailey, T. S.; Henthorn, H. A.; Pluth, M. D. The Intersection of NO and H_2S: Persulfides Generate NO from Nitrite through Polysulfide Formation. *Inorg. Chem.* **2016**, *55* (24), 12618–12625. https://doi.org/10.1021/acs.inorgchem.6b01660.

(165) Seel, F.; Kuhn, R.; Simon, G.; Wagner, M. PNP-Perthionitrit Und PNP-Monothionitrit / PNP-Perthionitrite and PNP-M Onothionitrite. *Z. Für Naturforschung B* **1985**, *40* (12), 1607–1617. https://doi.org/10.1515/znb-1985-1203.

(166) Victor, E. Reactions of S-Nitrosothiols with Biomimetic Iron Complexes and Other Transition Metals, University of Wisconsin, Madison, WI, 2014.

(167) Hosseininasab, V.; Bertke, J. A.; Warren, T. H. Thionitrite and Perthionitrite in NO Signaling at Zinc. *Angew. Chem. Int. Ed.* **2021**, *60* (39), 21184–21188. https://doi.org/10.1002/anie.202104906.

(168) Hosseininasab, V.; McQuilken, A. C.; Bakhoda, A. (Gus); Bertke, J. A.; Timerghazin, Q. K.; Warren, T. H. Lewis Acid Coordination Redirects S-Nitrosothiol Signaling Output. *Angew. Chem. Int. Ed.* **2020**, *59* (27), 10854–10858. https://doi.org/10.1002/anie.202001450.

(169) Sherbow, T. J.; Fu, W.; Tao, L.; Zakharov, L. N.; Britt, R. D.; Pluth, M. D. Thionitrite (SNO−) and Perthionitrite (SSNO−) Are Simple Synthons for Nitrosylated Iron Sulfur Clusters. *Angew. Chem. Int. Ed.* **2022**, *61* (30), e202204570. https://doi.org/10.1002/anie.202204570.

(170) Marcolongo, J. P.; Morzan, U. N.; Zeida, A.; Scherlis, D. A.; Olabe, J. A. Nitrosodisulfide [S2NO]− (Perthionitrite) Is a True Intermediate during the “Cross-Talk” of

Nitrosyl and Sulfide. *Phys. Chem. Chem. Phys.* **2016**, *18* (43), 30047–30052. https://doi.org/10.1039/C6CP06314D.

(171) Amanullah, S.; Dey, A. The Role of Porphyrin Peripheral Substituents in Determining the Reactivities of Ferrous Nitrosyl Species. *Chem. Sci.* **2020**, *11* (23), 5909–5921. https://doi.org/10.1039/D0SC01625J.

(172) Nash, K. M.; Rockenbauer, A.; Villamena, F. A. Reactive Nitrogen Species Reactivities with Nitrones: Theoretical and Experimental Studies. *Chem. Res. Toxicol.* **2012**, *25* (8), 1581–1597. https://doi.org/10.1021/tx200526y.

(173) Wade Wolfe, M. M.; Pluth, M. D. Understanding Reactive Sulfur Species through P/S Synergy. *Inorg. Chem.* **2023**, *62* (35), 14339–14343. https://doi.org/10.1021/acs.inorgchem.3c01976.

(174) Wong, P. S.-Y.; Hyun, J.; Fukuto, J. M.; Shirota, F. N.; DeMaster, E. G.; Shoeman, D. W.; Nagasawa, H. T. Reaction between S-Nitrosothiols and Thiols: Generation of Nitroxyl (HNO) and Subsequent Chemistry. *Biochemistry* **1998**, *37* (16), 5362–5371. https://doi.org/10.1021/bi973153g.

(175) Ferm, R. J. The Chemistry Of Carbonyl Sulfide. *Chem. Rev.* **1957**, *57* (4), 621–640. https://doi.org/10.1021/cr50016a002.

(176) Leman, L.; Orgel, L.; Ghadiri, M. R. Carbonyl Sulfide-Mediated Prebiotic Formation of Peptides. *Science* **2004**, *306* (5694), 283–286. https://doi.org/10.1126/science.1102722.

(177) Pursglove, L. A.; Wainwright, H. W. Colorimetric Determination of Carbony Sulfide in Synthesis Gas. *Anal. Chem.* **1954**, *26* (11), 1835–1839. https://doi.org/10.1021/ac60095a044.

(178) Cerda, M. M.; Fehr, J. M.; Sherbow, T. J.; Pluth, M. D. Progress toward Colorimetric and Fluorescent Detection of Carbonyl Sulfide. *Chem. Commun.* **2020**, *56* (67), 9644–9647. https://doi.org/10.1039/D0CC04528D.

(179) Hartmann, N. J.; Wu, G.; Hayton, T. W. Reactivity of a Nickel Sulfide with Carbon Monoxide and Nitric Oxide. *J. Am. Chem. Soc.* **2016**, *138* (38), 12352–12355. https://doi.org/10.1021/jacs.6b08084.

(180) Gale, P. A.; Sessler, J. L.; Král, V.; Lynch, V. Calix[4]Pyrroles: Old Yet New Anion-Binding Agents. *J. Am. Chem. Soc.* **1996**, *118* (21), 5140–5141. https://doi.org/10.1021/ja960307r.

(181) Anzenbacher, P.; Jursíková, K.; Lynch, V. M.; Gale, P. A.; Sessler, J. L. Calix[4]Pyrroles Containing Deep Cavities and Fixed Walls. Synthesis, Structural Studies, and Anion Binding Properties of the Isomeric Products Derived from the Condensation of *p* -Hydroxyacetophenone and Pyrrole. *J. Am. Chem. Soc.* **1999**, *121* (47), 11020–11021. https://doi.org/10.1021/ja993195n.

(182) Bowman-James, K. Alfred Werner Revisited: The Coordination Chemistry of Anions. *Acc. Chem. Res.* **2005**, *38* (8), 671–678. https://doi.org/10.1021/ar040071t.

(183) Li, A.-F.; Wang, J.-H.; Wang, F.; Jiang, Y.-B. Anion Complexation and Sensing Using Modified Urea and Thiourea-Based Receptors. *Chem. Soc. Rev.* **2010**, *39* (10), 3729–3745. https://doi.org/10.1039/B926160P.

(184) Sessler, J. L.; Davis, J. M. Sapphyrins: Versatile Anion Binding Agents. *Acc. Chem. Res.* **2001**, *34* (12), 989–997. https://doi.org/10.1021/ar980117g.

(185) Wang, D.-X.; Wang, M.-X. Anion−π Interactions: Generality, Binding Strength, and Structure. *J. Am. Chem. Soc.* **2013**, *135* (2), 892–897. https://doi.org/10.1021/ja310834w.

(186) Tirfoin, R.; Abdalla, J. A. B.; Aldridge, S. Extension of Conjugation: Probing Anion Binding Strength and Reporter Mechanisms in (Phenyl)Cyclopentadienyl and Indenyl Receptors. *Dalton Trans.* **2015**, *44* (29), 13049–13059. https://doi.org/10.1039/C5DT01955A.

(187) Dürr, K.; Macpherson, B. P.; Warratz, R.; Hampel, F.; Tuczek, F.; Helmreich, M.; Jux, N.; Ivanović-Burmazović, I. Iron(III) Complex of a Crown Ether−Porphyrin Conjugate and Reversible Binding of Superoxide to Its Iron(II) Form. *J. Am. Chem. Soc.* **2007**, *129* (14), 4217–4228. https://doi.org/10.1021/ja064984p.

(188) Lopez, N.; Graham, D. J.; McGuire, R.; Alliger, G. E.; Shao-Horn, Y.; Cummins, C. C.; Nocera, D. G. Reversible Reduction of Oxygen to Peroxide Facilitated by Molecular Recognition. *Science* **2012**, *335* (6067), 450–453. https://doi.org/10.1126/science.1212678.

(189) Rathore, R.; Lindeman, S. V.; Rao, K. S. S. P.; Sun, D.; Kochi, J. K. Guest Penetration Deep within the Cavity of Calix[4]Arene Hosts: The Tight Binding of Nitric Oxide to Distal (Cofacial) Aromatic Groups. *Angew. Chem. Int. Ed.* **2000**, *39* (12), 2123–2127. https://doi.org/10.1002/1521-3773(20000616)39:12<2123::AID-ANIE2123>3.0.CO;2-4.

(190) Zyryanov, G. V.; Kang, Y.; Rudkevich, D. M. Sensing and Fixation of NO_2 /N_2O_4 by Calix[4]Arenes. *J. Am. Chem. Soc.* **2003**, *125* (10), 2997–3007. https://doi.org/10.1021/ja029166l.

(191) Tuo, D.-H.; Ao, Y.-F.; Wang, Q.-Q.; Wang, D.-X. Benzene Triimide Cage as a Selective Container of Azide. *Org. Lett.* **2019**, *21* (17), 7158–7162. https://doi.org/10.1021/acs.orglett.9b02782.

(192) Wang, R. Physiological Implications of Hydrogen Sulfide: A Whiff Exploration That Blossomed. *Physiol. Rev.* **2012**, *92* (2), 791–896. https://doi.org/10.1152/physrev.00017.2011.

(193) Bieza, S.; Mazzeo, A.; Pellegrino, J.; Doctorovich, F. H_2S/Thiols, $NO^{\bullet}$, and NO^{-}/HNO: Interactions with Iron Porphyrins. *ACS Omega* **2022**, *7* (2), 1602–1611. https://doi.org/10.1021/acsomega.1c06427.

(194) Kang, S. O.; VanderVelde, D.; Powell, D.; Bowman-James, K. Fluoride-Facilitated Deuterium Exchange from DMSO- d_6 to Polyamide-Based Cryptands. *J. Am. Chem. Soc.* **2004**, *126* (39), 12272–12273. https://doi.org/10.1021/ja046078n.

(195) Kang, S. O.; Llinares, J. M.; Powell, D.; VanderVelde, D.; Bowman-James, K. New Polyamide Cryptand for Anion Binding. *J. Am. Chem. Soc.* **2003**, *125* (34), 10152–10153. https://doi.org/10.1021/ja034969+.

(196) Fatila, E. M.; Twum, E. B.; Sengupta, A.; Pink, M.; Karty, J. A.; Raghavachari, K.; Flood, A. H. Anions Stabilize Each Other inside Macrocyclic Hosts. *Angew. Chem. Int. Ed.* **2016**, *55* (45), 14057–14062. https://doi.org/10.1002/anie.201608118.

(197) Lee, S.; Chen, C.-H.; Flood, A. H. A Pentagonal Cyanostar Macrocycle with Cyanostilbene CH Donors Binds Anions and Forms Dialkylphosphate [3]Rotaxanes. *Nat. Chem.* **2013**, *5* (8), 704–710. https://doi.org/10.1038/nchem.1668.

(198) Vázquez, J.; Sindelar, V. Supramolecular Binding and Release of Sulfide and Hydrosulfide Anions in Water. *Chem. Commun.* **2018**, *54* (46), 5859–5862. https://doi.org/10.1039/C8CC00470F.

(199) Yawer, M. A.; Havel, V.; Sindelar, V. A Bambusuril Macrocycle That Binds Anions in Water with High Affinity and Selectivity. *Angew. Chem. Int. Ed.* **2015**, *54* (1), 276–279. https://doi.org/10.1002/anie.201409895.

(200) Hartle, M. D.; Hansen, R. J.; Tresca, B. W.; Prakel, S. S.; Zakharov, L. N.; Haley, M. M.; Pluth, M. D.; Johnson, D. W. A Synthetic Supramolecular Receptor for the Hydrosulfide Anion. *Angew. Chem. Int. Ed.* **2016**, *55* (38), 11480–11484. https://doi.org/10.1002/anie.201605757.

(201) Fargher, H. A.; Lau, N.; Zakharov, L. N.; Haley, M. M.; Johnson, D. W.; Pluth, M. D. Expanding Reversible Chalcogenide Binding: Supramolecular Receptors for the Hydroselenide (HSe−) Anion. *Chem. Sci.* **2018**, *10* (1), 67–72. https://doi.org/10.1039/C8SC03968B.

(202) Fargher, H. A.; Lau, N.; Richardson, H. C.; Cheong, P. H.-Y.; Haley, M. M.; Pluth, M. D.; Johnson, D. W. Tuning Supramolecular Selectivity for Hydrosulfide: Linear Free Energy Relationships Reveal Preferential C–H Hydrogen Bond Interactions. *J. Am. Chem. Soc.* **2020**, *142* (18), 8243–8251. https://doi.org/10.1021/jacs.0c00441.

(203) Lau, N.; Zakharov, L. N.; Pluth, M. D. Modular Tripodal Receptors for the Hydrosulfide (HS−) Anion. *Chem. Commun.* **2018**, *54* (19), 2337–2340. https://doi.org/10.1039/C7CC09405A.

(204) Mitchell, E. J.; Beecroft, A. J.; Martin, J.; Thompson, S.; Marques, I.; Félix, V.; Beer, P. D. Hydrosulfide (HS−) Recognition and Sensing in Water by Halogen Bonding Hosts. *Angew. Chem. Int. Ed.* **2021**, *60* (45), 24048–24053. https://doi.org/10.1002/anie.202110442.

(205) Kumar, P.; Kumar, V.; Pandey, S.; Gupta, R. Detection of Sulfide Ion and Gaseous H2S Using a Series of Pyridine-2,6-Dicarboxamide Based Scaffolds. *Dalton Trans.* **2018**, *47* (28), 9536–9545. https://doi.org/10.1039/C8DT01351A.

(206) Fargher, H. A.; Sherbow, T. J.; Haley, M. M.; Johnson, D. W.; Pluth, M. D. C–H···S Hydrogen Bonding Interactions. *Chem. Soc. Rev.* **2022**, *51* (4), 1454–1469. https://doi.org/10.1039/D1CS00838B.

(207) Alcalde, E.; Mesquida, N.; Pérez-García, L.; Alvarez-Rúa, C.; García-Granda, S.; García-Rodriguez, E. Hydrogen Bonded Driven Anion Binding by Dicationic [14]Imidazoliophanes. *Chem. Commun.* **1999**, No. 3, 295–296. https://doi.org/10.1039/a808503j.

(208) Fahlbusch, T.; Frank, M.; Schatz, J.; Schmaderer, H. Influence of the Number and Geometry of Binding Sites on Host–Guest Affinity: Imidazolium-Substituted Receptor Molecules for Small Inorganic Anions. *Eur. J. Org. Chem.* **2006**, *2006* (8), 1899–1903. https://doi.org/10.1002/ejoc.200500825.

(209) Hu, Y.; Long, S.; Fu, H.; She, Y.; Xu, Z.; Yoon, J. Revisiting Imidazolium Receptors for the Recognition of Anions: Highlighted Research during 2010–2019. *Chem. Soc. Rev.* **2021**, *50* (1), 589–618. https://doi.org/10.1039/D0CS00642D.

(210) Alcalde, E.; Mesquida, N.; Pérez-García, L. Imidazolium-Based [14]Heterophanes as Models for Anion Recognition. *Eur. J. Org. Chem.* **2006**, *2006* (17), 3988–3996. https://doi.org/10.1002/ejoc.200600269.

(211) Hartle, M. D.; Meininger, D. J.; Zakharov, L. N.; Tonzetich, Z. J.; Pluth, M. D. NBu4SH Provides a Convenient Source of HS− Soluble in Organic Solution for H2S and Anion-Binding Research. *Dalton Trans.* **2015**, *44* (46), 19782–19785. https://doi.org/10.1039/C5DT03355A.

(212) Hibbert, D. B.; Thordarson, P. The Death of the Job Plot, Transparency, Open Science and Online Tools, Uncertainty Estimation Methods and Other Developments in Supramolecular Chemistry Data Analysis. *Chem. Commun.* **2016**, *52* (87), 12792–12805. https://doi.org/10.1039/C6CC03888C.

(213) Thordarson, P. Determining Association Constants from Titration Experiments in Supramolecular Chemistry. *Chem Soc Rev* **2011**, *40* (3), 1305–1323. https://doi.org/10.1039/C0CS00062K.

(214) http://supramolecular.org

(215) Batsanov, S. S. Van Der Waals Radii of Elements. *Inorg. Mater.* **2001**, *37* (9), 871–885. https://doi.org/10.1023/A:1011625728803.

(216) Bowman-James, K. Supramolecular Cages Trap Pesky Anions. *Science* **2019**, *365* (6449), 124–125. https://doi.org/10.1126/science.aax9369.

(217) Cao, R.; Rossdeutcher, R. B.; Wu, X.; Gong, B. Oligo(5-Amino-N-Acylanthranilic Acids): Amide Bond Formation without Coupling Reagent and Folding upon Binding Anions. *Org. Lett.* **2020**, *22* (19), 7496–7501. https://doi.org/10.1021/acs.orglett.0c02696.

(218) Hua, Y.; Flood, A. H. Click Chemistry Generates Privileged CH Hydrogen-Bonding Triazoles: The Latest Addition to Anion Supramolecular Chemistry. *Chem. Soc. Rev.* **2010**, *39* (4), 1262–1271. https://doi.org/10.1039/B818033B.

(219) Liu, Y.; Zhao, W.; Chen, C.-H.; Flood, A. H. Chloride Capture Using a C–H Hydrogen-Bonding Cage. *Science* **2019**, *365* (6449), 159–161. https://doi.org/10.1126/science.aaw5145.

(220) Mullen, K. M.; Mercurio, J.; Serpell, C. J.; Beer, P. D. Exploiting the 1,2,3-Triazolium Motif in Anion-Templated Formation of a Bromide-Selective Rotaxane Host Assembly. *Angew. Chem. Int. Ed.* **2009**, *48* (26), 4781–4784. https://doi.org/10.1002/anie.200901313.

(221) Hossain, Md. A.; Llinares, J. M.; Powell, D.; Bowman-James, K. Multiple Hydrogen Bond Stabilization of a Sandwich Complex of Sulfate between Two Macrocyclic Tetraamides. *Inorg. Chem.* **2001**, *40* (13), 2936–2937. https://doi.org/10.1021/ic015508x.

(222) Kaur, S.; Day, V. W.; Bowman-James, K. Urea-Based Macrocycle Selective for Sulfate and Structurally Sensitive to Water. *Cryst. Growth Des.* **2020**, *20* (7), 4212–4216. https://doi.org/10.1021/acs.cgd.0c00411.

(223) Kundu, S.; Egboluche, T. K.; Hossain, Md. A. Urea- and Thiourea-Based Receptors for Anion Binding. *Acc. Chem. Res.* **2023**, *56* (11), 1320–1329. https://doi.org/10.1021/acs.accounts.2c00701.

(224) Bisson, A. P.; Lynch, V. M.; Monahan, M.-K. C.; Anslyn, E. V. Recognition of Anions through NH□π Hydrogen Bonds in a Bicyclic Cyclophane—Selectivity for Nitrate. *Angew. Chem. Int. Ed. Engl.* **1997**, *36* (21), 2340–2342. https://doi.org/10.1002/anie.199723401.

(225) Cao, R.; Rossdeutcher, R. B.; Zhong, Y.; Shen, Y.; Miller, D. P.; Sobiech, T. A.; Wu, X.; Buitrago, L. S.; Ramcharan, K.; Gutay, M. I.; Figueira, M. F.; Luthra, P.; Zurek, E.; Szyperski, T.; Button, B.; Shao, Z.; Gong, B. Aromatic Pentaamide Macrocycles Bind Anions with High Affinity for Transport across Biomembranes. *Nat. Chem.* **2023**, *15* (11), 1559–1568. https://doi.org/10.1038/s41557-023-01315-w.

(226) Lauer, J. C.; Bhat, A. S.; Barwig, C.; Fritz, N.; Kirschbaum, T.; Rominger, F.; Mastalerz, M. [2+3] Amide Cages by Oxidation of [2+3] Imine Cages – Revisiting Molecular Hosts for Highly Efficient Nitrate Binding. *Chem. – Eur. J.* **2022**, *28* (51), e202201527. https://doi.org/10.1002/chem.202201527.

(227) Samanta, J.; Tang, M.; Zhang, M.; Hughes, R. P.; Staples, R. J.; Ke, C. Tripodal Organic Cages with Unconventional CH···O Interactions for Perchlorate Remediation in Water. *J. Am. Chem. Soc.* **2023**. https://doi.org/10.1021/jacs.3c06379.

(228) Barišić, D.; Lešić, F.; Tireli Vlašić, M.; Užarević, K.; Bregović, N.; Tomišić, V. Anion Binding by Receptors Containing NH Donating Groups – What Do Anions Prefer? *Tetrahedron* **2022**, *120*, 132875. https://doi.org/10.1016/j.tet.2022.132875.

(229) Luo, N.; Li, J.; Yuan, L.; Wu, N.; Bao, X. Synthesis and Anion Binding Properties of Carbazole-Based Macrocycles with Bis-Sulfonamide and Bis-Amide Groups. *Tetrahedron* **2022**, *115*, 132795. https://doi.org/10.1016/j.tet.2022.132795.

(230) Ramírez Cortés, F.; Eigner, V.; Cuřínová, P.; Himl, M. Structurally Forced Ion Binding Affinity: Tetraurea-Based Macrocycle as a Receptor for Ion Pairs. *Eur. J. Org. Chem.* **2022**, *2022* (23), e202200422. https://doi.org/10.1002/ejoc.202200422.

(231) Chvojka, M.; Madea, D.; Valkenier, H.; Šindelář, V. Tuning CH Hydrogen Bond-Based Receptors toward Picomolar Anion Affinity via the Inductive Effect of Distant Substituents. *Angew. Chem. Int. Ed.* **2024**, *63* (5), e202318261. https://doi.org/10.1002/anie.202318261.

(232) Vogel, J.; Chen, Y.; Fadler, R. E.; Flood, A. H.; von Delius, M. Steric Control over the Threading of Pyrophosphonates with One or Two Cyanostar Macrocycles during Pseudorotaxane Formation. *Chem. – Eur. J.* **2023**, *29* (41), e202300899. https://doi.org/10.1002/chem.202300899.

(233) Kim, S. K.; Sessler, J. L. Calix[4]Pyrrole-Based Ion Pair Receptors. *Acc. Chem. Res.* **2014**, *47* (8), 2525–2536. https://doi.org/10.1021/ar500157a.

(234) Taylor, A. J.; Hein, R.; Patrick, S. C.; Davis, J. J.; Beer, P. D. Anion Sensing through Redox-Modulated Fluorescent Halogen Bonding and Hydrogen Bonding Hosts. *Angew. Chem. Int. Ed.* **2024**, *63* (6), e202315959. https://doi.org/10.1002/anie.202315959.

(235) Metzger, A.; Anslyn, E. V. A Chemosensor for Citrate in Beverages. *Angew. Chem. Int. Ed.* **1998**, *37* (5), 649–652. https://doi.org/10.1002/(SICI)1521-3773(19980316)37:5<649::AID-ANIE649>3.0.CO;2-H.

(236) Metzger, A.; Lynch, V. M.; Anslyn, E. V. A Synthetic Receptor Selective for Citrate. *Angew. Chem. Int. Ed. Engl.* **1997**, *36* (8), 862–865. https://doi.org/10.1002/anie.199708621.

(237) Xie, Y.; Chang, S.; Zhao, C.; Wang, F.; Liu, S.; Wang, J.; Delpire, E.; Ye, S.; Guo, J. Structures and an Activation Mechanism of Human Potassium-Chloride Cotransporters. *Sci. Adv.* **2020**, *6* (50), eabc5883. https://doi.org/10.1126/sciadv.abc5883.

(238) McCall, A. S.; Cummings, C. F.; Bhave, G.; Vanacore, R.; Page-McCaw, A.; Hudson, B. G. Bromine Is an Essential Trace Element for Assembly of Collagen IV Scaffolds in Tissue Development and Architecture. *Cell* **2014**, *157* (6), 1380–1392. https://doi.org/10.1016/j.cell.2014.05.009.

(239) Thomas, D. D.; Liu, X.; Kantrow, S. P.; Lancaster, J. R. The Biological Lifetime of Nitric Oxide: Implications for the Perivascular Dynamics of NO and O2. *Proc. Natl. Acad. Sci. U. S. A.* **2001**, *98* (1), 355–360.

(240) Gladwin, M. T.; Schechter, A. N.; Kim-Shapiro, D. B.; Feelisch, M. The Emerging Biology of the Nitrite Anion. *Nat. Chem. Biol.* **2005**, *1*, 308–314. https://doi.org/10.1038/nchembio1105-308.

(241) Beer, P. D.; Gale, P. A. Anion Recognition and Sensing: The State of the Art and Future Perspectives. *Angew. Chem. Int. Ed.* **2001**, *40* (3), 486–516. https://doi.org/10.1002/1521-3773(20010202)40:3<486::AID-ANIE486>3.0.CO;2-P.

(242) Romański, J.; Piątek, P. Selective Ammonium Nitrate Recognition by a Heteroditopic Macrotricyclic Ion-Pair Receptor. *J. Org. Chem.* **2013**, *78* (9), 4341–4347. https://doi.org/10.1021/jo4003322.

(243) Stefan-van Staden, R.-I.; Mincu, M.; van Staden, J. F.; Gugoasa, L. A. Molecular Recognition of Nitrites and Nitrates in Water Samples Using Graphene-Based Stochastic Microsensors. *Anal. Chem.* **2018**, *90* (16), 9997–10000. https://doi.org/10.1021/acs.analchem.8b02467.

(244) Barendt, T. A.; Docker, A.; Marques, I.; Félix, V.; Beer, P. D. Selective Nitrate Recognition by a Halogen-Bonding Four-Station [3]Rotaxane Molecular Shuttle. *Angew. Chem. Int. Ed.* **2016**, *55* (37), 11069–11076. https://doi.org/10.1002/anie.201604327.

(245) Davis, A. G.; Zakharov, L. N.; Pluth, M. D. Reversible Hydrosulfide (HS–) Binding Using Exclusively C–H Hydrogen-Bonding Interactions in Imidazolium Hosts. *Inorg. Chem.* **2024**, *63* (6), 3057–3062. https://doi.org/10.1021/acs.inorgchem.3c03922.

(246) Kang, S.-O.; Johnson, T. S.; Day, V. W.; Bowman-James, K. Pyridine-2,6-Dicarboxamide Pincer-Based Macrocycle: A Versatile Ligand for Oxoanions, Oxometallates, and Transition Metals *. *Supramol. Chem.* **2018**, *30* (4), 305–314. https://doi.org/10.1080/10610278.2017.1361534.

(247) Parks, F. C.; Liu, Y.; Debnath, S.; Stutsman, S. R.; Raghavachari, K.; Flood, A. H. Allosteric Control of Photofoldamers for Selecting between Anion Regulation and Double-to-Single Helix Switching. *J. Am. Chem. Soc.* **2018**, *140* (50), 17711–17723. https://doi.org/10.1021/jacs.8b10538.

(248) Pandian, T. S.; Srinivasadesikan, V.; Lin, M. C.; Kang, J. Nitrite Selective Anion Receptor Based on 1-Methyl-1*H*-Perimidine. *Tetrahedron* **2015**, *71* (40), 7782–7788. https://doi.org/10.1016/j.tet.2015.02.091.

(249) Alcalde, E.; Mesquida, N.; Pérez-García, L.; Alvarez-Rúa, C.; García-Granda, S.; García-Rodriguez, E. Hydrogen Bonded Driven Anion Binding by Dicationic [14]Imidazoliophanes. *Chem. Commun.* **1999**, No. 3, 295–296. https://doi.org/10.1039/A808503J.

(250) Cortese-Krott, M. M.; Kuhnle, G. G. C.; Dyson, A.; Fernandez, B. O.; Grman, M.; DuMond, J. F.; Barrow, M. P.; McLeod, G.; Nakagawa, H.; Ondrias, K.; Nagy, P.; King, S. B.; Saavedra, J. E.; Keefer, L. K.; Singer, M.; Kelm, M.; Butler, A. R.; Feelisch, M. Key Bioactive Reaction Products of the NO/H2S Interaction Are S/N-Hybrid Species, Polysulfides, and

Nitroxyl. *Proc. Natl. Acad. Sci.* **2015**, *112* (34), E4651–E4660. https://doi.org/10.1073/pnas.1509277112.

(251) Roobottom, H. K.; Jenkins, H. D. B.; Passmore, J.; Glasser, L. Thermochemical Radii of Complex Ions. *J. Chem. Educ.* **1999**, *76* (11), 1570. https://doi.org/10.1021/ed076p1570.

(252) Chou, J.-B.; Bahou, M.; Lee, Y.-P.; Rayner, D.; Simard, B. Isomers of GeNO and Ge(NO)2: Production and Infrared Absorption of GeNO and ONGeNO in Solid Ar. *J. Chem. Phys.* **2005**, *123* (5), 054321. https://doi.org/10.1063/1.1994851.

(253) Moore, S. S.; Tarnowski, T. L.; Newcomb, M.; Cram, D. J. Host-Guest Complexation. 4. Remote Substituent Effects on Macrocyclic Polyether Binding to Metal and Ammonium Ions. *J. Am. Chem. Soc.* **1977**, *99* (19), 6398–6405. https://doi.org/10.1021/ja00461a036.

(254) Hille, U. E.; Zimmer, C.; Vock, C. A.; Hartmann, R. W. First Selective CYP11B1 Inhibitors for the Treatment of Cortisol-Dependent Diseases. *ACS Med. Chem. Lett.* **2011**, *2* (1), 2–6. https://doi.org/10.1021/ml100071j.

(255) Dou, J.; Liu, Z.; Mahmood, K.; Zhao, Y. Synthesis of Poly(Ethylene Terephthalate) in Benzyl Imidazolium Ionic Liquids. *Polym. Int.* **2012**, *61* (9), 1470–1476. https://doi.org/10.1002/pi.4237.

(256) Sheldrick, G. M. *Bruker/Siemens Area Detector Absorption Correction Program*; Bruker AXS: Madison, WI, 1998.

(257) Sheldrick, G. M. Crystal Structure Refinement with SHELXL. *Acta Crystallogr. Sect. C Struct. Chem.* **2015**, *71* (1), 3–8. https://doi.org/10.1107/S2053229614024218.

(258) Haque, R. A.; Salman, A. W.; Budagumpi, S.; Abdullah, A. A.-A.; Abdul Hameed Al-Mudaris, Z. A.; Abdul Majid, A. M. S. Silver(I)-N-Heterocyclic Carbene Complexes of Bis-Imidazol-2-Ylidenes Having Different Aromatic-Spacers: Synthesis, Crystal Structure, and in Vitro Antimicrobial and Anticancer Studies. *Appl. Organomet. Chem.* **2013**, *27* (8), 465–473. https://doi.org/10.1002/aoc.3008.